PhD THESIS IN PHYSICS

NON-EQUILIBRIUM DYNAMICS OF VORTEX SYSTEMS IN SUPERCONDUCTORS

Alejandro B. Kolton

Daniel Domínguez	Alejandro B. Kolton	Francisco de la Cruz
ADVISOR	DOCTORAL CANDIDATE	SCIENTIFIC ADVISOR

May 2003

Instituto Balseiro
Universidad Nacional de Cuyo
Comisión Nacional de Energía Atómica
República Argentina

English translation of the original Spanish text

Abstract

In this thesis we numerically study the non-equilibrium steady dynamical regimes of driven vortex lattices in thin superconducting films and in strongly anisotropic layered superconductors with disorder. We analyze the non-equilibrium statistical mechanics and characterize the dynamical phases and transitions through experimentally accessible properties. We also study the non-equilibrium relaxation dynamics of a system of strongly localized electrons in an Anderson insulator.

In two-dimensional superconducting films we find that above the critical current F_c there are two dynamical phase transitions at F_p and F_t, which could be observed by simultaneous measurements of the longitudinal voltage and the transverse or Hall voltage. At F_p there is a transition from a plastic flow regime to a smectic flow regime in which the voltage noise is isotropic (Hall noise = longitudinal noise), and there is a peak in the differential resistance. At F_t there is a sharp transition to a frozen transverse solid where the Hall noise drops abruptly and vortex motion becomes localized in the transverse direction.

We find mode-locking steps in the current–voltage characteristics when an ac current is applied parallel or perpendicular to the dc current. For low frequencies there is mode-locking above a finite ac amplitude, while for high frequencies there is mode-locking for any small ac force. This is correlated with the nature of the longitudinal and transverse temporal order in the different regimes in the absence of the ac force. The synchronized state is a frozen solid pinned in the center-of-mass reference frame. In the case of longitudinal ac, depinning from the step shows plastic flow and hysteresis.

From a generalized fluctuation–dissipation relation we compute a transverse effective temperature in the moving fluid phase. We find that the effective temperature decreases with increasing driving force and is approximately equal to the equilibrium melting temperature of the unpinned system when the dynamical transverse freezing occurs. We also discuss how the effective temperature could be measured experimentally from a generalized Kubo formula.

We study the three-dimensional dynamical regimes of driven vortices in strongly layered superconductors with strong pinning. Above the critical current F_c, we find a plastic flow regime in which pancakes in different planes are decoupled, corresponding to a pancake gas. At a higher force F, there is a smectic flow regime with short-range interlayer order, corresponding to an entangled line liquid. At an even higher force, the transverse displacements freeze and the vortices become correlated along the c axis, resulting in a transverse solid. Finally, at a force F_s the longitudinal displacements freeze and we find a

coherent solid of rigid lines.

We study the slow non-equilibrium relaxation of electrons in an Anderson insulator by means of Monte Carlo simulations of the Efros–Shklovskii Coulomb glass model. The two-time correlation functions $C(t, t_w)$ show that at low temperatures the system falls out of equilibrium and displays simple aging, $C(t, t_w) \sim f(t/t_w)$, where t_w is the waiting time or "age" of the system. Upon increasing the temperature, stationarity is recovered after a long crossover. The results obtained agree with recent experiments in doped semiconductors and could also describe the relaxation of the vortex Bose glass in superconductors with columnar defects, in the variable-range-hopping regime, for magnetic fields $H_{c1} \ll B < B_\Phi$, where B_Φ is the matching field.

Contents

Abstract **i**

1 Introduction **5**
1.1 Vortices in superconductors 5
1.2 Vortex matter 9
1.2.1 Vortices in continuous isotropic superconductors 10
1.2.2 Pancake vortices in layered superconductors 13
1.2.3 Interactions between vortices: particle models 14
1.2.4 Motion: Lorentz force, pinning and dissipation 18
1.3 Langevin dynamics models of particles 21
1.3.1 Thin superconducting films 21
1.3.2 Strongly anisotropic layered superconductors 22
1.4 Organization of the thesis 24

2 Non-equilibrium dynamical regimes of vortices **27**
2.1 General discussion of the problem 27
2.2 Dynamical melting of the vortex lattice 34
2.3 Transport measurements 37
2.4 Dynamical structure of the vortex lattice 39
2.5 End of the moving crystal: what is there instead? 41

3 Transverse freezing in driven vortex lattices **55**
3.1 Motivation 55
3.2 Method 56
3.3 Results 56
3.3.1 Dynamical regimes 56
3.3.2 Temporal fluctuations: voltage noise and diffusion 61
3.4 Discussion 64
3.4.1 Model for anomalous longitudinal diffusion 64
3.4.2 Properties of the transverse solid 66
3.4.3 Analogy with supercooled liquids 67
3.4.4 Dynamical phases in two dimensions 68
3.4.5 Nature of the fast phase 69
3.4.6 Finite-temperature behavior 70

3.4.7 Comparison with experimental results . . . 71
3.5 Conclusions . . . 73

4 Driven vortices in layered superconductors: dynamical ordering along the c axis 75
4.1 Motivation . . . 75
4.2 Method . . . 76
4.3 Results . . . 77
4.3.1 Dynamical regimes . . . 77
4.3.2 Structural and dynamical correlations in the planes . . . 77
4.3.3 Dynamical ordering and fluctuations along the c axis . . . 79
4.4 Discussion . . . 84
4.4.1 Effect of the magnetic coupling between planes . . . 84
4.5 Conclusions . . . 85

5 Temporal synchronization in driven vortex lattices 87
5.1 Motivation . . . 87
5.2 Method . . . 89
5.3 Longitudinal mode-locking: $\mathbf{F}_{dc} \parallel \mathbf{F}_{ac}$ . . . 90
5.3.1 Temporal order at $F_{ac} = 0$ and mode-locking . . . 90
5.3.2 Dynamics and structure on the mode-locking steps . . . 91
5.3.3 Dependence on ac amplitude and frequency . . . 93
5.4 Transverse mode-locking: $\mathbf{F}_{dc} \perp \mathbf{F}_{ac}$ . . . 95
5.4.1 Temporal order at $F_{ac} = 0$ and mode-locking . . . 95
5.4.2 Trajectories and spectral response . . . 98
5.4.3 Dependence on ac frequency and amplitude . . . 98
5.5 Discussion . . . 100
5.5.1 A simple model to describe the steps . . . 100
5.5.2 Temporal order . . . 103
5.5.3 Non-linear effects of the ac force . . . 104
5.5.4 Important last-minute experimental results . . . 104
5.6 Conclusions . . . 107

6 Effective temperature in driven vortex lattices 109
6.1 Motivation . . . 109
6.2 Method . . . 110
6.3 Results . . . 113
6.3.1 Fluctuation–dissipation relations . . . 113
6.3.2 Transverse effective temperature . . . 113
6.3.3 Effective temperature from an experimentally accessible observable 114
6.4 Discussion . . . 115
6.4.1 Comparison with the “shaking” temperature . . . 115
6.4.2 Effective temperature of non-interacting vortices . . . 117
6.4.3 Can T_{ef}^{x} be defined at high velocities? . . . 126

6.4.4 Conclusions 128

7 Out-of-equilibrium relaxation in disordered systems with strongly localized states 131
7.1 Introduction 131
7.2 Interacting localized electrons 132
7.2.1 The Coulomb gap 132
7.2.2 Conductivity 134
7.2.3 Electron glass 136
7.3 Motivation 138
7.3.1 Slow non-equilibrium dynamics... of electrons? 138
7.3.2 Analogy between the electron glass and the vortex glass 139
7.4 Model and method 144
7.5 Results 145
7.5.1 One-particle density of states 146
7.5.2 Two-time correlation function 146
7.6 Discussion and conclusions 149

8 General conclusions 151

Bibliography 153

Chapter 1

Introduction

This thesis deals with some phenomenological aspects of disordered type II superconductors that are directly related to the collective non-equilibrium dynamics of vortex lattices. We aim to describe "vortex matter" out of equilibrium, when it is driven by applied external currents. In our study we have concentrated on those properties that are due to the dynamics of a large number of vortices and that can be explained (or perhaps predicted!) by reducing the extraordinary physical complexity underlying the existence of a vortex lattice in a superconducting material to a much simpler effective physics. This effective physics describes the motion of a set of well-defined classical objects, interacting among themselves, with external fields and with the disordered medium that hosts them. Besides making the problem numerically more tractable, this simplification makes the relation between the non-equilibrium physics of vortices and that of other disordered systems with many degrees of freedom more evident.

We devote section 1.1 of this introductory chapter to briefly recounting some of the most important advances achieved to date in the study of the intriguing but experimentally very accessible "vortex matter". In section 1.2 we present and briefly discuss the phenomenological justification of the models for the dynamics of point vortices used in this thesis: driven vortices in thin superconducting films and driven pancake vortices in strongly anisotropic layered superconductors. In section 1.3 we present the two Langevin dynamics models of interacting particles that we use for the numerical simulations. In section 1.4 we describe the organization of this thesis.

1.1 Vortices in superconductors

Since the discovery of superconductivity by Kamerlingh Onnes in 1911, many generations of physicists have devoted attention to the phenomenon. In 1935 Fritz and Heinz London developed a phenomenological theory that successfully describes the perfect conductivity and perfect diamagnetism of superconductors, based on constitutive relations suitable for their electrodynamic description [1]. In 1950 Fritz London showed that this theory could originate from considering superconductivity as a phenomenon in which the momentum $\mathbf{p}$ of the charge carriers has long-range order. The Bohr–Sommerfeld quantization on a

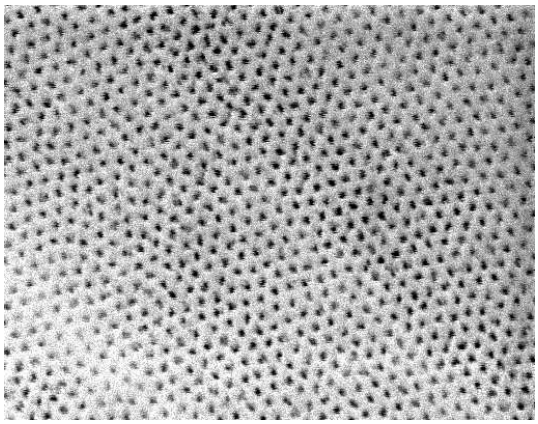


Figure 1.1: Image of a vortex lattice in $NbSe_2$ taken at the low temperature laboratory of Centro Atómico Bariloche using the Bitter decoration technique. Taken by Yanina Fasano [4].

torus $\oint \mathbf{p}_s \cdot d\mathbf{s} = nh$ then gives rise to the so-called fluxoid quantization [1]. Ginzburg and Landau [2] combined London's electrodynamics of superconductors with Landau's theory of phase transitions, creating a much more powerful phenomenological description of superconductivity. In this theory, the symmetry broken at the transition to the superconducting state is the $U(1)$ gauge symmetry of a complex order parameter Ψ.

Using the Ginzburg–Landau theory, Abrikosov [3] showed in 1957 that there exists a second class of superconductors in which the magnetic field (if it is large enough) can penetrate the sample as tubes of quantized flux that take the form of vortex lines. These lines minimize their interaction energy by arranging themselves in a triangular lattice, or "Abrikosov lattice". Figure 1.1 shows an image of the vortex lattice taken with the Bitter decoration technique (see for example [4, 5]).

Vortices are responsible for the reduction of the properties of perfect diamagnetism and perfect conductivity[1] in "type II" superconductors (to distinguish them from the first "type I" superconductors) over a wide region of the magnetic field–temperature ($H - T$) phase diagram known as the *mixed state*. The source of dissipation is the motion of the normal core of the vortex lines, driven by external transport currents. In pure type II superconductors in the mixed state both the $U(1)$ symmetry and the continuous translational symmetry are broken. The effect of thermal fluctuations in these superconductors, already studied in 1960, was considered negligible because of the large correlation lengths and low transition temperatures of conventional superconductors [6].

Static imperfections of superconducting materials tend to pin vortices and therefore represent a possible mechanism to recover perfect conductivity if the transport current is low enough. Typically, the static disorder present in samples can be modeled as a random array of pinning centers. Although it is also possible to have correlated pinning (natural during sample growth or artificially induced), in this thesis we will only consider

[1] In general we could say that the properties of perfect conductivity and diamagnetism are lost due to the appearance of different kinds of mobile magnetic structures induced by various mechanisms.

the effects of the ubiquitous uncorrelated point disorder. A first theory of the pinning of isolated vortex lines by Anderson and Kim [7] shows that, strictly speaking, dissipation vanishes only at $T = 0$, since thermally activated jumps of vortices are possible even at very low temperatures, leading to a finite dissipation. Larkin [8] extended this pinning theory to the Abrikosov vortex lattice, showing that long-range order is destroyed. The presence of disorder would then turn the Abrikosov vortex crystal into a structure with finite correlation lengths, asymptotically indistinguishable from a pinned vortex liquid.

The discovery of high critical temperature superconductors in 1986 by Bednorz and Müller [9] enormously renewed the interest in vortex physics. The pronounced anisotropies and high critical temperatures of these new materials make thermal fluctuations relevant in the mixed state, so that, for example, the melting of the vortex lattice is observed [10, 11]. The new phenomenology combined with the important advances achieved in the understanding of the statistical physics of disordered systems, such as spin glasses (see for example [12]), or systems with random fields in general. This led to a complete revision of the old picture left by Larkin, giving rise to the postulation of new and exotic vortex phases for clean or impure superconductors with different kinds of disorder. These phases are, for example, entangled and disentangled vortex liquids [13], and a whole variety of vortex glasses [14], such as the vortex glass [15], the Bragg glass [16, 17], and the Bose glass [18, 19]. The dynamical properties of vortices close to equilibrium are very different in each of the phases and therefore serve to characterize these new vortex liquids and glasses (see the review by Blatter *et al.* [14]).

So far we have mentioned the advances and the motivation for understanding the equilibrium physics of the vortex system with disorder. The non-equilibrium physics of the vortex lattice, on the other hand, which is the subject of this thesis, has in parallel received a great deal of attention for a long time, motivated mainly by transport measurements in superconductors. Fifty years ago Shoenberg noticed that magnetic structures in type I superconductors can be unstable in the presence of an electric current, and Gorter proposed that their motion is an important resistive mechanism in these superconductors [20]. Ten years later Gorter [21] and Anderson [22] extended this concept to the magnetic structures formed by vortex lines in the mixed state of type II superconductors, and Kim *et al.* were the first to obtain experimental evidence of this prediction [23]. An electric current $\mathbf{J}$ produces a Lorentz force that can move the vortices with a mean velocity $\mathbf{v}$, and as a consequence an electric field $\mathbf{E} = \mathbf{B} \times \mathbf{v}/c$ appears: this phenomenon made it possible to formulate the first theories of the motion of vortex lattices from transport measurements. These theories were developed mainly to explain IV curves, noise measurements and magnetic relaxation curves, as well as the electromagnetic response of type II superconductors to different kinds of excitations with time-dependent external currents or fields, etc. A milestone of this development was the formulation of the pioneering theories of Schmid and Hauger [24] and of Larkin and Ovchinnikov [25], motivated in particular by Fiory's observation in 1971 of steps in the current–voltage curves of superconducting films under the simultaneous action of dc and ac currents [26]. These are the first "microscopic" dynamical theories (this is how we will refer to the level of description of individual vortices), in which the total pinning energy is sensitive to the structure of the vortex lattice and to the nature of the disorder, and the coupled equations of motion of individual vortices are considered. However, these

pioneering theories only analyze the case of supposedly elastic moving vortex lattices, under weak disorder conditions, leaving dormant another interesting phenomenology (of collective effects), which, as we will see later, is the one that motivates all the work of this thesis.

As mentioned above, the discovery of high critical temperature superconductors brought with it the interest in the equilibrium statistical physics of vortices. It also motivated the interest in the non-equilibrium statistical physics of the vortex system, since it immediately became necessary to understand what kind of collective dynamical effects could occur in a vortex lattice moving over a disordered potential in the presence of thermal fluctuations. In 1993 Bhattacharya and Higgins observed dramatic effects near the so-called peak effect, which led them to construct an experimental dynamical phase diagram [27]. The interpretation of such a diagram was enriched by an experimental result obtained 20 years earlier by Thorel [28], who, using neutron diffraction, had obtained evidence of the development of positional correlations between vortices upon increasing the transport current. In 1994 Koshelev and Vinokur [29] proposed the first phenomenological model of a dynamical melting transition of the vortex lattice, drawing an analogy between the out-of-equilibrium vortex system and an equilibrium vortex system with a fictitious temperature, a temperature that would in principle incorporate the whole effect of the static disorder on the moving lattice. This work opened up an entire line of experimental, theoretical and numerical simulation work, the line within which the research of this thesis is framed.

Thanks to the use of new concepts and more powerful computational techniques, generally developed earlier for the study of other related systems, important advances have been made over the pioneering phenomenological model of Koshelev and Vinokur [29], above all in the large-scale description of the vortex lattice. However, the nature of the possible non-equilibrium dynamical phases and transitions of the vortex lattice is still today a controversial issue, both from the theoretical and the experimental point of view. As a function of the external current, the temperature, the disorder strength and the dimensionality, various possible dynamical phases with distinctive properties have been proposed theoretically, in which the moving vortices form anisotropic structures with long-range, quasi-long-range or short-range order, and in which the flow of the lattice can be elastic, plastic, or a combination of both. The theoretical controversy, of course, originates in the fact that dynamical phases with incompatible properties have been predicted for the same conditions or range of external parameters. On the other hand, new experimental observations, such as metastability and history effects, or the dynamical effects induced by the edges of superconducting samples, have generated, besides more questions to be solved, a more cautious attitude when interpreting experimental results in favor of one theory or another. Finally, numerical simulations, which often play the role of "intermediary" between analytical theories and experiments, can also produce apparently ambiguous results. Perhaps one of the most important and non-trivial emerging questions in this respect is to better understand finite-size and finite-time effects in non-equilibrium situations. Understanding the non-equilibrium physics of the vortex lattice in disordered superconductors is therefore a very current challenge, which demands not only further refinements in experiments, theories and numerical simulations, but also the resolution of

some fundamental questions.

To conclude this brief general introduction, it is worth stressing that the study of vortex systems out of equilibrium has many general motivations from the point of view of basic research: (i) The creation of general concepts and tools to describe condensed matter out of equilibrium in the presence of disorder is an important theoretical challenge. (ii) Vortex systems are unique experimental systems in condensed matter, where one can easily vary the density, introduce external forces and perturbations of different kinds in a controlled way, and study the combined effect of disorder and thermal fluctuations. (iii) Many other physical systems present a similar effective physics: Josephson junction arrays, magnetic domain walls, wetting contact lines, colloids, magnetic bubbles, liquid crystals, charge density waves, electron Wigner crystals, Luttinger liquids, crystal surface growth, domain walls in incommensurate solids, etc. [30–32]

1.2 Vortex matter

Physical systems that can be analyzed in terms of a set of many interacting bodies driven through disordered media are found very often in nature, and I believe a few very general observations suffice to convince us that the phenomenological physical description of such systems can become extremely rich. The phenomenological approach requires us to place ourselves at a given time, length and energy scale. This makes the effective physics describing the interaction of one body with the others, with the external fields and with the medium, as well as the dynamical laws governing the motion, possibly very particular. The very modeling of the system in terms of certain bodies with some permanence and distinguishability, interacting among themselves and moving in a given medium with which they exchange energy in a certain way, depends on this effective physics. The "bodies" in question can thus be objects of varied complexity and, depending on the case, their internal degrees of freedom may be relevant or irrelevant for describing, at the desired level of description, the transport of the whole structure under the action of a driving force. Moreover, even when the "permanence" of the bodies is guaranteed, depending on the situation it could happen that their distinguishability is lost (as happens for example with systems of identical particles in quantum physics or, more generally, with bodies that are ultimately more or less localized excitations of some field). Finally, let us note that however weak the static disorder in the medium may be, it plays a crucial role: disorder breaks translational symmetry, making even a uniform translation of the system something non-trivial in principle, and generating a dynamical competition among the different energy scales of the system.

The vortex system in superconductors is undoubtedly a paradigmatic example of the class of systems mentioned above. Vortices can be described as well-defined interacting "bodies" over a wide region of the phase diagram of type II superconductors, and they can be driven by external currents through the medium constituted by the disordered superconducting material, with which they also interact and exchange energy. Although the vortex system owes its existence to the complex macroscopic quantum phenomenon of superconductivity, the simple effective physics describing vortices as interacting classical

objects is enough to understand and predict well many experimentally observable properties of superconductors involving many vortices. It is from this perspective that we have carried out our research work.

To build a simple model for vortex transport we need to know: (i) how a vortex is defined, what its internal degrees of freedom are, what its stability is and under which conditions vortices exist; (iii) how vortices interact with each other; (iv) how they interact with an external current; (ii) how they interact with the disordered medium; (v) how they move and exchange energy with the disordered medium; (vi) how the disorder is described. In the following sections we intend to briefly answer these questions, based on the basic phenomenology of superconductors. The Ginzburg–Landau theory in the London approximation is a very convenient starting point, but to answer all the questions it must be supplemented with some results from time-dependent theories. The following sections are meant to serve as a reference or quick guide to the phenomenology behind the models. For more details we recommend consulting, for example, references [14, 33–35].

1.2.1 Vortices in continuous isotropic superconductors

In the phenomenological theory of Ginzburg and Landau, a complex order parameter $\Psi(\mathbf{r}) = |\Psi(\mathbf{r})|e^{i\phi(\mathbf{r})}$ is coupled in a gauge-invariant way to the magnetic field, described by the vector potential $\mathbf{A}(\mathbf{r})$. The density of superconducting charge carriers $n_s(\mathbf{r})$ (or Cooper pairs) of London's theory [1] is given by $n_s(\mathbf{r}) = |\Psi(\mathbf{r})|^2$. The Ginzburg–Landau free energy functional [2] is basically given by

$$H_{GL} = \int d^d r \left\{ \alpha|\Psi|^2 + \frac{\beta}{2}|\Psi|^4 + \frac{1}{2m^*}\left|\left(\frac{\hbar}{i}\nabla - \frac{e^*}{c}\mathbf{A}\right)\Psi\right|^2 + \frac{|\mathbf{B}|^2}{8\pi}\right\} \tag{1.1}$$

where $\beta > 0$, $\alpha(T) \propto (T - T_{c0})$, T_{c0} is the mean-field transition temperature, $\mathbf{B} = \nabla \times \mathbf{A}$ is the magnetic field, and m^*, e^* are the mass and the charge of a Cooper pair, respectively. The free energy (1.1) has two characteristic lengths, the coherence length ξ and the penetration depth λ, which are given by

$$\xi^2(T) = \frac{\hbar^2}{2m^*|\alpha(T)|} \tag{1.2}$$

$$\lambda^2(T) = \frac{m^* c^2}{4\pi|\Psi_0|^2 e^{*2}} \tag{1.3}$$

where $|\Psi_0|^2 = |\alpha|/\beta$ denotes the saturation value of $|\Psi|^2$ in a homogeneous state for $T < T_{c0}$ and $\mathbf{B} = 0$. In a *mean-field theory* the energy of Eq. (1.1) is minimized with respect to the fields $\Psi(\mathbf{r})$ and $\mathbf{A}(\mathbf{r})$, giving rise to the Ginzburg–Landau differential equations [2] for $\Psi(\mathbf{r})$ and $\mathbf{A}(\mathbf{r})$,

$$\alpha\Psi + \beta|\Psi|^2\Psi + \frac{1}{2m^*}\left(\frac{\hbar}{i}\nabla - \frac{e^*}{c}\mathbf{A}\right)^2\Psi = 0 \tag{1.4}$$

$$\mathbf{J} = \frac{c}{4\pi}\nabla \times \mathbf{B} = \frac{e^*}{m^*}|\Psi|^2\left(\hbar\nabla\phi - \frac{e^*}{c}\mathbf{A}\right) \tag{1.5}$$

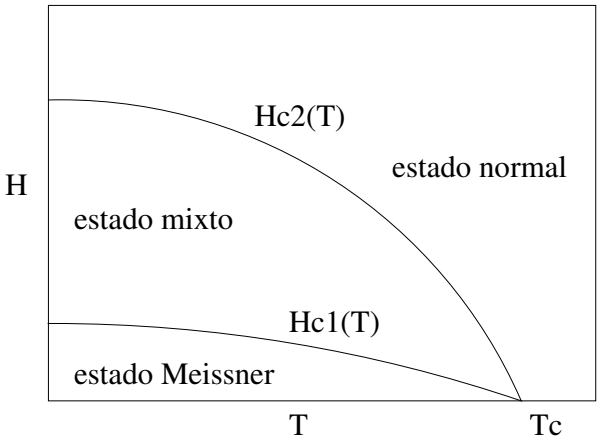


Figure 1.2: Mean-field phase diagram of a type II superconductor (labels: *estado normal* = normal state, *estado mixto* = mixed state, *estado Meissner* = Meissner state). In the mixed state the magnetic field induces the formation of a vortex lattice (see Fig. 1.1).

The solutions of these equations can be clearly separated by the value of $\kappa = \lambda/\xi$. For $\kappa < 1/\sqrt{2}$ (type I superconductors), mean-field theory gives, for $T < T_{c0}$ and $H < H_c(T)$, a resistanceless and perfectly diamagnetic phase (Meissner state). For $\kappa > 1/\sqrt{2}$ (type II superconductors) perfect diamagnetism exists only up to the field $H_{c1} \approx (H_{c2}/2\kappa^2)(\ln\kappa + 0.08)$, where $H_{c2} = \Phi_0/2\pi\xi^2$ is the upper critical field above which the material becomes normal. Above H_{c1} the magnetic flux penetrates, quantized, in the form of *vortex lines*, each one carrying the flux quantum $\Phi_0 = hc/e^*$, in a region of the phase diagram known as the mixed state. In the absence of disorder the vortex lines form the triangular Abrikosov lattice with lattice parameter $a_0 = (2/\sqrt{3})^{1/2}(\Phi_0/B)^{1/2}$. The mean-field $H - T$ phase diagram is shown in Fig. 1.2 and the structure of an isolated vortex in Fig. 1.3.

Vortex lines are topological defects of the superconducting order parameter, energetically favorable and stable in the mixed state, when the magnitude of the applied magnetic field H satisfies $H_{c1} < H < H_{c2}$. However, one must keep in mind that this is a mean-field result, obtained from Eqs. (1.5) that minimize the Ginzburg–Landau functional. In this approximation thermal fluctuations affect the order parameter only uniformly, through the temperature dependence of the parameters α and β in the Ginzburg–Landau free energy. Spatial fluctuations of the order parameter in this approximation are due only to the presence of the vector potential $\mathbf{A}$. In high-T_c superconductors, however, thermal fluctuations can become very important, giving rise to finite-lifetime fluctuations of the modulus of the order parameter in the form of vortex-line "loops" or vortex–antivortex pairs. It is worth mentioning that besides thermal fluctuations there are other mechanisms (for example with static disorder and large applied currents) that can also give rise to this kind of excitations, which are not described in the mean-field approximation. In this thesis we will concentrate on situations where the mentioned effects are negligible, vortices being well-defined objects induced only by the applied magnetic field. Thermal effects will interest us only in relation to the dynamics of stable vortex lines.

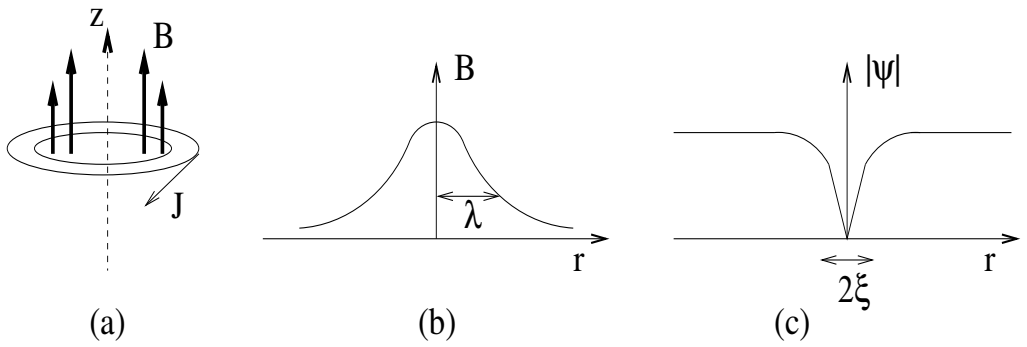


Figure 1.3: Structure of an isolated vortex aligned with the z axis. (a) Sketch of the superconducting currents and magnetic field lines around the vortex. (b) Radial profile of the magnetic field showing the magnetic penetration depth λ. (c) Radial profile of the modulus of the superconducting order parameter $|\psi|$ showing the coherence length ξ.

Two main approximations have been used to treat the vortex system: the lowest Landau level approximation, valid sufficiently close to H_{c2}, and the *London approximation*, valid at intermediate and low fields $B \lesssim 0.2H_{c2}$, where $\xi \ll (\Phi_0/B)^{1/2}$. In the London approximation the inhomogeneities of the modulus of the order parameter are neglected, taking $|\Psi| = |\Psi_0|$. This leads to a divergence of the energy density at the position of the vortex cores $\mathbf{r}_i(s)$, where i labels a particular vortex and s parametrizes the line. In the London approximation the Ginzburg–Landau functional takes the form

$$H_{London} = \int d^d r \left\{ \frac{\hbar^2 |\Psi_0|^2}{2m^*} \left| \left(\nabla\phi - \frac{2\pi}{\Phi_0}\mathbf{A} \right) \right|^2 + \frac{|\mathbf{B}|^2}{8\pi} \right\} \tag{1.6}$$

This functional has to be regularized near the vortex cores by excluding tubes of radius ξ from the integration volume. The phase of the order parameter is multivalued, since ϕ must change by 2π along a path enclosing a vortex. Apart from the reduction in the number of degrees of freedom, the advantage of the London functional over the Ginzburg–Landau one is that its minimization gives rise to *linear* equations for the fields ϕ and $\mathbf{A}$. Using the multivaluedness condition of the phase around the vortices, the London equations can be written in terms of the positions $\mathbf{r}_i(s)$ of the vortex lines and the magnetic field $\mathbf{B}(\mathbf{r})$ only (see for example [35]),

$$\lambda^2 \nabla^2 \mathbf{B}(\mathbf{r}) - \mathbf{B}(\mathbf{r}) = \Phi_0 \mathbf{m}(\mathbf{r}) \tag{1.7}$$

where $\mathbf{m}(\mathbf{r})$ is the vortex density field,

$$\mathbf{m}(\mathbf{r}) = \sum_i m_i \int ds \, \frac{d\mathbf{r}_i(s)}{ds} \, \delta(\mathbf{r}_i(s) - \mathbf{r}) \tag{1.8}$$

with $m_i = \pm 1$ the vorticity. The magnetic field $\mathbf{B}$ in the London approximation is then determined solely by the given vortex density. Using Eq. (1.5) in the functional (1.6) we obtain the London energy,

$$E_{London} = \frac{1}{8\pi} \int d^d r \left\{ \lambda^2 |\nabla \times \mathbf{B}|^2 + |\mathbf{B}|^2 \right\} \tag{1.9}$$

The first term of E_{London} represents the kinetic energy of the supercurrents and the second one the energy of the magnetic field. In the presence of vortices one must remember to exclude a tube of radius ξ containing each of the vortex lines. We can now compute the energy of any vortex configuration given by $\mathbf{m}(\mathbf{r})$ by inserting the corresponding solution $\mathbf{B}$ of Eq. (1.7) into Eq. (1.9) (see for example [33]).

1.2.2 Pancake vortices in layered superconductors

High critical temperature superconductors have a layered structure that can be modeled as a stack of thin superconducting films of thickness $d \ll \lambda$, separated by a distance $s > d$. One must distinguish here between the *intrinsic* penetration depth λ of the superconducting material of the planes, and the penetration depths of the sample in the directions parallel, $\lambda_\parallel$, and perpendicular, $\lambda_\perp$, to the planes. The small separation s between planes makes Cooper-pair tunneling possible, giving a *Josephson coupling* between planes along the stacking direction c. The order parameter $\Psi_n = |\Psi_n| \exp(i\phi_n)$ is defined only in the planes, and since in general $\lambda_\parallel \gg \xi_\parallel$ we can make the London approximation taking $|\Psi_n| = \text{const}$ (except in the vortex cores). The London functional for continuous isotropic superconductors (Eq. 1.6) is replaced by the Lawrence–Doniach functional [36],

$$H_{LD} = E_0 \sum_n \int d^2r \left\{ \frac{1}{2} \left(\nabla\phi_n - \frac{2\pi}{\Phi_0} \mathbf{A_n} \right)^2 + \frac{1}{\lambda_J^2} (1 - \cos\gamma_{n,n+1}) \right\} + \int d^3r \, \frac{|\mathbf{B}|^2}{8\pi} \tag{1.10}$$

where $\nabla = (\partial/\partial x, \partial/\partial y)$, $\mathbf{A}_n(\mathbf{r}) \equiv \mathbf{A}(\mathbf{r}, z = ns)$ is the vector potential in layer n, $E_0 = \frac{\Phi_0^2 s}{16\pi^3 \lambda_\parallel^2}$, and

$$\gamma_{n,n+1} = \phi_n - \phi_{n+1} - \frac{2\pi}{\Phi_0} \int_{ns}^{(n+1)s} dz \, A_z \tag{1.11}$$

is the gauge-invariant phase difference between planes n, $n+1$. Minimizing the functional H_{LD} of Eq. (1.10) one obtains, in a mean-field theory, equations for ϕ_n and $\mathbf{A}_n$. Complemented with Maxwell's equations, these equations close a system that can be solved for ϕ_n and $\mathbf{A}_n$. In this model vortex lines are represented as stacks of "pancake" vortices confined to the superconducting planes. Bulaevskii *et al.* [37] showed that the energy of a vortex line (with one pancake in each plane), expressed in terms of the positions of the pancakes, consists of equally important two-, three- and four-pancake interactions, the last two being due to the interaction of Josephson strings formed between pairs of pancakes in neighboring planes. We see then that already for a single vortex line a numerical treatment of the problem in terms of interacting pancakes becomes very difficult, due to the Josephson effect. However, the Josephson coupling can be neglected in the case of extreme anisotropy $\gamma = \xi_\parallel/\xi_\perp = \lambda_\perp/\lambda_\parallel \gg 1$. This is because $\lambda_J = s\gamma \gg 1$, and therefore the maximum Josephson supercurrent $J_0 \propto \lambda_J^{-2} \to 0$ (and therefore the Josephson term in Eq. 1.10 disappears). In this case the interactions are only between pairs of pancakes and are of purely magnetic origin. Clem [38] computed the resulting magnetic interaction between pancakes in the same plane and pancakes in different planes (see section 1.2.3).

1.2.3 Interactions between vortices: particle models

The great advantage of the London equations (1.7) is that they are linear. This allows us to compute $\mathbf{B}(\mathbf{r})$ for a vortex configuration $\mathbf{m}(\mathbf{r})$ by superposing the solutions $\mathbf{B}_i(\mathbf{r})$ of individual vortices. Evaluating expression (1.9) with the solution $\mathbf{B}(\mathbf{r})$ one obtains the corresponding energy $H(\{\mathbf{r}_i(s)\})$ of the configuration. Since the superposition principle holds, it is possible to decompose $H(\{\mathbf{r}_i(s)\})$ into a sum of contributions due to individual vortices and contributions due to pairs of vortices. The former give the energy associated exclusively with the internal degrees of freedom of the vortex line (self-energy), while the latter are the vortex–vortex interaction energies we are looking for in this section. We will analyze the simplest cases, in which the dynamics of the internal degrees of freedom of the vortices can be neglected. Under this assumption all vortices are identical in shape and can be characterized solely by a position vector $\mathbf{r}_i$. The models we will arrive at will therefore be *interacting particle models*. We will first consider, only for the sake of comparison, the unrealistic case of straight parallel vortices in thick superconducting films. Then we will consider the cases analyzed in this thesis: vortices in thin superconducting films and pancake vortices in strongly anisotropic layered superconductors.

Thick superconductors

Consider a straight isolated vortex in a superconductor of thickness d with $\mathbf{m}(\mathbf{r}) = \delta_2(\mathbf{r})\hat{z}$, where $\mathbf{r}$ represents the position vector in the xy plane. Eq. (1.7) written in cylindrical coordinates (ρ, θ, z) becomes

$$\lambda^2 \nabla^2 \mathbf{B}(\mathbf{r}) - \mathbf{B}(\mathbf{r}) = \Phi_0 \hat{z}\, \delta(\rho) \tag{1.12}$$

If $d \gg \lambda$ we can neglect edge effects, so that this equation does not depend on z and has the exact solution

$$\mathbf{B}_v(\mathbf{r}) = \hat{z}\, \frac{\Phi_0}{2\pi\lambda^2} K_0\!\left(\frac{\rho}{\lambda}\right) \tag{1.13}$$

Replacing the single-vortex solution $\mathbf{B}_v$ of Eq. (1.13) into Eq. (1.9), and dividing by the thickness d, we obtain the *line energy* of a vortex,

$$\epsilon_v = \left(\frac{\Phi_0}{4\pi\lambda}\right)^2 \ln\kappa \tag{1.14}$$

Even if the vortex is not straight, one can show that its energy per unit length is also given by (1.14) in this approximation. The vortex is therefore a one-dimensional *elastic* object. Since the modified London equations (1.7) are linear, we can use the solution $\mathbf{B}_v$ of Eq. (1.13) just obtained to compute the interaction energy between two straight vortices at positions $\mathbf{r}_1$ and $\mathbf{r}_2$ in the xy plane, replacing $\mathbf{B}(\mathbf{r}) = \mathbf{B}_v(\mathbf{r} - \mathbf{r}_1) + \mathbf{B}_v(\mathbf{r} - \mathbf{r}_2)$ in Eq. (1.9). The London energy per unit length then consists of a term representing the line energies of each vortex, independent of the positions $\mathbf{r}_1$ and $\mathbf{r}_2$, plus a vortex–vortex interaction energy per unit length of the form

$$U_v(\mathbf{r_{12}}) = \frac{\Phi_0}{4\pi}\mathbf{B}_v(\mathbf{r}_1 - \mathbf{r}_2) = \frac{\Phi_0}{8\pi^2\lambda^2} K_0\!\left(\frac{r_{12}}{\lambda}\right) \tag{1.15}$$

where $r_{12} = |\mathbf{r}_1 - \mathbf{r}_2|$. The asymptotic forms of U_v are

$$U_v(\mathbf{r}) \approx \frac{\Phi_0}{8\pi^2\lambda^2}\left[\ln\frac{\lambda}{\rho} + 0.12\right] \qquad \rho \ll \lambda \tag{1.16}$$

$$U_v(\mathbf{r}) \approx \frac{\Phi_0}{8\pi^2\lambda^2}\left(\frac{\pi\lambda}{2\rho}\right)e^{-\rho/\lambda} \qquad \rho \gg \lambda \tag{1.17}$$

The interaction force $\mathbf{F}_v$ exerted by vortex 1 on vortex 2 is then

$$\mathbf{F}_v(\mathbf{r}_{12}) = \frac{\Phi_0}{8\pi^2\lambda^3}K_1\left(\frac{r_{12}}{\lambda}\right)\hat{\mathbf{r}}_{12} = \mathbf{J}_v(\mathbf{r}_1 - \mathbf{r}_2)\times\hat{z}\frac{\Phi_0}{c} \tag{1.18}$$

where in the last equality we have used that $\nabla\times\mathbf{B}_v(\mathbf{r}) = 4\pi\mathbf{J}_v(\mathbf{r})/c$, with $\mathbf{J}_v(\mathbf{r})$ the current distribution of a vortex. The interaction force in the London approximation between straight parallel vortices, with their magnetic fluxes pointing in the same direction, is therefore repulsive and *short-ranged* in thick superconductors.

It is worth mentioning here that the third equality in Eq. (1.18) is general. A vortex at position $\mathbf{r}$ in the presence of a superconducting current density $\mathbf{J}$, not including the one it generates itself, experiences a "Lorentz force" per unit length

$$\mathbf{F}_v(\mathbf{r}) = \mathbf{J}(\mathbf{r})\times\hat{z}\frac{\Phi_0}{c} \tag{1.19}$$

This is the expression we will use for the force experienced by a vortex due to an external current density $\mathbf{J}$. We will justify this result later.

Thin superconducting films

In thin superconducting films such that $d \ll \lambda$ the results derived above are not valid, since the superconducting currents inside the film depend strongly on the boundary conditions. To find the interaction energy between vortices in a thin film, Pearl solved [39] Eq. (1.7) with a vortex at the origin of the film. The current distribution $\mathbf{K}$ is confined to the superconducting plane located at $z = 0$. The solution for the vector potential is

$$\mathbf{A}(\rho, z) = \hat{\phi}\frac{\Phi_0}{2\pi}\int_0^\infty dq\,\frac{J_1(q\rho)}{1+q\Lambda}e^{-q|z|} \tag{1.20}$$

where $\Lambda = 2\lambda^2/d$ is the *effective penetration depth*. A sketch of the magnetic field lines $\mathbf{B} = \nabla\times\mathbf{A}$ is shown in Fig. 1.4 (left). The two-dimensional current distribution $\mathbf{K}(\rho) = \hat{\phi}(c/4\pi)[b_\rho(\rho, 0^+) - b_\rho(\rho, 0^-)]$ then turns out to be

$$\mathbf{K}(\mathbf{r}) = \hat{\phi}\frac{c\Phi_0}{8\pi\Lambda^2}\left[H_1\left(\frac{\rho}{\Lambda}\right) - Y_1\left(\frac{\rho}{\Lambda}\right) - 2/\pi\right] \tag{1.21}$$

where $\Lambda = 2\lambda^2/d$ is the *effective penetration depth*, H_1 is the Struve function and Y_1 the Bessel function of the second kind.

We can use Eq. (1.19) to compute the force exerted by one vortex on another at a distance ρ: $\mathbf{F}(\rho) = \mathbf{K}(\rho) \times \hat{z}\Phi_0/c$. From this force we can compute the interaction potential between vortices

$$U_v(\mathbf{r}) = \frac{\Phi_0^2}{8\pi\Lambda}\left[H_0\Big(\frac{\rho}{\Lambda}\Big) - Y_0\Big(\frac{\rho}{\Lambda}\Big)\right] \tag{1.22}$$

The asymptotic forms of this potential are

$$U_v(\mathbf{r}) \approx \frac{\Phi_0^2}{4\pi^2\Lambda}\ln\left(\frac{\Lambda}{\rho}\right) \qquad \rho \ll \Lambda \tag{1.23}$$

$$U_v(\mathbf{r}) \approx \frac{\Phi_0^2}{4\pi^2\rho} \qquad \rho \gg \Lambda \tag{1.24}$$

Therefore the interaction between vortices (of equal vorticity) in a thin film is *long-ranged*, unlike what happens in thick superconductors (Eq. 1.18).

Strongly anisotropic layered superconductors

As mentioned in section 1.2.2, the physics of vortices in highly anisotropic layered superconductors reduces to that of interacting pancakes confined to the superconducting planes. The absence of Josephson coupling in the limit of extreme anisotropy makes it possible to express the total interaction energy between pancakes (in the London approximation) as a sum of purely magnetic pairwise interaction energies. Since each of the planes is a superconducting film of thickness $d \ll \lambda$, Clem's calculation [38] can be thought of as an extension of Pearl's problem: one now has to compute the field due to a pancake at the origin of the plane $z = 0$, within a periodic stack of superconducting planes at $z = ns$, with n integer. The limit $s \to \infty$ must correspond to Pearl's solution, sec. 1.2.3. The solution for $\mathbf{B}$ is [38]

$$\mathbf{B}(\rho, z) = \hat{z}\frac{\Phi_0}{2\pi\Lambda r}e^{-r/\lambda_\parallel} + \hat{\rho}\frac{\Phi_0}{2\pi\Lambda\rho}\left[(z/|z|)e^{-|z|/\lambda_\parallel} - (z/r)e^{-r/\lambda_\parallel}\right] \tag{1.25}$$

A sketch of the magnetic field lines is shown in Fig. 1.4 (right). Using that $\mathbf{F}(\rho, z) = \mathbf{K}(\rho, z) \times \hat{z}\Phi_0/c$, the force exerted by the pancake at the origin on another one at $(\mathbf{r}, z) = (\hat{\rho}\rho, z_n)$ turns out to be

$$\mathbf{F}(\rho, 0) = \hat{\rho}\frac{\Phi_0^2}{4\pi^2\Lambda\rho}\left[1 - \frac{\lambda_\parallel}{\Lambda}\left(1 - e^{-\rho/\lambda_\parallel}\right)\right] \tag{1.26}$$

$$\mathbf{F}(\rho, z_n) = -\hat{\rho}\frac{c\Phi_0\lambda_\parallel}{4\pi^2\Lambda^2\rho}\left[e^{-|z_n|/\lambda_\parallel} - e^{-r_n/\lambda_\parallel}\right] \qquad n \neq 0 \tag{1.27}$$

where $z_n = ns$ with n integer, $\rho = |\mathbf{r}|$, $r_n = \sqrt{\rho^2 + z_n^2}$. We see then that the interaction between pancakes in the same plane is *repulsive* and logarithmic at all distances, not only within the range Λ as happens in isolated films (see Eq. 1.22). The interaction between pancakes in different planes is also logarithmic but *attractive*, favoring the coaxial alignment of pancakes, or the formation of straight vortex lines. Since generally $\lambda_\parallel/\Lambda \ll 1$,

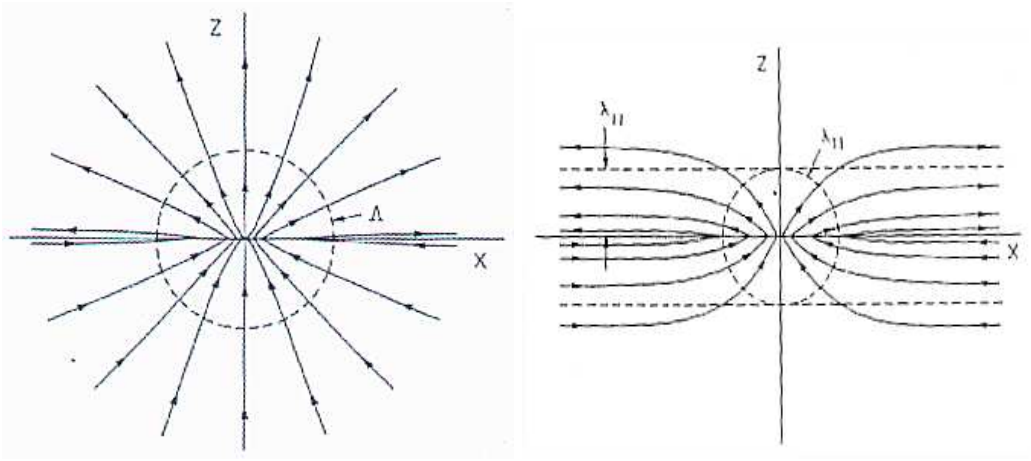


Figure 1.4: Magnetic field lines generated by a two-dimensional pancake vortex in a thin superconducting film. Left: the film, with effective penetration depth Λ, is isolated. Note the different behavior for $r > \Lambda$ and $r < \Lambda$. Right: the film is the central layer of a stack of parallel superconducting planes separated by a distance $s \ll \lambda_\parallel$ (not shown), where $\lambda_\parallel$ is the penetration depth of the layered superconductor in the direction parallel to the planes. The superconducting currents of the other planes screen the magnetic field of the pancake and the flux is essentially guided radially to infinity within a disk of radius $\lambda_\parallel$.

this attractive interaction is much weaker than the repulsive one between pancakes in the same plane.

In Fig. 1.4 we show the magnetic field distribution for a pancake in an isolated thin superconducting film and for a pancake in a stack of thin superconducting films. We can see that in the layered superconductor the field of the pancake is screened in the z direction by the superconducting currents in the other planes. This screening is what controls the exponential decay of the attractive interaction between pancakes in different planes. It is worth mentioning that the vortex models of the previous two subsections can be obtained as limiting cases of Clem's model. The solution of Eq. (1.20) for a vortex in a thin superconducting film corresponds to the limit $s \to \infty$ of Clem's solution, Eq. (1.25). The solution for a straight vortex in a thick superconductor is obtained by summing the contributions given by Eq. (1.25) of an infinite stack of pancakes coaxially aligned along the z axis, taking $s \to 0$. Clem's model for layered superconductors thus makes it possible, in some way, to describe internal degrees of freedom of vortex lines in thick samples, through the degrees of freedom of a stack of aligned pancakes. Since the coupling between pancakes in different planes is weak, the model also makes it possible to describe the phenomena of entanglement, cutting and reconnection of vortex lines. This gives rise to an interesting phenomenology along the c axis of the superconductor, which we will analyze in chapter 4.

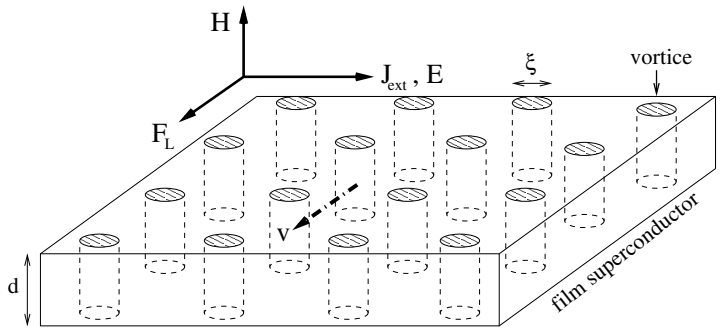


Figure 1.5: Geometry of the transport problem. The superconducting sample can be an isolated thin film or one of the superconducting planes of a layered superconductor. The magnetic field $\mathbf{H}$ induces the vortex lattice, whose vortices move with a velocity $\mathbf{v}$ in response to a Lorentz force $\mathbf{F}_L = \mathbf{J}_{ext} \times \mathbf{\Phi}/c$ originating from an external current $\mathbf{J}_{ext}$. The motion of the vortex lattice induces a macroscopic electric field $\tilde{\mathbf{E}} = \tilde{\mathbf{B}} \times \mathbf{v}/c$. In the figure we have neglected the Magnus force.

1.2.4 Motion: Lorentz force, pinning and dissipation

Consider a flat type II superconducting sample, like the one in Fig. 1.5 (which in this thesis may be either an isolated thin superconducting film or one of the CuO_2 planes of a strongly anisotropic layered superconductor) in the presence of a transverse magnetic field $\mathbf{H}$ strong enough to induce a lattice of pancake vortices. We are interested in the two-dimensional transport problem in the film. We will apply an external current $\mathbf{J}_{ext} = \hat{x} J_{ext}$ in the direction perpendicular to $\mathbf{H} = H\hat{z}$, and parallel to the wide surface of the superconducting film or to the *ab* planes of the layered superconductor. Phenomenologically it is found that, when the transport current J_{ext} is strong enough, the vortex structure reaches a steady state with a velocity $\mathbf{v}$ that satisfies the equation

$$\frac{\mathbf{J}_{ext} \times \mathbf{\Phi}}{c} - f n_s \frac{\mathbf{v} \times \mathbf{\Phi}}{c} - \mathbf{f}_p - \eta \mathbf{v} = 0 \tag{1.28}$$

where a Lorentz force $\mathbf{J}_{ext} \times \mathbf{\Phi}/c$ is balanced by a Magnus force $f n_s \mathbf{v} \times \mathbf{\Phi}/c$, a pinning force $\mathbf{f}_p$ and a dissipative or viscous force $\eta \mathbf{v}$. We have defined $\mathbf{\Phi} = \Phi_0 \hat{z}$. Eq. (1.28) was used for the first time by Kim *et al.* to interpret experimental data [23] and constitutes what was called the "flux flow model". We will now discuss how the origin of each term is explained and how this simple model is generalized to obtain a differential equation for the motion of individual vortices.

The Lorentz force $\mathbf{J}_{ext} \times \mathbf{\Phi}/c$ can be interpreted in terms of the Maxwell stress tensor, as is done in classical magnetohydrodynamics, using for the calculation of the tensor the total magnetic field due to all currents [34]. In the London approximation the Lorentz force can be written as the sum of the Lorentz forces on each vortex $\mathbf{J}_i \times \mathbf{\Phi}/c$, where $\mathbf{J}_i$ is the total current experienced by the vortex. As we can see from the second equality of Eq. (1.18), this force will include, besides the interaction with the external current $\mathbf{J}_{ext}$,

the vortex–vortex interaction, as follows,

$$\mathbf{J}_i \times \mathbf{\Phi}/c = \mathbf{J}_{ext} \times \mathbf{\Phi}/c + \sum_j \mathbf{J}_v(\mathbf{r}_j - \mathbf{r}_i) \times \mathbf{\Phi}/c = \mathbf{J}_{ext} \times \mathbf{\Phi}/c + \sum_j \mathbf{F}_v(\mathbf{r}_j - \mathbf{r}_i) \quad (1.29)$$

where $\mathbf{J}_v$ is the current density due to a vortex and $\mathbf{F}_v(\mathbf{r}) = \mathbf{J}_v(\mathbf{r}) \times \mathbf{\Phi}/c$ the vortex–vortex interaction force. Note that by summing Eq. (1.29) over all vortices we recover the original Lorentz force $\mathbf{J}_{ext} \times \mathbf{\Phi}/c$, since the interaction terms cancel each other due to the action–reaction principle. The real advantage of this separation of the Lorentz force will be appreciated later, in relation to the pinning force.

The Magnus force $f n_s \mathbf{v} \times \mathbf{\Phi}/c$ on vortices in superconductors is a generalization of the hydrodynamic force expressed in the Kutta–Joukowski relation, and the constant f indicates the fraction of the Magnus force that is active [14, 34]. The most important consequence of the Magnus force on the transport properties is the Hall effect (see ref. [34]). However, except for extremely pure superconductors, $f \ll 1$ and therefore the Magnus force can be neglected compared with the dissipative force $\eta\mathbf{v}$ and the pinning force $\mathbf{f}_p$. In this thesis we will neglect this force.

The origin of the dissipative force $\eta\mathbf{v}$ can be explained basically by the appearance of a finite macroscopic electric field $\tilde{\mathbf{E}}$ that is able to move normal electrons, and has the form

$$\tilde{\mathbf{E}} = \tilde{\mathbf{B}} \times \mathbf{v}/c \quad (1.30)$$

where $\tilde{\mathbf{B}}$ is the spatially averaged magnetic field. Note that $\tilde{\mathbf{E}} \parallel \mathbf{J}$, since both are perpendicular to $\mathbf{v}$, and we have neglected the Magnus force. We can then write the transport relation $\tilde{\mathbf{E}} = \sigma\mathbf{J}$, where σ is the electrical conductivity. The direct interpretation of this electric field in terms of Faraday's law (i.e. the moving vortex generates a time-varying magnetic field that gives rise to $\tilde{\mathbf{E}}$) is not clear, since one needs to understand how an electric field can be sustained in a multiply connected superconductor. A possible answer is given by the Josephson effect: when a vortex line crosses a region between two points $\mathbf{r}_1$ and $\mathbf{r}_2$, a time-dependent, high-frequency voltage $V = (\Phi_0/2c)\, d\Delta\phi/dt$ develops (where $\Delta\phi = \phi(\mathbf{r}_1) - \phi(\mathbf{r}_2)$ is the phase difference of the order parameter between the two points). It turns out that when this voltage is time-averaged it gives the same result as using Faraday's law directly. Thus the uniform motion of many vortices produces a voltage equal to the superposition of individual voltage pulses [34]. The dissipation coefficient η can be estimated from the analysis of the different dissipative processes occurring in and near the vortex core. The Bardeen–Stephen model allows a simple estimate of η. The vortex core is assumed to be a completely normal cylinder of radius ξ. Applying the London equations outside this cylinder, the electric field is computed assuming a given vortex velocity. The continuity condition (Maxwell's equations) at the wall of the cylindrical core gives a finite electric field inside it. This field moves the normal electrons, generating Joule dissipation. In this way one obtains

$$\eta \approx \Phi_0 H_{c2}/\rho_n c^2 \quad (1.31)$$

where ρ_n is the normal-state resistivity and H_{c2} the upper critical field. Therefore dissipation is reduced by a factor $\tilde{B}/H_{c2}$ with respect to that of the normal state. No

inertial effects have been observed for vortices, or else it seems that the friction force $\eta\mathbf{v}$ is in general more important, and the motion of vortices can be considered overdamped. The Bardeen–Stephen model is a single-vortex-line calculation. For a number N_v of (two-dimensional) vortices we have

$$\tilde{\mathbf{E}} = \tilde{\mathbf{B}} \times \frac{1}{N_v} \sum_i \frac{\mathbf{v}_i}{c} = \tilde{\mathbf{B}} \times \frac{\mathbf{v}}{c} \tag{1.32}$$

The macroscopic pinning force $\mathbf{f}_p$ on the vortex structure is due basically to the fact that impurities or defects in the material can locally depress the superconducting order parameter. Leaving aside other possible mechanisms, since the order parameter is already reduced in the vortex core, part of the condensation energy lost there can be recovered if the core adjusts itself to the position of the impurity. This energetic advantage translates into a pinning force against motion. Since the defects are in general small compared with ξ and uncorrelated, they constitute a random array of pinning centers for each vortex, with a range of the order of the core size ξ. The force on a vortex $\mathbf{F}_p(\mathbf{r}_i)$ can then be expressed as

$$\mathbf{F}_p(\mathbf{r}_i) = \sum_p \nabla U_p(\mathbf{r}_p - \mathbf{r}_i) \tag{1.33}$$

where p labels one of the pinning centers located at $\mathbf{r}_p$, which exerts the force $\nabla U_p(\mathbf{r}_p - \mathbf{r}_i)$ on vortex i. Thus U_p is the potential of a pinning center. A very important consequence of the pinning force on the transport properties is the appearance of a critical current density $J_c \times \Phi_0/c = \max[\mathbf{f}_p]_{v=0} > 0$ and a critical heat current density, below which the electrical and thermal resistance of the material are nearly zero at sufficiently low temperatures. Pinning allows, for example, a static gradient of vortex density to be sustained, known as the Bean critical state (see [33]). Another consequence of pinning is that it can prevent the superconductor from reaching thermodynamic equilibrium in its magnetic properties and cause irreversible and glassy behavior. In a truly landmark work, Larkin and Ovchinnikov showed that the total pinning force on the static vortex lattice depends on spatial correlation lengths, which in turn result from the competition between vortex–vortex interactions and static disorder. While the interactions between vortices tend to form an ordered structure, with elastic constants, the pinning centers tend to deform it. As a result of this competition one can define a correlation volume or area, known as the Larkin domain. This is a very valuable concept that allows us to obtain an estimate of the critical depinning current. In more modern pinning theories of vortex lattices [17] the Larkin domain is recognized as the largest domain in which disorder can be treated perturbatively, because it belongs to a single metastable state.

The complete problem of describing well the transport properties of superconductors using Eq. (1.28) for the whole magnetic vortex structure reduces to being able to compute $\mathbf{f}_p$. From this point of view the great difficulty lies in the fact that, unlike the static case studied by Larkin and Ovchinnikov, when $\mathbf{v} \neq 0$ the total pinning force $\mathbf{f}_p$ is a time-fluctuating quantity that depends on the dynamical structure of the moving lattice (that is, on its spatio-temporal order). Energetic arguments such as those of Larkin and Ovchinnikov are of no use in the dynamical case, since the system is out of equilibrium

and there is in principle no free energy to minimize in order to find an "optimal" function $\mathbf{f}_p$ of the different parameters. New transport experiments have thus led to considering the motion of the vortex lattice as a non-linear collective transport phenomenon, involving many degrees of freedom. In this sense the phenomenological "flux flow" equation (1.28), with some expression for $\mathbf{f}_p$, can be seen as an empirical approximation for the dynamics of the "zero mode", or center-of-mass dynamics. To better understand the new experiments it is then necessary to analyze the dynamics of many coupled degrees of freedom. From the theoretical point of view, one option is to analyze the hydrodynamics describing the motion of the lattice. A careful derivation of the hydrodynamics can nowadays be carried out thanks to powerful analytical techniques, such as the dynamical functional renormalization group. Another option (the one we adopt in this thesis) is to perform numerical simulations of a simple model describing the dynamics of individual vortices. This requires suitable numerical simulation techniques for systems with many degrees of freedom. Using Eqs. (1.28), (1.29) and (1.33), the basic phenomenology described in this section leads us to write the following equation of motion for a vortex,

$$\eta \mathbf{v}_i = \mathbf{J}_{ext} \times \mathbf{\Phi}/c + \sum_j \mathbf{F}_v(\mathbf{r}_j - \mathbf{r}_i) + \mathbf{F}(\mathbf{r}_i) \tag{1.34}$$

where $\mathbf{v}_i$ is the velocity of vortex i and $\mathbf{F}(\mathbf{r}_i) = \sum_p \nabla U_p(\mathbf{r}_p - \mathbf{r}_i)$ if the disorder is point-like and uncorrelated. The dissipation of the vortex system will be given by Eq. (1.32). By neglecting the internal degrees of freedom of the vortices, we have finally arrived at the system of coupled differential equations of a system of interacting particles. In the next section we specialize these equations to the type of superconductors analyzed in this thesis and add thermal fluctuations.

1.3 Langevin dynamics models of particles

In the previous section we presented the basic dynamical phenomenology of vortex transport. In this section we describe Langevin dynamics models for interacting vortices in the presence of thermal fluctuations, using the vortex–vortex interactions already computed in section 1.2.3. Thermal fluctuations are taken into account by adding a Langevin noise term that guarantees that the system relaxes to an equilibrium state (without external forces) well described by Boltzmann statistics (see for example [40]).

1.3.1 Thin superconducting films

We present here the two-dimensional model that we will use in chapters 3, 5 and 6 to study the motion of vortices in thin superconducting films. The equation of motion of a vortex at position $\mathbf{r}_i$ is:

$$\eta \frac{d\mathbf{r}_i}{dt} = -\sum_{j \neq i} \nabla_i U_v(r_{ij}) - \sum_p \nabla_i U_p(r_{ip}) + \mathbf{F} + \boldsymbol{\zeta}_i(t), \tag{1.35}$$

where $r_{ij} = |\mathbf{r}_i - \mathbf{r}_j|$ is the distance between vortices i, j, $r_{ip} = |\mathbf{r}_i - \mathbf{r}_p|$ is the distance between vortex i and a pinning center at $\mathbf{r}_p$,

$$\eta = \frac{\Phi_0 H_{c2} d}{c^2 \rho_n} \tag{1.36}$$

is the Bardeen–Stephen friction coefficient, Eq. (1.31), and

$$\mathbf{F} = \frac{d\Phi_0}{c} \mathbf{J} \times \hat{z} \tag{1.37}$$

is the driving force due to an applied current $\mathbf{J}$, Eq. (1.29). The effect of the thermal bath at temperature T is given by the stochastic force $\boldsymbol{\zeta}_i(t)$, which satisfies $\langle \zeta_i^\mu(t) \rangle = 0$ and $\langle \zeta_i^\mu(t) \zeta_j^{\mu'}(t') \rangle = 2\eta T \delta(t - t') \delta_{ij} \delta_{\mu\mu'}$ ($k_B = 1$ from here on). A strictly two-dimensional superconductor is realized in thin films of thickness d, where $d \ll \lambda$. These have an effective penetration depth $\Lambda = 2\lambda^2/d$. Since Λ is typically of the order of the sample size ($\Lambda \approx 200\,\mu$m in [41]), the vortex–vortex interaction is logarithmic, Eq. (1.23):

$$U_v(r) = -A_v \ln(r/\Lambda), \tag{1.38}$$

with $A_v = \Phi_0^2/8\pi\Lambda$. As a model for the pinning force due to uncorrelated point disorder we will consider a distribution of attractive pinning centers with interaction potential

$$U_p(r) = -A_p e^{-(r/\xi)^2}, \tag{1.39}$$

where the pinning range is given by the coherence length ξ (because we consider pinning centers smaller than the vortex core). As discussed in the previous section, the moving vortices induce a total electric field, Eq. (1.32)

$$\mathbf{E} = \frac{B}{c} \mathbf{v} \times \hat{z}, \tag{1.40}$$

with

$$\mathbf{v} = \frac{1}{N_v} \sum_i \mathbf{v}_i. \tag{1.41}$$

Figure 1.6 schematically shows the geometry described by this model.

1.3.2 Strongly anisotropic layered superconductors

We present here the three-dimensional model that we use in chapter 4 to study pancake vortices in a strongly anisotropic layered superconductor. We consider the magnetic interactions between all pancakes and neglect the Josephson coupling [38], see section 1.2.3. As we saw in section 1.2.2, this model is adequate when the periodicity d is much smaller than the in-plane penetration depth $\lambda_\parallel$ [38]. Previous simulations of driven vortices in 3D have been carried out using Langevin dynamics of particles with short-range

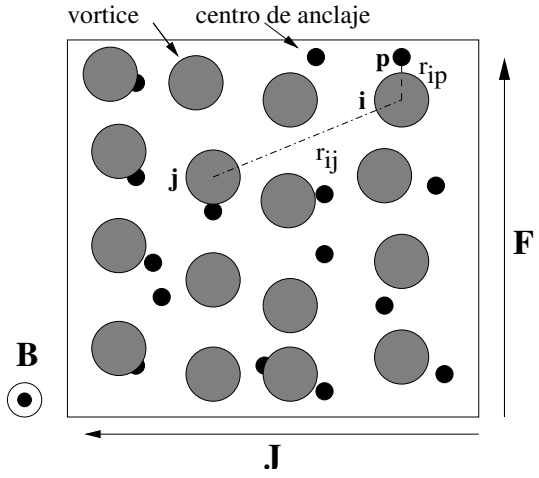


Figure 1.6: Two-dimensional model for vortices in disordered thin superconducting films (labels: *vórtice* = vortex, *centro de anclaje* = pinning center). The interaction potential between vortices i and j is $U_v(r) = -A_v \ln(r_{ij}/\Lambda)$ and the interaction potential of vortex i with pinning center p is $U_p(r_{ip}) = -A_p \exp[-(r_{ip}/\xi)^2]$. The Lorentz force is $\mathbf{F} = \frac{d\Phi_0}{c}\mathbf{J} \times \hat{z}$, where $\mathbf{J}$ is the applied external current density.

interactions [42–44] or the isotropic 3D XY model [45]. The equation of motion for a pancake located at position $\mathbf{R}_i = (\mathbf{r}_i, z_i) = (x_i, y_i, n_i d)$, $(\hat{z} \equiv \hat{c})$, is:

$$\eta \frac{d\mathbf{r}_i}{dt} = \sum_{j \neq i} \mathbf{F}_v(\rho_{ij}, z_{ij}) + \sum_p \mathbf{F}_p(\rho_{ip}) + \mathbf{F} + \boldsymbol{\zeta}_i(t), \tag{1.42}$$

where $\rho_{ij} = |\mathbf{r}_i - \mathbf{r}_j|$ and $z_{ij} = |z_i - z_j|$ are the in-plane and inter-plane distances between pancakes i, j, $\rho_{ip} = |\mathbf{r}_i - \mathbf{r}_p|$ is the in-plane distance between vortex i and a pinning center at $\mathbf{R}_p = (\mathbf{r}_p, z_i)$, as shown in Fig. 1.7 (pancakes interact only with pinning centers in the same plane). η is the Bardeen–Stephen friction, and

$$\mathbf{F} = \frac{\Phi_0}{c}\mathbf{J} \times \hat{z} \tag{1.43}$$

is the driving force due to an in-plane current $\mathbf{J}$. The effect of the thermal bath at temperature T is given by the stochastic force $\boldsymbol{\zeta}_i(t)$, which satisfies $\langle \zeta_i^\mu(t) \rangle = 0$ and $\langle \zeta_i^\mu(t) \zeta_j^{\mu'}(t') \rangle = 2\eta T \delta(t - t') \delta_{ij} \delta_{\mu\mu'}$ $(k_B = 1)$. We consider a distribution of attractive pinning centers in each plane exerting a force

$$\mathbf{F_p} = -2A_p e^{-(\rho/a_p)^2} \mathbf{r}/a_p^2, \tag{1.44}$$

where a_p is the pinning range. The magnetic interaction between pancakes $\mathbf{F}_v(\rho, z) = F_\rho(\rho, z)\hat{r}$ is given by [38, 46]:

$$F_\rho(\rho, 0) = \frac{A_v}{\rho}\left[1 - \frac{\lambda_\parallel}{\Lambda}\left(1 - e^{-\rho/\lambda_\parallel}\right)\right] \tag{1.45}$$

$$F_\rho(\rho, z_n) = -\frac{\lambda_\parallel}{\Lambda}\frac{A_v}{\rho}\left[e^{-|z_n|/\lambda_\parallel} - e^{-R_n/\lambda_\parallel}\right]. \tag{1.46}$$

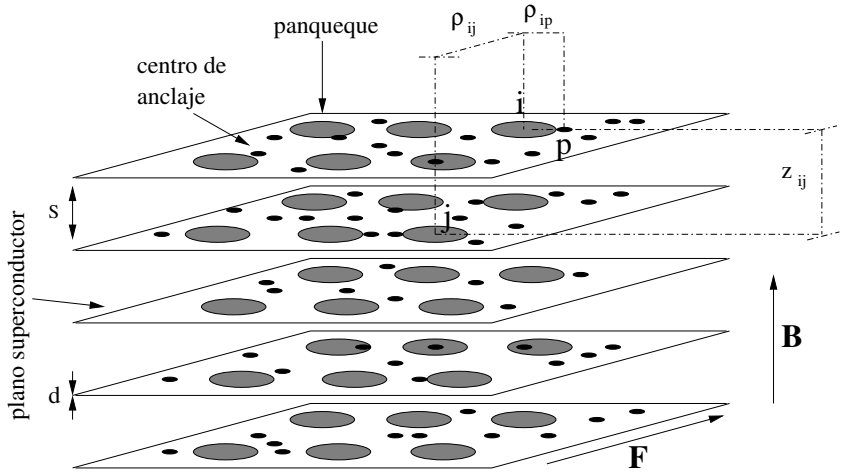


Figure 1.7: Clem's model for vortices in disordered highly anisotropic layered superconductors (labels: *panqueque* = pancake, *centro de anclaje* = pinning center, *plano superconductor* = superconducting plane). The Josephson coupling between planes is negligible and the interaction force between pancakes is purely magnetic and long-ranged, repulsive if they are in the same superconducting plane and attractive if they are in different superconducting planes. Pinning centers attract pancakes in the same plane. The Lorentz force **F** is applied parallel to the superconducting planes.

Here, $R = \sqrt{z^2 + \rho^2}$ and $\Lambda = 2\lambda_\parallel^2/d$ is the penetration depth of the thin films or superconducting layers, $\lambda_\parallel$ being the penetration depth parallel to the planes. An analogous model was used in [47]. Figure 1.7 schematically shows the geometry described by this model.

1.4 Organization of the thesis

In this thesis we study various aspects of the non-equilibrium dynamics of vortices and other related systems. The analysis of the non-equilibrium steady regimes of driven vortices, in thin superconducting films and strongly anisotropic layered superconductors, spans chapters 3, 4, 5 and 6. In chapter 7 we analyze non-stationary non-equilibrium regimes in the relaxation of an electron system in an Anderson insulator. All studies are based on the analysis of spatial and temporal correlation functions and response functions, in the linear or non-linear response regime. The thesis is organized as follows:

- Chapter 2: we discuss the basic issues of the problem of non-linear collective transport in a disordered medium and present experimental and theoretical results.

- Chapter 3: we study the non-equilibrium dynamical regimes of the driven vortex lattice in thin superconducting films with disorder as a function of the external force. We characterize the dynamical regimes and their transitions through the analysis of the velocity–force curves, of translational and topological order, of diffusion and of the anisotropic temporal fluctuations of the instantaneous mean velocity.

- Chapter 4: we carry out a study similar to that of chapter 3 but analyzing the non-equilibrium dynamical regimes of the vortex lattice in strongly anisotropic layered superconductors. In this case we add the analysis of spatial and temporal correlations along the c axis.
- Chapter 5: we characterize the dynamical regimes studied in chapter 3 by their temporal order and their response to an ac force superimposed on the dc force.
- Chapter 6: we analyze correlation functions and response functions to small perturbations for different observables. The aim is to make precise the concept of effective temperature in the vortex lattice through the study of generalized fluctuation–dissipation relations.
- Chapter 7: we analyze the non-equilibrium relaxation of strongly localized electronic systems in semiconductors. This system is related to the Bose glass in the "variable-range hopping" regime.
- Chapter 8: general conclusions of the thesis.

Chapter 2

Non-equilibrium dynamical regimes of vortices

All the work in this thesis is devoted to analyzing and characterizing non-equilibrium dynamical regimes of the vortex lattice, or of other related systems, in the presence of disorder. In this chapter we will show that the basic issues of the problem can be discussed in a very general way, in terms of a non-linear competition between disorder, thermal fluctuations and interactions. After a brief heuristic introduction to the basic issues and concepts of the problem, we will present some of the most important experimental and theoretical results on the subject.

2.1 General discussion of the problem

The vortex system in disordered superconductors can be considered as a set of interacting classical objects that spontaneously tend to form a periodic structure (the Abrikosov lattice). These objects are immersed in a disordered potential that tends to make the structure amorphous. In section 1.2 we showed that this is indeed the effective physics describing vortices when fluctuations of the modulus of the superconducting order parameter and fluctuations of the magnetic field can be neglected (London approximation). In this approximation vortex lines can be well represented as interacting elastic strings or as interacting particles (pancakes) confined to two-dimensional layers: the first case applies to continuous (or not very strongly layered) type II superconductors and the second to thin superconducting films or to strongly layered superconductors with a magnetic field applied perpendicular to the superconducting planes (see section 1.2). In any case, and for a wide family of systems, if $\mathbf{x}$ denotes the configuration of the system, its energy can be expressed in the form

$$H(\mathbf{x}) = H_{int}(\mathbf{x}) + H_{des}(\mathbf{x}) \tag{2.1}$$

where $H_{int}(\mathbf{x})$ is the interaction energy and $H_{des}(\mathbf{x})$ the pinning (disorder) energy. $H_{int}(\mathbf{x})$ can be thought of as the sum of the interaction energies between the objects plus the energies associated with their internal degrees of freedom. Since the interactions depend only on the relative distances between objects, H_{int} is *translationally invariant*. $H_{des}(\mathbf{x})$

simply contains the potential energy of the whole structure on the disordered potential, and therefore H_{des} *is not translationally invariant*. In this thesis we will only consider the ubiquitous case of *uncorrelated point disorder*. In general, for a set of objects (manifolds) immersed in a space of dimension d, with internal dimension D, we can write $\mathbf{x} \equiv \mathbf{x}(i, \mathbf{z})$, where i labels the object and $\mathbf{z}$ parametrizes its extension in space. We will assume that the objects cannot move "along themselves" but only in the direction transverse to $\mathbf{z}$. This requires $\mathbf{x}(i, \mathbf{z})$ to live in a space of dimension N such that $d = D + N$. We will be mainly interested in objects that describe vortices (in the London approximation): lines or points. To describe a set of elastic lines, $\mathbf{x} \equiv \mathbf{x}(i, s)$, where $\mathbf{x}(i, s)$ then describes the position of line i parametrized along its length by s ($\mathbf{z}$ has dimension one in this case). For a set of interacting particles it is enough to simply specify their positions $\mathbf{x} \equiv \mathbf{x}(i)$ ($\mathbf{z}$ has dimension zero in this case). We will think of these two cases, although the same discussion can be carried out for elastic manifolds in general.

The problem we want to analyze is the *non-equilibrium collective dynamics* of the system, governed by an overdamped, stochastic and relaxational equation of motion,

$$\eta \dot{\mathbf{x}} = -\frac{\delta H[\mathbf{x}]}{\delta \mathbf{x}} + \mathbf{F} + \boldsymbol{\zeta}(t) \tag{2.2}$$

where we assume that $\mathbf{F}$ is a homogeneous external force and $\boldsymbol{\zeta}$ is the thermal noise, satisfying

$$\langle \zeta_{\alpha i}(\mathbf{z}, t) \zeta_{\beta i}(\mathbf{z}', t') \rangle = 2\eta T \delta_{ij} \delta_{\alpha\beta} \delta(\mathbf{z} - \mathbf{z}') \delta(t - t') \tag{2.3}$$

so that the equation of motion (2.2) properly describes the equilibrium state (and its vicinity) when there is no external force, guaranteeing the validity of the fluctuation–dissipation theorem. The justification of this dissipative and overdamped equation for vortices is discussed in section 1.2, but it is worth noting that its simplicity makes it ubiquitous and paradigmatic. Equations of the type of (2.2) appear associated not only with the motion of vortex lattices in type II superconductors under the action of a Lorentz force, but also with electron Wigner crystals under the action of an external voltage, lattices of magnetic bubbles under the action of a magnetic field gradient, charge density waves or colloids under the action of an electric field, Josephson junction arrays, etc. In all these cases the presence of static disorder H_{des} *breaks the continuous translational symmetry* of H, making even a uniform translation of the system non-trivial. The dynamical and in general *non-linear* competition between periodicity and disorder in the moving lattice gives rise to a state that is *out of equilibrium*, since the system experiences dynamical effects that are absent in the equilibrium case $\mathbf{F} = \mathbf{0}$, and that in general cannot be mapped onto an equilibrium formalism with an effective Hamiltonian.

Let us begin the discussion with the static case, when $\mathbf{F} = 0$. The equation to be solved is

$$\eta \dot{\mathbf{x}} = -\frac{\delta H[\mathbf{x}]}{\delta \mathbf{x}} + \boldsymbol{\zeta}(t) = -\frac{\delta H_{int}[\mathbf{x}]}{\delta \mathbf{x}} - \frac{\delta H_{des}[\mathbf{x}]}{\delta \mathbf{x}} + \boldsymbol{\zeta}(t) \tag{2.4}$$

The stationary solution of this equation corresponds to a state that can be described by Boltzmann statistical mechanics, and in particular the dynamical fluctuation–dissipation theorem holds, relating the spontaneous fluctuations of an observable to the (linear)

responses to small perturbations (we will come back to this issue later in this chapter and especially in chapter 6). It is worth mentioning that computing the statistical properties of the system is a non-trivial problem requiring theoretical tools such as replica theory, first to eliminate the dependence on the disorder realization, and variational methods or the renormalization group to make progress in the large-scale description of the replicated Hamiltonian. This equilibrium problem has been extensively studied, both theoretically and experimentally, for vortex lattices in superconductors. We will describe the main results very briefly. When there is no disorder, the Abrikosov crystal lattice melts into a vortex liquid in a first-order transition. When there is disorder, the crystalline order of the solid Abrikosov lattice is destroyed, giving rise, in principle, to two glassy solid phases. These solid phases can in turn melt across a transition line $H_m(T)$ into a vortex liquid. In Fig. 2.1 we show a schematic $H-T$ phase diagram for a superconductor without disorder compared with one with disorder. The Bragg glass phase, proposed by Giamarchi and Le Doussal [17], is a solid with quasi-long-range (triangular) translational order (giving rise to Bragg peaks in the structure factor), stable against the proliferation of dislocations. This phase can lose its topological order by increasing the temperature, increasing the disorder or increasing the magnetic field, see Fig. 2.1. In the first case the Bragg glass becomes unstable to the proliferation of topological defects and melts in a first-order transition into a vortex liquid. In the second case the Bragg glass also becomes unstable to the proliferation of topological defects but makes a transition to another solid, glassy phase, known as the vortex glass. Both phases are "glasses" in the sense that they are phases with many metastable states separated by diverging barriers. This "frozen order" is the analogue, in spin glasses, of a finite value of the Edwards–Anderson glass order parameter, which also implies a breaking of ergodicity. It is worth mentioning here that, unlike the Bragg glass, there are some issues about the vortex glass that are not definitively well understood, but their discussion is beyond the scope of this thesis. In any case, the glassy nature does not manifest itself as well in the equilibrium properties as in the dynamical behavior. This immediately leads us to the discussion of the dynamical case.

Let us now consider the dynamical case, when $\mathbf{F} \neq 0$. This problem is of great interest in superconductors, since it is the one we must solve to understand the transport properties. For illustrative purposes, let us first consider the case without pinning, $H_{des} = 0$. Through the change of variables $\mathbf{x}' = \mathbf{x} - \mathbf{F}t$, Eq. (2.2) becomes

$$\eta \dot{\mathbf{x}}' = -\frac{\delta H_{int}[\mathbf{x}' + \mathbf{F}t]}{\delta \mathbf{x}'} + \boldsymbol{\zeta}(t) \tag{2.5}$$

Since H_{int} is translationally invariant, $H_{int}[\mathbf{x}' + \mathbf{F}t] = H_{int}[\mathbf{x}']$, and therefore this equation becomes

$$\eta \dot{\mathbf{x}}' = -\frac{\delta H_{int}[\mathbf{x}']}{\delta \mathbf{x}'} + \boldsymbol{\zeta}(t) \tag{2.6}$$

This equation is identical to (2.4) and therefore has the same solutions in the $H-T$ plane as the equilibrium problem without disorder: a crystalline vortex phase that melts into a vortex liquid. The stationary solution for $\mathbf{x}$ with $\mathbf{F} \neq 0$ therefore describes (going back to the original variables) a moving vortex crystal for $H < H_m(T)$ or a moving vortex liquid for $H > H_m(T)$. The mean velocity of the moving phases is $\dot{\mathbf{x}} = \mathbf{F}/\eta$. Therefore,

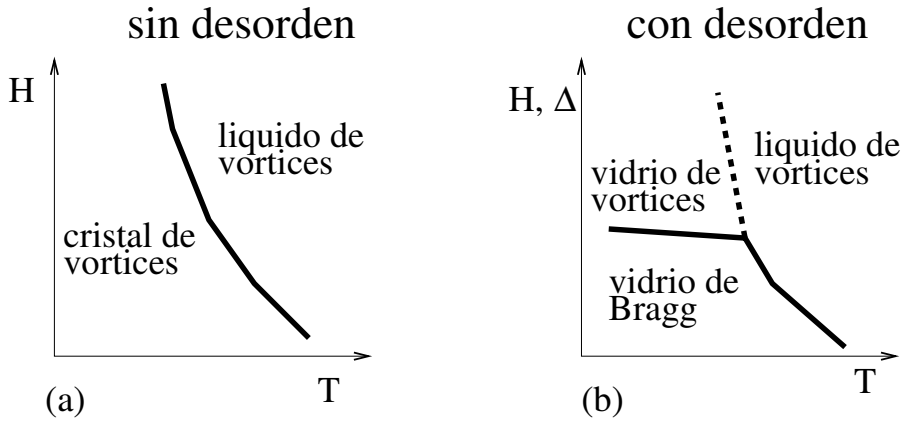


Figure 2.1: $H-T$ phase diagrams of vortices (labels: *sin desorden* = without disorder, *con desorden* = with disorder, *cristal de vórtices* = vortex crystal, *líquido de vórtices* = vortex liquid, *vidrio de vórtices* = vortex glass, *vidrio de Bragg* = Bragg glass). (a) Without disorder ($\Delta = 0$) there is a crystalline solid phase and a vortex liquid. (b) With disorder ($\Delta > 0$) the long-range translational order of the vortex crystal is destroyed, giving rise to the Bragg glass and the vortex glass, which melt into a vortex liquid.

without disorder, the mean velocity V vs. F curve is linear (ohmic), $V = F/\eta$, independent of the interactions in the steady state. We can extend the static $H-T$ phase diagram of Fig. 2.1(a) without problems to a dynamical $H-T-F$ phase diagram such as the one shown in Fig. 2.2(a). The result is very simple: the dynamical phases are directly connected with the static ones through a Galilean transformation, and given (H, T, F) one can uniquely describe the static or moving macroscopic state. For the same values of H and T, the only difference between the static phase with $\mathbf{F} = 0$ and the dynamical phase with $\mathbf{F} \neq 0$ is that the latter dissipates constantly, giving a voltage $V = F/\eta$, but without affecting the structure of the vortex lattice as seen from the center of mass.

Let us now consider the dynamical case with disorder. Is it now possible to extend the static $H-T$ phase diagram of Fig. 2.1(b) to a dynamical $H-T-F$ one, like the one proposed in Fig. 2.2(b)? We saw that when there is no disorder this is a trivial problem. When there is disorder, instead, translational invariance is broken in H and the Galilean-transformation argument fails. We will start from the assumption that Eq. (2.2) has a stationary solution corresponding to a moving dynamical phase with mean (center-of-mass, CM) velocity $\mathbf{v}$, which will surely depend on (T, H, F). This is a very reasonable assumption for most systems described by the dissipative and overdamped equation (2.2), and we will not dwell on the possible but few exceptions. To analyze the dynamical phase it is convenient to transform to the CM reference frame, $\mathbf{x}' = \mathbf{x} - \mathbf{v}t$, in the equation of motion (2.2)

$$\eta\dot{\mathbf{x}}' = -\frac{\delta H[\mathbf{x}'+\mathbf{v}t]}{\delta \mathbf{x}'} + \mathbf{F} - \eta\mathbf{v} + \boldsymbol{\zeta}(t) = -\frac{\delta H_{int}[\mathbf{x}']}{\delta \mathbf{x}'} - \frac{\delta H_{des}[\mathbf{x}'+\mathbf{v}t]}{\delta \mathbf{x}'} + (\mathbf{F} - \eta\mathbf{v}) + \boldsymbol{\zeta}(t) \quad (2.7)$$

where in the second equality we have made explicit the fact that H_{int} is translationally invariant. The statistical properties of the stationary solutions of this equation will in

general not be described by Boltzmann equilibrium statistical mechanics. This is due to the presence of a time-dependent pinning force $\mathbf{F}^{des}(\mathbf{x}', t) = -\frac{\delta H_{des}[\mathbf{x}'+\mathbf{v}t]}{\delta \mathbf{x}'}$ and to the term $(\mathbf{F} - \eta\mathbf{v})$, which does not derive from a potential. Without yet specifying the nature of the disorder, we can write, without loss of generality,

$$\mathbf{F}^{des}(\mathbf{x}', t) = \mathbf{F}^{est}(\mathbf{x}') + \mathbf{F}^{din}(\mathbf{x}', t) \tag{2.8}$$

where $\mathbf{F}^{est}$ represents a possible *static* contribution of the pinning force, such that the time average in the steady state is $\langle \mathbf{F}^{des}(\mathbf{x}', t)\rangle_t = \mathbf{F}^{est}(\mathbf{x}')$, and $\mathbf{F}^{din}$ represents a fluctuating dynamical contribution of the pinning force, *explicitly* time dependent, such that $\langle \mathbf{F}^{din}(\mathbf{x}', t)\rangle_t = \mathbf{0}$. Both contributions to $\mathbf{F}^{des}$ have the effect of generating inhomogeneous stresses on the moving lattice, static and fluctuating respectively. The magnitude of these stresses will determine whether it is possible to have, for example, a moving (elastic) solid phase, or whether it is always destroyed when the lattice is set in motion. Suppose for a moment that the terms $\mathbf{F}^{din}(\mathbf{x}', t)$ and $\mathbf{F} - \eta\mathbf{v}$ can be neglected. Equation (2.7) is then of the same type as Eq. (2.4). It therefore describes the dynamics of a system that relaxes to a state of thermal equilibrium in which, in particular, the dynamical fluctuation–dissipation theorem applies. The same methods used to solve the static problem could then be used to characterize the dynamical phase, since we have turned it into an *equilibrium* problem with an effective Hamiltonian. One would expect the structure of the moving phase (seen from the CM) to be nevertheless different from that of the static phase, since the former experiences the effective disorder H_{est} instead of the disorder H_{des} of the latter. Since $\mathbf{F}$ breaks rotational symmetry, in general H_{est} will describe an anisotropic pinning potential, unlike H_{des}, which we have assumed to be statistically isotropic (in the disorder ensemble). It is therefore plausible that in general *the dynamical phases are anisotropic*. The main difficulty of the problem posed by Eq. (2.7) is then the presence of the explicitly time-dependent term $\mathbf{F}^{din}(\mathbf{x}', t)$ and of the dissipative term $\mathbf{F} - \eta\mathbf{v}$. These two terms make the equation of motion with thermal noise no longer satisfy the conditions for relaxation to an equilibrium steady state, and in particular cause the fluctuation–dissipation theorem to be violated. $\mathbf{F}^{din}(\mathbf{x}', t) + \mathbf{F} - \eta\mathbf{v}$ therefore turns the dynamical problem into a genuine non-equilibrium problem, which cannot be mapped by a Galilean transformation onto an equilibrium statistical mechanics problem with an effective static disorder. Since there is no "universal" (i.e. system-independent) statistical mechanics for describing systems out of equilibrium, as Boltzmann's effectively is for describing systems in thermal equilibrium[1], there are many questions to ask about a system driven over a disordered medium, for example:

- Can one construct a non-equilibrium phase diagram, Fig. 2.2(b), with the dynamical phases classified by order parameters and symmetries, in a way analogous to what is done in equilibrium? (see chapters 3, 4).

- Given that a moving vortex liquid very plausibly exists, can moving solid phases also exist at low temperatures and weak disorder? If so, what is their nature? If not,

[1]We leave aside here the discussion of how "universal" Boltzmann statistics is for describing situations of thermal equilibrium. The proposal of a non-extensive statistical mechanics, for example [48], suggests that Boltzmann statistics is not so universal.

do new phases (different from a moving liquid) arise when the static vortex glasses are set in motion? (see chapters 3, 4).

- What is the relation between spontaneous fluctuations and the response to small perturbations in the non-equilibrium phases? (see chapter 6). What relation is there in this respect with other systems out of equilibrium? (see chapter 7).

- Which macroscopic properties serve to characterize the non-equilibrium phases and phase transitions? (see chapters 3, 5, 4).

- What information about the dynamical phases and transitions is contained in the $F - V$ curves, of driving force F vs. mean velocity v? (see chapters 3, 5, 4).

and many others. The last question is very important in the context of superconductors. As we showed in section 1.2, the force–velocity curve of the vortex lattice is practically equivalent to the current–voltage (IV) curve of a superconductor with vortices. The IV curve is one of the most relevant and experimentally most directly accessible properties of superconductors, and in fact it was transport measurements that motivated the first studies of dynamical phases.

The typical velocity–force response (fairly generic for elastic manifolds in disordered media) is shown in Fig. 2.3 for a temperature $T = 0$ and for $T > 0$. The dashed line is the $V - F$ curve for a system without disorder, $V = F/\eta$. Three regimes are clearly distinguished. For small forces it is very important to distinguish between the zero-temperature and finite-temperature cases. At $T = 0$ the driving force must exceed a critical value F_c to set the system in motion at a finite velocity v (strictly speaking this is true only if there are no quantum fluctuations, see [14]). This phenomenon is known as the *depinning transition*. For $T > 0$, instead, there is a finite velocity even for $F < F_c$ due to thermal activation, and the IV curve is sub-linear, in a *creep regime*. For large forces $F \gg F_c$ the effect of disorder decreases and the "free" flow $V \sim F/\eta$ is asymptotically reached. This regime, known as the *flow regime*, is the one on which we concentrate most in the work of this thesis. To end this general discussion we will very briefly describe these three regimes.

In the creep regime the system is in a state close to equilibrium and its motion is thermally activated. The dynamical response will therefore be related to the effective barriers $U(F)$ between different metastable states,

$$V(F) \sim (F/\eta) e^{-U(F)/T} \tag{2.9}$$

The typical barriers $U(F)$ can be directly related to the spatial structure of the static phase. For the liquid phase $U(F) \sim$ const, while for the glassy phases a diverging dependence on F of the type $U(F) \sim F^{-\mu}$, with $\mu > 0$, is predicted. μ takes a different value for the Bragg glass and for the vortex glass, since it is sensitive to the structure. Therefore the response to small forces is linear (ohmic) in the liquid and non-linear (sub-ohmic) in the glassy phases, with different scaling laws with F. This fact has been used extensively to characterize the static phases and the melting transition. There are, however, certain

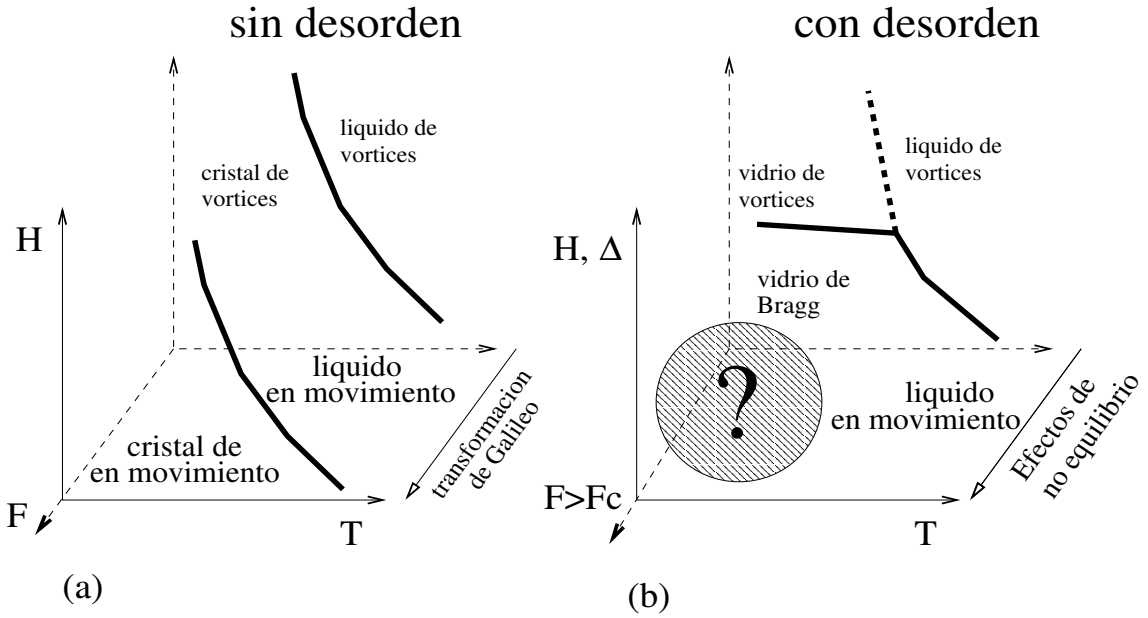


Figure 2.2: Possible "dynamical" $H - T - F$ phase diagrams of vortices (labels: *en movimiento* = moving, *transformación de Galileo* = Galilean transformation, *efectos de no equilibrio* = non-equilibrium effects). (a) Without disorder the moving phases are identical to the static phases seen from the moving reference frame, due to translational invariance. (b) With disorder translational invariance is lost and the moving lattice experiences non-equilibrium effects (static and fluctuating inhomogeneous stresses) that cannot in general be mapped onto an equilibrium formalism. The work of this thesis is focused on what happens in the region of the question mark.

unresolved issues in the complete characterization of this regime on which I will not elaborate [49].

The critical force is perhaps one of the most important characteristics of dynamics in a disordered medium. Larkin and Ovchinnikov showed that this quantity can be related to the structure of the static phase of the vortex lattice (when $T \sim 0$). In their collective pinning theory the critical force F_c is directly related to a characteristic static correlation length R_c [8] (which defines the maximum size of the lattice domain in which disorder can be treated perturbatively). The basic physical content of this prediction is that the more ordered the lattice, the larger R_c and the smaller F_c, and vice versa, the more distorted the lattice, the smaller R_c and the larger F_c. For example, in a rigid ordered lattice we would have $R_c = \infty$ and therefore $F_c = 0$, because the local pinning forces add up incoherently. A soft lattice, instead, deforms a lot to take advantage of the pinning energy, causing R_c to decrease and F_c to increase up to the saturation limit of individual pinning. The depinning transition when F exceeds F_c is very subtle. Initially this transition was studied by analogy with dynamical critical phenomena: one proposes $V \sim (F - F_c)^\beta$ with a critical exponent β that is in general computed from scaling arguments [50]. Although this description works in general for elastic systems, it does not seem to describe in general

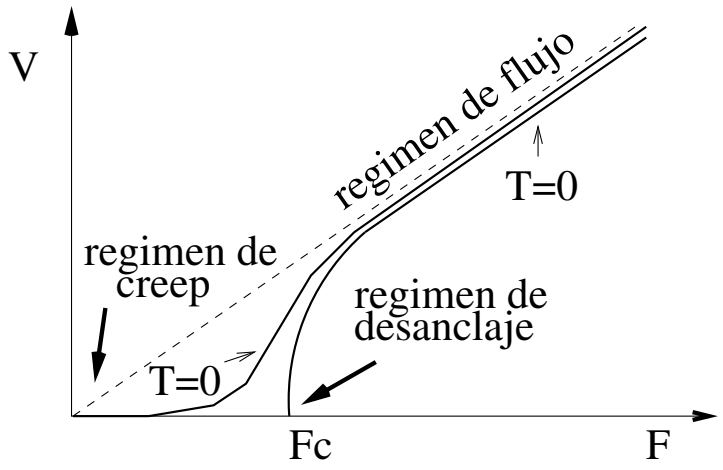


Figure 2.3: Basic dynamical regimes of a vortex lattice in the velocity–force curve at $T = 0$ and at $T \neq 0$ (labels: *régimen de creep* = creep regime, *régimen de desanclaje* = depinning regime, *régimen de flujo* = flow regime). Without disorder the response is linear (ohmic), indicated by the dashed line. With disorder the curves are non-linear. At $T = 0$ the lattice depins and starts to move at a critical force F_c. At $T > 0$ there is thermally activated motion already for $F \ll F_c$. For $F \gg F_c$ the effects of disorder decrease and the curve becomes linear.

the depinning transition of vortex lattices in certain situations. Both in experiments [41] and in simulations [51] of vortices in thin superconducting films it is found, for example, that the depinning transition can be strongly hysteretic and abrupt, which clearly violates the law $V \sim (F - F_c)^\beta$.

Finally we arrive at the regime of intermediate forces $F > F_c$ and large forces $F \gg F_c$, which we study in this thesis by means of numerical simulations. We will therefore describe in more detail the theoretical, experimental and numerical simulation studies of this flow regime.

2.2 Dynamical melting of the vortex lattice

One of the main motivations of our work was the theoretical prediction of dynamical phase transitions in the vortex lattice. The high-velocity regime $V \gg F_c/\eta$ was for a long time considered the easiest to understand. The argument was that when the system moves very fast it experiences temporally fluctuating pinning forces (seen from its center-of-mass reference frame), similar to a velocity-dependent "thermal noise". The intensity of this noise should go to zero at large velocities because, since the vortex lattice has a finite response time at finite length scales, the displacements induced by the pinning forces decrease the faster these forces fluctuate. Under this assumption it is reasonable to think that, if the external temperature is lower than the melting temperature of the system in equilibrium, a moving crystalline vortex solid, induced by the interactions, should be stable at high velocities. From the point of view of the general discussion developed in the

previous section, this amounts to making the following approximation in Eq. (2.7)

$$\mathbf{F}^{des}(\mathbf{x}',t) = \mathbf{F}^{est}(\mathbf{x}') + \mathbf{F}^{din}(\mathbf{x}',t) \approx \mathbf{F}^{din}(\mathbf{x}',t) \tag{2.10}$$

that is, it amounts to neglecting any possible static component of the pinning force (on the lattice seen from the center-of-mass frame). The assumed dependence on velocity translates into saying that $\langle F_{din}^2 \rangle_t \to \mathbf{0}$ when $V \to \infty$. Therefore at large velocities the interaction forces dominate and the moving crystalline solid is stable. To quantify the weak effect of the fluctuating pinning forces on this *supposed crystalline solid* it is convenient to define the displacements $\mathbf{u}(\mathbf{X},\mathbf{z},t) \equiv \mathbf{x}(\mathbf{X},\mathbf{z},t) - \mathbf{X} - \mathbf{v}t$, where $\mathbf{X}$ is the ideal position (in the crystal) of a vortex, seen from the reference frame moving at the mean velocity of the system $\mathbf{v}$. $\mathbf{X}$, replacing the object index i, is simply a more convenient form for a later *coarse-grained* description. The equation of motion for $\mathbf{u}$ then reads

$$\eta\dot{\mathbf{u}} = \mathbf{F}^{int} + \mathbf{F}^{des} + \mathbf{F} - \eta\mathbf{v} + \boldsymbol{\zeta}(t) \tag{2.11}$$

where $\mathbf{F}^{int} = \delta H_{int}/\delta\mathbf{u}$ is the interaction force of a vortex with the others and $\mathbf{F}^{des} = \delta H_{des}/\delta\mathbf{u}$ the pinning force. The advantage of working with $\mathbf{u}$ instead of $\mathbf{x}$ is that, based on our assumptions, we can consider $\mathbf{u}$ a small quantity. We can therefore make a harmonic approximation for the *elastic* phase, $\mathbf{F}^{int} \approx \mathbf{F}^{el}$, where the instantaneous elastic force depends linearly on $\mathbf{u}$,

$$F_\alpha^{el} = \Gamma_{\alpha\beta}(\mathbf{q})u_\beta(\mathbf{q},t) \tag{2.12}$$

$$\Gamma_{\alpha\beta} = \sum_p [c_p q_\perp^2 + c_{44} q_\parallel^2] P_{\alpha\beta}^p(\mathbf{q}_\perp) \tag{2.13}$$

where Γ represents the elastic dispersion, $p = L, T$ labels the longitudinal and transverse polarization, $c_p \equiv c_{11}, c_{66}$ the elastic constants, and $q_\perp^2 = q_x^2 + q_y^2$. The pinning force $\mathbf{F}^{des}$ can be written as

$$\mathbf{F}^{des}(\mathbf{X},\mathbf{z},t) = -\nabla_\perp V(\mathbf{X} + \mathbf{v}t + \mathbf{u}(\mathbf{X},\mathbf{z},t), \mathbf{z}) \tag{2.14}$$

and therefore depends implicitly on $\mathbf{u}$. The pinning potential and the thermal noise are assumed Gaussian with autocorrelation functions

$$\langle \zeta_\alpha(\mathbf{X},\mathbf{z},t)\zeta_\beta(\mathbf{0},\mathbf{0},t)\rangle = 2\eta T\delta_{\mathbf{X},\mathbf{0}}\delta_{\alpha\beta}\delta(t) \tag{2.15}$$

$$\overline{V(\mathbf{r})V(\mathbf{0})} = \Delta(\mathbf{x})\delta(\mathbf{z}) \tag{2.16}$$

Equations (2.11)–(2.16) are those that describe the dynamics of the supposed elastic phase. Schmid and Hauger [24] and Larkin and Ovchinnikov [25] were the first to write equivalent equations to compute the corrections to the mean velocity $\boldsymbol{\delta}\mathbf{v} = \mathbf{v} - \mathbf{F}/\eta$ and to explain the steps in the IV curves observed by Fiory [26] when $\mathbf{F} = \mathbf{F} + \mathbf{F}_{ac}\cos(\Omega t)$ (see chapter 5). Much more recently, Koshelev and Vinokur [29] went further with these same equations, imagining a very interesting physical scenario that later triggered a great deal of activity in the study of dynamical phase transitions in vortex lattices. Their idea was to estimate $\overline{\langle|\mathbf{u}^2|\rangle}$ by treating disorder perturbatively in the elastic approximation and

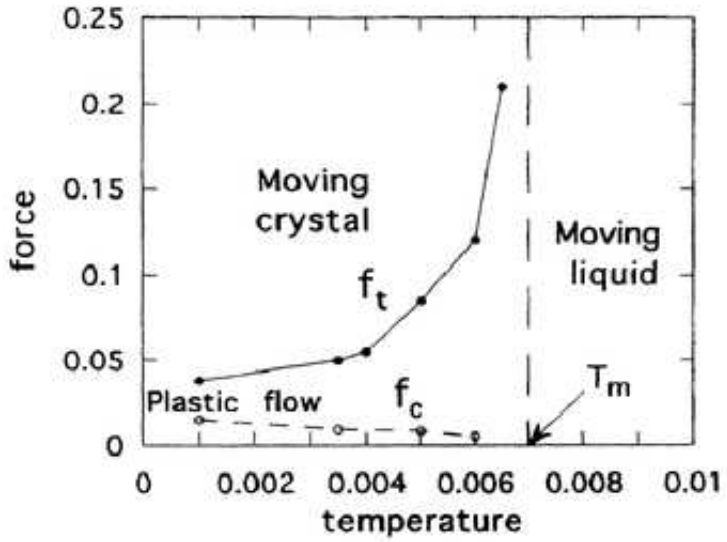


Figure 2.4: Dynamical phase diagram proposed by Koshelev and Vinokur [29] in $d = 2$. The force f_c is the critical depinning force of the lattice. The force f_t marks the dynamical melting line of the vortex lattice, between a plastic flow regime with the structure of a liquid and a moving crystal. The temperature T_m is the equilibrium melting temperature, above which there is a moving liquid at any velocity.

then to use a Lindemann melting criterion to estimate approximately the critical velocity v_f at which a *dynamical melting* of the moving vortex lattice, or the destabilization of the crystalline solid, could occur[2]. Koshelev and Vinokur found that the displacements due to the pinning force are analogous to those produced by thermal fluctuations, $\overline{\langle|\mathbf{u}^2(q)|\rangle} \propto 1/q^2$. This led them to introduce a *fictitious temperature* of coherent motion $T^{coh}_{sh} \sim 1/v^2$, such that $\overline{\langle|\mathbf{u}^2(q)|\rangle} = T^{sh}_{coh}/C_{66}q^2$. On the other hand, they studied what happens for $v < v_f$, in the non-elastic phase. Here they assumed that the motion is completely incoherent and neglected the effect of the interactions between vortices (see chapter 6). Drawing an analogy between the fluctuating pinning force $\mathbf{F}^{des}$ of Eq. (2.14) and the thermal noise $\boldsymbol{\zeta}$ of Eq. (2.3), they defined another fictitious temperature T^{sh}, or "shaking temperature", as follows,

$$T^{sh} \equiv \frac{1}{4\eta} \sum_\alpha \int dtds\, \overline{F^{des}_\alpha(\mathbf{X}, \mathbf{z}, t) F^{des}_\alpha(\mathbf{X}, \mathbf{0}, t)} \propto \frac{1}{v} \tag{2.17}$$

They then assumed that when the system is in its incoherent flow regime it can be qualitatively described as a system without disorder but with an effective temperature $T_{ef} = T + T_{sh}(v)$. In this way they "mapped" a non-equilibrium problem onto an equilibrium

[2]One might ask why the proposal of dynamical melting of the vortex lattice was made only in 1994 and not twenty years earlier by Schmid and Hauger, Larkin and Ovchinnikov or others, given that the validity of the elastic approximation is an automatic issue when writing down the equations of motion! One reason is surely that in the 1970s there was no experimental evidence that would make one suspect the existence of such an effect, whereas there was after the discovery of high-T_c superconductors [27]. Numerical simulation, not so common in the 1970s but common in the 1990s, surely helped to develop intuition or to confirm suspicions.

one (seen from the reference frame moving with velocity v). They then computed the critical melting velocity v_f by equating the effective temperature to the equilibrium melting temperature T_f of the system without pinning, $T_{ef}(v_f) = T_f$. With this analogy they predicted that the non-equilibrium melting temperature of the vortex lattice is velocity dependent and given by

$$T_f(v) = T_f - T_{sh}(v) \tag{2.18}$$

where $T_f \equiv T_f(v = \infty)$. The lattice out of equilibrium therefore always melts at a lower temperature than in equilibrium, due to the additional stresses caused by the pinning force. Comparing the fictitious temperatures introduced for coherent and incoherent motion, Koshelev and Vinokur found that $T^{sh}_{coh} \approx (v_{rel}/v)T^{sh}(v)$, where v_{rel} is a characteristic velocity. The fact that these two temperatures do not coincide at v_f, and that typically $v_{rel}/v_f > 1$, led them to predict that the dynamical melting transition is first order, with hysteresis. The phenomenon of "superheating", for example, implies that the coherently moving phase can penetrate slightly into the region $v < v_f$. Note that many approximations are involved in arriving at (2.18), such as the elastic approximation to describe a supposed crystalline phase, the neglected anisotropic effects, the equilibrium analogy with the introduction of fictitious temperatures, and perturbation theory. Despite this, relation (2.18) seems to be consistent with some experimental observations [27, 41] and numerical simulations [29]. Figure 2.4 shows the dynamical phase diagram obtained by numerical simulations of interacting vortices in 2D in ref. [29]. The dynamical melting transition line f_t was determined as the force at which the concentration of topological defects increases abruptly.

2.3 Transport measurements

The work of Koshelev and Vinokur was the first theoretical work in which a non-equilibrium dynamical transition in the vortex lattice was proposed and its nature qualitatively described. However, it was transport experiments in superconductors with vortices that provided the starting point for research on the non-equilibrium dynamical phases of the vortex lattice, although from transport data alone it is not easy to discern their nature. In particular, the observation [27] of dramatic effects in the evolution of the IV curves in 2H-$NbSe_2$, upon changing field or temperature, near the so-called "peak effect" (a peak in the critical current or force F_c as a function of field or temperature) led to the construction of the empirical dynamical phase diagram shown in Fig. 2.5. Earlier, by neutron diffraction, experimental evidence had been obtained of an equally dramatic evolution of the correlations between vortices [28]. What was observed in these neutron diffraction studies is that the Bragg peaks observed in the pinned vortex structure ($F < F_c$) broadened appreciably at the depinning transition at F_c, and that then, upon increasing F, the Bragg peaks narrowed again. It thus became necessary to understand the nature of the moving phases. The $F - H$ phase diagram of Fig. 2.5 was then interpreted in accordance with this evidence of dynamical reordering, which suggests that the dynamical effects of disorder are important only near F_c. Figure 2.5 (left) shows several $I - dV/dI$ curves extracted from the IV curves for different fields H. In it, the characteristic forces F_c and

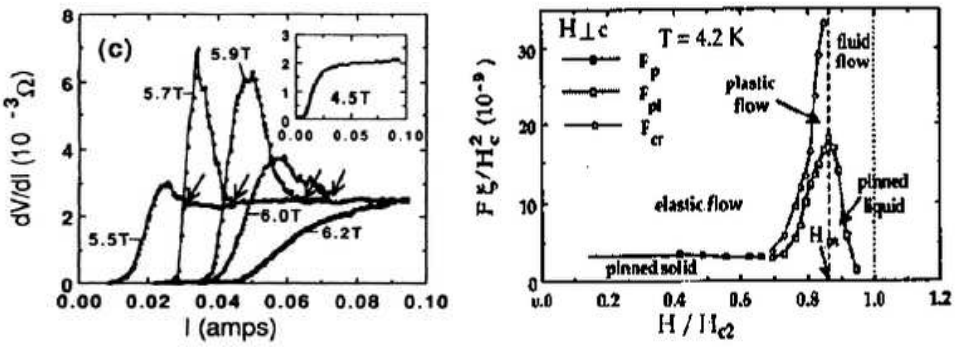


Figure 2.5: Right: experimental current–field dynamical phase diagram of a 2H-$NbSe_2$ superconductor [27]. The first transition line is the critical depinning current and the second is the current at which the IV curve becomes linear and the fluctuations of the differential resistance dV/dI vs. I are reduced. Left: differential resistance dV/dI–I curves from which the characteristic currents were extracted.

I_{cr} that were used to construct the diagram of Fig. 2.5 (right) are indicated. As we can see in Fig. 2.5 (right), ref. [27] proposes that, increasing F from zero at low fields, there is a dynamical transition at F_c from a pinned solid to an elastic flow regime or moving solid. Below the melting field H_m but close to the peak effect, they propose that an intermediate plastic flow phase appears, separating the pinned solid from the elastic flow regime. Above the melting field H_m they propose a single dynamical transition, from a pinned liquid to a moving liquid.

Another experimental dynamical phase diagram was proposed by Hellerqvist *et al.* for amorphous superconducting films of $Mo_{77}Ge_{23}$ [41]. The diagram is shown in Fig. 2.6 (right), and the characteristic forces are the critical depinning force and the force at which a peak in the differential resistance dV/dI is observed. Figure 2.6 (left) shows $dV/dI - I$ curves for several temperatures together with their corresponding IV curves. Since in this system the penetration depth is much larger than the film thickness, it is an example of a two-dimensional superconductor with point vortices. On the other hand, the disorder is stronger than in the three-dimensional superconductor of Fig. 2.5. The phase diagram of Fig. 2.6 is very similar to that of Koshelev and Vinokur in Fig. 2.4 and has been interpreted in the same terms. In this experiment it is suggested that the peak in the differential resistance signals the Koshelev–Vinokur dynamical melting transition to an elastic flow regime. Note that, to construct the diagram of Fig. 2.5 (right), a different criterion from that of Fig. 2.6 was used to determine the same transition. The force F_{cr} does not correspond to the peak in the differential resistance but to the force at which the IV curve becomes linear (and the fluctuations in dV/dI vs. I are reduced).

In order to interpret these experiments it is necessary to know the nature of the transitions or crossovers observed in the IV curves. This is an important motivation for carrying out numerical simulations, in which one can access both the IV characteristics and the underlying dynamical structure. We will discuss the interpretation of these two experiments in particular in chapter 3 of this thesis, in relation to the results obtained by

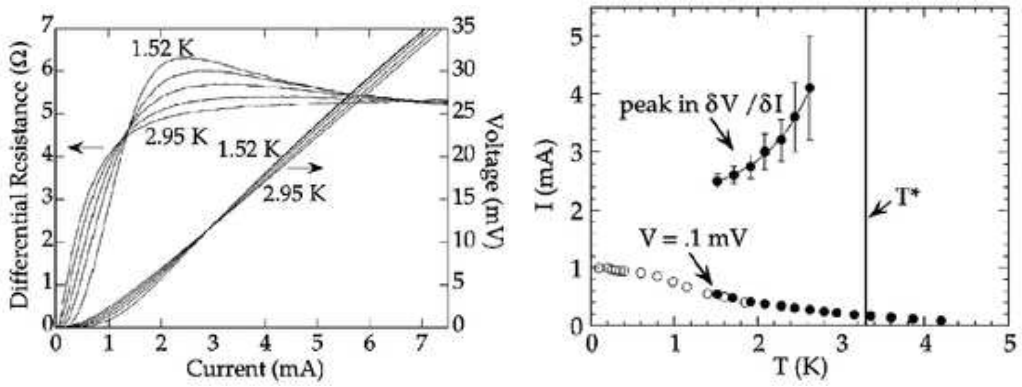


Figure 2.6: Right: experimental current–temperature dynamical phase diagram of a thin superconducting film of $Mo_{77}Ge_{23}$ [41]. The first transition line is the critical depinning current and the second is the current at the peak of the differential resistance. Left: typical IV and dV/dI–I curves from which the characteristic currents were extracted.

our numerical simulations.

2.4 Dynamical structure of the vortex lattice

Another very important motivation for our work has been the direct experimental evidence of the dynamical spatial structure of the vortex lattice, achieved very recently. The dynamical structure of the moving vortex lattice has recently been observed by means of magnetic decoration techniques and tunneling microscopy. Figure 2.7 shows images obtained by F. Pardo *et al.* [52] by "dynamical" magnetic decoration for different magnetic fields and velocities of the vortex lattice. The first column shows the real-space image, the second the modulus of its Fourier transform or structure factor, and the third the inverse transform of the structure factor. We can see that in general the structure has triangular order but is anisotropic, with greater translational order in the direction transverse to the direction of motion than in the longitudinal one. At low fields this anisotropy is much larger, and the ordering is similar to that observed in the smectic phase of liquid crystals. By analogy with liquid crystals we are faced with the interesting possibility of having structures that are ordered in one direction and disordered in another, which have no counterpart in the static case (provided pinning is uncorrelated and isotropic). This is clearly inconsistent with the simple picture of an isotropic crystal moving at high velocities [29], and tells us that the effect of pinning on the moving lattice is more complicated than that of an effective temperature describing fluctuations in addition to the thermal ones. Understanding the origin of the anisotropy from the dynamical point of view is important, since it provides valuable information on the anisotropic dynamical response of the vortex lattice out of equilibrium.

With tunneling microscopy [53], direct successive images of moving vortices have also been obtained in a plastic flow regime, due to strong disorder in the sample, and in

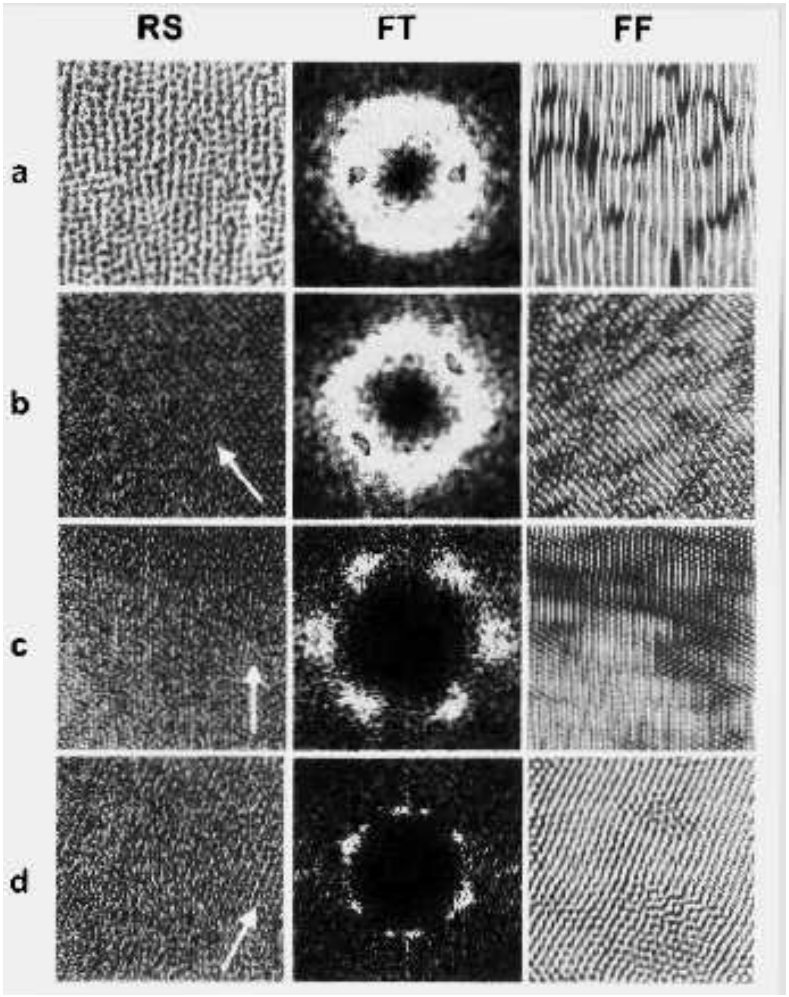


Figure 2.7: Magnetic decoration images of the vortex lattice at different fields and flow velocities [52]. The first column shows the real-space image, the second shows the modulus of its Fourier transform, and the third column shows the image after a Fourier filtering process. Rows (a) and (b), corresponding to low fields and to high and low velocity respectively, show a smectic structure. Rows (c) and (d), corresponding to high fields and to high and low velocity respectively, show a structure called the moving Bragg glass.

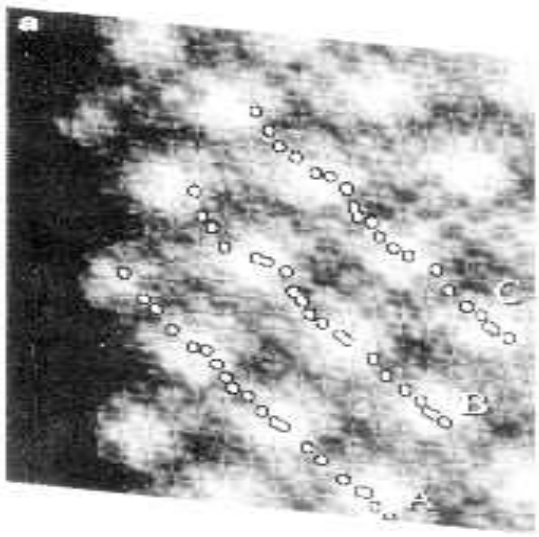


Figure 2.8: Tunneling microscopy image of a vortex lattice in an $NbSe_2$ sample with low disorder [53]. The image is frame 85 of a series of 168 images. The dots represent the trajectories of three vortices. The motion is along the local direction of one of the principal symmetry axes of the lattice.

an elastic flow regime (at least over the short observation time), due to weak disorder. Figure 2.8 shows how the vortex lattice moves in a situation of weak disorder. As we can see, the motion is locally coherent, and the vortices move along the direction of one of the principal axes of the local triangular order. Another interesting observation made in this work is that the center-of-mass velocity of the vortices (those they manage to image) displays periodic fluctuations, typical of periodic elastic structures on a disordered potential. An important question is to know the degree of coherence of this temporal order, since it could have consequences on the response properties of the system to ac currents, as we analyze in chapter 5.

2.5 End of the moving crystal: what is there instead?

The calculation of Koshelev and Vinokur was made under the important assumption that the displacements with respect to the ideal position of the vortices (i.e. the one they would have without disorder) induced by the pinning force become smaller and smaller as the velocity becomes very large. Under this assumption they used perturbation theory in $1/v$ to obtain the displacements. This leads, almost by construction, to the description of a moving crystal with fluctuations in addition to the thermal ones, which decrease with velocity. That is, this whole calculation is based on the assumption that the moving lattice with disorder tends to a moving lattice without disorder at high velocities. In the high-velocity limit translational symmetry would then be recovered. Continuing the general discussion begun in section 2.1, this implies that the moving lattice is statistically

isomorphic to the static lattice without disorder through a Galilean transformation[3]. Let us rewrite the general equation of motion (2.7),

$$\eta\dot{\mathbf{x}}' = \mathbf{F}^{int}(\mathbf{x}') + \mathbf{F}^{est}(\mathbf{x}') + \mathbf{F}^{din}(\mathbf{x}', t) + \mathbf{F} - \eta\mathbf{v} + \boldsymbol{\zeta}(t) \tag{2.19}$$

where $\delta H_{int}/\delta\mathbf{x}' = \mathbf{F}^{int}$ and $\delta H_{des}/\delta\mathbf{x}' \equiv \mathbf{F}^{des}(\mathbf{x}', t) = \mathbf{F}^{est}(\mathbf{x}') + \mathbf{F}^{din}(\mathbf{x}', t)$, with $\mathbf{F}^{est}(\mathbf{x}') = \langle\mathbf{F}^{des}(\mathbf{x}', t)\rangle_t$. Equation (2.19) describes a moving crystal only if $\mathbf{F}^{int}(\mathbf{x}')$ becomes more important than all the other terms. Both the fluctuating component of the pinning force $\mathbf{F}^{din}(\mathbf{x}', t)$ and $\mathbf{F} - \eta\mathbf{v}$ are functions of velocity, and it is reasonable to think that their effect decreases with v and that they become less important than $\mathbf{F}^{int}(\mathbf{x}')$. On the other hand, the intensity of the thermal noise term can be reduced by lowering the temperature (below the melting temperature of the crystal without disorder). Of course one cannot rule out the possibility that the combined action of the three terms mentioned is more appreciable than that of each one separately, but we will assume so for illustrative purposes. What happens with the term $\mathbf{F}^{est}(\mathbf{x}')$? Note that this static component of the pinning force cannot depend on velocity, since it comes from a time average of a function that depends on time through $\mathbf{v}t$, so that, if it exists, the only way of making this term small is by reducing the strength of the disorder (again without taking into account the combined actions with the other terms). In any case, note that if $\mathbf{F}^{est}(\mathbf{x}')$ exists it breaks translational symmetry and can give rise to glassy behavior. The immediate consequence of this is that there is then no such thing as the "ideal" position of a vortex in a moving crystal, and perturbation theory fails.

Indeed (and nothing else was to be expected after such a biased introduction!) it was recently discovered that the perturbation theory used by Koshelev and Vinokur fails essentially for this reason. Giamarchi and Le Doussal [54] focused on the large-scale structure of the vortex lattice and found that, even at high velocities, it retained glassy features, like those of the static phase. Other investigations later found new non-equilibrium effects [31, 32], which have to do with the combined action of all the terms (not only $\mathbf{F}^{est}$) in a coarse-grained description. Computing the resulting order in the moving lattice is complicated. When perturbation theory fails it is necessary to resort to techniques of replica theory and (dynamical) renormalization that go beyond this thesis (and beyond me, although I do not lack interest in learning them). I will therefore sketch the main results.

To analyze the large-scale structure of the moving lattice it is necessary to start from a coarse-grained description. In this description the lattice could be described, for example, by a vortex density field $\rho(\mathbf{r})$, where $\mathbf{r} \equiv (\mathbf{r}, \mathbf{z})$ ($\mathbf{x}$ denotes the transverse coordinates of the vortex (or manifold), along which it can move, and $\mathbf{z}$ parametrizes it). In general, we can decompose $\rho(\mathbf{x}, \mathbf{z})$ as follows [31],

$$\rho(\mathbf{r}, t) = \rho_0 + \frac{1}{2}\sum_{\mathbf{Q}} \rho_{\mathbf{Q}}(\mathbf{r}, t) e^{i\mathbf{Q}.[\mathbf{x}+\mathbf{v}t]} \tag{2.20}$$

[3]This, if it were true, would be very interesting, since it would be possible to investigate the static phase diagram in the ideal limit of totally "clean" samples starting from ordinary samples with a large applied current.

where $\mathbf{Q}$ is the set of reciprocal lattice vectors of the ordered lattice. A quantity of immediate interest would be, for example, the autocorrelation function of the order parameter $\rho_{\mathbf{Q}}$, $C_{\mathbf{Q}}(\mathbf{Q},t) = [\langle \rho_{\mathbf{Q}}(\mathbf{r},t)\rho^*_{\mathbf{Q}}(0,0)\rangle]$. One could then try to construct a Landau-type or density-functional theory for the order parameter $\rho_{\mathbf{Q}}$. This description would be very complete, since it would allow fluctuations of the modulus of the order parameter that would naturally describe dislocations. Unfortunately, from this point of view the problem becomes intractable. It is interesting to draw an analogy with the Ginzburg–Landau equations for the superconducting order parameter. Since these equations are difficult to solve, one resorts to the convenient London approximation (see section 1.2), in which the fluctuations of the modulus of the order parameter are neglected. Here the situation is similar, and one resorts to the same type of approximation. Neglecting the fluctuations of $|\rho|$ results in an *elastic description of the vortex lattice*. The great disadvantage is that dislocations are left out of the description. However, they could be reintroduced by hand later to complete the description, as was done to study systems in equilibrium. An example is the two-dimensional Kosterlitz–Thouless melting transition (or, analogously, the way vortices are introduced in the London approximation). In the elastic approximation, as in the London approximation, the order parameter reduces to its "phase". In the case of $\rho_{\mathbf{Q}}$ the phase represents the displacement field $\mathbf{u}(\mathbf{r},t)$. A large-scale *coarse-grained* description of $\mathbf{u}(\mathbf{r},t)$ requires a careful derivation of its equations of motion (hydrodynamics), since short wavelength modes are important when the correlation length of the pinning potential is much smaller than the lattice parameter. This derivation was made recently, and almost simultaneously, by Le Doussal and Giamarchi [30], Balents, Marchetti and Radzihovsky [31], and Scheidl and Vinokur [32]. Although these works make important progress in the understanding of non-equilibrium and glassy effects, the results do not fully agree and give rise to a controversy that we will discuss at the end of this section. Without going into the technical details, we will briefly describe the physical results they obtain.

Le Doussal and Giamarchi conclude that the physics of the moving lattice is dominated by the fluctuations of the displacements in the direction *transverse* to the velocity, and that the high-velocity phase is an anisotropic *moving glass* and not a moving crystal. To understand these statements, let us write the *coarse-grained* equation for $\mathbf{u}$ [30],

$$\eta\partial_t u_\alpha(\mathbf{r},t) + \eta\mathbf{v}.\nabla u_\alpha(\mathbf{r},t) = \int_{\mathbf{r}'} \Phi_{\alpha\beta}(\mathbf{r}-\mathbf{r}')u_\beta(\mathbf{r},t) + F^{des}_\alpha(\mathbf{r},t) - \eta v_\alpha + \zeta_\alpha \qquad (2.21)$$

where Φ is the elastic matrix. The convective term comes from the Eulerian representation when the displacement field is expressed in the laboratory reference frame. Note that this term is *not* the gradient of a potential, as a consequence of the fact that the system is out of equilibrium, with energy constantly injected and dissipated when the system moves. The pinning force is given by

$$F^{des}(\mathbf{r},t) = -\frac{\delta H_{des}}{\delta u_\alpha(\mathbf{r},t)} = V(\mathbf{r})\rho_0 \sum_{Q_y} iQ_\alpha \exp[i\mathbf{Q}.(\mathbf{r}-\mathbf{v}t-\mathbf{u}(\mathbf{r},t))] \qquad (2.22)$$

The physics described by Le Doussal and Giamarchi becomes transparent by looking at Eq. (2.22) for the pinning force: all disorder modes such that $\mathbf{Q}.\mathbf{v} = 0$ have no explicit

time dependence and therefore their time average will not go to zero even at very high velocities. This is the reason why perturbation theory in $1/v$ [24, 25, 29] fails. There is then, as we had anticipated, a static component of the disorder in the direction transverse to the motion of the lattice,

$$F^{est}(\mathbf{r},t) = V(\mathbf{r})\rho_0 \sum_{\mathbf{Q}.\mathbf{v}=0} iQ_\alpha \exp[i\mathbf{Q}.(\mathbf{r}-\mathbf{u}(\mathbf{r},t))] \tag{2.23}$$

Since this force is perpendicular to the velocity, it has no effect on the velocity correction $\delta\mathbf{v} = \mathbf{v} - \mathbf{F}/\eta$, for which the perturbative expansion is valid. However, this force has a dramatic effect on the displacement correlation functions. The crucial element that determines this force is the transverse periodicity.

One of the most interesting properties of F^{est} (Eq. 2.23) is that it pins the displacements u_y, transverse to the velocity $\mathbf{v} = \mathbf{x}v$. The resulting flow can then be described in terms of *static channels* that the vortices follow like beads on a necklace (or cars on a winding one-way road). In the laboratory reference frame these channels are determined by the static disorder and do not fluctuate in time. From the center-of-mass reference frame we would see the vortices fluctuating transversally, because they are confined to the channels, which in this frame are seen to be moving. This fluctuation of the motion of vortices along the channels is highly correlated in space and time, therefore giving a radically different picture from that of the "shaking" temperature [29], which is based on the assumption of motion with incoherent, thermal-like fluctuations.

The channels are the easiest paths followed by the vortices, and one can see that the cost of deforming a channel in the transverse direction is an increase in dissipation. The channels are determined by a complicated competition between elastic energy, disorder and dissipation. As a consequence the channels are *rough*. It is very illustrative to compare the trajectories of vortices in a superconductor without and with disorder. Figure 2.9 shows what happens when there is no disorder. For $F = 0$ and $T = 0$ we have a vortex crystal, Fig. 2.9(a). If we set $F > 0$ the lattice will start to move in the direction of the force and the vortex trajectories will be straight lines, 2.9(b). If we now add thermal fluctuations these trajectories become blurred. In three dimensions, at temperatures lower than the melting temperature of the vortex lattice, the trajectories broaden somewhat, 2.9(c). In two dimensions, since thermal fluctuations are stronger, the trajectories are completely blurred, 2.9(d). When there is disorder, instead, the vortices move in elastically coupled rough channels, Fig. 2.10(a). Le Doussal and Giamarchi predict that in $d = 3$ the system forms a topologically ordered structure, which they called the *moving Bragg glass*, Fig. 2.10(b). For $d = 2$ or strong disorder in $d = 3$ they predict that particles in different channels can decouple and dislocations with Burgers vectors parallel to $\mathbf{F}$ appear. The latter is the *moving transverse glass*.

An important property predicted in [30], related to the existence of stable channels, is the existence of "transverse barriers". At $T = 0$ these barriers give rise to a transverse critical force F_{cy}, such that the transverse velocity $v_y = 0$ for $F_y < F_{cy}$, while the system moves at high velocity in the longitudinal direction x. The transverse critical force is a very curious effect. It does not exist for a single particle at $T = 0$ moving in a disordered potential with short-range correlations. However, a longitudinal critical force does exist for

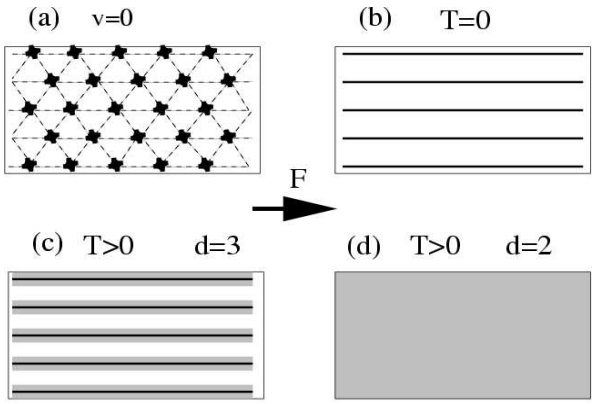


Figure 2.9: Moving vortex lattice without disorder. (a) Image of the vortex lattice at rest. (b) Straight vortex trajectories at $T = 0$ when a force F is added. (c) The straight trajectories of the previous case broaden somewhat when $T > 0$ (but low) and $d = 3$. (d) The trajectories are completely blurred for $T > 0$ and $d = 2$, since thermal fluctuations are stronger than in $d = 3$.

this same particle. A transverse critical force does not exist either for a single vortex line. It does exist, however, for a particle or vortex moving in a potential that is sufficiently correlated in the direction of motion, as happens for example with vortices in Josephson junction arrays [55]. We can therefore interpret the existence of F_{cy} as a spontaneous breaking of rotational symmetry. This purely dynamical effect can also give rise to an interesting hysteretic behavior [30], making the motion in the regime with $\mathbf{F} = F_x\mathbf{x} + F_y\mathbf{y}$ different depending on the order in which F_x and F_y are applied [30]. It is clear that none of the properties mentioned here can exist in a moving crystal with a shaking temperature [29].

Le Doussal and Giamarchi analyzed (a posteriori) the topological stability of the moving Bragg glass (see Fig. 2.10(b)) and concluded (a debated conclusion, see below) that if the disorder is weak enough, in $d = 3$, no dislocations appear. In $d = 2$, or in $d = 3$ at strong disorder or at intermediate velocities, the Bragg glass can become unstable, giving rise to the moving transverse glass. These two structures can be clearly distinguished by their translational order, as shown in Fig. 2.11. The moving Bragg glass has quasi-long-range translational order (see Fig. 2.11 (left)), while the moving transverse glass has quasi-long-range order in the transverse direction and short-range order in the longitudinal direction (see Fig. 2.11 (right)). Decreasing the velocity further, or increasing the disorder, it is plausible, although it has not been analytically described, that the periodicity of the moving transverse glass is lost due to the appearance of dislocations with Burgers vectors not oriented along the flow direction, giving rise to a plastic flow with the structure of a moving liquid (only the central Bragg peak in Fig. 2.11 (left) remaining, while the other peaks become short-ranged, or "gray" in the figure).

In Figs. 2.12, 2.13, 2.14 we show the dynamical phase diagrams proposed by Le Doussal and Giamarchi in two and three dimensions. Figure 2.12 (left) schematically shows the disorder–temperature–force $\Delta - T - F$ diagram in three dimensions. This is a direct

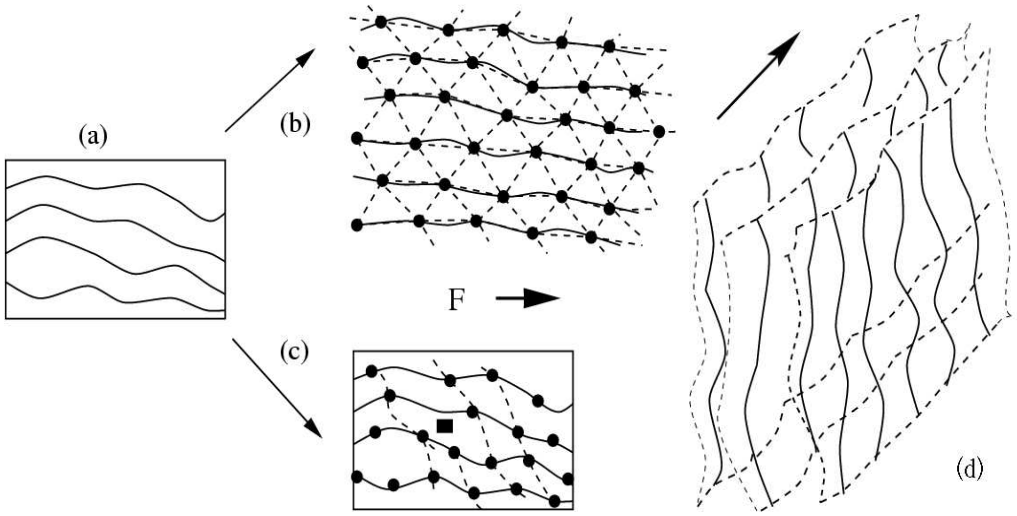


Figure 2.10: Moving vortex lattice with disorder. (a) Vortex motion takes place through static rough channels, elastically coupled in the transverse direction y. Depending on the dimension, velocity and disorder strength, two cases can occur: (b) Elastic flow, where the vortex positions are elastically coupled between channels ($d = 3$, weak disorder or large velocities). This regime, in which the lattice is topologically ordered, is the moving Bragg glass. (c) In $d = 2$ or for strong disorder in $d = 3$, the vortex positions in different channels can decouple, giving rise to dislocations with Burgers vectors aligned with the x direction (dislocation indicated by the black square). This regime with smectic order is the moving transverse glass. (d) Schematic image in $d = 3$ of the moving Bragg glass.

answer to the question posed in Fig. 2.2 in the general discussion of section 2.1.

As we can see, we recover the static phase diagram of Fig. 2.1 for $F = 0$. At $T = 0$ it is possible for the static Bragg glass to depin without breaking, into the moving Bragg glass, as shown in Fig. 2.12 (right) (consistent with the interpretation of the experimental Fig. 2.5 (right)). At $T = 0$ and $F < F_c$ the Bragg glass turns into an "amorphous glass", a topologically disordered phase about which very little is known (the $T = 0$ version of the vortex glass). The depinning transition of this phase is plastic. Increasing the velocity, the plastic flow can dynamically reorder in the transverse direction, possibly making a transition to a moving transverse glass. It is also possible for the moving transverse glass itself to make a transition to the moving Bragg glass at high velocities, with the elastic channels coupled longitudinally. In Fig. 2.13 (left) we see that if disorder is weak, the Bragg glass at $T > 0$ can connect continuously with the moving Bragg glass, passing through a creep regime at small forces $F < F_c$. It is interesting to note the reentrance of the dynamical melting line near F_c, which indicates strong stresses in the system at the crossover from the creep regime to the flow regime (see 2.3). For a finite velocity we can have three dynamical phases depending on the disorder strength, see Fig. 2.13 (right). The moving Bragg glass can melt, through thermal fluctuations, into a moving liquid, or, through disorder, into a moving transverse glass if disorder is strong enough to decouple the elastic channels and make dislocations with Burgers vectors parallel to the flow appear.

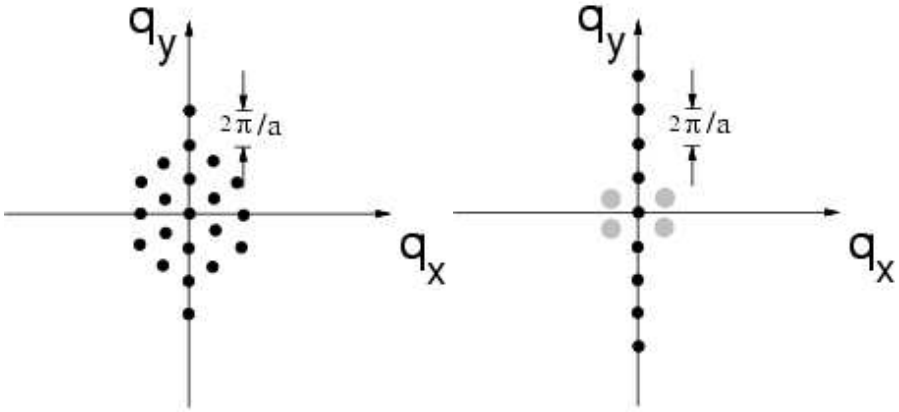


Figure 2.11: Left: structure factor of the moving Bragg glass. It shows Bragg peaks of a triangular lattice with quasi-long-range order. Right: structure factor of the moving transverse glass. It shows Bragg peaks in the direction transverse to the motion, where it has quasi-long-range order. In the longitudinal direction there are non-divergent (gray) peaks, which correspond to short-range translational order.

If we increase the temperature we can melt the moving transverse glass into a liquid, and by increasing the disorder further we obtain plastic flow, indistinguishable in its large-scale structure from a moving liquid.

In $d = 2$ the static phase diagram is not yet settled, and the dynamical one even less so. If we assume that there is no topologically ordered static phase in $d = 2$, we can expect most transitions to be simple crossovers at $T > 0$, and therefore the static phase to be continuously connected to a liquid. At $T = 0$ there will nevertheless be transitions as a function of force, see Fig. 2.14, which could be observed as strong crossovers at finite T. The static amorphous glass depins with plastic flow. Upon increasing the force, this plastic flow dynamically orders into elastic channels, possibly giving rise to the moving transverse glass.

Balents, Marchetti and Radzihovsky questioned the existence of the moving Bragg glass of Giamarchi and Le Doussal in $d = 3$. According to their calculations [31], the displacements in the longitudinal direction dominate at large scales over the transverse ones and are enough to destabilize the moving Bragg glass against the proliferation of dislocations with Burgers vectors parallel to $\mathbf{v}$. Due to the presence of these dislocations the channels dynamically decouple. Despite this, a structure of static channels persists. They called the resulting phase, with quasi-long-range order in the transverse direction and short-range order in the longitudinal direction, the "moving smectic". The question of whether or not the moving Bragg glass exists is nevertheless still controversial, since some experiments in superconductors show evidence of both dynamical phases depending on the magnetic field (see 2.7).

Figure 2.15 schematically shows the moving smectic for lines in three dimensions. Although from the structural point of view this phase is completely equivalent to the moving transverse glass predicted in ref. [30] (same structure factor as that shown in

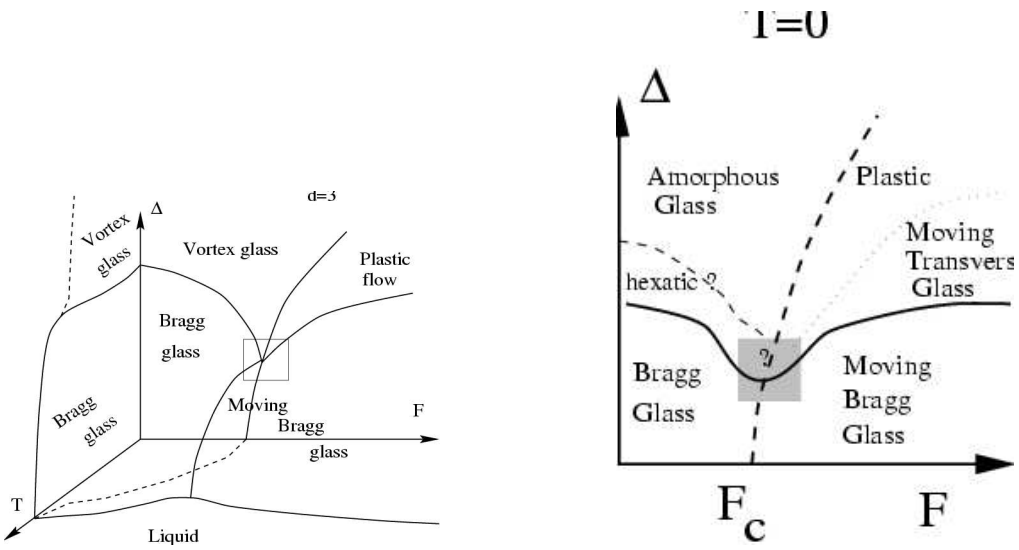


Figure 2.12: Dynamical phase diagram proposed by Le Doussal and Giamarchi for $d = 3$ [30]. Left: schematic diagram in temperature T, disorder Δ, and applied force F. For weak disorder and low temperatures the moving Bragg glass may be stable at all forces. For strong disorder the moving Bragg glass is only possible at high forces. At intermediate forces there is plastic flow (the moving transverse glass is not shown for clarity). The transition lines are schematic and the lower plane corresponds to a small but non-zero Δ. Right: schematic disorder–force cut at $T = 0$.

Fig. 2.11 (right)), it was initially given a different name due to some apparent differences. Balents, Marchetti and Radzihovsky [31] used a less simplified (although also effective) model for the moving smectic than the one used by Le Doussal and Giamarchi to describe the moving transverse glass [30]. In their model the hydrodynamic equations describing the moving smectic have the density as a variable in addition to the transverse displacements. This gives rise to a permeation mode that allows vortices to hop transversally between the static channels, spontaneously, as seen in Fig. 2.15 for $d = 3$. These hops do not appear in the description of Le Doussal and Giamarchi, in which the only variables are the transverse displacements. However, whether or not the permeation mode is taken into account, an ohmic transverse response is found at $T > 0$ [30, 31]. Hence the most recent review by Nattermann and Scheidl makes no distinction between the moving transverse glass and the moving smectic [35] (we will discuss this issue in chapters 3 and 6).

Figure 2.16 shows the disorder–force dynamical phase diagrams proposed by Balents, Marchetti and Radzihovsky [31]. They considered only the case $T > 0$. In Fig. 2.16 (left) we show the dynamical phase diagram for vortex lines in $d = 3$. For $F = 0$ we recover the static phase diagram with the Bragg glass for weak disorder and the vortex glass for strong disorder. The only stable phases at $F > 0$ in $d = 3$ are the moving liquid and the moving smectic. At low velocities a moving liquid, without translational order, is expected. Upon increasing the force this phase makes a transition to the moving smectic. The moving smectic can have a crossover to a moving Bragg glass. They leave open the possibility that

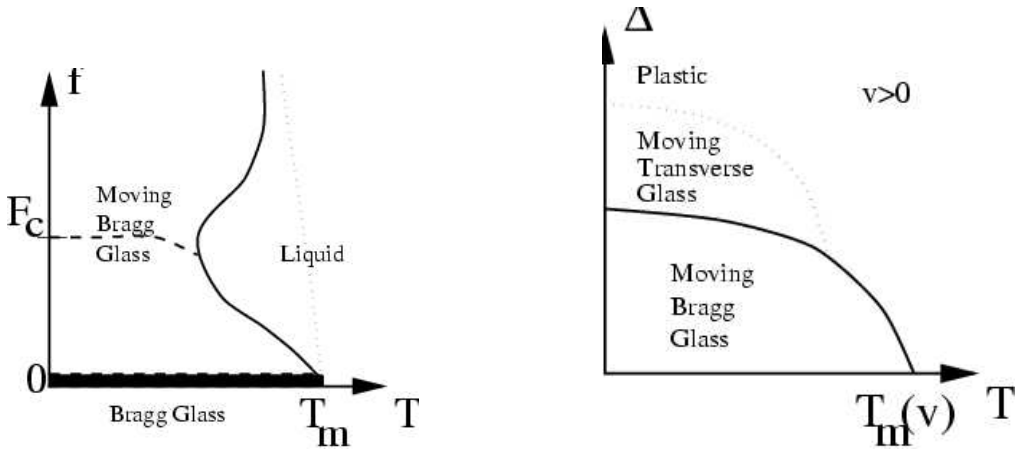


Figure 2.13: Dynamical phase diagrams proposed by Le Doussal and Giamarchi for $d = 3$ [30]. Left: disorder–temperature cut at a velocity above the thermally activated regime. This diagram is a dynamical version of the static one, Fig. 2.1(b). The moving Bragg glass can melt at T_m (first-order transition), or else its elastic channels can decouple upon increasing Δ, giving rise to the moving transverse glass. Right: force–temperature cut for weak disorder. The moving Bragg glass is stable at low temperatures and high forces and connects continuously, upon lowering F, with the static Bragg glass, passing through the thermally activated regime for $F < F_c$.

this moving Bragg glass extends even down to the low-velocity region, close to depinning. In this way they contemplate the possibility of an elastic depinning, like the one suggested in ref. [27], Fig. 2.5. In Fig. 2.16 (right) we show the dynamical phase diagram for point vortices in $d = 2$. The only stable phase in $d = 2$ is the moving liquid, but a crossover to a moving smectic is possible at high forces and weak disorder.

Scheidl and Vinokur also analyzed the problem of the large-scale description of the moving vortex lattice. The dynamical phase diagrams they propose for strong and weak disorder are shown in Figs. 2.17(a-b) respectively. Whether disorder is strong or weak, they expect a topologically ordered moving phase at high velocities. When the velocity decreases and disorder is strong, the fluctuations cause a massive production of topological defects, and a dynamical phase transition is expected between the coherent flow regime and the incoherent flow regime, Fig. 2.17(a). This transition line is associated with the dynamical melting first described in [29]. In this work the nature of the plastic flow phase is left open, as it could be a moving smectic or directly a moving liquid, but they propose a possible crossover between these phases due to the anisotropy of the Larkin domain. Lowering the force further, the moving fluid falls into the "pinned" phase, where the system moves by thermally activated jumps (creep). For weak disorder, 2.17(b), it is possible that at low temperatures the coherent flow regime extends down to the pinned regime, without going through the smectic or fluid regime.

Unlike the work of Balents, Marchetti and Radzihovsky, in this work the idea of the dynamical melting of the vortex lattice first proposed in [29] prevails, between an elastic

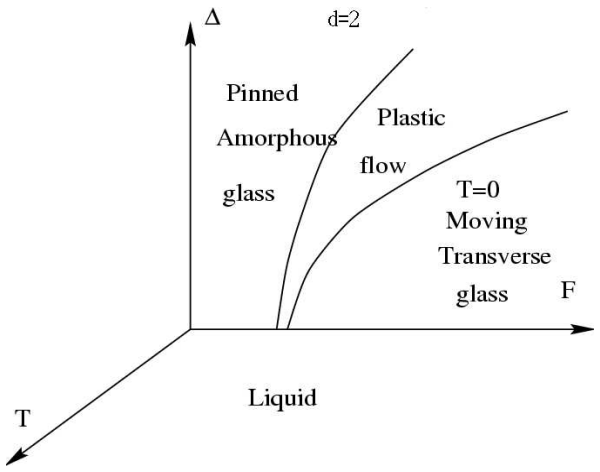


Figure 2.14: Schematic dynamical phase diagram proposed by Le Doussal and Giamarchi for $d = 2$ [30]. There are no topologically ordered structures. At $T = 0$ an amorphous glass depins with plastic flow, and upon increasing the force there is a transverse dynamical reordering that gives rise to the moving transverse glass. Upon increasing the temperature a very long crossover (not shown) to a moving liquid is expected. This phase diagram is only qualitative and has not yet been analytically justified.

flow regime (but no longer a crystal) and a plastic one. In this sense it is consistent with the work of Le Doussal and Giamarchi [30]. As we showed in section 2.3, there is experimental evidence of a dynamical melting transition, although its nature is not very clear [27, 41]. On the other hand, in section 2.4 we showed experimental evidence of the moving smectic structure and of the moving Bragg glass [52, 53]. Furthermore, numerical evidence of the dynamical melting transition was found in $d = 2$ by Koshelev and Vinokur [29], Ryu *et al.* [42], Faleski *et al.* [56] and by Domínguez *et al.* in $d = 3$ [45].

In $d = 2$ the dynamical melting transition can show up only as a crossover, which can nevertheless be very sharp for weak disorder and small systems. Spencer and Jensen [57] showed numerical evidence of the absence of topological order in $d = 2$ even at very high velocities. This instability was demonstrated analytically by Aranson *et al.* [58], who explicitly analyzed the dynamics of dislocations and their interactions on the moving lattice. They showed that the interaction between dislocations is screened over a finite length scale which, however, grows exponentially with velocity. From this they concluded that dislocation–antidislocation pairs would unbind with thermal fluctuations, and even more so due to the fluctuating components of the pinning force. Based on these studies, Nattermann and Scheidl propose in ref. [35] the dynamical phase diagrams of Fig. 2.18 for $d = 2$ and $d = 3$. The diagram for $d = 2$, Fig. 2.18(a), is identical to the diagram of Fig. 2.16 (right), with the moving liquid as the stable phase and a possible crossover to a moving smectic at high velocities. The diagram for $d = 3$ does not show the possibility of an elastic depinning of the Bragg glass, but presents a dynamical melting transition at high velocities from a smectic flow regime to a coherent elastic flow regime.

In conclusion, although since the pioneering works of Bhattacharya and Higgins [27]

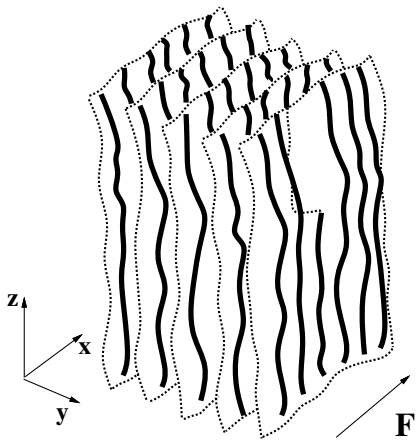


Figure 2.15: Schematic illustration of the smectic flow regime of vortex lines in $d = 3$. The channels are sheets along which the lines preferentially move. Hops between channels are allowed by permeation modes.

and of Koshelev and Vinokur [29] there has been great progress in the understanding of the collective dynamics of the vortex lattice, no agreement has yet been reached on the nature of the dynamical phases and their transitions. This can be appreciated by comparing the different dynamical phase diagrams proposed. In direct relation to the interpretation of experiments it is also necessary to understand many other issues, such as metastability and history effects, non-stationary relaxation dynamics (see chapter 7), edge or nucleation effects, etc.

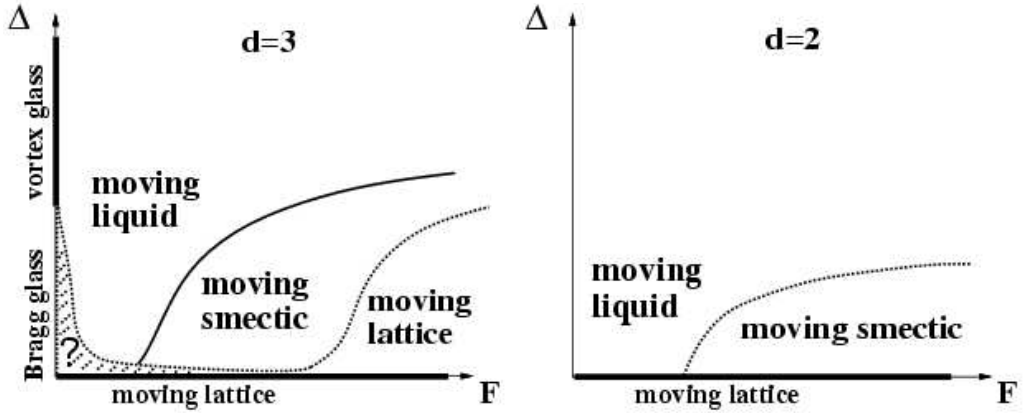


Figure 2.16: Schematic disorder–force dynamical phase diagrams proposed by Balents, Marchetti and Radzihovsky for $d = 2$ and $d = 3$ at finite temperature [31]. (a) In $d = 2$ the dotted line indicates that the smectic regime may be unstable and asymptotically indistinguishable from a moving liquid. In (b) the dotted line indicates that a moving elastic lattice is unstable against the proliferation of dislocations with Burgers vectors parallel to the flow and is therefore asymptotically a smectic regime. The region with the question mark indicates the possibility of a Bragg glass at low velocities.

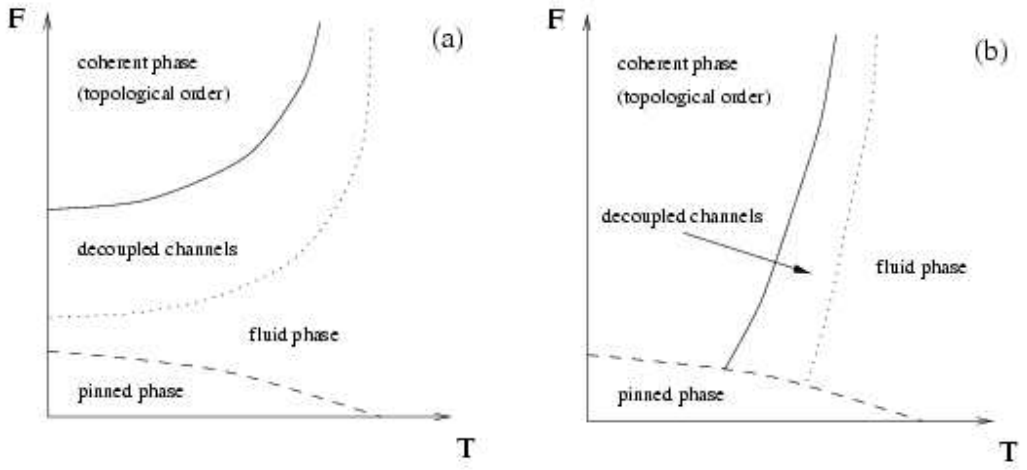


Figure 2.17: Schematic force–temperature dynamical phase diagrams proposed by Scheidl and Vinokur [32]. (a) When disorder is strong the pinned phase depins with plastic flow. Upon increasing the force this plastic flow orders into decoupled flow channels. The channels then couple in the direction of motion, giving rise to a coherent phase with topological order. (b) When disorder is weak the pinned phase can depin directly into a topologically ordered coherent phase, if the temperature is low enough. At higher temperatures we have the behavior of (a).

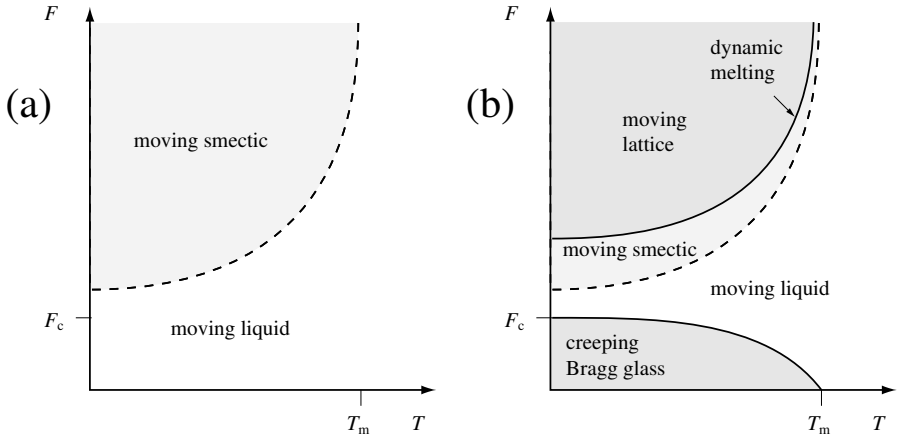


Figure 2.18: Schematic force–temperature dynamical phase diagrams proposed by Nattermann and Scheidl [35]. (a) In $d = 2$ the stable regime is the moving liquid. Upon increasing the force, a crossover to a smectic flow regime with short-range translational order is possible, which is therefore asymptotically indistinguishable from a moving liquid. (b) In $d = 3$ at high forces there is a coherent elastic phase. Upon lowering the force this phase melts dynamically into a smectic flow regime with short-range transverse translational order. Below the critical force the moving liquid turns into a Bragg glass with thermally activated motion.

Chapter 3

Transverse freezing in driven vortex lattices

We study driven vortex lattices in thin superconducting films. Above the critical current F_c we find two dynamical phase transitions at F_p and F_t, which could be observed through simultaneous measurements of the longitudinal voltage and of the transverse or Hall voltage. At F_p there is a transition from a plastic flow regime to a smectic flow regime where the voltage noise is isotropic (Hall noise = longitudinal noise), there is a peak in the differential resistance and the transverse diffusivity is maximal. At F_t there is a sharp transition to a frozen transverse solid where the Hall noise drops abruptly and vortex motion becomes localized in the transverse direction.

In this chapter we begin the study of the non-equilibrium steady dynamical regimes of vortex lattices in disordered superconductors. We start by analyzing the motion of vortices in thin superconducting films as a function of the external force. We analyze the translational and topological order, diffusion, the force–velocity characteristics and the noise in the temporal fluctuations of the instantaneous voltage. Particular emphasis is placed on the characterization of the different regimes through experimentally accessible properties, especially transport properties.

3.1 Motivation

The study of the collective motion of vortex lattices in superconductors has given rise to new concepts in the non-equilibrium statistical physics of systems driven in disordered media [27, 29–32, 41, 42, 45, 51, 52, 56–73]. The prediction [29] of a dynamical phase transition upon increasing the driving force, from a fluid-like plastic flow regime [56, 59–63, 74] to a moving coherent solid [29], has motivated a large number of recent theoretical [30–32, 58, 64–66], experimental [27, 41, 52, 67–69] and simulation [42, 45, 57, 70–73] works. The relevant physics of the high-velocity phases is controlled by the transverse displacements (in the direction perpendicular to the driving force) [30, 64], giving rise to a new class of driven systems characterized by anisotropic spatial structures with transverse

periodicity [30–32, 58, 64–66]. These anisotropic vortex structures have recently been observed experimentally by F. Pardo *et al.* [52], and their different features have been studied in simulations in two dimensions (2D) [42, 57, 70–72] and in three dimensions (3D) [45, 73]. In this chapter we show that additional information on the dynamical phases can be obtained by studying the anisotropic temporal fluctuations. We find two dynamical phase transitions that could be observed experimentally by measurements of the longitudinal and transverse voltage noise [75–79]. In the transverse direction, the direction in which the system is not driven, we can study diffusion, from which we define an effective temperature by analogy with equilibrium physics [29, 32, 58, 65, 66].

3.2 Method

We simulate a thin superconducting film using the model described in section 1.3.1. We study the dynamical regimes in the velocity–force (voltage–current) characteristics at $T = 0$, solving Eq. (1.35) for increasing values of $\mathbf{F} = F\mathbf{y}$. We normalize length scales by $l_0 = 4\xi$, energy scales by A_v, and time is normalized by $\tau = \eta l_0^2/A_v$. We consider N_v vortices and N_p pinning centers in a rectangular box of size $L_x \times L_y$, and the normalized vortex density is $n_v = N_v l_0^2/L_x L_y = B l_0^2/\Phi_0$. We consider a constant vortex density $n_v = 0.12$ in a box with $L_x/L_y = \sqrt{3}/2$, and $N_v = 64$, 144, 196, 256, 400, 784 (we show results for $N_v = 400$). We take a pinning strength $A_p/A_v = 0.2$ with a pinning center density $n_p = 0.24$. We use periodic boundary conditions, and the periodic long-range interaction is evaluated with an exact, rapidly convergent sum [51]. The equations are integrated with a time step $\Delta t = 0.01\tau$, and averages are computed over 32768 integration steps after 2000 iterations for equilibration (when the total energy reaches a stationary value). Each simulation is started at $F = 0$ with an ordered triangular lattice, and the driving force is slowly increased in steps of $\Delta F = 0.05$ up to values as high as $F = 8$.

3.3 Results

3.3.1 Dynamical regimes

We begin by looking at the vortex trajectories and at the translational and topological order of the lattice in the steady-state phases, as was done in [42, 45, 57, 70–73]. In Fig. 3.1(a-c) we show the vortex trajectories $\{\mathbf{r}_i(t)\}$ for typical values of F, by plotting the vortex positions for all integration steps. In the steady state these trajectories define the static channels for vortex flow. We also study the time-averaged structure factor, defined as the time average of the squared modulus of the Fourier transform of the instantaneous vortex density,

$$S(\mathbf{k}) = \left\langle \left| \frac{1}{N_v} \sum_i \exp[i\mathbf{k}\cdot\mathbf{r}_i(t)] \right|^2 \right\rangle , \tag{3.1}$$

which is shown in Fig. 3.1(d-f). In Fig. 3.2 we show typical Voronoi tessellations [80] for instantaneous configurations at different driving forces. The Voronoi polygons are the

Wigner–Seitz cells of each vortex, and therefore the number of sides of the polygons is the coordination number of each vortex. Disclinations correspond to vortices with coordination number different from 6. In Fig. 3.3(a) we plot the average vortex velocity

$$V = \langle V_y(t) \rangle = \left\langle \frac{1}{N_v} \sum_i \frac{dy_i}{dt} \right\rangle , \tag{3.2}$$

in the direction of the force as a function of F, and its corresponding derivative dV/dF. ($V = E/\rho_f J_0$, where ρ_f is the flux-flow resistivity and $J_0 = cA_v/d\xi\Phi_0$, so that dV/dF is proportional to the differential resistance, $dV/dF = \rho_f^{-1} dE/dJ$.) Below the critical force $F_c \approx 0.25$ all vortices are pinned and there is no motion, $V = 0$. Above F_c, we can distinguish three different dynamical regimes:

(i) *Plastic flow*: $F_c < F < F_p$. At F_c the vortices start to move in a few filamentary channels, as was also observed in [51]. A typical situation is shown in Fig. 3.1(a), where a fraction of the vortices moves in an intricate network of channels. As the force is increased, a larger fraction of vortices moves. In this regime vortices can also move in the transverse direction (perpendicular to $\mathbf{F}$) through a tortuous channel structure [63]. In Fig. 3.1(d) we see that $S(\mathbf{k})$ has only a central peak, showing the absence of spatial ordering in this plastic flow regime [51, 56, 59–63]. In Fig. 3.2(a) we see moreover that there is no topological order either in this regime. The high density of dislocations and the average orientation characterized by their Burgers vectors (see chapter 9 of [40]) do not indicate a privileged direction. Therefore the structure of the lattice in the plastic flow regime is similar to that of a moving liquid. However, it is not equivalent to a Galilean transformation ($\mathbf{r}' = \mathbf{r} - \mathbf{v}t$) of an equilibrium liquid, due to the presence of static flow channels and of fluctuations that are not well described by an equilibrium formalism (see chapter 6).

(ii) *Smectic flow*: $F_p < F < F_t$. We observe a peak in the differential resistance at the characteristic force $F_p \approx 1.3$. At $F = F_p$ we see that all vortices move in an apparently isotropic network of channels with maximal interconnectivity. In other simulations it was found that the peak in the differential resistance coincided with the maximum number of dislocations [71] and with the onset of orientational order [42]. The value of F_p was also taken in the experiment of Hellerqvist *et al.* [41] as an indication of a dynamical phase transition. Indeed, we find that above F_p a new dynamical regime sets in. In this case, as shown in Fig. 3.1(b), all vortices move along trajectories that are almost parallel to the force, forming "elastic channels". Two small Bragg peaks appear in the structure factor on the $K_y = 0$ axis, as seen in Fig. 3.1(e), which correspond to $\mathbf{G}_1 = (\pm 2\pi/a_0, 0)$. This is consistent with the onset of "smectic" ordering [31, 70] in the transverse direction, with elastic channels separated by a distance $\sim a_0 = n_v^{-1/2}$. In this regime the transverse motion consists of jumps of vortices from one channel to another, analogous to "thermally" activated transitions induced by local chaos. The frequency of these transitions decreases with increasing force, and they correspond to the permeation modes discussed in [31]. In Fig. 3.3(b) we plot the magnitude of the Bragg peaks at $\mathbf{G}_1$, $S_s = S(\mathbf{G}_1)$, corresponding to smectic order ($K_y = 0$), and of the other neighboring peaks at $\mathbf{G}_2 = \pm 2\pi/a_0(1/2, \sqrt{3}/2)$ and $\mathbf{G}_3 = \pm 2\pi/a_0(-1/2, \sqrt{3}/2)$, $S_l = (S(\mathbf{G}_2) + S(\mathbf{G}_3))/2$, corresponding to longitudinal order ($K_y \neq 0$). We see that above F_p the intensity of the smectic peak S_s starts to

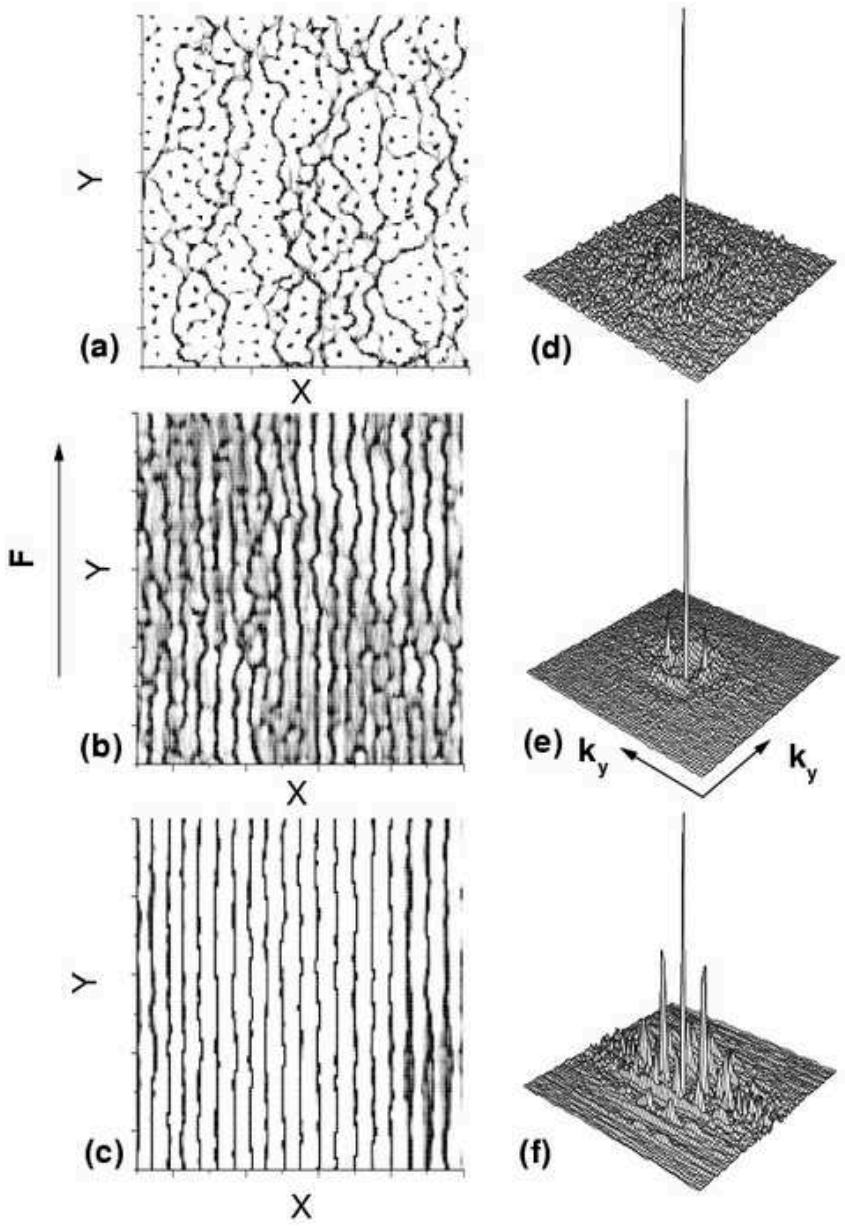


Figure 3.1: Vortex trajectories: (a) $F = 0.5$, (b) $F = 2.5$, (c) $F = 7$. Intensity surface plot of the averaged structure factor $S(\mathbf{k})$: (d) $F = 0.5$, (e) $F = 2.5$, (f) $F = 7$.

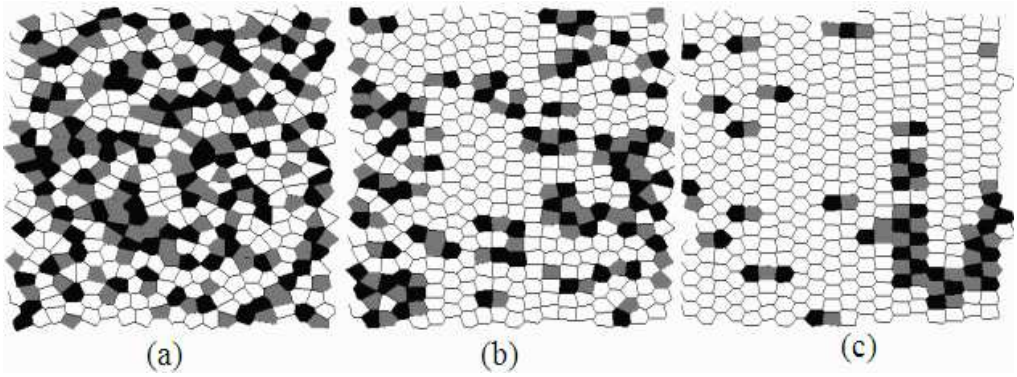


Figure 3.2: Typical instantaneous Voronoi tessellations: (a) $F = 0.5$, (b) $F = 2.5$, (c) $F = 7$. White polygons correspond to vortices with coordination number 6, gray ones to vortices with coordination number less than 6, and black ones to vortices with coordination number greater than 6. The driving force is applied in the vertical direction.

grow and $S_s \gg S_l$, while below F_p the spatial structure is isotropic, $S_s \approx S_l \ll 1$. The heights of the Bragg peaks depend on system size as $S(\mathbf{G}) \sim N_v^{-\sigma_G}$, where $\sigma_G = 0$ means long-range order (LRO), $0 < \sigma_G < 1$ means quasi-long-range order (QLRO) and $\sigma_G = 1$ means short-range order (SRO). In Fig. 3.3(c) we show the corresponding results for the smectic peak $S_s = S(\mathbf{G}_1)$ for sizes $N_v = 256$, 400, 784. We see that $\sigma_G \gtrsim 1$ in this regime: there is only short-range smectic order, so this phase corresponds to a liquid. In this sense the transition at F_p is a dynamical transition in the flow, as was found in [72] for strong disorder ($n_p = 1$). As we approach F_t (see below) we see a precursor of QLRO ($\sigma_G < 1$) but with strong fluctuations. In Fig. 3.2(b) we see that the density of dislocations is lower than in the plastic flow regime, showing the dynamical reordering effect predicted in [29] and observed experimentally in [52]. The Burgers vectors of the dislocations now point on average in the direction of the flow, consistent with the development of smectic ordering.

(iii) *Frozen transverse solid*: $F > F_t$. At a new characteristic force F_t, the jumps between channels suddenly stop and vortex motion freezes in the direction perpendicular to $\mathbf{F}$. An example for $F > F_t$ is shown in Fig. 3.1(c), where we see well-defined elastic channels parallel to $\mathbf{F}$. In the corresponding structure factor of Fig. 3.1(f), new peaks appear in $S(\mathbf{k})$ for directions with $K_y \neq 0$, at $\mathbf{G}_2$, $\mathbf{G}_3$, showing that there is some longitudinal order between channels. These extra peaks are smaller than the smectic peaks, and $S(\mathbf{k})$ is very anisotropic. We note in Fig. 3.3(a) that F_t is the point where the noisy behavior in dV/dF ceases. A similar criterion was used by Bhattacharya and Higgins to define their dynamical phase diagram [27, 67, 68]. In Fig. 3.3(b) we see that at F_t there is an increase in the longitudinal order S_l, and both S_s and S_l tend to saturate to an almost constant value for $F \gg F_t$. In Fig. 3.3(c) we find that there is QLRO smectic order [30, 31, 64, 70] with a value $0.5 < \sigma_G < 0.7$. However, we were not able to obtain a reliable finite-size analysis for the longitudinal peaks, since these showed large fluctuations from one size to the next. Moreover, we found hysteresis in S_s around F_t upon decreasing F. In Fig. 3.2(c) we see that the density of dislocations has decreased with respect to the smectic flow

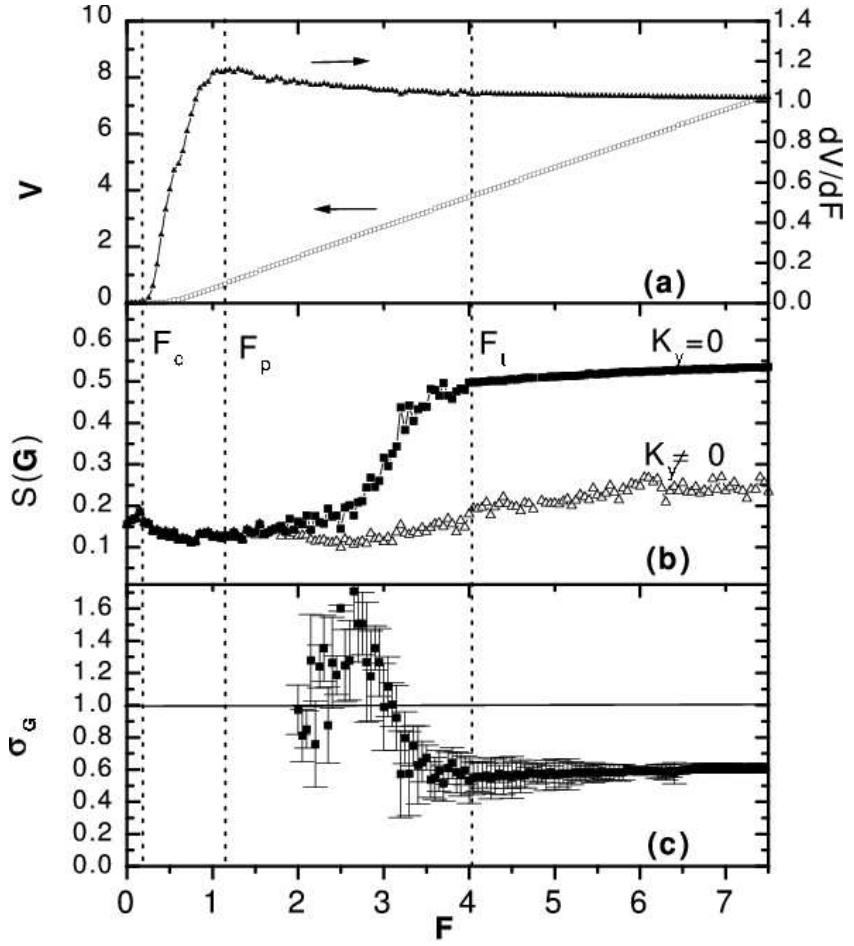


Figure 3.3: (a) Velocity–force curve (voltage–current characteristics), left scale, open symbols. dV/dF curve (differential resistance), right scale, filled symbols. (b) Intensity of the Bragg peaks. For smectic ordering, $S(\mathbf{G}_1)$, $K_y = 0$: filled symbols. For longitudinal ordering, $S(\mathbf{G}_{2,3})$, $K_y \neq 0$: open symbols. (c) Finite-size exponent σ_G ($S(\mathbf{G}_1) \sim N_v^{-\sigma_G}$).

regime, and that their Burgers vectors are strongly oriented in the direction of the flow.

3.3.2 Temporal fluctuations: voltage noise and diffusion

The dynamical transitions can be better understood by studying the temporal behavior of the system in both directions. Experimentally it was observed that the longitudinal voltage can display low-frequency noise [75–79][1], and it was found that its intensity reaches a very large value above the critical current, attributed to plastic flow [76–79], and then decreases for large currents. Moreover, even when the dc transverse voltage

$$\langle V_x \rangle = \left\langle \frac{1}{N_v} \sum_i \frac{dx_i}{dt} \right\rangle \tag{3.3}$$

is zero, it can also display fluctuations and noise [81]. In fact, it is easy to understand that this Hall noise will provide additional information, since it will be closely related to the tortuosity of the plastic flow channels around the direction of the force and to the jumps between elastic channels in the smectic phase. We have computed the power spectrum of both the longitudinal voltage,

$$S_y(f) = \left| \frac{1}{T} \int_0^T dt \, (V_y(t) - V) \exp(i2\pi f t) \right|^2 , \tag{3.4}$$

and the transverse voltage,

$$S_x(f) = \left| \frac{1}{T} \int_0^T dt \, V_x(t) \exp(i2\pi f t) \right|^2 . \tag{3.5}$$

The low-frequency noise is defined as $P_{x,y} = \lim_{f \to 0} S_{x,y}(f)$. In Fig. 3.4(a) we show the values of the longitudinal noise P_y and the Hall noise P_x as a function of force ($P_{x,y}$ was approximated as the average of the 10 lowest frequencies of the spectrum obtained).

We see that near the critical force the longitudinal noise is large, while the Hall noise is an order of magnitude smaller. In this plastic flow regime the noise is dominated by fluctuations in the direction of motion and by the tortuosity of the channels [63], and since there are few channels the Hall noise is small. When the number of channels increases, the vortices explore more in the x direction and the Hall noise grows. At F_p the voltage noise becomes isotropic, $P_x = P_y$. This is the point where we observed the maximum interconnection in the channel network. Above F_p, the appearance of smectically ordered elastic channels reduces the longitudinal noise. On the other hand, the Hall noise remains large due to "activated" jumps between elastic channels. At F_t the Hall noise drops abruptly, by almost two orders of magnitude. This corresponds to a freezing transition of vortex motion in the transverse direction. Above F_t there are no more jumps between elastic channels.

[1] In chapter 5 we analyze the high-frequency noise.

The low-frequency noise can be directly related to the diffusive motion at long times. We analyze the mean square displacement of the vortices in both directions from the center-of-mass position $(X_{cm}(t), Y_{cm}(t))$ as a function of time. We define

$$w_x(t) = \frac{1}{N_v} \sum_i [\tilde{x}_i(t) - \tilde{x}_i(0)]^2, \tag{3.6}$$

and

$$w_y(t) = \frac{1}{N_v} \sum_i [\tilde{y}_i(t) - \tilde{y}_i(0)]^2 \tag{3.7}$$

where $\tilde{x}_i(t) = x_i(t) - X_{cm}(t)$, $\tilde{y}_i(t) = y_i(t) - Y_{cm}(t)$. We observe that vortex motion for $F_c < F < F_t$ is diffusive in the transverse direction, $w_x(t) \sim D_x t$. In Fig. 3.4(b) we show the behavior of the transverse diffusion coefficient D_x. It closely follows the behavior of the Hall noise, $D_x \propto P_x$. Transverse diffusion is maximal at the peak of the differential resistance, F_p, and jumps abruptly to zero at F_t, indicating the transverse freezing transition. It is interesting to note that equilibrium melting transitions also show a jump in the diffusion coefficient. Above F_t, the transverse mean square displacement is time independent, since vortex motion is localized in the x direction: $w_x(t) \approx \langle(\Delta x)^2\rangle$. In the inset of Fig. 3.4(b) we show $\langle(\Delta x)^2\rangle$ vs. F for $F > F_t$. We find that $\langle(\Delta x)^2\rangle \approx 0.008a^2$ at F_t, consistent with a Lindemann criterion for melting [32, 58, 65, 66]. We can interpret D_x as an indication of an "effective temperature" T_{ef}. If D_x were a monotonically increasing function of T_{ef}, as happens in many particle systems (interacting or not) in equilibrium at the external temperature T, this would mean that T_{ef} grows above the critical force, has a maximum at the peak of the differential resistance, and decreases when the motion starts to order. Following the analogy with the equilibrium situation, above F_t we can interpret $\langle(\Delta x)^2\rangle$ as proportional to T_{ef}, as occurs in elastic solids in equilibrium at the external temperature T [40]. Here we find that $\langle(\Delta x)^2\rangle$ decreases with F, consistent with a behavior $T_{ef} \sim 1/V$ [29, 32, 58, 65, 66]. These qualitative observations served as motivation for the work presented in chapter 6, where we define a T_{ef} more rigorously and analyze its behavior as a function of force and temperature.

The long-time behavior is better understood by studying the diffusion exponents $w_x(t) \sim t^{\zeta_x}$ and $w_y(t) \sim t^{\zeta_y}$. In Fig. 3.4(c) we show the behavior of $\zeta_{x,y}$. We see that for $F_c < F < F_t$, $\zeta_x \approx 1$, corresponding to normal diffusion, while for $F > F_t$, $\zeta_x \approx 0$, corresponding to a freezing of the transverse motion. Motion in the longitudinal direction is on the other hand always superdiffusive, $\zeta_y > 1$. Above F_t, in the frozen phase, the longitudinal fluctuations enter a ballistic regime, $\zeta_y \approx 2$. Since the vortex positions are localized in the x direction, we see that $w_y(t) = \langle(y(t) - y(0))^2\rangle \approx A_y t^2$, with $A_y = \langle(\Delta v_y)^2\rangle$ the dispersion of the average velocities of the elastic channels. In the inset of Fig. 3.4(c) we find that A_y decreases exponentially with force, $A_y \sim \exp(-\alpha F)$. [This suggests a "thermal" distribution of the channel velocities: since $T_{ef} \sim 1/F$, then $\langle(\Delta v_y)^2\rangle \sim \exp(-\alpha'/T_{ef})$.]

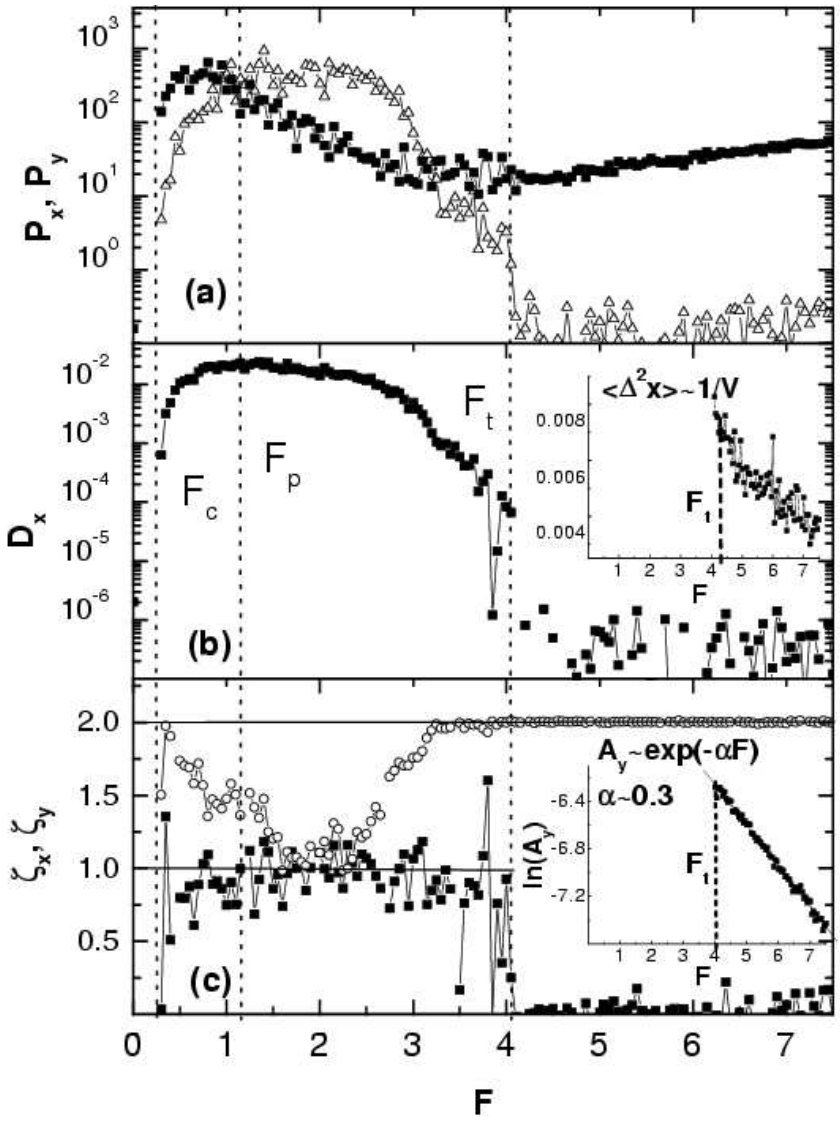


Figure 3.4: (a) Low-frequency voltage noise vs. F. Longitudinal voltage noise, P_y, filled symbols. Hall noise, P_x, open symbols. (b) Diffusion coefficient for the transverse motion, D_x. The inset shows the transverse mean square displacement $\langle \Delta^2 x \rangle$ in the frozen phase, $F > F_t$. (c) Diffusion exponents ζ_x (filled symbols) and ζ_y (open symbols) defined from: $\langle [\tilde{x}(t) - \tilde{x}(0)]^2 \rangle \sim t^{\zeta_x}$, $\langle [\tilde{y}(t) - \tilde{y}(0)]^2 \rangle \sim t^{\zeta_y}$. The inset shows a plot of A_y defined from a fit $\langle [\tilde{y}(t) - \tilde{y}(0)]^2 \rangle = A_y t^2$ for $F > F_t$.

3.4 Discussion

3.4.1 Model for anomalous longitudinal diffusion

It is interesting to analyze in more detail the anomalous longitudinal diffusion found in the smectic and transverse solid regimes, since it originates in long-range temporal correlations generated by the dynamics, which are absent in the undriven system. From a purely statistical point of view, the central limit theorem does not apply to the displacement of a Brownian particle if its velocity autocorrelation function decays as slowly as or more slowly than t^{-1}. If this happens the diffusion is anomalous [82], that is, the mean square displacement does not grow linearly with t (which would be normal diffusion). We can first show that the anomalous diffusion with diffusion exponent $1 < \zeta_y < 2$ (superdiffusion) observed in the smectic regime can be qualitatively explained with a very simple model, assuming that vortices move most of the time along the elastic channels separated by a distance a_0 and that they occasionally make normal diffusive jumps between them in the transverse direction. The sketch illustrating this model for the smectic regime is shown in Fig. 3.5. We will assume that the velocity of each channel $V_y(X)$ is a random variable that depends only on the channel X, that there are no correlations between channels (that is, we neglect the coupling between channels), and that, since we are observing diffusion from the center of mass, the mean value of V is zero. That is,

$$\begin{aligned} \langle V_y \rangle &= 0 \\ \langle V_y(X) V_y(X') \rangle &= \sigma_V \delta(X - X') \end{aligned} \tag{3.8}$$

We assume that the transverse motion is Brownian,

$$\begin{aligned} X_t &= \int^t \eta(t')dt' \\ \overline{\eta(t)} = 0, \qquad \overline{\eta(t')\eta(t)} &= 2D_x\delta(t-t') \\ \overline{X_t^2} &= 2D_x t \end{aligned} \tag{3.9}$$

The longitudinal displacement Y_t depends on the realizations of the "thermal noise" (see chapter 6) $\eta(t)$ and on the realizations of the velocity profiles $\{V_y(X)\}$,

$$Y_t = \int^t V_y[X_{t'}]dt' \tag{3.10}$$

A model completely analogous to Eqs. (3.8), (3.9), (3.10) was first considered by Matheron and de Marsily [83] to study diffusion in porous rocks that exhibit a large-scale permeability, and therefore velocity fluctuations (in this case the channels represent the layers in which the fluid can move easily, and the porosity between layers gives rise to transverse diffusion). The quantity we are interested in computing is the longitudinal mean square displacement $\langle Y_t^2 \rangle$. Using (3.8), (3.9), (3.10) it is not difficult (see Appendix "C" of [82]) to find the solution

$$\langle Y_t^2 \rangle = \frac{4}{3} \frac{\sigma_V}{\sqrt{\pi D_x}} t^{3/2}, \tag{3.11}$$

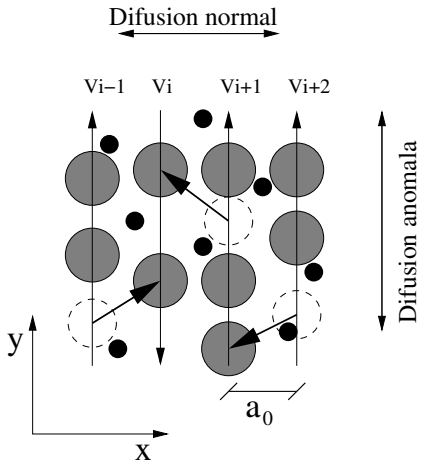


Figure 3.5: Model to explain longitudinal superdiffusion in the smectic flow regime (labels: *difusión normal* = normal diffusion, *difusión anómala* = anomalous diffusion). We assume that vortices move preferentially along the elastic channels and occasionally make normal diffusive jumps between channels, activated by the transverse fluctuations of the pinning force. We also assume a non-zero distribution of average velocities in each channel. This simple model displays long-range temporal correlations in the longitudinal direction, giving rise to anomalous longitudinal diffusion (superdiffusion).

Therefore there is superdiffusion in the longitudinal direction with a diffusion exponent $\zeta_y = 3/2$. Furthermore, one can compute [82] the longitudinal velocity autocorrelation function of a vortex,

$$\langle \dot{Y}_{t=0} \dot{Y}_t \rangle \sim \frac{\sigma_V}{\sqrt{D_x t}} \tag{3.12}$$

It is these long-range temporal correlations, induced by the transverse motion, that are responsible for the violation of the central limit theorem. This is easy to understand if we keep in mind that $\langle Y_t^2 \rangle \sim t \int^t C(t')dt'$, where $C(t) = \langle \dot{Y}_{t=0} \dot{Y}_t \rangle$. Assuming $C(t) \sim t^{-\gamma}$ we have $\langle Y_t^2 \rangle \sim t^{2-\gamma}$ if $\gamma < 1$ and $\langle Y_t^2 \rangle \sim t \ln(t)$ if $\gamma = 1$. We see then that long-range correlations lead in general to superdiffusion (not considering the possible cases in which $C(t)$ oscillates), basically because the net displacement cannot be divided into an effective number of independent variables or blocks. The exponent given by our simple model is $\zeta_y = 3/2$, intermediate between the values found in the simulation for the whole smectic regime (see Fig. 3.4(c)). A more complicated model taking into account the dependence of the transverse diffusion constant D_x on the external force F, as well as the effect of the weak coupling between channels and the consequent correlation of their velocities, could explain the variation of the superdiffusion exponent with force.

With the same model with which we qualitatively explained superdiffusion we can also explain ballistic diffusion in the transverse solid. In the transverse solid $D_x = 0$, so

$$Y_t = \int^t V_y[X_{t'}]dt' = V_y[X_{t'=0}]t \tag{3.13}$$

which implies that

$$\langle Y_t^2 \rangle = \sigma_V t^2 \tag{3.14}$$

with exponent $\zeta_y = 2$, as found in the simulation in the transverse solid regime (see Fig. 3.4(c)). It is interesting to note that the ballistic diffusion coefficient A_y computed in the simulation corresponds, in terms of this simple model, to the dispersion of the channel velocities σ_V. Therefore (within this interpretive framework) $A_y = \sigma_V \sim \exp(-\alpha F)$ implies that the channel velocities approach the mean value of the velocity (voltage) exponentially upon increasing F. In other words, the distribution of longitudinal velocities narrows as its mean value grows. This is because the coupling between channels, related to the short-range longitudinal translational order, improves at high velocities. The dynamical effect of disorder on the dispersion of the average velocities of the individual channels therefore decreases with velocity. The picture left by this model, of channels that slide and rub against each other like the layers of a viscous fluid (see [84]), is however a macroscopic simplification that does not take into account the local triangular order. The true microscopic mechanism of sliding between channels is the motion of dislocations.

3.4.2 Properties of the transverse solid

As we see in Fig. 3.1(f), the high-velocity phase locally displays some degree of triangular order. It is then interesting to analyze the result $\zeta_y \approx 2$ for the high-velocity phase from the point of view of the dynamics of dislocations on that moving triangular lattice. The existence of longitudinal diffusion implies that the moving lattice undergoes continuous plastic deformation. This tells us that even at high velocities the dislocations of the transverse solid, Fig. 3.2(c), move in the center-of-mass reference frame in response to the inhomogeneous stresses, with rapidly fluctuating components, produced by the pinning forces. As we see in Fig. 3.2(c), the longitudinal direction (in which the system is driven) coincides with the direction of the Burgers vectors of the dislocations. Analyzing short time sequences of Voronoi tessellations in the transverse solid we were able to observe that the dislocations move only in the longitudinal direction [85]. It is well known that this sliding or "gliding" motion of dislocations is the main mechanism of plastic deformation in two-dimensional solids subjected to stress. This is because gliding is controlled by the Peierls barriers, which are much smaller than the energy barriers for dislocation "climb". This result for the high-velocity dynamical phase in two dimensions agrees with recent analytical predictions based on models for the dynamics of dislocations on the rapidly moving vortex lattice. In [58, 66] it is shown that the moving vortex solid in two dimensions is unstable even at high velocities, due to the presence of free dislocations that move with a finite mean velocity with respect to the center-of-mass reference frame of the lattice. In [58] it is shown on the one hand that there is a finite screening length in the interaction of dislocations, and in [66] it is found that the mean velocity $V_d = V - \tilde{V}_d$ of test dislocations is lower than that of the vortex lattice V, with $\tilde{V}_d \sim V^{-4}$. The result we find in our simulations for the longitudinal diffusion, $A_y \sim \exp(-\alpha F) \sim \exp(-\alpha V)$, tells us that the mobility of the dislocations relative to the center of mass of the vortex lattice indeed decreases with V, but with an exponential decrease rather than a power

law. The difference could be due to the fact that [66] considers the case of very dilute non-interacting dislocations on the vortex lattice (that is, with a density much lower than that of the vortices) under weak pinning, while our simulations are for strong pinning and show a high density of dislocations. Even taking into account that the interaction between dislocations out of equilibrium is short-ranged [58], if the mean separation between dislocations is smaller than the screening length, something that can happen since the latter grows exponentially with velocity [58], one could have a phenomenon analogous to "work hardening" (where the interaction between dislocations hinders their mobility), provided the "entropic" effect of the fluctuating components of the pinning force is weak, as happens at high velocities. This hardening would lead to a faster decrease of the mobility of dislocations than in the dilute case. It would be very interesting to address this question systematically, since little is known about how the collective dynamics of dislocations affects the rheological properties of locally ordered structures out of equilibrium.

3.4.3 Analogy with supercooled liquids

The behavior of the longitudinal plasticity of the transverse solid also motivates the following discussion. Let us first note that the dispersion of the longitudinal velocities, or ballistic diffusion coefficient, in the transverse solid grows exponentially fast at high velocities. What makes this behavior very interesting and suggestive is the observation that many supercooled liquids display a dramatic exponential increase of the viscosity as a function of $1/T$ (instead of the velocity V), typically well described by a Vogel–Fulcher law $\eta \sim \exp[-A/(T-T_0)]$ [86]. The case $T_0 \neq 0$ describes the so-called fragile glasses, while the case $T_0 = 0$, in which the Vogel–Fulcher law takes the form of an Arrhenius law $\eta \sim \exp[-A/T]$, describes the so-called strong glasses. Although there is no characteristic temperature, in the latter it is customary to define an empirical crossover temperature T_g, above which it is practically impossible to equilibrate the system (for example, thermodynamic quantities begin to depend on the cooling rate, etc.). The comparison of $A_y \sim \exp(-\alpha V)$ with the Arrhenius law $\eta \sim \exp[-A/T]$ suggests defining an "effective temperature" $T_{ef} \sim 1/V$, with the possibility of a dynamical crossover of the moving vortex lattice at a velocity V_g, analogous to a "glass transition". This dynamical crossover would be relevant as long as V_g is not larger than the Cooper-pair-breaking velocity. With this analogy with supercooled liquids, above V_g the dynamics would be slow and the properties of the steady state could depend on its preparation history, as was observed in some dynamical regimes in [87]. There is then the interesting possibility that the strongly driven vortex lattice behaves similarly to a window glass (or supercooled liquid), with an elastic response to fast shear stresses (with dislocations practically frozen on top of the moving lattice) and like a fluid under slow stresses. This highlights the relevance of a detailed analysis (as a function of frequency, for example) of the viscoelastic response of the lattice [88].

Curiously, a velocity-dependent temperature $T_{ef} \sim 1/V$, which here we defined by analogy with an Arrhenius law, was proposed in [29] by drawing an analogy between the temporal correlations of the pinning force and the correlations of a Langevin thermal noise. It must be admitted, however, that both here and in [29] such an association has been

purely heuristic. It would be desirable for the definition of a non-equilibrium temperature not to be merely a simple parameter serving as a link to establish an analogy with an equilibrium formulation in a particular situation, but a concept retaining as much as possible all the empirical properties of the thermodynamic temperature, such as being measurable with a thermometer and controlling the direction of heat flow [89]. In chapter 6 we will deal more rigorously with the definition of an effective temperature T_{ef} for the moving vortex lattice.

3.4.4 Dynamical phases in two dimensions

Our simulations of two-dimensional thin superconducting films do not give evidence, at any finite velocity, of the existence of a moving crystal [29], nor of a vortex solid with coupled channels and frozen dislocations on the moving lattice [71, 87]; rather, they agree with [56, 57, 66]. The observation of a vortex solid in simulations of vortices in two dimensions could be due to the fact that, in weak pinning situations such as those considered for example in [71, 87], finite-size and finite-time effects become very relevant. On the one hand, finite-size effects are important because they lead in general to an overestimate of the translational and topological order of the lattice. In the static case in two dimensions, for example, where there is no Bragg glass due to the existence of unpaired dislocations [17], it was found that the mean separation between dislocations ξ_D and the characteristic length of translational order R_a (defined from $u(R_a) - u(0) \sim a$, where $u(x)$ are the displacements of the vortices with respect to the perfect lattice with lattice parameter a) satisfy $\xi_D \gg R_a$ [54] when pinning is weak, at any temperature below the melting temperature of the lattice. Therefore a numerical simulation of the vortex lattice with weak disorder in the static case could appear, due to finite-size effects, as a crystal if $L_{sim} < R_a \ll \xi_D$, as a Bragg glass if $R_a < L_{sim} < \xi_D$, or as a topologically disordered structure if $R_a < \xi_D < L$ (whose rigidity would depend on the thermal mobility of the dislocations). Finite-size effects in the system out of equilibrium are much more complicated to analyze, because energy-balance considerations are inadequate for estimating the characteristic lengths. However, one would expect a variety of dynamical crossovers due to finite-size effects to be possible. The following important points are worth mentioning. (i) The dynamical reordering effect makes the characteristic lengths depend on the velocity v (very strongly if disorder is weak), which generates crossovers as a function of v. (ii) Although in general keeping the reflection symmetry with respect to the direction of the driving force, the structure of the moving lattice is anisotropic [30–32], and therefore the translational order lengths split, $R_a \to R_{ax}(v), R_{ay}(v)$, describing anisotropic correlation volumes. (iv) Non-equilibrium effects add in some cases new characteristic lengths (absent in the static case), such as the existence in two dimensions of a finite screening length in the interaction between dislocations, of the type $L_s(v)$, due to "KPZ" (Kardar–Parisi–Zhang) terms generated in the coarse-graining of the bare equation of motion of the vortices [58]. In the dynamical case in two dimensions we thus have an expanded family of characteristic lengths such as $R_{ax}(v)$, $R_{ay}(v)$, $\xi_D(v)$, $L_s(v)$. If disorder is weak enough, the size of the simulated sample L_{sim} could be comparable to any of them for a velocity lower than the pair-breaking velocity, which can generate various dynamical

crossovers. The new phases observed in simulations for very weak disorder, although not observed for strong disorder, could nevertheless have an experimental counterpart if the dependence on v is so strong that the characteristic lengths can become of the order of the experimental scale L_{exp}.

Finite-time effects are also very important at high velocities because, as we saw, the dynamics becomes slow. The finite observation time scale can lead us to confuse, for example, a viscoelastic flow with a purely elastic flow of the lattice at high velocities [56]. Many materials are known [86] that behave as solids under fast stresses and as liquids under slow stresses (cf. window glass, some pastes, etc.). In order to understand the dynamical behavior of the vortex lattice it would then be very interesting to study, for example, the time-dependent viscoelastic response of the vortex lattice. In numerical simulations where disorder is weak, the separation of time scales is more pronounced than for strong disorder. The plastic deformation of the moving transverse solid could then go unnoticed in a simulation if the observation time scale is not long enough, and be mistaken for example for a solid with frozen dislocations [87]. Directly related to the slow dynamics are metastability and history effects.

To compare our results with those of earlier simulations in two dimensions, it is also worth mentioning that the great majority of them [29, 56, 57, 70, 71, 87] used a short-range vortex–vortex interaction potential. As we saw in section 1.3.1, a realistic simulation in two dimensions corresponds to that of a thin film with thickness $d \ll \lambda$, and in that case the interactions between vortices are long-ranged. From a macroscopic point of view the difference between the interaction potentials can be well appreciated by comparing the elastic constants C_{11} (compression) and C_{66} (shear) of the vortex lattice without disorder [51]. With short-range interactions corresponding to the interaction between rigid vortices in three dimensions, these are $C_{66} = B\Phi_0/16\pi\mu_0\lambda^2$ and $C_{11}(k) = B^2/\mu_0(1+\lambda^2k^2)$, where k is the wave vector of the deformation [90]. This gives $C_{66}/C_{11} = (a_0/\lambda^2)/16\pi$, since $k\lambda \gg 1$. Since in most simulations $\lambda \gtrsim a_0$, then $C_{66} \lesssim C_{11}$. For logarithmic interactions, instead, $C_{66}d = B\Phi_0/8\pi\mu_0\Lambda^2$ and $C_{11}(k)d = 2B^2/\mu_0k^2\Lambda$. Since Λ is typically of the order of the experimental sample, the elasticity of the vortex lattice in thin films is non-local at all length scales and moreover incompressible, $C_{11}(k) \to \infty$ when $k \to 0$. For films $C_{66}/C_{11} = (ka_0)^2/16\pi$, and since typically $ka_0 \ll 1$ we have $C_{66} \ll C_{11}$. This favors uniform filamentary flow [51] much more than in the case of short-range interactions. The stability of the coherently moving vortex solid is therefore much more compromised in the realistic two-dimensional case, due to shear stresses. This makes it more plausible that the high-velocity phase is the transverse solid.

3.4.5 Nature of the fast phase

Comparing with the theoretical predictions for the high-velocity vortex phase, we find that the moving transverse solid at $T = 0$ qualitatively resembles the moving transverse glass proposed by Giamarchi and Le Doussal, since: (i) it has quasi-long-range order in the transverse direction (it is therefore not asymptotically a liquid [31]); (ii) at least at $T = 0$ there are no permeation modes in the transverse direction, as predicted for the smectic regime by Balents, Marchetti and Radzihovsky [31]; (iii) the channels are elastically

coupled only in the transverse direction, which rules out the coherent motion [29, 32] of a crystal or the moving Bragg glass [30]; (iii) although we did not test in this work the existence of a finite transverse critical current F_{ct}, other simulations show that it exists even in a regime of decoupled channels analogous to our transverse solid. We believe it very plausible that the transverse freezing transition is directly related to the appearance of a finite value of $F_{ct}(F)$ at $F = F_t$, that is, that $F_{ct} = 0$ if $F < F_t$ and $F_{ct} > 0$ if $F > F_t$. The plausibility argument ultimately rests on a supposed fluctuation–dissipation relation between the response of the transverse voltage to a small transverse current and the spontaneous fluctuations of the transverse voltage (see chapter 6). The sharp drop of the Hall noise at the transverse freezing transition would then be related to the appearance of a finite F_{ct}. Although we can make a good qualitative correspondence between the transverse solid and the transverse glass of Giamarchi and Le Doussal [30], we cannot rule out the possibility that the transverse solid observed at $T = 0$ actually represents a low-temperature crossover of a smectic flow regime, or even of a liquid [31], with transverse diffusion and $F_{ct} = 0$. Settling this question requires simulations at finite T for the high-velocity regime with finite-size and finite-time analyses. One should determine well: (i) the analyticity of the response of the transverse voltage to a small transverse transport current; (ii) the transverse diffusion at temperatures low compared with the other energy scales; (iii) the transverse translational order. Since we do not have such a detailed analysis, in the next subsection we will qualitatively discuss the effects at low T compared with the pinning strength.

3.4.6 Finite-temperature behavior

The dynamical phases and transitions reported here are at $T = 0$ in two dimensions. Since the effect of thermal fluctuations is all the more important the lower the dimension of the space in which the system is embedded, it is very relevant to ask how the results obtained would be modified if T were finite, although very small. Due to lack of time we have not yet carried out the necessary systematic study of what happens. However, in the hope that even the least grounded speculations of this thesis may serve someone as motivation for future studies, we will mention some qualitative results of simulations at finite T. These first observations lead us to believe that the effect of static disorder on the driven vortex lattice at $T = 0$ is qualitatively independent of, and can be superimposed to a good approximation on, the thermal effects present at finite T, as long as $k_B T \ll A_p$, where A_p is the pinning strength (for $k_B T \sim A_p$ we expect the simple superposition not to hold). Due to thermally activated motion, the depinning transition at $F \sim F_c$ at finite T does not represent a true depinning but remains a pronounced crossover where the force–velocity (FV) curve is non-linear and the longitudinal voltage noise grows sharply. Although difficult to observe at very low T due to finite-time effects, the voltage does not vanish completely for $F < F_c$, and a low dissipation persists due to thermally activated vortex motion (creep). The main qualitative effect of thermal noise in the plastic flow regime $F_c < F < F_p$ is to broaden the channels somewhat, and to restore ergodicity by making the tortuous structure of static channels at $T = 0$ evolve, exploring different configurations on the pinning potential (we believe there would, however, be a finite

average tortuosity). The transport properties of the plastic flow regime, on the other hand, are very insensitive to these differences in the microscopic motion, being very similar to those at $T = 0$. The same holds for the spatio-temporal order, which continues to resemble that of a liquid. Qualitatively, the transition to the regime with smectic order at $F \sim F_p$, coinciding with the peak of the differential resistance, is still associated with a transition in the average tortuosity of the channel structure. The transverse jumps between elastic channels of the smectic regime are now activated by both the fluctuations of the pinning force and the thermal fluctuations. We will prove this last statement quantitatively in chapter 6, in relation to the dependence of the transverse effective temperature on the temperature of the thermal bath. As we showed in Fig. 3.1, the transition to the transverse solid at $T = 0$ is marked by the sudden disappearance of the jumps between channels at $F = F_t$. One would then expect thermal activation to make an important difference for $F \sim F_t$, since the pinning-activated transverse diffusion becomes negligible compared with the thermal one. If for $F > F_t$ the dynamical barriers for transverse motion are finite, there is a non-zero probability of having thermally activated jumps between channels, and therefore a purely thermal mechanism for transverse diffusion. We do not yet have results supporting this statement, since to compute transverse diffusion well at low T it is necessary to simulate the system for a much longer time than had been done. We must also mention the possibility that the dynamical barriers for transverse motion are effectively divergent, as suggested by the existence of a critical current in the transverse glass of Giamarchi and Le Doussal. The transverse freezing transition at $F \sim F_t$, a key result of this work, still shows up for sufficiently low T as a pronounced crossover where the transverse diffusion constant and the Hall noise drop by several orders of magnitude. It is interesting to note that this change of regime of the transverse motion upon increasing the driving force near F_t, from a regime with transverse diffusion activated by pinning and thermal forces to a regime with thermal activation only, is analogous to the longitudinal depinning transition at $F = F_c$.

To end this discussion of thermal effects, it should be said that without systematic simulations at finite T with adequate finite-size and finite-time analyses we cannot go deeply into the most important questions of the theoretical controversy about the dynamical phases, based on the large-scale description of the moving vortex lattice. Unfortunately our computational capacity is for now insufficient for this task, if we restrict ourselves to reasonable computation times.

3.4.7 Comparison with experimental results

An important result of this chapter is that the transitions between dynamical regimes that we find can be well characterized by transport measurements.

As we showed in Fig. 3.3(a), the transition at F_p between the plastic flow regime and the smectic flow regime is well signaled by the peak in the differential resistance. This characteristic force was used in [41] to construct the dynamical phase diagram of Fig. 3.6. The interpretation given in [41] to this transition at the peak of the differential resistance was in terms of the dynamical phase diagram of Koshelev and Vinokur, Fig. 2.4, as a transition from a moving liquid to a moving crystal. Here we therefore show that this

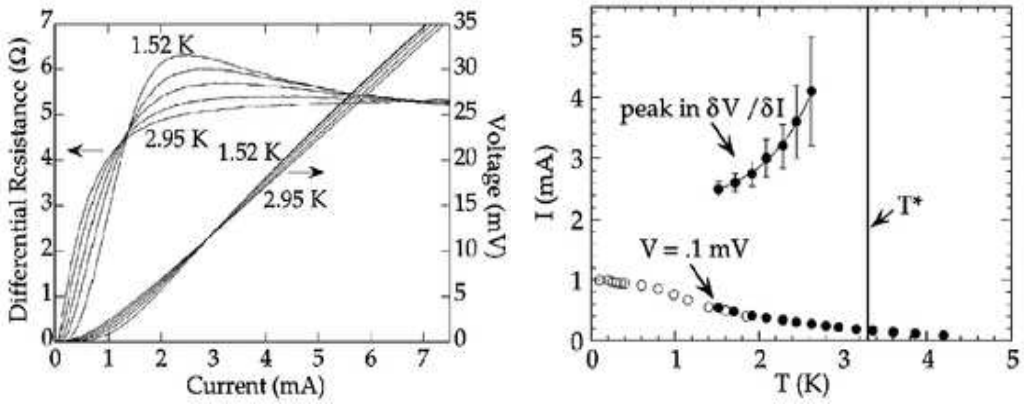


Figure 3.6: Right: experimental current–temperature dynamical phase diagram of a thin superconducting film of $Mo_{77}Ge_{23}$ [41]. The first transition line is the critical depinning current and the second is the current at the peak of the differential resistance. Left: typical IV and dV/dI–I curves from which the characteristic currents were extracted.

interpretation is incorrect. Moreover, in our simulations of two-dimensional thin films like those of [41] we have no evidence of a moving crystal, consistent with refs. [30–32].

The transition at F_t from the smectic flow regime to the moving transverse solid is well signaled by the transverse or Hall low-frequency noise. Since this measurement has not yet been made, we need another criterion. One possibility is to note in Fig. 3.3(a) that the differential resistance becomes practically constant at F_t and its fluctuations are appreciably reduced. In the experiments of ref. [27], Bhattacharya and Higgins used a similar criterion to construct their (pioneering) dynamical phase diagram for $NbSe_2$ near the peak effect, as can be seen in the differential resistance curves of Fig. 3.7. The interpretation of this transition was the passage to an elastic flow regime. What they called plastic flow is compatible with our smectic regime, but the elastic flow is not compatible with the transverse solid. One must keep in mind, however, that the 2H-$NbSe_2$ superconducting samples are very clean and three-dimensional, unlike our two-dimensional simulations with strong disorder.

Recently Xiao *et al.* used the two characteristic currents F_p and F_t, as defined in our work, to construct a new $F - T$ dynamical phase diagram for 2H-$NbSe_2$ near the peak effect [91], Fig. 3.8. This diagram is similar to the one found by Koshelev and Vinokur [29] but distinguishes two transitions, which can be interpreted in terms of the transitions between dynamical regimes that we find in our thin-film simulations. It would be interesting to have noise measurements in this superconductor in the different dynamical regimes, in order to better test the degree of consistency between models, simulations and experiments.

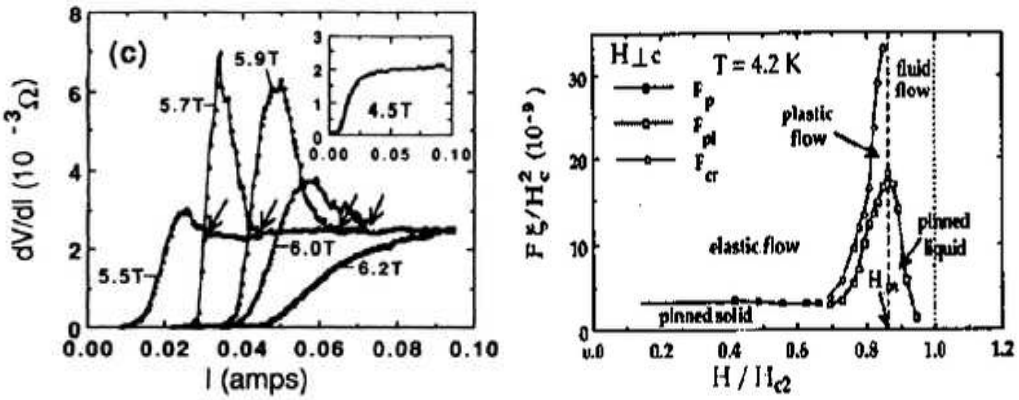


Figure 3.7: Right: experimental current–field dynamical phase diagram of a 2H-$NbSe_2$ superconductor [27]. The first transition line is the critical depinning current and the second is the current at which the IV curve becomes linear and the fluctuations in the differential resistance are reduced. Left: differential resistance dV/dI–V curves from which the characteristic currents were extracted.

3.5 Conclusions

In conclusion, we have obtained evidence of two dynamical phase transitions which can be verified experimentally with measurements of voltage noise and Hall noise. The first transition, at F_p, is the point where the noise is isotropic and the transverse diffusion is maximal (i.e., maximal effective temperature), and it corresponds to the peak observed in the differential resistance. The second transition, at F_t, is a freezing transition in the transverse direction, where the transverse diffusion vanishes abruptly and the Hall noise drops by several orders of magnitude. The high-velocity phase is a transverse solid with decoupled channels due to the presence of dislocations with Burgers vectors parallel to the driving force, which are mobile (gliding) in the center-of-mass reference frame. The rapid decrease of the mobility of these dislocations with the velocity of the vortex lattice suggests the interesting possibility of a pronounced dynamical crossover to an anisotropic moving glass at $T = 0$.

Part of the work presented in this chapter was published in [92] in collaboration with Niels Grønbech-Jensen. We thank A. R. Bishop, P. Cornaglia, Y. Fasano, F. de la Cruz, S. Bhattacharya, V. B. Geshkenbein, F. Pardo, V. M. Vinokur, M. B. Weissman, and G. Zimányi for useful discussions.

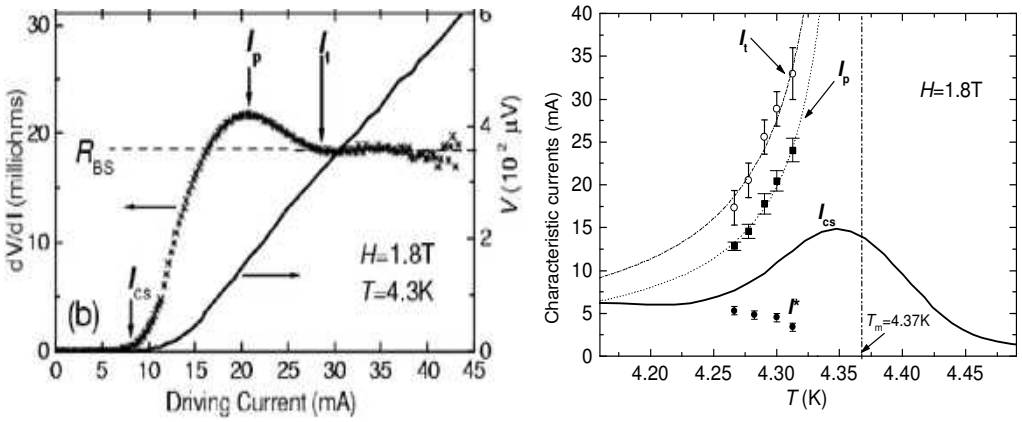


Figure 3.8: Right: experimental current–temperature dynamical phase diagram of a 2H-$NbSe_2$ superconductor [91] with two dynamical transitions, as suggested by our simulations. The first transition line is the critical depinning current, the second is the current at the peak of the differential resistance dV/dI–I, and the third is the current at which the IV curve becomes linear. Left: typical IV and differential resistance dV/dI–V curves from which the characteristic currents were extracted. Based on our results, below T_m the phases that occur upon increasing the current are: pinned lattice, plastic flow, smectic flow, and moving transverse solid. Compare with Fig. 3.3(a).

Chapter 4

Driven vortices in layered superconductors: dynamical ordering along the c axis

We study a three-dimensional model of driven vortices in layered superconductors with weakly coupled planes and strong pinning. Above the critical current F_c, we find a plastic flow regime in which pancakes in different planes are decoupled, corresponding to a "pancake gas". At a higher force F, there is a "smectic flow" regime with short-range interlayer order, corresponding to an entangled "line liquid". At an even higher force, the transverse displacements freeze and the vortices become correlated along the c axis, resulting in a "transverse solid". Finally, at a force F_s the longitudinal displacements freeze and we find a "coherent solid" of rigid lines.

A strongly anisotropic layered superconductor can be modeled as a stack of superconducting films like those studied in isolation in the previous chapter. The additional ingredient in the layered superconductor is the magnetic coupling between planes. One would expect that when this coupling is weak enough we recover, in each plane, the two-dimensional dynamical regimes of chapter 3. The effect of the magnetic coupling in turn depends on the dynamical state in each plane. Based on this, it is plausible that the largest differences with respect to the case of thin superconducting films are seen at high velocities. In this chapter we will investigate these effects, adding the analysis of properties specific to the c axis, in particular experimentally accessible ones.

4.1 Motivation

It is well known that an external current can induce ordering of the vortex structure in superconductors with disordered pinning [28]. For a long time it was believed that the high-current phase would have crystalline order, even when the vortex structure at zero current could be disordered. It has recently been found that different types of order are possible at high currents, depending on the strength of the pinning force and the

dimensionality [27, 29–32, 42, 51, 52, 56, 57, 59–64, 69–72, 92]. This led to numerous theoretical [29–32, 64], experimental [27, 41, 52, 69] and numerical [42, 51, 56, 57, 59–63, 70–72, 92] studies, since this is a problem of general interest in the field of driven systems out of equilibrium. A crystalline-type structure, which could be a perfect crystal [29] or a Bragg glass [30–32, 64], is only possible in $d = 3$ at high currents. In $d = 2$, and in $d = 3$ for intermediate currents, a transverse glass is expected, with order only in the direction perpendicular to the driving force [30–32, 42, 57, 64, 70–72, 92]. In the equilibrium phase diagram of vortices, the behavior of correlations along the direction of the magnetic field (c axis) has been discussed intensively both experimentally [93] and theoretically [94]. In the case of driven vortices, little is known about how correlations along the c axis would behave in the different dynamical regimes. In this chapter we focus on that question, starting with the least favorable case: weakly coupled superconducting planes with strong uncorrelated point disorder. We will show how order along the c axis and structural order take place in a sequence of dynamical phases as we increase the driving current from zero.

4.2 Method

We study pancake vortices in a layered superconductor, considering the magnetic interactions between all pancakes and neglecting the Josephson coupling [38]. This model is adequate when the interlayer spacing d is much smaller than the in-plane penetration depth $\lambda_\parallel$ [38]. Previous simulations of driven vortices in 3D have been carried out using Langevin dynamics of particles with short-range interactions [42–44, 95] or the isotropic 3D XY model [45]. The model we use was described in section 1.3.2. We normalize length scales by $\lambda_\parallel$, energy scales by $A_v = \phi_0^2/4\pi^2\Lambda$, and time is normalized by $\tau = \eta\lambda_\parallel^2/A_v$. We consider N_v pancake vortices and N_p pinning centers in N_l rectangular layers of size $L_x \times L_y$, and the normalized vortex density is $n_v = B\lambda_\parallel^2/\Phi_0 = (a_0/\lambda_\parallel)^2$. We consider $n_v = 0.29$ with $L_y = 16\lambda_\parallel$ and $L_x = \sqrt{3}/2L_y$, $N_l = 8$ and $N_v = 64$. We take a pinning range $a_p = 0.2$, a large pinning strength $A_p/A_v = 0.2$, with a high density of pinning centers $n_p = 3.125n_v$. The model of section 1.3.2 is valid in the limit $d \ll \lambda_\parallel \ll \Lambda$. We take $d/\lambda_\parallel = 0.01$, which corresponds to BSCCO compounds [38]. Moving pancake vortices induce a total electric field $\mathbf{E} = \frac{B}{c}\mathbf{v} \times \mathbf{z}$, with $\mathbf{v} = \frac{1}{N_v N_l}\sum_i \mathbf{v}_i$.

We analyze the dynamical regimes in the velocity–force curve at $T = 0$, solving Eq. (1.42) for increasing values of $\mathbf{F} = F\mathbf{y}$ [46]. We use periodic boundary conditions both in the planes and in the z direction, and the interactions between all pancakes in all planes were considered [46]. The periodic long-range interaction is evaluated using Ref. [96]. The equations are integrated with a time step $\Delta t = 0.01\tau$ and averages are computed over 16384 integration steps after waiting 2000 iterations to achieve equilibration (when the total energy reaches a stationary value). Each simulation is started at $F = 0$ with a triangular lattice and the driving force is slowly increased in steps of $\Delta F = 0.1$ up to values as high as $F = 8$.

4.3 Results

4.3.1 Dynamical regimes

We begin with a qualitative description of the different steady states that appear upon increasing the driving force. In Fig. 4.1(a-d) we show the vortex trajectories $\{\mathbf{R}_i(t)\}$ for typical values of F, by plotting the positions of the pancakes in five of the planes for all times t. In Fig. 4.1(e-h) we show the averaged in-plane structure factor

$$S(\mathbf{k}) = \left\langle \frac{1}{N_l} \sum_n \left| \frac{1}{N_v} \sum_i \exp[i\mathbf{k} \cdot \mathbf{r}_{ni}(t)] \right|^2 \right\rangle, \tag{4.1}$$

with $\mathbf{k} = (k_x, k_y)$. Above the critical force F_c, we find the following dynamical phases.

(i) *Plastic flow* ($F_c < F < F_p$): The pancakes move in an intricate network of channels, similar to the behavior found in 2D [51, 56, 59–63, 92]. The motion in different planes is completely uncorrelated [Fig. 4.1(a)] and there is no sign of order in the structure factor [Fig. 4.1(e)].

(ii) *Smectic flow* ($F_p < F < F_t$): The motion is organized in "elastic" channels that are almost parallel and separated by a distance $\sim a_0$, see Fig. 4.1(b). Small, broad "smectic" peaks appear in $S(\mathbf{k})$ for $\mathbf{k} \cdot \mathbf{F} = 0$ [Fig. 4.1(f)]. There are "activated" jumps of pancakes between channels. Along the c direction the channels tend to align, lying one on top of the other in neighboring planes.

(iii) *Transverse solid* ($F_t < F < F_s$): There are well-defined channels in all planes and the pancakes do not jump between channels [Fig. 4.1(c)]. The structure factor has sharp smectic peaks, and small "longitudinal" peaks ($\mathbf{k} \cdot \mathbf{F} \neq 0$) appear [Fig. 4.1(g)]. The location of the channels is correlated along the c axis.

(iv) *Coherent solid* ($F > F_s$): The channels become straighter, with small transverse deviations [Fig. 4.1(d)]. $S(\mathbf{k})$ shows well-defined peaks for all $\mathbf{k}$ in the reciprocal lattice [Fig. 4.1(h)]. The dynamical phases (i)–(iii) are similar to those previously found in two-dimensional thin superconducting films [92], presented in the previous chapter, as far as the in-plane behavior is concerned.

4.3.2 Structural and dynamical correlations in the planes

The characteristic forces F_c, F_p, F_t, F_s separating the different dynamical phases are obtained from the analysis of the structural and dynamical correlations in the planes. In Fig. 4.2 we show the in-plane structure factor and the temporal fluctuations, obtained in the same way as in 2D [92] in chapter 3. In Fig. 4.2(a) we plot the average velocity

$$V = \langle V_y(t) \rangle = \left\langle \frac{1}{N_v N_l} \sum_{n,i} \frac{dy_{ni}}{dt} \right\rangle, \tag{4.2}$$

in the direction of the force as a function of F, and its corresponding derivative dV/dF (differential resistance). The force F_p corresponds to the peak in the differential resistance. We also see a second small maximum in dV/dF for a force between F_t and F_s [97]. In

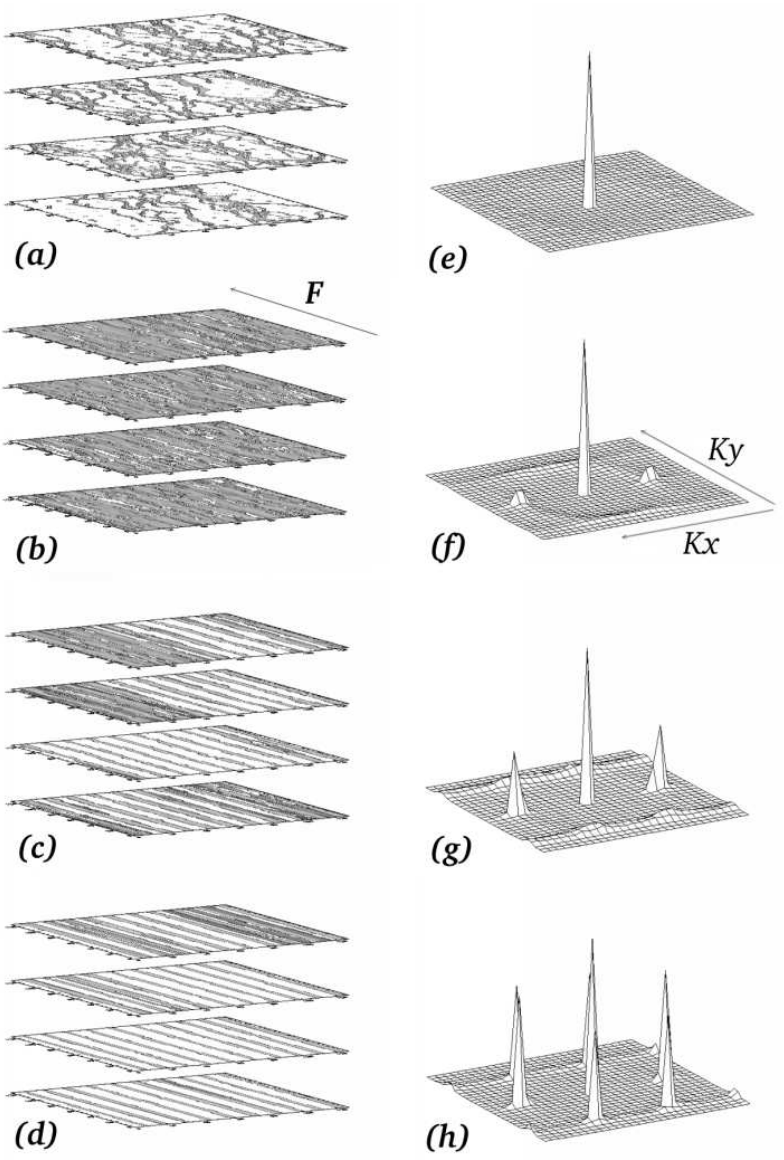


Figure 4.1: Pancake trajectories in the first five layers: (a) $F = 0.6$, (b) $F = 1.1$, (c) $F = 2.0$, (d) $F = 3.9$. Intensity surface plot of the averaged in-plane structure factor $S(\mathbf{k})$: (e) $F = 0.6$, (f) $F = 1.1$, (g) $F = 2.0$, (h) $F = 3.9$.

Fig. 4.2(b) we plot the magnitude of the peaks in the in-plane structure factor. We show the height of the peak at $\mathbf{G}_1 = 2\pi/a_0\hat{x}$, corresponding to smectic ordering, and the average height of the peaks corresponding to longitudinal ordering at $\mathbf{G}_2 = \pm 2\pi/a_0(1/2, \sqrt{3}/2)$ and $\mathbf{G}_3 = \pm 2\pi/a_0(-1/2, \sqrt{3}/2)$. We see that at F_p the smectic peak grows from zero, at F_t it reaches an almost constant value, and then at F_s it has a small jump. The longitudinal peak has a small finite value for forces above F_p, and only at F_s does it show a significant increase towards a large value. Comparing with the results of chapter 3 in 2D [92], we can make the reasonable assumption that for $F_p < F < F_t$ there is only short-range smectic order (since there is activated transverse diffusion between elastic channels, see below), and that for $F_t < F < F_s$ there is probably quasi-long-range smectic order but short-range longitudinal order. What is new, compared with the case of two-dimensional films [92] of chapter 3, is that above a force F_s there is an appreciable intensity of longitudinal order. This could correspond either to a moving crystalline phase (if there is long-range order) or to a moving Bragg glass (if there is quasi-long-range order) [30–32, 64]. We have verified that, for a given $F > F_s$, there is both longitudinal and transverse order for system sizes $N_v \times N_l = 36 \times 5$, 64×8, 100×8, 100×10. However, a detailed size analysis is not possible with these few samples.

We now complement our discussion of the in-plane physics with the study of the temporal fluctuations, which are shown in Fig. 4.2(c). We compute the transverse diffusion coefficient of the vortices from their center-of-mass position $(\bar{X}_n, \bar{Y}_n)$, $\frac{1}{N_v N_l}\sum_i [x_i(t) - \bar{X}_{n_i}(t) - x_i(0) + \bar{X}_{n_i}(0)]^2 \approx D_x t$. We find that D_x is maximal at F_p, coinciding with the peak in dV/dF. Below F_p diffusion occurs through the intricate network of plastic channels, above F_p through activated jumps between elastic channels. D_x drops abruptly to zero at F_t, indicating that the transverse displacements are localized in the transverse solid phase [92]. The longitudinal displacement from the center of mass, $\langle[\Delta y(t)]^2\rangle = \langle[y_i(t) - \bar{Y}_{n_i}(t) - y_i(0) + \bar{Y}_{n_i}(0)]^2\rangle$, is superdiffusive for $F < F_s$, similar to what is observed in 2D [92], in chapter 3. For $F > F_s$ the longitudinal displacements freeze at a constant value $\langle[\Delta y(t)]^2\rangle < a_0/N_l$, as shown in Fig. 4.2(c). Since the in-plane displacements are localized and there are large transverse and longitudinal Bragg peaks, we call this phase a coherent solid.

4.3.3 Dynamical ordering and fluctuations along the c axis

We now discuss how ordering along the c axis takes place. We analyze the pair distribution function:

$$g(\rho, n) = \frac{L_x L_y}{N_v} \left\langle \sum_{i \neq j} \delta(\rho - \rho_{ij}) \delta_{n, n_{ij}} \right\rangle . \tag{4.3}$$

From $g(\rho, n)$ we define a correlation function along the c axis

$$C_z(n) = \lim_{\rho \to 0} g(\rho, n). \tag{4.4}$$

Short-range order will be given by a finite value of $C_z(n = 1)$, meaning that pancakes in neighboring planes are coupled and a "vortex line" can therefore be defined. In principle,

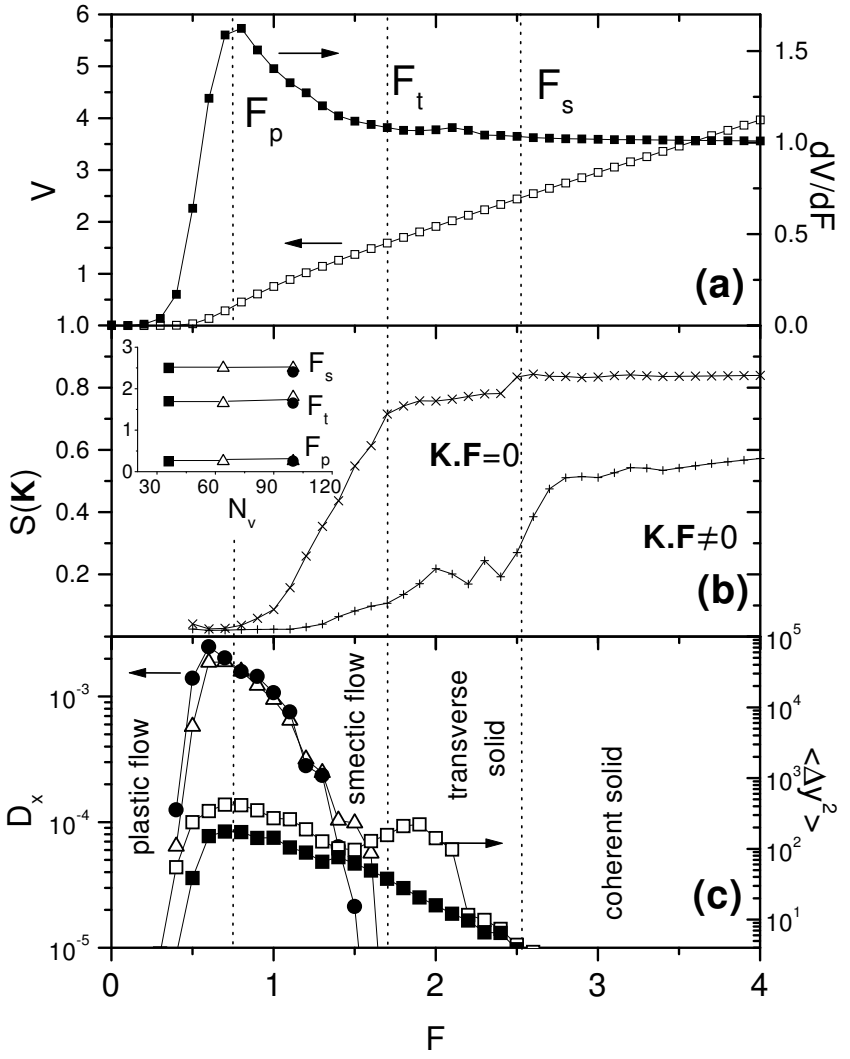


Figure 4.2: (a) Velocity–force curve, left scale, filled symbols; dV/dF (differential resistance), right scale, open symbols. (b) Intensity of the Bragg peaks. For smectic order $S(\mathbf{G}_1)$, $K_y = 0$, symbols ($\times$). For longitudinal order $S(\mathbf{G}_{2,3})$, $K_y \neq 0$, symbols ($+$). The inset shows the characteristic forces F_p, F_t, F_s vs. N_v for $N_l = 5$ ($\square$), $N_l = 8$ ($\triangle$) and $N_l = 10$ planes ($\bullet$). (c) Diffusion coefficient for the transverse motion D_x, ($\triangle$) for $N_v \times N_l = 64 \times 8$, and ($\bullet$) for $N_v \times N_l = 100 \times 10$, left scale. Longitudinal displacements $\langle[\Delta y(t)]^2\rangle$ for a given t as a function of F, ($\square$) for $N_v \times N_l = 64 \times 8$, and ($\circ$) for $N_v \times N_l = 100 \times 10$, right scale.

an exponential decay $C_z(n) \sim \exp(-n/\xi_z)$ would define a correlation length for the vortex line [94]. On the other hand, long-range order will be given by $C_z(n \to \infty) \to C_z^\infty > 0$. (Of course, quasi-long-range order is also possible, giving a power-law decay of $C_z(n)$.) In Fig. 4.3(a) we show $C_z(n)$ as a function of F for $n = 1, 2, 3, 4$. We see that at F_p short-range order along the c axis appears, with a finite value of $C_z(n = 1)$. At higher forces, between F_p and F_t, $C_z(n > 1)$ starts to grow. The absence of correlations for $F < F_p$ means that the motion of pancakes is completely random and uncorrelated between different planes. We therefore propose that the plastic flow regime corresponds to a *pancake gas*. Above F_p, in the smectic flow regime, it is possible to define a vortex line with short-range correlations along the c axis. Since in the planes there are jumps between elastic channels (i.e., cutting and reconnection of vortex lines), we could consider this phase as an *entangled line liquid*. Above F_t, $C_z(n)$ is finite for all the n considered and tends to saturate upon increasing n (here we can only consider up to $n = N_l/2 = 4$). This indicates that the vortex lines become more rigid above F_t.

We have also analyzed the c-axis correlation between time-averaged vortex densities. We first define the instantaneous vortex density,

$$\rho_v(\mathbf{r}, n, t) = \frac{1}{N_v} \sum_i \delta(\mathbf{r} - \mathbf{r}_{ni}(t)) \tag{4.5}$$

approximated in the simulation as the histogram of positions on a grid of squares of width $\Delta r = a_0/2$ (the results do not vary much for $\Delta r = a_0/4$). The regions where the average density $\langle \rho_v(\mathbf{r}, n) \rangle$ is large define the paths of the steady-state motion. We can therefore compute the overlap function of vortex trajectories between different planes as

$$O_n = C_\rho(n)/C_\rho(0), \tag{4.6}$$

with

$$C_\rho(n) = \frac{L_x L_y}{N_l} \left[\sum_m \int d\mathbf{r} \langle \rho_v(\mathbf{r}, m) \rangle \langle \rho_v(\mathbf{r}, m + n) \rangle \right] - 1. \tag{4.7}$$

This is shown in Fig. 4.3(b). We see that O_n also starts to grow at F_p. For $F_p < F < F_t$ we have some overlap of elastic channels, which decreases upon increasing n, consistent with the picture of the entangled line liquid. Remarkably, at F_t the overlap function O_n becomes independent of n. This means that there is long-range coupling along the c axis between the paths defined in each plane by the elastic channels. When the transverse displacements become localized in the x direction, they also become localized in the c direction. Therefore, the freezing of the transverse displacements in the planes occurs simultaneously with a transverse disentanglement of vortex lines at F_t. In Fig. 4.4 we show two instantaneous configurations of pancakes, one corresponding to the plastic flow regime, 4.4(a), and the other to the transverse solid regime, 4.4(b). We can qualitatively appreciate how the vortex lines become well defined upon increasing the velocity.

A very interesting result is also that we find $O_n \approx 1$ above F_s, i.e., a perfect coupling of elastic channels along the c axis (within the scale $\sim a_0/4$). Another important point to consider is the correlation in the velocities of the vortices. If vortices in different planes

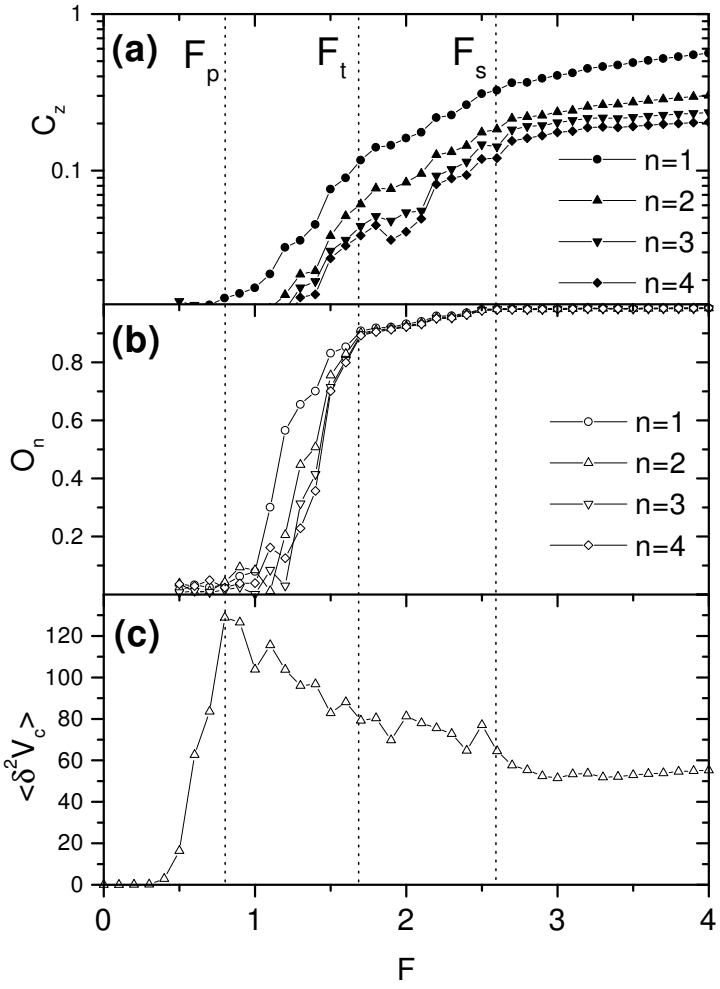


Figure 4.3: (a) Overlap of trajectories along the c direction, $C_z(n)$ vs. F for interplane distances $n = 1, 2, 3, 4$. (b) Correlation parameter along the c direction, O_n vs. F, for interplane distances $n = 1, 2, 3, 4$. (c) Voltage fluctuations along the c direction, $\langle \delta^2 V_c \rangle$ vs. F.

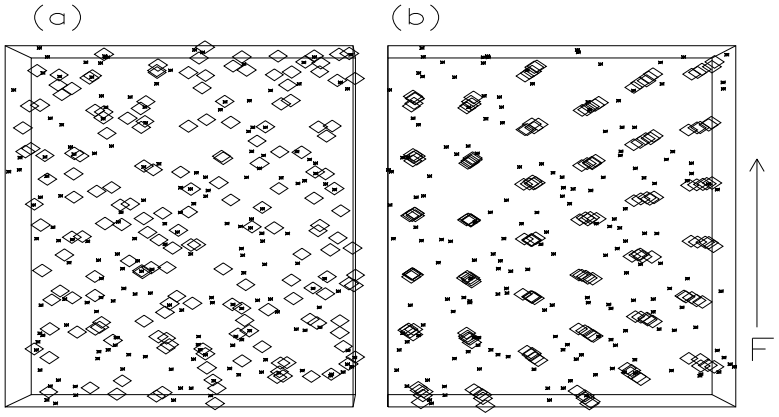


Figure 4.4: Typical instantaneous configuration of pancakes in the plastic flow regime (a) and in the transverse solid regime (b).

move at different velocities, they will induce a Josephson voltage difference along the c axis given by

$$V_{n,n+1}(\mathbf{r},t) = \frac{\Phi_0}{2\pi c}\frac{d}{dt}\phi_{n,n+1}(\mathbf{r},t), \tag{4.8}$$

where $\phi_{n,n+1}$ is the superconducting phase difference between planes n and $n+1$. A good approximation for pancakes at positions $\mathbf{r}_{n,i}$ is to write

$$\phi_{n,n+1}(\mathbf{r},t) = \sum_i [f(\mathbf{r}-\mathbf{r}_{n,i}) - f(\mathbf{r}-\mathbf{r}_{n+1,i})] \tag{4.9}$$

with $f(\mathbf{r}) \approx \arctan(x/y)$. We can then estimate the voltage fluctuations along the c axis as

$$\begin{aligned}\langle \delta^2 V_c \rangle = \sum_n \int [\langle V_{n,n+1}^2(\mathbf{r},t)\rangle - \langle V_{n,n+1}(\mathbf{r},t)\rangle^2] d\mathbf{r} \approx \\ A \sum_n [\langle \mathbf{V}_n^2 \rangle - \langle \mathbf{V}_n \rangle^2] - [\langle \mathbf{V}_n \cdot \mathbf{V}_{n+1} \rangle - \langle \mathbf{V}_n \rangle \cdot \langle \mathbf{V}_{n+1} \rangle];\end{aligned} \tag{4.10}$$

with $\mathbf{V}_n(t) = \frac{1}{N_v}\sum_i \mathbf{v}_{n,i}(t)$, and the constant $A \sim \log\Lambda$ if $L > \Lambda$ or $A \sim \log(L)$ otherwise. It is clear that $\langle \delta^2 V_c \rangle = 0$ for pancakes moving with the same velocity in all planes. We see in Fig. 4.3(c) that the voltage fluctuations have a maximum at F_p. For $F > F_p$, $\langle \delta^2 V_c \rangle$ decreases, and above F_s it reaches a value almost independent of F. The fact that $\langle \delta^2 V_c \rangle$ does not vanish above F_s is consistent with the result that $C_z(n) < 1$ for all values of F in Fig. 4.3(a). In other words, while the transverse displacements are strongly correlated along the c direction at high forces [Fig. 4.3(b)], the longitudinal displacements in different planes are weakly correlated.

4.4 Discussion

4.4.1 Effect of the magnetic coupling between planes

It is interesting to analyze the fact that in three dimensions the high-velocity phase is a coherent solid of rigid lines. If there were no coupling between planes, the high-velocity regime in each plane would be a transverse solid. The coherent solid of rigid lines is therefore a phase specific to three dimensions. An important question is then to understand why the coupling along the c axis makes the coherent solid stable. Qualitatively this could be explained by taking into account that the dynamical Larkin–Ovchinnikov correlation volume can grow, in three dimensions, also in the c direction (unlike the two-dimensional case). This leads to a much faster decrease with velocity of the effective amplitude of the pinning force, compared with the two-dimensional case. Therefore the shear stresses responsible for the plasticity of the transverse solid are of smaller amplitude and could be supported elastically by the lattice, giving rise to the coherent solid of rigid lines. Another effect to take into account is that pancakes in a layered superconductor interact attractively with a very large number of pancakes in neighboring planes. This is because the interaction along the c axis decays over the characteristic length $\lambda_\parallel$ and typically $s \ll \lambda_\parallel$, with s the separation between planes. For the parameters of BSCCO, for example, this means that a pancake interacts appreciably with pancakes in hundreds of neighboring planes. Since the pinning forces in each plane are uncorrelated (i.e. pancakes in different planes experience very different pinning forces in their motion), the interplane interaction forces contribute incoherent fluctuating components to the motion of each pancake. This dynamical disorder effect, being similar to a thermal effect, could have the property of reducing or smoothing the effective pinning on each pancake, compared with the two-dimensional case.

The model used in this chapter to simulate strongly anisotropic layered superconductors has serious limitations from the computational point of view, since the interactions between pancakes are long-ranged and their decay in the z direction, although exponential, involves hundreds of neighboring planes. One should therefore simulate a very large number of interacting pancakes to obtain reasonable statistics. This great computational difficulty motivated the proposal, for the static case, of a model in which the interaction between pancakes in different planes is replaced by a self-consistent mean field. The mean field is incorporated as a "substrate" potential on the pancakes of a plane [98]. This has clear computational advantages, since one ends up simulating a two-dimensional system with a self-consistently determined substrate potential. The basis of the mean-field approximation is to neglect temporal correlations along the c axis, which is reasonable for the equilibrium situation. Although it is not evident that this approximation is good in the non-equilibrium situation, it would be interesting to investigate the possibility of extending this method to the dynamical case by defining a substrate potential at rest in the center-of-mass frame of the driven lattice.

4.5 Conclusions

In conclusion, we have clearly identified different dynamical phases in layered superconductors in three dimensions, considering both the ordering in the planes and the ordering along the c axis [97]. It would be desirable to have a finite-size analysis in order to determine the long-range or quasi-long-range nature of the translational order in the different cases. Unfortunately, such a study is beyond reach with our current computational resources. The onset of short-range correlations along the c axis could be studied experimentally by means of plasma resonance measurements [99, 100]. Long-range ordering along the c axis could be studied by simultaneous measurements of the resistivity ρ_c and of the in-plane current–voltage response [101], which should follow the behavior of $\langle \delta^2 V_c \rangle$.

Part of the work presented in this chapter was published in [102] in collaboration with Cynthia Olson and Niels Grønbech-Jensen. We thank L. N. Bulaevskii, P. S. Cornaglia, F. de la Cruz, Y. Fasano, and M. Menghini for discussions.

Chapter 5

Temporal synchronization in driven vortex lattices

We find mode-locking steps in the current–voltage characteristics of driven vortex lattices with random point pinning when the applied ac current is parallel or perpendicular to the dc current. For low frequencies there is mode-locking above a finite ac amplitude, while for high frequencies there is mode-locking for any small ac force. This is correlated with the nature of the longitudinal and transverse temporal order in the different regimes in the absence of the ac force. The synchronized state is a frozen solid pinned in the center-of-mass reference frame. In the case of longitudinal ac, depinning from the step shows plastic flow and hysteresis. The results obtained show a strong contrast with respect to the case of periodic pinning, due to the very different nature of the temporal order in each case.

In this chapter we continue the study of the dynamical regimes of vortices in thin superconducting films of chapter 3, but now beginning with the analysis of response functions of the different regimes to different perturbations. In particular we analyze here the response of the velocity–force curves to the action of an ac force superimposed on the dc force. The effect studied is one of temporal synchronization between the ac force and certain modes of the lattice. We will show that this is another possible characterization of the non-equilibrium dynamical regimes and their transitions through transport measurements alone.

5.1 Motivation

In 1971 A. T. Fiory [26] observed steps in the current–voltage (IV) characteristics of superconducting films with vortices driven by ac+dc currents, analogous to the Shapiro steps found in Josephson junctions [103]. The steps were observed for voltages such that $2\pi\langle v\rangle/a_0 = (p/q)\Omega$, where $\langle v\rangle$ is the average vortex velocity, a_0 the periodicity of the triangular vortex lattice, Ω the frequency of the external ac current, and p, q integers. This is a particular case of mode-locking, where an internal frequency of the system (in

this case the "washboard" frequency $\omega_0 = \langle v \rangle 2\pi/a_0$) locks to a rational multiple of the external frequency over a finite range of dc current. Many other systems with many degrees of freedom, such as charge density waves [104–109], spin density waves [110], Josephson junction arrays [111] and superconductors with periodic pinning arrays [112–114], also exhibit mode-locking behavior experimentally. Recently, Harris *et al.* [115] observed Fiory steps in YBCO compounds and found that they disappeared when the melting line of the vortex lattice was crossed. Historically, Fiory's experiment motivated the pioneering works of Schmid and Hauger [24] and of Larkin and Ovchinnikov [25] on the dynamics of moving vortex lattices.

In [24, 25] it was assumed that at large velocities the vortices form a perfect triangular lattice, on which the effect of disorder could be treated perturbatively, and the steps observed in [26] were computed. In principle, the motion of a triangular lattice with period a_0 at velocity v will feel the effect of a weak potential U_p as an ac component in its velocity with frequency $\omega_0 = 2\pi\langle v \rangle / a_0$. Interference with an ac force of frequency Ω naturally leads to steps of constant mean velocity $V_{p,q} = \frac{p}{q}\frac{a_0}{2\pi}\Omega$. Even though the presence of pinning is essential for this effect, neither ω_0 nor $V_{p,q}$ depend on the pinning parameters, but only on the periodicity a_0. However, it is now clear that this simple picture has to be revised, since instead of a perfect triangular lattice there are many other dynamical phases of driven vortices: plastic flow [51, 56, 59–63], moving smectic, moving transverse glass, and moving Bragg glass [29–31, 64]. These regimes have been observed experimentally [52] and in numerical studies [42, 45, 51, 62, 63, 70, 72, 92, 102]. It could therefore be of interest to study how Fiory steps can appear in the different moving vortex phases. Moreover, a peak in the power spectrum of the voltage noise at the washboard frequency ω_0 has recently been observed experimentally in superconductors with dc current [53, 116]. This is a signature of temporal order in the high-current steady states of moving vortices [31, 117]. We present here a numerical study of mode-locking for the different velocity regimes of the vortex lattice and its relation to temporal order.

It is important to note that the mode-locking phenomenon in vortex lattices with disordered pinning presents two important features that clearly distinguish it from mode-locking in systems such as Josephson junction arrays [111], charge density waves [104], or superconductors with periodic pinning [112–114]. (i) There is no intrinsic periodicity, as there is for example in Josephson junction arrays and in superconductors with periodic pinning. Instead, temporal order and periodicity are induced dynamically due to the vortex–vortex interaction, which favors the formation of a structure close to a triangular vortex lattice at high velocities [29–32, 64]. Temporal order and periodicity are then a result of the collective dynamics, unlike superconductors with periodic pinning, where, for example, single-vortex mode-locking is possible. (ii) Vortex displacements are two-dimensional vectors. This is an important difference with respect to charge density wave systems, where the displacement is a scalar [107–109]. In particular, the behavior of the displacements in the direction perpendicular to the driving force shows phenomena such as a transverse critical current [29–32, 42, 45, 51, 62–64, 70, 72, 87, 95, 118] and a transverse freezing transition [29–32, 64, 92] at high velocities. This opens the interesting possibility of also studying mode-locking when the ac force is applied in the direction perpendicular to the direction of the driving force. Recently, it was found in a rectangular periodic pinning

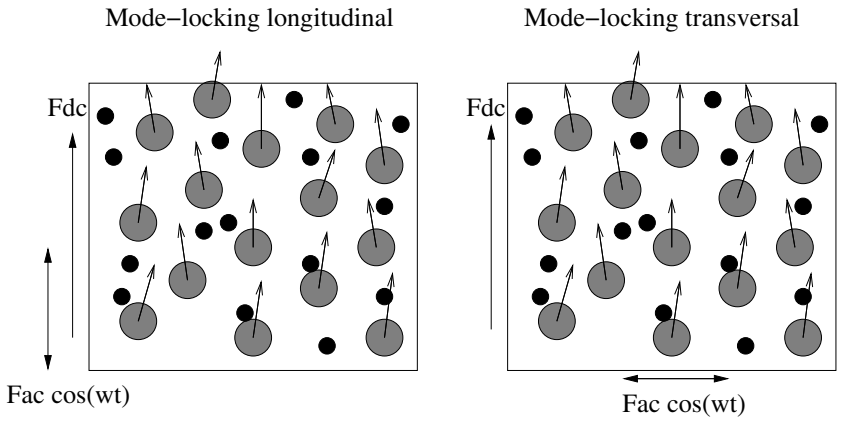


Figure 5.1: Geometries in which the mode-locking response was studied. On the left the usual case of longitudinal mode-locking is shown and on the right the novel case of transverse mode-locking.

array in superconductors [119] and in Josephson junction arrays [120] that a transverse ac force leads to a new type of "transverse" mode-locking.

In this chapter we will present a numerical study of mode-locking for the different velocity regimes of the vortex lattice on a disordered potential, in relation to temporal order. We study longitudinal mode-locking, when the ac current is parallel to the dc one, and transverse mode-locking, when the ac current is perpendicular to the dc one.

5.2 Method

We simulate a thin superconducting film using the model described in section 1.3.1. We study the response of the vortex lattice to an external ac+dc force of the form

$$\mathbf{F} = F_{dc}\mathbf{y} + F_{ac}\cos(\Omega t)\mathbf{u} \tag{5.1}$$

at $T = 0$, solving the equation of motion of the vortices, Eq. (1.35), for different values of F_{ac} and Ω. We consider the cases of longitudinal mode-locking $\mathbf{F}_{dc} \parallel \mathbf{F}_{ac}$ ($\mathbf{u} = \mathbf{y}$) and of transverse mode-locking $\mathbf{F}_{dc} \perp \mathbf{F}_{ac}$ ($\mathbf{u} = \mathbf{x}$) separately. Figure 5.1 shows the geometry of the two cases. In both cases we simulate a constant vortex density $n_v = 0.04$ in a box with $L_x/L_y = \sqrt{3}/2$, and $N_v = 64$, 100, 144, 196, 256, 400 (we show results for $N_v = 256$), and we consider a weak pinning strength $A_p/A_v = 0.05$ (compared with $A_p/A_v = 0.2$ used to obtain the results of chapter 3), with a pinning center density $n_p = 0.08$. We impose periodic boundary conditions on the computational box, and the resulting long-range interaction is determined following references [74, 96]. The equations are integrated using a time step $\Delta t = 0.001\tau$, and averages are computed over 131072 steps after 3000 steps for equilibration (when the total energy reaches a stationary mean value).

5.3 Longitudinal mode-locking: $\mathbf{F}_{dc} \parallel \mathbf{F}_{ac}$

5.3.1 Temporal order at $F_{ac} = 0$ and mode-locking

Let us first review the behavior of the vortex lattice for $F_{ac} = 0$. As we saw in chapter 3, increasing F_{dc} above the critical depinning force F_c there are three dynamical regimes in the case $F_{ac} = 0$: plastic flow for $F_c < F_{dc} < F_p$, smectic flow for $F_p < F_{dc} < F_t$, and a transverse solid for $F_t < F_{dc}$ [92] (see chapter 3). The characteristic forces in the case considered here are $F_c \approx 0.15$, $F_p \approx 0.6$ and $F_t \approx 1.2$. Since the nature of mode-locking is related to the existence of temporal order at the washboard frequency ω_0, we analyze the voltage noise spectrum

$$S_y(f) = \left| \frac{1}{T} \int_0^T dt \, (V_y(t) - V) \exp(i2\pi f t) \right|^2 \tag{5.2}$$

in each dynamical regime. In the insets of Fig. 5.2(a-c) we show the spectral densities corresponding to each regime and indicate the corresponding washboard frequency ω_0. In the inset of Fig. 5.2(a) we see that there is no temporal order at the washboard frequency, and only the broadband noise typical of plastic flow [59, 60, 116] is observed. For the smectic flow regime, in the inset of Fig. 5.2(b) we see that there is a small, broad peak at ω_0. Only at large driving forces, $F > F_t$, in the transverse solid flow regime, do well-developed peaks appear at the washboard frequency [116] and its harmonics (see the inset of Fig. 5.2(c)).

We will now study how each of these dynamical regimes, with the lattice moving at velocity $V = V(F_{dc})$, responds to a superimposed ac force $F_{ac}\cos(\Omega t)$, for different values of F_{ac}, fixing the value of Ω. We expect to obtain the main interference step ($p = q = 1$) when $V = V_{step} = \Omega a/2\pi$ (i.e., $\Omega = \omega_0$) if there is mode-locking. We can therefore choose the values of Ω such that the expected step, $V_{step} = \Omega a/2\pi$, corresponds to velocities V belonging to a given dynamical regime of the $F_{ac} = 0$ limit. Each simulation is started with an ordered triangular lattice moving at a velocity $\langle v_y \rangle \approx 0.975\Omega a/2\pi$, up to $\langle v_y \rangle \approx 1.025\Omega a/2\pi$, slowly increasing the dc force F_{dc} in steps of $\Delta F_{dc} = 0.001$. For low frequencies Ω, for which we have plastic flow when $F_{ac} \to 0$, we find that there are no interference steps over a wide range of F_{ac} (as shown in Fig. 5.2(a) for $F_{ac}/V_{step} < 1$ (left curve) and $F_{ac}/V_{step} > 1$ (right curve)). This is consistent with the absence of temporal order observed in the inset of Fig. 5.2(a) and indicates that possibly very large values of F_{ac} are needed to produce mode-locking. For intermediate frequencies Ω, for which we have smectic flow when $F_{ac} \to 0$, we find that there are no steps for small amplitudes, $F_{ac}/V_{step} < 1$, while there are steps for $F_{ac}/V_{step} > 1$, as shown in Fig. 5.2(b) in the left and right curves, respectively. This means that the small washboard peak observed in the inset of Fig. 5.2(b) is not large enough to induce mode-locking steps for small amplitudes F_{ac}. However, this short-range temporal order can be amplified for intermediate values of F_{ac}, giving rise to steps in this case. For high Ω, corresponding to the transverse solid regime when $F_{ac} \to 0$, we find that there are steps both for small ac amplitudes $F_{ac}/V_{step} < 1$ and for large ac amplitudes $F_{ac}/V_{step} > 1$, as can be observed in Fig. 5.2(c). This agrees

with the spectral response at $F_{ac} = 0$ observed in the inset of Fig. 5.2(c). In this case the temporal order is robust enough to produce mode-locking even at small values of F_{ac}.

5.3.2 Dynamics and structure on the mode-locking steps

Let us now examine in detail the dynamics and structural order within and in the vicinity of a mode-locked step, in the case of the transverse solid. In Fig. 5.3(a) we show a typical $V - F_{dc}$ curve around the step. In the inset of Fig. 5.3(a) we show a finite-size analysis for $N_v = 64$, 100, 144, 196, 256, 400, where the error bars are due to the observed dependence of the step width on three different disorder realizations. We observe that for $N_v > 256$ the step width tends to saturate at a size-independent value. To analyze the dynamical behavior we define the mean square displacements of the vortices in the directions parallel, $w_y(t)$, and perpendicular, $w_x(t)$, to the external dc force, computed from the center-of-mass position $(X_{cm}(t), Y_{cm}(t))$ as follows:

$$w_x(t) = \frac{1}{N_v} \sum_i [\tilde{x}_i(t) - \tilde{x}_i(0)]^2 \tag{5.3}$$

and

$$w_y(t) = \frac{1}{N_v} \sum_i [\tilde{y}_i(t) - \tilde{y}_i(0)]^2, \tag{5.4}$$

where $\tilde{x}_i(t) = x_i(t) - X_{cm}(t)$ and $\tilde{y}_i(t) = y_i(t) - Y_{cm}(t)$. In Fig. 5.3(b) we show the time average of these quantities, $\langle w_x(t) \rangle$ and $\langle w_y(t) \rangle$, as a function of F_{dc}. Outside the step we observe that the transverse mean square displacement (TMD) is bounded, $\langle w_x(t) \rangle \ll a_0^2$, while the longitudinal mean square displacement (LMD) is not, $\langle w_y(t) \rangle \gg a_0^2$. This corresponds to a state with longitudinal diffusion only (i.e., a transverse solid [92]). Remarkably, at the synchronization transition, the LMD freezes at a value $\langle w_y(t) \rangle \ll a_0^2$, while the TMD remains practically constant. This longitudinal freezing by mode-locking can even be observed as a dramatic decrease of the low-frequency voltage noise in both directions. The mode-locked state is then a frozen solid. To study the translational order we compute the structure factor as

$$S(\mathbf{k}) = \left\langle \left| \frac{1}{N_v} \sum_i \exp[i\mathbf{k} \cdot \mathbf{r}_i(t)] \right|^2 \right\rangle. \tag{5.5}$$

In this regime there are smectic peaks of magnitude $S_s = S(\mathbf{G}_1)$ with $\mathbf{G}_1 = (\pm 2\pi/a_0, 0)$ and longitudinal peaks of magnitude $S_l = (S(\mathbf{G}_2) + S(\mathbf{G}_3))/2$ with $\mathbf{G}_2 = \pm 2\pi/a_0(1/2, \sqrt{3}/2)$ and $\mathbf{G}_3 = \pm 2\pi/a_0(-1/2, \sqrt{3}/2)$. In Fig. 5.3(c) we plot S_s and S_l. We do not observe any important change at the transition to the mode-locked state. Within the steps we observe jumps in S_l, indicating that there are different metastable mode-locked structures. In Fig. 5.4 we analyze in detail the depinning process from the step: we show a detailed view of the $V - F_{dc}$ curve at the transition from the synchronized regime. Sweeping F_{dc} back and forth, we observe a clear hysteresis loop. In the lower right inset of Fig. 5.4 we show the evolution of $w_y(t)$ with time inside and outside the step. While $w_y(t) \ll a_0$ for all t inside the step, outside there is ballistic diffusion $w_y(t) \sim t^2$. To visualize the spatial

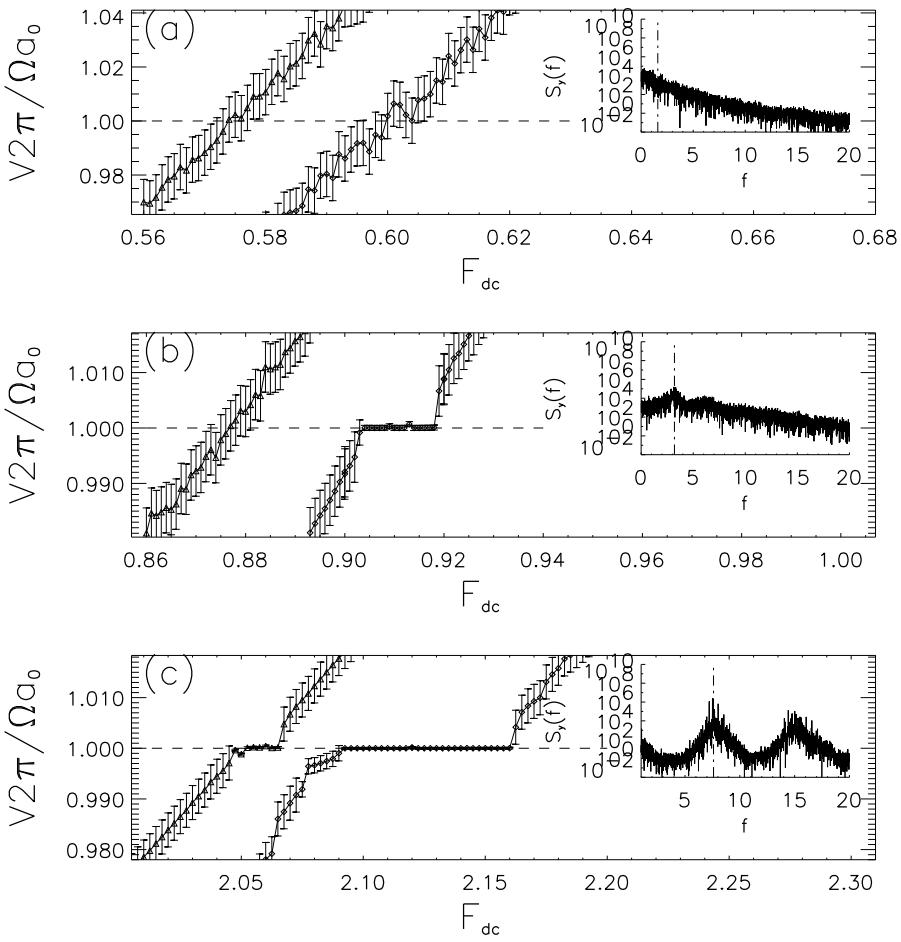


Figure 5.2: Velocity–force curve around the main interference condition $V = \Omega a_0/2\pi$ for three typical external frequencies Ω. Each case shows results for two values of the ac amplitude F_{ac} (the curves were shifted in F_{dc} for clarity). The insets show the voltage power spectra corresponding to $F_{ac} = 0$ and $V \approx V_{step}$. The vertical dashed line in the spectral density indicates the washboard frequency. (a) $\Omega = 0.5$, $F_{ac} = 0.4$ (left), $F_{ac} = 1.8$ (right). (b) $\Omega = 1$, $F_{ac} = 0.4$ (left), $F_{ac} = 3$ (right). (c) $\Omega = 2.5$, $F_{ac} = 0.75$ (left), $F_{ac} = 4$ (right).

structure at the transition we define a coarse-grained vortex density $\rho'_v(\mathbf{r}, t)$ seen from a reference frame moving with velocity V_{step}, as follows:

$$\rho'_v(\mathbf{r}, t) = \frac{1}{N_v} \sum_i \delta(\mathbf{r} - \mathbf{r}'_i(t)), \tag{5.6}$$

where $\mathbf{r}'_i(t) = \mathbf{r}_i(t) - \mathbf{y} V_{step} t$. We take a coarse-graining scale $\Delta r < a_0$. In the upper left inset of Fig. 5.4 we show the time average

$$\langle \rho'_v(\mathbf{r}, t) \rangle \tag{5.7}$$

of the density, inside (mode-locked) and outside (mode-unlocked) the step. This quantity shows the steady-state trajectories of the vortices seen from a reference frame with velocity V_{step}. Inside the step we see that the vortices are localized, oscillating around their equilibrium positions in a lattice moving with velocity V_{step}. This agrees with the frozen mode-locked solid inferred from the result shown in Fig. 5.3(b), which is "pinned" in the reference frame with velocity V_{step}. Just above depinning from the step we see that some vortices become delocalized, following straight trajectories parallel to the direction of the force around "pinned" vortices, producing coexistence of synchronized (mode-locked) and desynchronized (mode-unlocked) flow channels. This could be interpreted as a one-dimensional "plastic" depinning from the step.

5.3.3 Dependence on ac amplitude and frequency

The mode-locking steps in the $V - F_{dc}$ curve can be qualitatively characterized by the dependence of the dc current range of mode-locking on F_{ac} and Ω (as was done for example in [111–114]).

In Fig. 5.5(a-b) we show the range (width) ΔF_{dc} for the cases $F_p < F_{dc} < F_t$ and $F_t < F_{dc}$ respectively. The error bars and mean values were estimated by repeating the simulation for three different disorder realizations. In Fig. 5.5(a) we show ΔF_{dc} for $\Omega = 1$ vs. F_{ac}, which corresponds to the smectic flow regime for $F_{ac} \to 0$. We see that there is mode-locking above a finite critical value $F_{ac}/V_{step} \approx 1$ (see Fig. 5.2(b)). For large amplitudes we are not able to obtain a systematic dependence on amplitude, because the step widths depend strongly on the disorder realization in this case. In Fig. 5.5(b) we show ΔF_{dc} for two frequencies $\Omega = 2.5$, 5 vs. F_{ac}, which correspond to the transverse solid in the $F_{ac} = 0$ limit. We can (approximately) collapse both curves onto a single curve if we plot ΔF_{dc} vs. F_{ac}/V_{step}. A dependence $\Delta F_{dc} \sim (1/C_{66})|J_1(F_{ac}/V_{step})|^2$ was found by Schmid and Hauger [24] (and also in other elastic models), where $V_{step} = a_0\Omega/2\pi$ and C_{66} is the shear modulus. This result was obtained using a perturbative scheme in an elastic model of the vortex lattice. Remarkably, our results seem to follow more closely a dependence of the form $\Delta F_{dc} \approx A|J_1(F_{ac}/V_{step})|$, with A a constant. This dependence is the same as that found in the one-dimensional problem of an overdamped Josephson junction or a particle moving in a periodic potential. In our case, a linear dependence on F_{ac} of the mode-locking intensity would be a consequence of the existence of temporal order in the $F_{ac} = 0$ limit. This was not taken into account in the perturbative calculation of Schmid and Hauger [24], where mode-locking appears as a second-order effect.

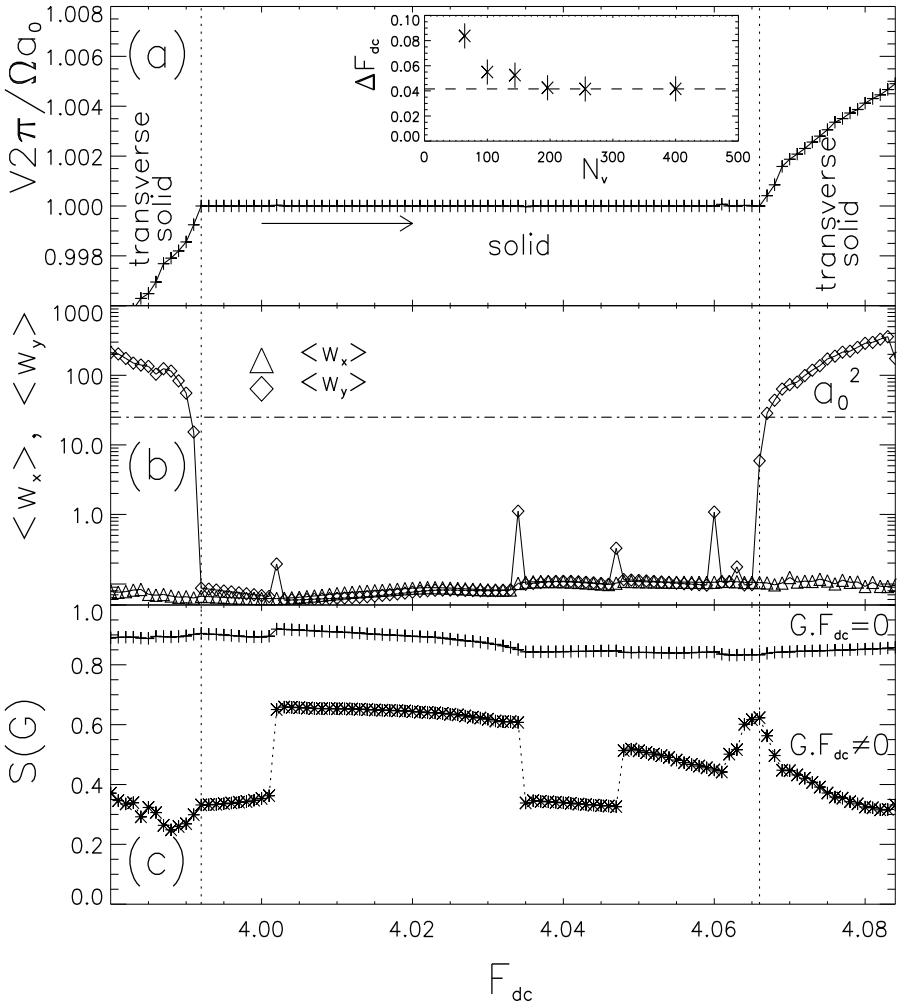


Figure 5.3: (a) Velocity–force curve around the main interference step for $\Omega = 5$ and $F_{ac} = 6$. The inset shows the size dependence of the step width. (b) Mean square displacement in the longitudinal direction $\langle w_y(t)\rangle$, symbols ($\diamond$), and in the transverse direction $\langle w_x(t)\rangle$, symbols ($\triangle$). The dash-dotted line indicates a_0^2. (c) Intensity of the Bragg peaks. For smectic ordering $S(\mathbf{G}_1)$, $K_y = 0$: symbols ($+$). For longitudinal ordering $S(\mathbf{G}_{2,3})$, $K_y \neq 0$: symbols ($*$).

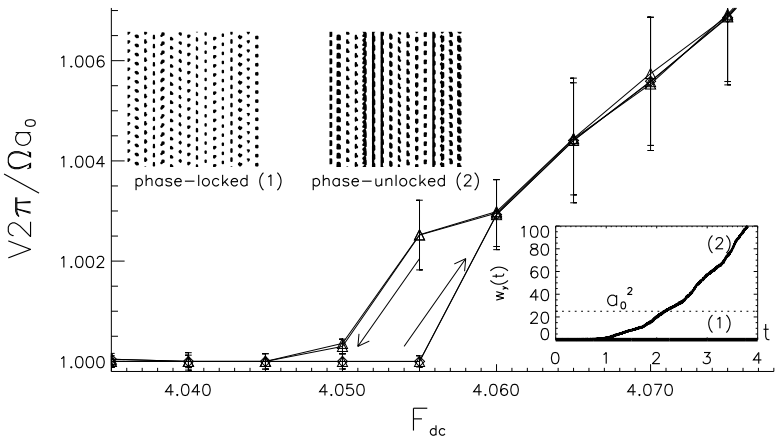


Figure 5.4: Velocity–force curve around depinning from the main step for $\Omega = 5$ and $F_{ac} = 6$. The upper left inset shows the typical time-averaged vortex density seen from a reference frame moving with velocity $v_{step} = \Omega a_0/2\pi$, for a mode-locked state $F_{dc} = 4.045$ (left) and for an unlocked state $F_{dc} = 4.085$ (right). The lower right inset shows the corresponding typical longitudinal mean square displacements for both cases. The dashed line indicates a_0^2.

5.4 Transverse mode-locking: $\mathbf{F}_{dc} \perp \mathbf{F}_{ac}$

5.4.1 Temporal order at $F_{ac} = 0$ and mode-locking

In the previous section we studied the case of a longitudinal ac force, relating the mode-locking response to the temporal order in the longitudinal component of the velocity. Here we now analyze the transverse temporal order in the power spectrum of the transverse voltage (of the fluctuations of the transverse velocity), which are shown in the insets of Fig. 5.6. These are computed as

$$S_x(\omega) = \left| \frac{1}{T} \int_0^T dt\, V_x(t) \exp(i\omega t) \right|^2 \tag{5.8}$$

in the dynamical regimes for $F_{ac} = 0$ [92]. The first regime above the critical depinning force F_c is the plastic flow regime ($F_c < F_{dc} < F_p$, $F_c \approx 0.01$, $F_p \approx 0.03$). In this case we find a broadband spectrum without temporal order [inset of Fig. 5.6(a)]. A similar behavior is found in the "smectic flow" regime ($F_p < F_{dc} < F_t$, $F_t \approx 0.06$), shown in the inset of Fig. 5.6(b). This is reasonable, since we know that the transverse motion is diffusive in both regimes [92]. Only for $F_{dc} > F_t$, in the "transverse solid" regime, do we find clear evidence of temporal order in the transverse velocity. This is seen in the inset of Fig. 5.6(c), where well-developed peaks appear at the washboard frequency, ω_0, and its harmonics. We are now ready to study the response to a superimposed ac force $F_{ac}\cos(\Omega t)$, for different values of F_{ac}. For a given Ω, we expect the main interference step ($p = q = 1$) to occur when $V = V_{step} = \Omega a/2\pi$ (i.e., $\Omega = \omega_0$) if there is mode-locking. Then, as we did in the previous section, we choose the values of Ω such that the expected

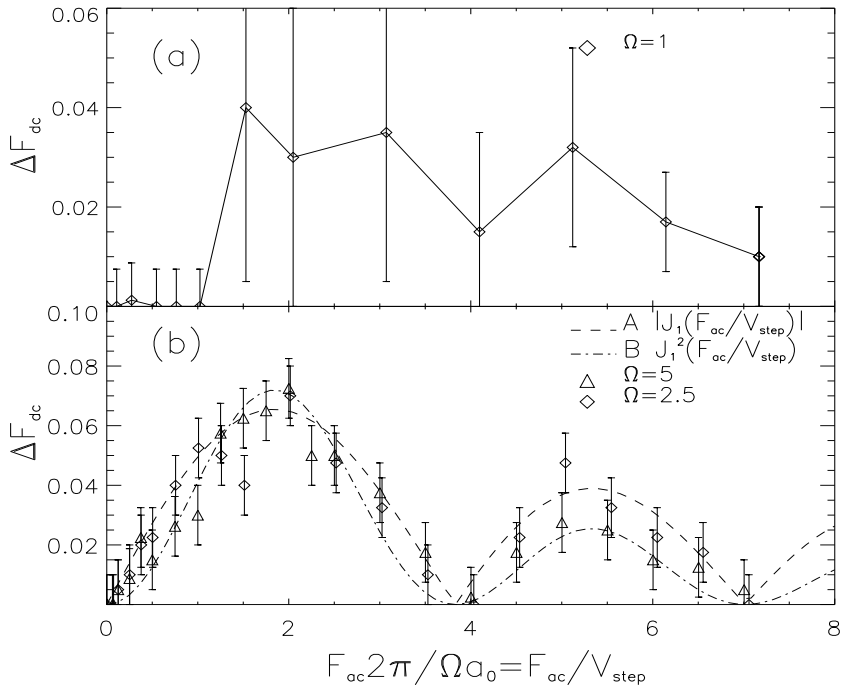


Figure 5.5: Step width ΔF_{dc} vs. $F_{ac}2\pi/\Omega a_0 = F_{ac}/V_{step}$. (a) $\Omega = 1$. (b) $\Omega = 5$ with symbols ($\triangle$) and $\Omega = 2.5$ with symbols ($\diamond$). The dashed line shows a fit to $A|J_1(F_{ac}/V_{step})|$ and the dash-dotted line a fit to $B|J_1(F_{ac}/V_{step})|^2$.

step, $V_{step} = \Omega a/2\pi$, corresponds to velocities V belonging to a given dynamical regime in the $F_{ac} = 0$ limit. Each simulation is started at $\langle v_y \rangle \approx 0.975\Omega a/2\pi$ with an ordered triangular lattice, up to values $\langle v_y \rangle \approx 1.025\Omega a/2\pi$, slowly increasing the dc force F_{dc} with $\Delta F_{dc} = 0.00005$–0.00025. We chose ΔF_{dc} such that $\Delta F_{dc}/F_c \lesssim 0.01$, which is small enough to obtain a behavior independent of the "rate of ramping" of the dc driving force in all the IV curves. For low Ω, for which we have plastic flow when $F_{ac} \to 0$, we find that there are no interference steps over a wide range of F_{ac} (shown in Fig. 5.6(a) for $F_{ac}/V_{step} < 1$ (left curve) and $F_{ac}/V_{step} > 1$ (right curve)). For intermediate Ω, for which we have smectic flow when $F_{ac} \to 0$, we find that there are no steps for small amplitudes, $F_{ac}/V_{step} < 1$, while there are steps for $F_{ac}/V_{step} > 1$, as shown in Fig. 5.6(b) in the left and right curves, respectively. For high Ω, corresponding to the transverse solid regime when $F_{ac} \to 0$, we find that there are steps both for small $F_{ac}/V_{step} < 1$ and large $F_{ac}/V_{step} > 1$ values of the ac amplitude, as can be seen in Fig. 5.6(c). We thus find a behavior similar to the case of a longitudinal ac force [121]. In the present case, when a dynamical regime has transverse temporal order, any small finite value of F_{ac} will induce transverse mode-locking, while in the regimes that do not have transverse temporal order, a finite (critical) value of F_{ac} is needed to induce transverse mode-locking.

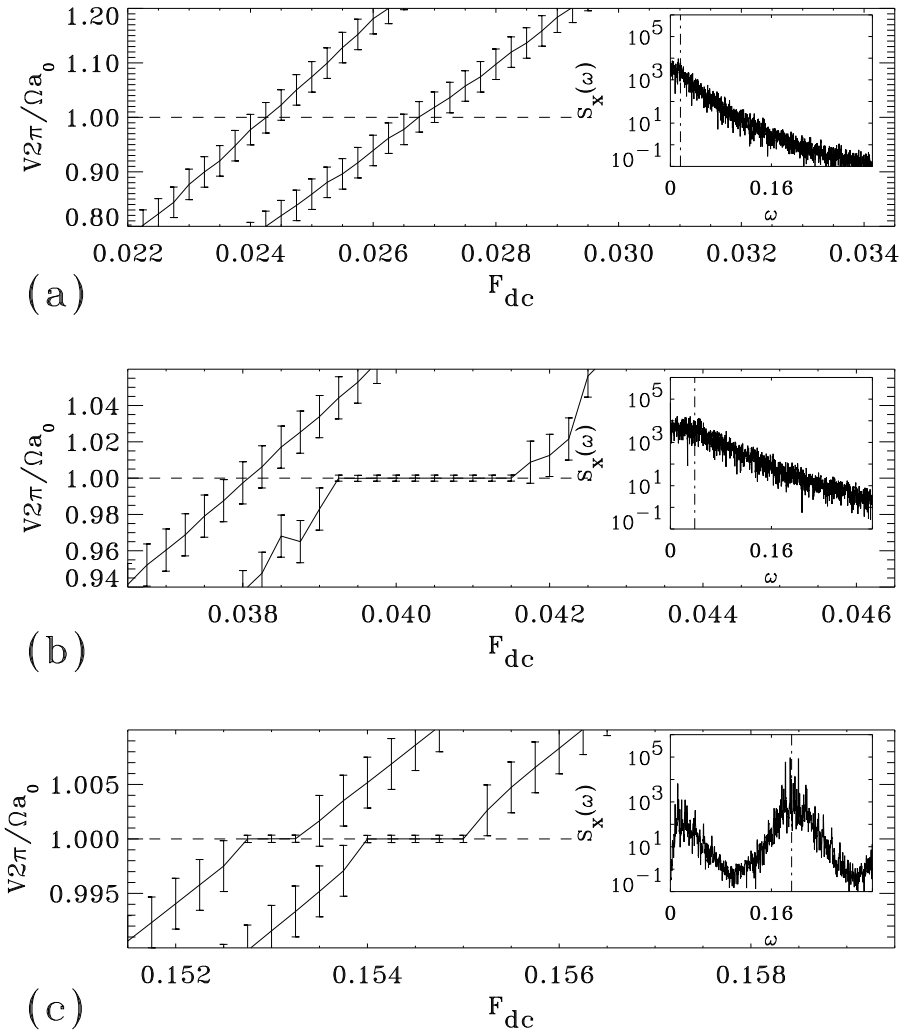


Figure 5.6: Velocity–force curve around the main interference condition $V = \Omega a_0/2\pi$ for three typical external frequencies Ω. Each case shows results for two values of the ac amplitude F_{ac} (the curves were shifted in F_{dc} for clarity). The insets show the corresponding voltage power spectra for $F_{ac} = 0$ and $V \approx V_{step}$. The vertical dashed line in the spectral density indicates the expected washboard frequency ω_0. (a) $\Omega = 0.02$, $F_{ac} = 0.01$ (left), $F_{ac} = 0.03$ (right). (b) $\Omega = 0.04$, $F_{ac} = 0.02$ (left), $F_{ac} = 0.08$ (right). (c) $\Omega = 0.19$, $F_{ac} = 0.09$ (left), $F_{ac} = 0.23$ (right).

5.4.2 Trajectories and spectral response

In Fig. 5.7(a) we show in detail a typical $V - F_{dc}$ curve around the transverse mode-locking step. To visualize the structure of the trajectories at the transition we define a coarse-grained vortex density $\rho_v(\mathbf{r}, t)$. We take a coarse-graining scale $\Delta r < a_0$. In Fig. 5.7(b)-(c)-(d) we show the time average $\langle \rho_v(\mathbf{r}, t) \rangle$ of the density for three typical values of F_{dc}, corresponding to voltages $V < V_{step}$ (Fig. 5.7(b)), $V = V_{step}$ (Fig. 5.7(c)), and $V > V_{step}$ (Fig. 5.7(d)). In Fig. 5.7(b) we see that within the mode-locked states the vortices follow one-dimensional trajectories. The wavy shape of the trajectories is due, of course, to the transverse ac force. Figures 5.7(e)-(f)-(g) show typical spectral densities $S_x(\omega)$ for the three cases just mentioned. We see that there is a significant reduction of the width of the washboard peak inside the step; a typical signature of mode-locking [104].

In Fig. 5.8(a) we show the low-frequency voltage noise in both directions, perpendicular, P_x, and longitudinal, P_y, to the dc force, defined as $P_{x,y} = \lim_{\omega \to 0} S_{x,y}(\omega)$. We see that the low-frequency noise is dramatically reduced inside the step (there is a noise peak inside the step that corresponds to a transition between different synchronized structures). In Fig. 5.8(b) we show the phase $\phi(\omega_0)$ of the washboard-frequency component of the Fourier transform of the longitudinal voltage $\tilde{V}(\omega_0)$, defined as $\tilde{V}(\omega_0) = \sqrt{S_y(\omega_0)} \exp(i\phi(\omega_0))$. Here we see explicitly that inside the "phase-locked" state there is a well-defined "phase", which varies within the range $0 \leq \phi \leq \pi$. We have analyzed finite-size effects by computing the phase-locking range (step width) ΔF_{dc} with the number of vortices in the range $N_v = 64$–400. In Fig. 5.9 we show the size dependence of the step width ΔF_{dc} for the step corresponding to $F_{ac} = 0.2$ and $\Omega = 0.19$, where the error bars are due to the observed dependence of the width on three different disorder realizations. We observe that for $N_v > 256$, ΔF_{dc} tends to a size-independent value.

In Fig. 5.10(a-b) we show the range (width) ΔF_{dc} for the cases $F_p < F_{dc} < F_t$ and $F_t < F_{dc}$ respectively. The error bars and mean values were estimated by repeating the simulation for three different disorder realizations.

5.4.3 Dependence on ac frequency and amplitude

In Fig. 5.10(a) we show ΔF_{dc} for $\Omega = 0.04$ vs. F_{ac}, which corresponds to the smectic flow regime when $F_{ac} \to 0$. We see that there is mode-locking only above a finite value $F_{ac}/V_{step} \approx 1$ (see Fig. 5.6(b)). In Fig. 5.10(b) we show ΔF_{dc} for two frequencies $\Omega = 0.13$, 0.19 vs. F_{ac}, which correspond to the transverse solid in the $F_{ac} = 0$ limit. We can (approximately) collapse both curves onto a single one if we plot ΔF_{dc} vs. F_{ac}/V_{step}. The results closely follow a dependence of the form $\Delta F_{dc} \approx A|J_1(F_{ac}/V_{step}\sqrt{3})|$, with A a constant and J_1 the first-order Bessel function. In the inset of Fig. 5.10(b) we can see that there is a linear dependence of the mode-locking intensity on F_{ac}. This is very different from transverse mode-locking in periodic pinning systems [84, 119], in which the step width follows a dependence $\Delta F_{dc} \propto (F_{ac})^2$.

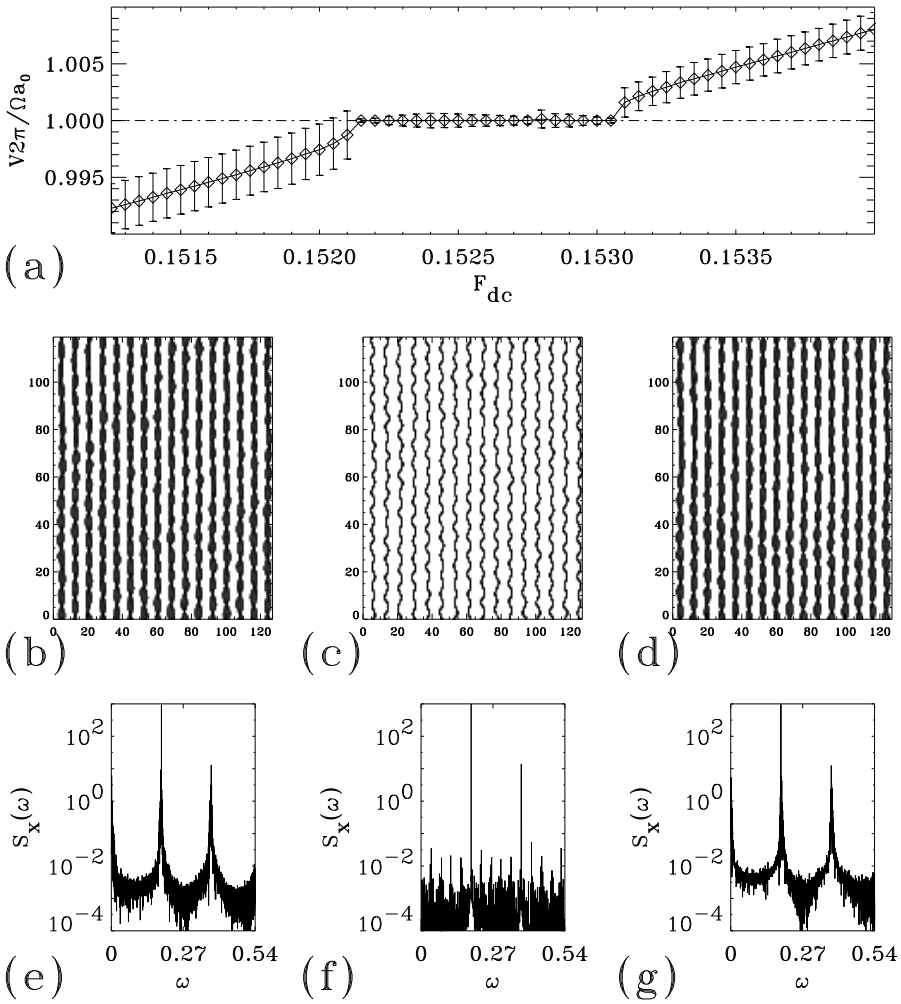


Figure 5.7: (a) Velocity–force curve around the main interference step for $\Omega = 0.08$ and $F_{ac} = 0.3$. (b)-(c)-(d) Typical time-averaged coarse-grained vortex density for a mode-unlocked state below a step, a mode-locked state on the step, and a mode-unlocked state above the step, respectively. (e)-(f)-(g) Typical voltage power spectra for the three regimes with applied ac current.

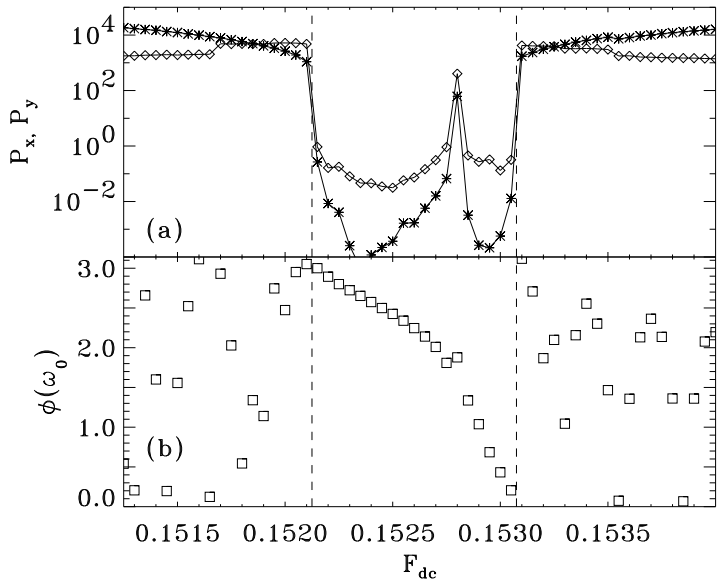


Figure 5.8: (a) Low-frequency voltage noise in the transverse and longitudinal directions around the main interference step. The dashed lines indicate the mode-locking transitions. (b) Phase of the washboard-frequency Fourier component of the longitudinal voltage around the step.

5.5 Discussion

5.5.1 A simple model to describe the steps

The surprising result that in the case of random pinning the mode-locking intensity has a linear dependence on F_{ac} can be explained as a consequence of the existence of temporal order in the $F_{ac} = 0$ limit. We can show this with a very simple effective model. The moving lattice can be approximately described by an equation of motion for the velocity $\mathbf{v}$ of its center of mass,

$$\mathbf{v} = \mathbf{F_{dc}} + \mathbf{F_{ac}} \cos(\Omega t) - \sum_{\mathbf{G}} \mathbf{G} U_{\mathbf{G}} \sin(\mathbf{G} \cdot \mathbf{r}). \tag{5.9}$$

The $U_{\mathbf{G}}$ are the components of an effective periodic force, due to the interaction of the almost periodic moving lattice (with reciprocal vectors $\mathbf{G}$) with the pinning centers. For weak disorder (small $U_{\mathbf{G}}$) a first-order correction can be obtained by assuming that, to zeroth order,

$$\mathbf{r} = \mathbf{r_0} + \langle \mathbf{v} \rangle t + \mathbf{F_{ac}} \sin(\Omega t)/\Omega \tag{5.10}$$

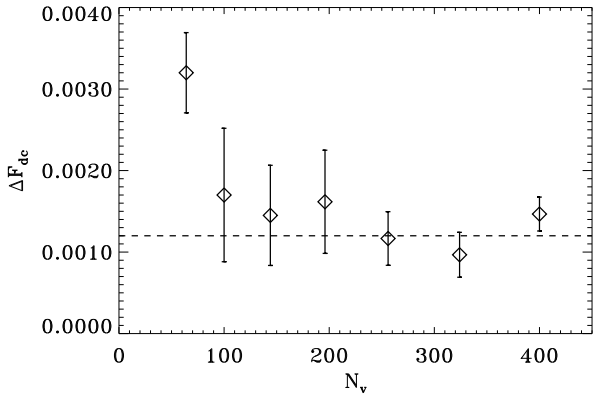


Figure 5.9: Dependence of the step width ΔF_{dc} on the number of vortices N_v, for $F_{ac} = 0.2$ and $\Omega = 0.19$.

This gives for the instantaneous velocity $\mathbf{v}$ and the mean velocity $\langle \mathbf{v} \rangle$ the following expressions to first order in F_{ac}:

$$\mathbf{v} = \mathbf{F_{dc}} - \sum_{\mathbf{G}} \mathbf{G} U_{\mathbf{G}} \sin\left[\mathbf{G}.\left(\mathbf{r_0} + \langle \mathbf{v} \rangle t\right)\right] \left[J_0\left(\frac{\mathbf{G}.\mathbf{F_{ac}}}{\Omega}\right) + 2J_1\left(\frac{\mathbf{G}.\mathbf{F_{ac}}}{\Omega}\right)\sin(\Omega t)\right] \tag{5.11}$$

$$\langle \mathbf{v} \rangle = \mathbf{F_{dc}} - \sum_{\mathbf{G}} \mathbf{G} U_{\mathbf{G}} \sin(\mathbf{G}.\mathbf{r_0}) \left\{ J_0\left(\frac{\mathbf{G}.\mathbf{F_{ac}}}{\Omega}\right) \delta(\mathbf{G}.\langle \mathbf{v} \rangle) - 2J_1\left(\frac{\mathbf{G}.\mathbf{F_{ac}}}{\Omega}\right) \delta(\mathbf{G}.\langle \mathbf{v} \rangle - \Omega) \right\} \tag{5.12}$$

We now consider an anisotropic triangular lattice with one of its principal axes parallel to $\mathbf{F_{dc}} = \mathbf{y} F_{dc}$, and for simplicity we keep only the shortest reciprocal vectors,

$$\{\mathbf{G}\} = \{\mathbf{g_s}, \mathbf{g_l}, \mathbf{g_l} - \mathbf{g_s}\} \tag{5.13}$$

where

$$\begin{aligned} \mathbf{g_s} &= \mathbf{x} \frac{2\pi}{a_0} \frac{2}{\sqrt{3}} \\ \mathbf{g_l} &= \mathbf{x} \frac{2\pi}{a_0} \frac{1}{\sqrt{3}} + \mathbf{y} \frac{2\pi}{a_0} \end{aligned} \tag{5.14}$$

We then consider

$$\begin{aligned} U_{\mathbf{g_l}} = U_l &= U_{\mathbf{g_l} - \mathbf{g_s}} + \Delta U_l \\ U_{\mathbf{g_s}} &= U_s. \end{aligned} \tag{5.15}$$

Here ΔU_l represents a deformation of the perfect triangular lattice such that $\frac{\Delta U_l}{U_l} \ll 1$. U_s and U_l could be related, respectively, to the smectic and longitudinal structure factor

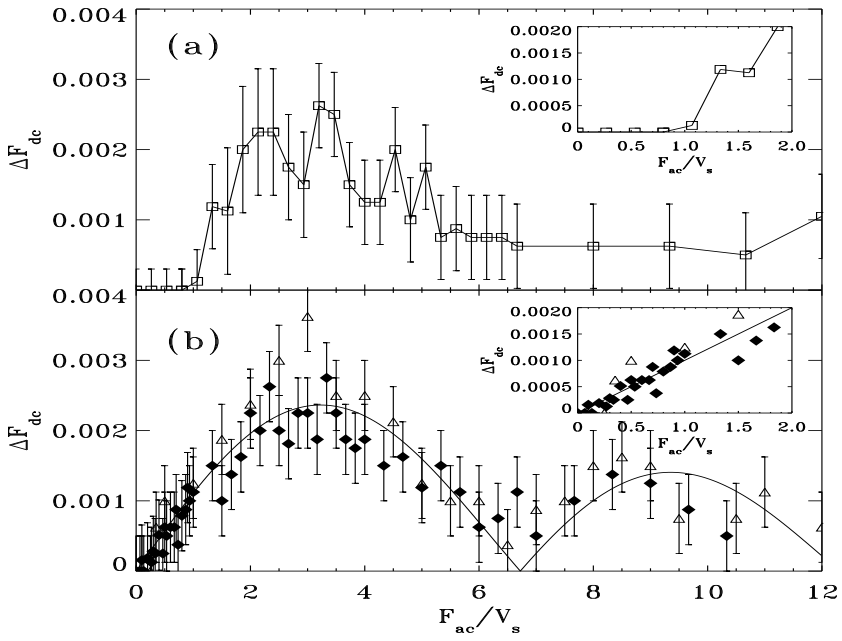


Figure 5.10: Step width ΔF_{dc} vs. $F_{ac}2\pi/\Omega a_0 = F_{ac}/V_{step}$. (a) $\Omega = 0.04$. (b) $\Omega = 0.13$ with symbols ($\triangle$) and $\Omega = 0.19$ with symbols ($\diamond$). The solid line shows a fit to $A|J_1(F_{ac}/V_{step}\sqrt{3})|$.

peaks of the moving vortex system. Let us first apply this simple model to the longitudinal case $\mathbf{F_{ac}} \parallel \mathbf{F_{dc}}$, discussed in the previous section. Writing $\mathbf{F_{ac}} = F_{ac}\mathbf{y}$ we obtain, from Eq. (5.11), the longitudinal velocity in the $F_{ac} = 0$ limit,

$$v_y = -\frac{4\pi U_l}{a_0} \sin\left[\frac{2\pi}{a_0}(r_0 + \langle v\rangle t)\right]. \tag{5.16}$$

In this way we obtain, from Eq. (5.12), the phase-locking range for the first interference step $\Omega = \omega_0$,

$$\Delta F_{dc} = \frac{8\pi|U_l|}{a_0}\left|J_1\left(\frac{\mathbf{g_l}.\mathbf{F_{ac}}}{\Omega}\right)\right| = \frac{8\pi|U_l|}{a_0}\left|J_1\left(\frac{F_{ac}}{V_{\rm step}}\right)\right|. \tag{5.17}$$

Although this result was derived for small F_{ac} and weak disorder, Eq. (5.17) corresponds to the relation $\Delta F_{dc} \propto |J_1(F_{ac}/V_{step})|$ found numerically in the previous section (Ref. [121]). It is important to note that this result requires U_l to be finite, that is, that there be long- or quasi-long-range temporal order in the longitudinal direction. From Eqs. (5.16) and (5.17) we see that, for small F_{ac}, the temporal order in the *longitudinal* direction is directly related through U_l to the linear dependence of ΔF_{dc} on F_{ac}. If we now apply the model to the case of transverse phase-locking just discussed, with $\mathbf{F_{ac}} = F_{ac}\mathbf{x}$, we obtain, for the transverse velocity in the $F_{ac} = 0$ limit,

$$v_x = -\frac{2\pi\Delta U_l}{a_0\sqrt{3}} \sin\left[\frac{2\pi}{a_0}(r_0 + \langle v\rangle t)\right]. \tag{5.18}$$

and for the phase-locking range of the first interference step $\Omega = \omega_0$,

$$\Delta F_{dc} = \frac{4\pi|\Delta U_l|}{a_0}\left|J_1\left(\frac{\mathbf{g_l}.\mathbf{F_{ac}}}{\Omega}\right)\right| = \frac{4\pi|\Delta U_l|}{a_0}\left|J_1\left(\frac{F_{ac}}{V_{step}\sqrt{3}}\right)\right|. \tag{5.19}$$

We see that Eq. (5.19) is also the approximate relation found in the simulation, shown in Fig. 5.10(b). Comparing Eqs. (5.19) and (5.17) we see that there is a difference of a factor $\sqrt{3}$ in the argument of the Bessel function J_1 in the transverse case with respect to the longitudinal case. Note that this predicted difference is also found numerically, since we obtain $\Delta F_{dc} \propto |J_1(F_{ac}/V_{step}\sqrt{3})|$ in the transverse case shown in Fig. 5.10(b), and $\Delta F_{dc} \propto |J_1(F_{ac}/V_{step})|$ in Fig. 5.5(b) of section 5.3.3 [121]. From Eqs. (5.18) and (5.19) we see that in this case, for small F_{ac}, the temporal order in the transverse direction is directly related through ΔU_l to the linear dependence of ΔF_{dc} on F_{ac}. It is interesting to note that in the perfectly periodic case, $\Delta U_l = 0$ and $U_l \neq 0$, and then there is "longitudinal temporal order" but no "transverse temporal order". In this case the widths of the mode-locking steps would be linear in F_{ac} when $\mathbf{F_{ac}} \parallel \mathbf{F_{dc}}$ but quadratic in F_{ac} when $\mathbf{F_{ac}} \perp \mathbf{F_{dc}}$. This is because in the perfectly periodic case the vortices would move along straight lines without any transverse component of the velocity, and therefore transverse mode-locking would occur as an effect of higher than linear order. In conclusion, a small distortion of the lattice is necessary to induce transverse temporal order, and, hence, a linear dependence of the width of the transverse mode-locking steps on F_{ac}.

5.5.2 Temporal order

As we can see in Figs. 5.2 and 5.6, and as we have already discussed, temporal order without ac current is directly related to the occurrence of mode-locking at small ac amplitudes. Based on our results we believe it plausible that long- and quasi-long-range temporal order gives rise to a linear dependence of the step width on the ac force amplitude in the limit where the latter goes to zero, and to a non-linear dependence when the order is short-ranged. To make the correspondence precise it would be necessary to study in detail the range of the temporal order at the washboard frequency without ac force. This implies a detailed finite-time analysis with "scaling" functions for the height and width of the washboard peaks [117].

Another interesting issue is the relation between temporal and translational order. Temporal order is expected to be in general more robust than translational order [31]. Since the moving structure is anisotropic, the joint analysis of transverse temporal order (demonstrated in this work for the first time) and of longitudinal temporal order could give a lot of information. Although it is evident that the existence of a certain degree of periodicity of the vortex lattice is a necessary condition for having temporal order at the washboard frequency, the relation between translational and temporal order could be non-trivial, as our simple model for the case of transverse mode-locking shows, for example.

Finally, it is interesting to note that the equilibrium analogy of Koshelev and Vinokur [29] with the fictitious shaking temperature is inconsistent with the observation of

temporal order, since in equilibrium, by the equipartition theorem, the spectral density should have no peaks. The inconsistency lies in the fact that the supposed "thermal" shaking noise would then display long-range temporal correlations. Koshelev and Vinokur already noted this problem in the high-velocity phase, and for this reason they used, for the moving solid, a different definition of the shaking temperature than for the moving fluid regime. This shows that the shaking temperature is not very well defined. As we will see in chapter 6, it is possible to define in a better way (closer to the empirical definition of temperature), and uniquely for all dynamical regimes, effective temperatures for the moving vortex lattice, at the price of restricting their applicability to the fluctuations of observables at a given time scale. An interesting issue is then that temporal order at low frequencies could be affected by a different effective temperature than temporal order at high frequencies, such as the washboard one.

5.5.3 Non-linear effects of the ac force

The non-linear effects for large amplitudes of the ac force are well appreciated in Figs. 5.2(b) and 5.6(b) for longitudinal and transverse mode-locking respectively, corresponding to the smectic flow regime. In both cases the temporal order necessary for mode-locking is induced by the ac force, since there are no steps for arbitrarily small amplitudes. This indicates that the ac force causes changes in the dynamical structure of the lattice moving without ac force. It is interesting to note that ordering or disordering effects with an ac force have been observed experimentally and in simulations without dc force. In some experiments it was found that the effect depends critically on the shape (asymmetry) of the ac force pulse [122, 123]. It would then be very interesting to carry out a similar study for mode-locking in the smectic flow regime, using asymmetric pulses on the lattice moving with finite mean velocity.

5.5.4 Important last-minute experimental results

At the time of publication of our results on longitudinal mode-locking [121], presented in detail in section 5.3 of this thesis, the only known experimental evidence of mode-locking steps in disordered superconductors was that of Fiory [26] and that of Harris *et al.* [115]. However, neither of these references reports results on the dependence of the step width on the amplitude and frequency of the ac force. Both in ref. [26] and in ref. [115] mode-locking steps are only shown for dc currents large compared with the critical current, and ac currents of amplitude comparable to the magnitude of the dc current. In section 5.3.3 we described the dependence of the width of the simulated steps as a function of the frequency and amplitude of the ac force. As we can see in Figs. 5.5(a-b), the frequency dependence allows us to clearly distinguish between the response of the smectic flow regime and that of the moving transverse solid. Moreover, in the latter, the dependence on the ac force amplitude seems to be describable by a simple first-order Bessel function.

Very recently (during the writing of this thesis), motivated by our study [121] of section 5.3, in which we extend the analysis of longitudinal mode-locking steps carried out in refs. [24–26, 115] to all dynamical phases, Besseling *et al.* reported the first measurements

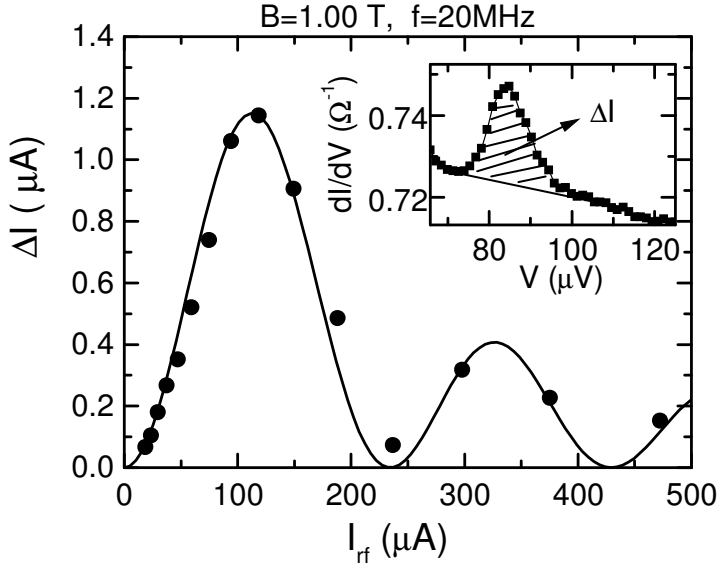


Figure 5.11: Width of the fundamental mode-locking step $\Delta I_{1,1}$ (defined as shown in the inset) as a function of the ac current amplitude I_{rf}, determined experimentally in ref. [124] in a NbGe superconducting film for $B = 1.00$ T and $f = 20$ MHz. The fit to the experimental data is $\Delta I_{1,1} \propto |J_1(I_{rf}R_f/V_{1,1})|^2$, where $V_{1,1}$ is the voltage on the step and R_f is the resistance due to vortex flow. Compare with Fig. 5.5(b).

of the dependence of the width of the mode-locking steps on the amplitude and frequency of the ac current in thin NbGe superconducting films with weak disorder [124, 125]. The results for high dc currents [125], corresponding both to high frequencies of the ac current and to high velocities of the vortex lattice, are shown in Fig. 5.11. One difference that can be noticed in the inset of Fig. 5.11 is that a finite peak in dI/dV means that the steps are not completely flat as in the simulations (complete mode-locking), but have a slope (incomplete mode-locking). This is mainly because our simulations are at $T = 0$ (although other more subtle effects can also give rise to sloped steps). However, the width of a step can still be very well defined, and the data of Fig. 5.11 can be compared directly with the results of our numerical simulations, shown in Fig. 5.5(b). The fit shown in Fig. 5.11 is $\Delta I_{1,1} \propto |J_1(I_{rf}R_f/V_{1,1})|^2$, consistent with the analytical prediction of Schmid and Hauger [24]. In our notation this is equivalent to fitting $\Delta F_{dc} \propto |J_1(F_{ac}/V_{step})|^2$. As we can see, even though our simulations were performed at $T = 0$, the simulation and experimental results are very similar. However, in Fig. 5.5(b) we have fitted the simulation data with both $\Delta F_{dc} \propto |J_1(F_{ac}/V_{step})|$ and $\Delta F_{dc} \propto |J_1(F_{ac}/V_{step})|^2$. The first fit corresponds to the same dependence that would be obtained for a particle in a periodic potential, while the second fit corresponds to the analytical prediction of Schmid and Hauger obtained using perturbation theory for a moving elastic lattice [24]. Note that we have in principle no good arguments to choose between the two fits, since on the one hand it is very clear that the picture of a particle in a periodic potential is an oversimplification of the problem, and on the other it is well established that the perturbation theory used

in [24] fails. To discern more clearly which of the two simple fits is better it would be necessary, for example, to reduce the error of the simulated points of Fig. 5.5(b) and to have more experimental points in Fig. 5.11. By increasing the number and reducing the error of the points corresponding to low ac amplitudes, we could compare the two cases well if we can distinguish between the linear dependence $\Delta F_{dc} \propto |J_1(F_{ac}/V_{step})| \sim F_{ac}$ predicted by the first fit and the quadratic dependence $\Delta F_{dc} \propto |J_1(F_{ac}/V_{step})|^2 \sim F_{ac}^2$ predicted by the second. Since measuring small steps involves a large error, it would be more convenient to better determine the magnitude of the first two maxima of ΔF_{dc}, ΔF_{dc}^1 and ΔF_{dc}^2 respectively, and to compare their relative magnitude $\Delta F_{dc}^1/\Delta F_{dc}^2$. If $\Delta F_{dc} \propto |J_1(F_{ac}/V_{step})|$ holds we would have $\Delta F_{dc}^1/\Delta F_{dc}^2 \sim 0.595$, while if $\Delta F_{dc} \propto |J_1(F_{ac}/V_{step})|^2$ holds we would have $\Delta F_{dc}^1/\Delta F_{dc}^2 \sim 0.354$. Note that quantifying more precisely the form of ΔF_{dc} vs. F_{ac} also requires carrying out simulations at $T \neq 0$. In conclusion, we can say that within the error bars of the simulation the functional dependence predicted in our work (Fig. 5.5(b)) has been verified experimentally (Fig. 5.11).

As we showed in sections 5.3 and 5.4, the analysis of the mode-locking steps *as a function of frequency*, or of the mean velocity of the vortex lattice, at ac force amplitudes small compared with the dc current, allows us to clearly characterize the different dynamical phases. This was the main motivation and the most important result of the work of this chapter since, besides extending previous studies of mode-locking [24–26, 115] to the whole range of velocities of the vortex lattice, it allows us to propose a new experimental method to extract information on the dynamical phases and transitions. As we showed in both sections 5.3 and 5.4, mode-locking steps are particularly useful to characterize the transverse freezing transition, from the smectic flow regime to the moving transverse solid regime (see chapter 3): in the transverse solid regime the steps can be induced at arbitrarily small ac force amplitudes, while in the smectic flow regime it is necessary to exceed a critical ac force amplitude to induce the steps. This is very interesting since in principle it would then be possible to *probe* the transverse freezing transition through direct transport measurements, without the need for more complicated Hall noise measurements, as we had proposed in chapter 3. We are pleased to report here that the proposed experiment has been achieved and its results reported very recently in [125]. The systems studied were thin NbGe superconducting films, in which vortices are confined to move in mesoscopic flow channels [126]. Figure 5.12 shows the analysis of the dependence of the magnitude of the step width ΔI as a function of magnetic field and temperature. In Fig. 5.12(a) we can observe ΔI for two different frequencies f and for several ac current amplitudes I_{rf}. We can see that the value of the critical field B_c, at which the steps disappear, is well determined, being practically independent of the amplitude of I_{rf}. This is a good indication that I_{rf} is really probing the response of the dynamical regimes that exist in its absence (i.e. it is a perturbation to the dynamical regime with dc current only). According to the interpretation that emerges from our simulations, $B_c = B_c(f) \equiv B_c(V_{step})$ represents the dynamical transverse freezing line between the smectic flow regime and the moving transverse solid. Figure 5.12(b) shows the resulting dynamical phase diagram in a voltage–magnetic field plane. It is worth noting that this diagram is very similar to the one originally proposed by Koshelev and Vinokur, using the concept of the shaking temperature [29]. However, there is an important difference in the interpretation of the

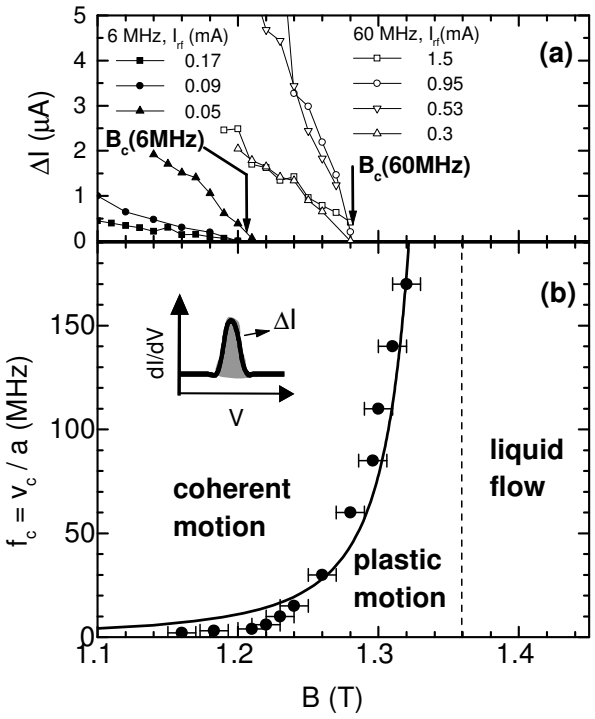


Figure 5.12: Experimental results from ref. [125]. (a) Width of the fundamental mode-locking step as a function of magnetic field for frequencies $f = 6$ MHz and $f = 60$ MHz and several values of the ac current amplitude I_{rf}. The arrows indicate the dynamical melting field. (b) Frequency–field dynamical phase diagram. The dashed line indicates the equilibrium melting field $B_{m,e}$ of the lattice. The fit is $f_c \sim (B_{m,e} - B)^{-2}$.

"coherent motion" regime (see Fig. 5.12(b)). It is now known that the perturbation theory used by Koshelev and Vinokur fails, implying that a moving crystal at high velocities, like the one proposed in [29], is unstable. For this reason, in ref. [125], the "coherent motion" phase has been identified as the moving transverse solid that we proposed in [92], whose properties we described in detail in chapter 3.

5.6 Conclusions

We have shown numerically that it is possible to have mode-locking in vortex lattices with random pinning for sufficiently high frequencies, for the cases of an ac force parallel or perpendicular to the dc force. The case of an ac force parallel to the dc one agrees with the experiments of Fiory [26] and Harris *et al.* [115]. The novel case of an ac force perpendicular to the dc force provides complementary information about the dynamical regimes, and could be measured experimentally. We related the response to the longitudinal (transverse) ac force to the longitudinal (transverse) temporal order at the washboard frequency of the dynamical regimes in the absence of ac force. The mode-locked state can be seen as a frozen solid pinned in the moving reference frame, and depinning from

longitudinal mode-locking is plastic and hysteretic. We found important differences between mode-locking with random pinning and with periodic pinning. We showed with a simple model that the observed synchronization effects can be qualitatively explained in terms of a simple equation for the center of mass that effectively incorporates the translational order of the lattice. Remarkably, we find with this model that the distortions of the perfect moving triangular lattice play an important role in producing transverse mode-locking. In conclusion, the response to an ac force at different frequencies could be an interesting experimental probe of the dynamical regimes in driven vortex lattices. In this sense, the first experimental observations have very recently been achieved, confirming many of the features of mode-locking in the different dynamical regimes observed in our simulations [124, 125].

Part of the results of this chapter were published in [121, 127] in collaboration with Niels Grønbech-Jensen. We thank L. Balents, V. I. Marconi, and C. Reichhardt for discussions.

Chapter 6

Effective temperature in driven vortex lattices

We numerically study correlation functions and response functions in vortex lattices driven out of equilibrium over random pinning potentials. From a generalized fluctuation–dissipation relation we compute a transverse effective temperature in the moving fluid phase. We find that the effective temperature decreases as the driving force is increased and is approximately equal to the equilibrium melting temperature of the unpinned system when the dynamical transverse freezing occurs. We also discuss how the effective temperature could be measured experimentally from a generalized Kubo formula.

In chapter 3 we analyzed spatio-temporal correlations of the different dynamical regimes of vortices in a thin superconducting film, and in chapter 5 we showed how they respond to ac forces. In this chapter we analyze these dynamical regimes again from a different perspective. The idea is not so much to give an alternative characterization of the different dynamical regimes as to understand some interesting aspects of the non-equilibrium statistical mechanics of this system. In chapter 3 we suggested, with no more grounds than an equilibrium analogy, that some features of the diffusive behavior could be described in terms of the concept of an effective temperature, very similarly to the shaking temperature of Koshelev and Vinokur explained in chapter 2. In this chapter we focus on defining an effective temperature better, based on the study of fluctuation–dissipation relations of different observables. This study is directly motivated by recent advances in the dynamical theory of glasses.

6.1 Motivation

Knowing when and how it is possible to extend thermodynamic concepts to systems out of equilibrium is a very important challenge in theoretical physics. Many definitions of non-equilibrium temperatures have been proposed in different contexts, but it has rarely been verified that they satisfy the properties expected of a temperature.

Cugliandolo, Kurchan and Peliti [89, 128] introduced the notion of "effective temperatures" T_{ef} from a modification of the fluctuation–dissipation theorem (FDT) in out-of-equilibrium systems that evolve slowly in time. T_{ef} is defined as the inverse of the slope of a parametric plot of the integrated response vs. the correlation function of a pair of observables when the latter is bounded, or from half of this slope when the correlation function is unbounded. This definition leads to a temperature that satisfies the properties expected of a temperature in the thermodynamic sense, since it can be measured with a thermometer, controls the direction of heat flow for a given time scale, and satisfies a zeroth law within each scale. T_{ef} was found analytically in mean-field models of glasses [89, 129–131] and was successfully studied in structural and spin glasses, both numerically [132–135] and experimentally [136–138], in granular matter [139–141] and in fluids under weak shear [142–144].

As we saw in section 2.2, Koshelev and Vinokur [29] defined a "shaking" temperature T_{sh} from the fluctuating force felt by a vortex configuration moving in a random pinning potential. This led to the prediction of a dynamical phase transition between a liquid-like vortex phase moving at small forces and a crystalline vortex lattice moving at large forces, when T_{sh}, defined in Eq. (2.17), equals the equilibrium melting temperature of the vortex system without disorder [29, 73], Eq. (2.18). However, as we already discussed in section 2.5, later works [30–32, 64] showed that the perturbation theory used in [29] fails and that the vortex phase at high velocities could be an anisotropic transverse glass instead of a crystal. Despite this, the shaking temperature introduced in [29] has been a very useful qualitative concept, at least phenomenologically. Indeed, the dynamical transitions discussed in [29–32, 64, 73] have been observed experimentally [27, 41, 52, 69, 91] (see Figs. 2.5, 2.6, 2.7 and 3.8) and in numerical simulations [42, 45, 51, 62, 63, 70, 72, 92, 102, 121] (see chapters 3 and 4). On the other hand, in our study of the dynamical regimes in chapter 3 we noticed that certain features of vortex diffusion in the center-of-mass reference frame could be qualitatively interpreted in terms of the shaking temperature.

In this chapter we apply a definition of T_{ef} based on the modifications of the fluctuation–dissipation theorem to vortex lattices within the moving fluid phase. We compare our results with the shaking temperature of [29] and discuss how to obtain T_{ef} experimentally from measurements of the transverse voltage noise and the transverse resistance.

6.2 Method

We simulate a thin superconducting film using the model described in section 1.3.1. To analyze the validity and the modifications of the fluctuation–dissipation theorem (FDT) we compute the fluctuation–dissipation relation (FDR), i.e., the relation between the correlation function and the response function of a given observable. It is convenient to choose [132–135] the observable

$$A_\mu(t) = \frac{1}{N_v} \sum_{i=1}^{N_v} s_i r_i^\mu(t), \tag{6.1}$$

where $s_i = -1, 1$ are random numbers with $\overline{s_i} = 0$ and $\overline{s_i s_j} = \delta_{ij}$, $r_i^\mu = R_i^\mu - R_{cm}^\mu$ with $\mu = x, y$, and $\mathbf{R}_{cm}$ is the center-of-mass coordinate. We separately study the FDR in the transverse and longitudinal directions with respect to $\mathbf{F} = F\mathbf{y}$. The autocorrelation function of the observable A_μ is

$$C_\mu(t, t_0) \equiv \overline{\langle A_\mu(t) A_\mu(t_0)\rangle} = \frac{1}{N_v^2} \sum_{i,j=1}^{N_v} \overline{\langle s_i r_i^\mu(t) s_j r_j^\mu(t_0)\rangle} = \frac{1}{N_v^2} \sum_{i=1}^{N_v} \langle r_i^\mu(t) r_i^\mu(t_0)\rangle,$$

where in the last equality we have used that the r_i^μ are independent of the s_i in the absence of the perturbation. The integrated response function χ_μ for the observable A_μ is obtained by applying a perturbing force

$$\mathbf{f}_i^\mu = \epsilon s_i \hat{\mu} \tag{6.2}$$

where $\hat{\mu} = \hat{x}, \hat{y}$, at time t_0 and keeping it constant from then on on each vortex:

$$\chi_\mu(t, t_0) = \lim_{\epsilon \to 0} \frac{1}{\epsilon} \left[\overline{\langle A_\mu(t)\rangle}_\epsilon - \overline{\langle A_\mu(t)\rangle}_{\epsilon=0} \right]. \tag{6.3}$$

At this point we can see the usefulness of using the random numbers s_i: (i) they decrease the statistical error in the determination of the correlation function by decoupling the contributions of the positions of different vortices, and (ii) they make the perturbation due to the random force weak [132–135], since the factors s_i are independent and random for each vortex. The perturbation (6.2) can then be thought of as a random force of magnitude ϵ acting constantly on the representative point of the system $\{r_i^\mu\}$ in the projection μ of configuration space. Since $\overline{s_i} = 0$ and $\overline{s_i s_j} = \delta_{ij}$ this force is statistically isotropic in this subspace, and therefore does not favor action in any particular direction. Hence it is in general a "weak" perturbation for a given value of ϵ compared with other possible perturbations.

We then analyze the FDR,

$$\chi_\mu(t, t_0) = \frac{1}{2T_{ef}^\mu(t, t_0)} \Delta_\mu(t, t_0), \tag{6.4}$$

where

$$\Delta_\mu(t, t_0) = N_v^{-1} \sum_i \langle |r_i^\mu(t) - r_i^\mu(t_0)|^2 \rangle = N_v [C_\mu(t, t) + C_\mu(t_0, t_0) - 2C_\mu(t, t_0)] \tag{6.5}$$

is the mean square displacement in the $\hat{\mu}$ direction. For a system in equilibrium at temperature T the FDT requires $T_{ef}^x = T_{ef}^y = T$. In a system out of equilibrium, the FDT is not valid. An example that has been successfully studied using exactly the same Eqs. (6.4) and (6.5) is a binary system of Lennard-Jones particles (which cannot crystallize), as a model of a structural glass. These systems fall out of equilibrium upon lowering the temperature, because the viscosity grows very rapidly as the temperature decreases and the relaxation time to equilibrium τ_{eq} becomes extremely long. When $\tau_{eq} \gg t_0$, the non-equilibrium relaxation of this system is well characterized by the plot of $\chi_\mu(t, t_0)$ vs. $\Delta_\mu(t, t_0)$, which shows two slopes: (i) $d\chi_\mu/d\Delta_\mu \approx 1/2T$, with T the temperature of the

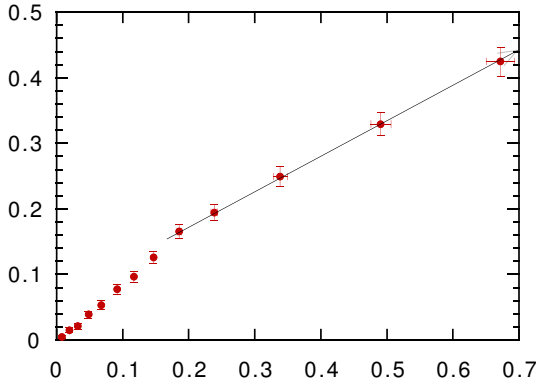


Figure 6.1: Fluctuation–dissipation relation $\chi(t,t_0)$ vs. $\Delta(t,t_0)/T$ found in the slow non-equilibrium relaxation of a binary system of Lennard-Jones particles in the glassy phase [133]. This is an example with two time scales, where an effective temperature can be defined at long times as $d\chi_\mu/d\Delta_\mu \approx 1/2T_{ef}$.

external bath, for small values of $\Delta_\mu(t,t_0)$ or short times $t \ll t_0$, and (ii) $d\chi_\mu/d\Delta_\mu \approx 1/2T_{ef}$ with $T_{ef} > T$ at long times $\tau_{eq} \gg t \gg t_0$, or when the diffusion $\Delta_\mu(t,t_0)$ is large. The plot obtained in Ref. [133] for this system is shown in Fig. 6.1. The same system, but brought to a steady state by applying a constant shear force, shows the same type of $\chi_\mu(t,t_0)$ vs. $\Delta_\mu(t,t_0)$ relation, with T_{ef} depending on the strength of the shear force [144]. The difference between these two examples is that in the first case time-translation invariance is broken, while in the second case it is not. However, we see that both cases show the same type of violation of the FDT, with an effective temperature T_{ef} (different in each case) at long times. The pinned vortex lattice has an important similarity with the second example: it is in a non-equilibrium steady state because in its motion it experiences forces that cannot be derived from a potential. In both cases energy is being continuously injected and dissipated in the steady state. This similarity is an important motivation for using the method given by Eqs. (6.4) and (6.5) for the vortex lattice.

Since we are interested in the steady states reached by the driven vortex lattice, where there are no aging effects [142–145], all observables depend on the difference $t - t_0$ if we choose t_0 long enough to ensure convergence to the steady state, where $\Delta_\mu(t,t_0) = \Delta_\mu(t-t_0)$. From the parametric plot of $\chi_\mu(t)$ vs. $\Delta_\mu(t)$ we can then define an effective temperature $T^\mu_{ef}(t)$, using Eq. (6.4), provided that $T^\mu_{ef}(t)$ is a constant in each time scale [89, 128].

We study the transverse and longitudinal FDR for the moving vortex lattice as a function of the driving force, F, for different values of A_p, n_v, and T. The simulations are carried out with a pinning center density $n_p = N_p r_p^2/L_x L_y = 0.14$ in a box with $L_x/L_y = \sqrt{3}/2$ and $N_v = 256$. We consider $A_p/A_v = 0.35,\ 0.2,\ 0.25,\ 0.1$, $n_v = N_v r_p^2/L_x L_y = 0.05$, 0.07, and $T \leq 0.01$. We impose periodic boundary conditions with the algorithm of references [74, 96]. Averages are computed over 80000 steps of $\Delta t = 0.1\tau$ after 65536 steps to reach stationarity. To compute the response function $\chi_\mu(t)$, given by Eq. (6.3), we simulate two replicas of the system, with the perturbing force $\mathbf{f}_i^\mu = \epsilon s_i \hat{\mu}$ applied to one of them. Starting from the same initial condition, we let the perturbed and unperturbed

systems evolve for 5000 time steps and compute $A_\mu(t)$ and $A_\mu(t)_{\epsilon=0}$ respectively. The replicas then evolve again, changing the realization of the random factors s_i and taking the final configuration of the unperturbed system as the new common initial condition. Thus 16 realizations of the $\{s_i\}$ have been considered in the averages. From this we obtain $\overline{\langle A_\mu(t)\rangle}$, for $\epsilon = 0$ and for $\epsilon \neq 0$, and hence the response function $\chi_\mu(t)$ is determined. We have verified the linearity of $\overline{\langle A_\mu(t)\rangle}$ with ϵ in the range $[0.0002, 0.01]$, and we then used $\epsilon = 0.005 \ll F_c$ in our calculations.

6.3 Results

6.3.1 Fluctuation–dissipation relations

At $T = 0$, as we already saw in chapter 3, there are three different dynamical regimes [92] as we increase F above the critical depinning force F_c: two fluid phases, with plastic flow for $F_c < F < F_p$ and smectic flow for $F_p < F < F_t$, and a transverse solid for $F > F_t$. For a pinning density n_p, the characteristic forces F_c, F_p and F_t depend on the disorder strength A_p and on the vortex density n_v. We begin by analyzing the FDR in the smectic flow regime for different values of A_p, n_v and T. In Fig. 6.2(a) we show typical transverse mean square displacements, $\Delta_x(t)$, and in Fig. 6.2(b) the integrated transverse response, $\chi_x(t)$, for this dynamical regime. In Fig. 6.2(c) we show the parametric plot of $\chi_x(t)$ vs. $\Delta_x(t)$. We see that the equilibrium fluctuation–dissipation theorem does not hold in general, but we find two approximate linear relations for $\Delta_x(t) < 0.05 r_p^2$ and for $\Delta_x(t) > r_p^2$, with a non-linear crossover between them. Following Eq. (6.4), we find that the short-displacement region corresponds to the bath temperature $T = 0.01$, and therefore the fluctuation–dissipation theorem holds only at short times. For the large-displacement region we obtain a transverse effective temperature $T_{ef}^x(T) = 0.045 > T$. In the inset of Fig. 6.2(a) we show the fluctuation–dissipation relation for $T = 0$. Comparing the results for different T, we find $T_{ef}^x(T) \approx T_{ef}^x(0) + T$. In Fig. 6.3 we analyze the fluctuation–dissipation relation for the same time scales as in Fig. 6.2. Figure 6.3(a) shows the mean square displacement, Δ_y, and Fig. 6.3(b) shows the response, χ_y. In Fig. 6.3(c) we obtain the corresponding fluctuation–dissipation relation. We observe that the fluctuation–dissipation theorem holds for $\Delta_y(t) < 0.05 r_p^2$ at the bath temperature T. There is no constant $T_{ef}^y(t)$ for long displacements, because there is a superdiffusive behavior with $\Delta_y \sim t^\zeta$, $\zeta > 1$ (see Fig. 3.4 of section 3.3.2) [92], while $\chi_y \sim t$.

6.3.2 Transverse effective temperature

In Fig. 6.4 we show the computed transverse effective temperature T_{ef}^x, for $T = 0$, as a function of the voltage (i.e., average velocity V). We observe that above the critical force T_{ef}^x is a decreasing function of V that reaches a value close to the equilibrium melting temperature of the unpinned system, $T_m \approx 0.007$ [146], when the system approaches the transverse freezing transition at $F = F_t$ (obtained from the vanishing of the transverse diffusion coefficient D_x, shown in the inset). It becomes very difficult to compute T_{ef}^x for

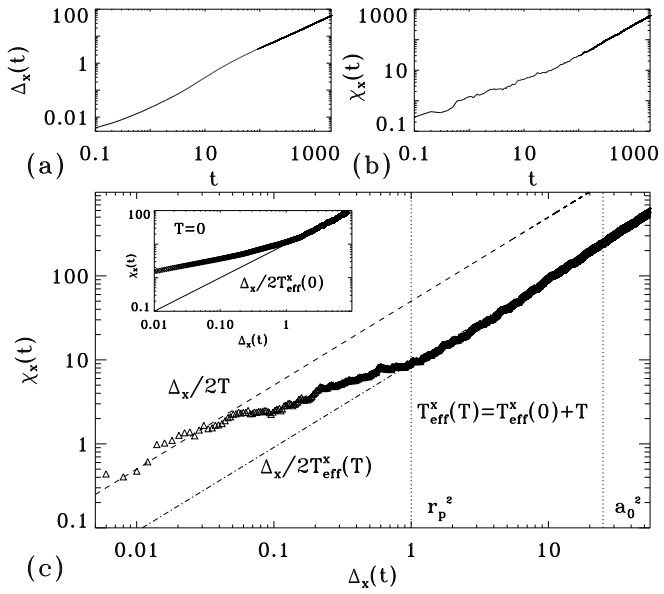


Figure 6.2: Transverse mean square displacement $\Delta_x(t)$ (a), and transverse response function $\chi_x(t)$ (b), for $A_p = 0.2$, $T = 0.01$ and $V = 0.11$, in the smectic flow regime. (c) Transverse FDR $\chi_x(t)$ vs. $\Delta_x(t)$ for $T = 0.01$. The dashed line indicates $\Delta_x/2T$, with $T = 0.01$ the temperature of the thermal bath. $T_{ef}(T)$ is obtained from the linear fit to $\chi_x(t)$ for $\Delta_x > r_p^2$ (dash-dotted line). We find $T^x_{ef}(T) \approx T^x_{ef}(0) + T$, where $T^x_{ef}(0)$ is the transverse effective temperature corresponding to $T = 0$ (inset).

forces $F > F_t$, since Δ_x and χ_x are bounded at $T = 0$, while for finite T the relaxation times involved are very long. We leave the interesting cases of obtaining $T^x_{ef}(T)$ for $F > F_t$ and for $F \to 0$ for a future study (see the discussion of sec. 6.4.3). In Fig. 6.5 we show the dependence of T^x_{ef} on the pinning strength A_p and the vortex density n_v. In all cases we observe that $T^x_{ef} \to T_m$ when $F \to F_t$, even though F_t depends on A_p and n_v. The shaking temperature of [29] predicts $T_{sh} \sim (V/A_p^2)^{-1}$, a value that corresponds to the limit of non-interacting vortices or incoherent motion, since it is a single-vortex result [32]. As we show in the inset of Fig. 6.5, we find that a plot of all the curves as $T^x_{ef}(0)$ vs. $V/A_p^{2-\alpha}$ is better collapsed with $\alpha \approx 0.5$ instead of $\alpha = 0$. In the case of the motion of a rigid lattice one can apply the single-particle result to a Larkin–Ovchinnikov correlation volume, where the sum of pinning forces gives an effective pinning strength $\sqrt{A_p}$, and therefore $\alpha = 1$ in this limit. It is worth noting that the value we find is intermediate between these two limits.

6.3.3 Effective temperature from an experimentally accessible observable

We now show that the same T^x_{ef} can be obtained from experimentally accessible quantities such as the transverse resistivity and the voltage fluctuations. If T^x_{ef} is well defined at a

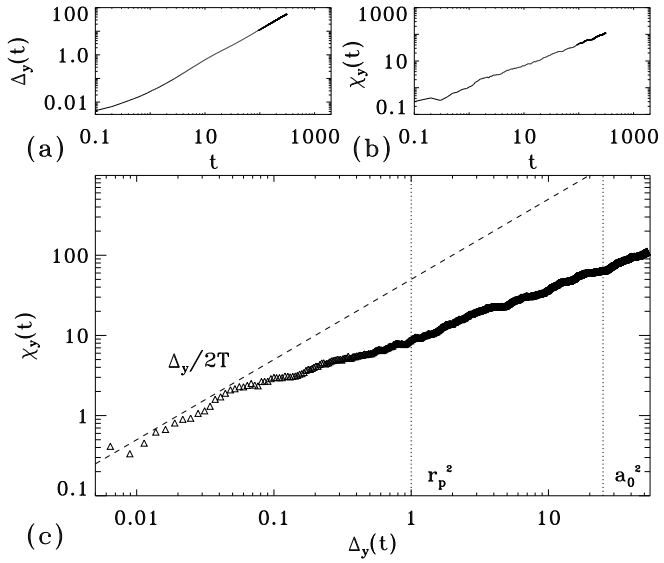


Figure 6.3: Longitudinal mean square displacement $\Delta_y(t)$ (a), and longitudinal response function $\chi_y(t)$ (b), for $A_p = 0.2$, $T = 0.01$ and $V = 0.11$, in the smectic flow regime. (c) Longitudinal FDR $\chi_y(t)$ vs. $\Delta_y(t)$ for $T = 0.01$. The dashed line indicates $\Delta_y/2T$, with $T = 0.01$.

given time scale, we can expect a generalized Kubo formula to hold [147],

$$R_x(t) = \frac{N_v}{T^x_{ef}(t)} \int_0^t dt' \langle V_x(t) V_x(t') \rangle, \tag{6.6}$$

where

$$R_x(t) = \left\langle \frac{dV_x(t)}{d\epsilon} \right\rangle_{\epsilon=0} - \left\langle \frac{dV_x(0)}{d\epsilon} \right\rangle_{\epsilon=0} \tag{6.7}$$

is the transverse linear resistance. From a parametric plot of the integrals of both sides of Eq. (6.6) we again find a linear relation with slope equal to $1/T$ for $t < r_p^2/D_x$ and a second linear relation with slope $1/T^x_{ef}$ for $t > r_p^2/D_x$. In Fig. 6.4 we compare the two effective temperatures obtained using Eqs. (6.4) and (6.6). We see that they are similar within the error bars.

6.4 Discussion

6.4.1 Comparison with the "shaking" temperature

The shaking temperature of Koshelev and Vinokur, T_{sh}, defined in the work [29], is proportional to the time integral of the correlation function of the pinning force $F_p = \sum_{i,p} f_{ip}(t)/N_v$:

$$T_{sh} = \frac{N_v}{\eta} \int_0^\infty dt \, \langle F^x_p(0) F^x_p(t) \rangle \propto \frac{A_p^2}{V}, \tag{6.8}$$

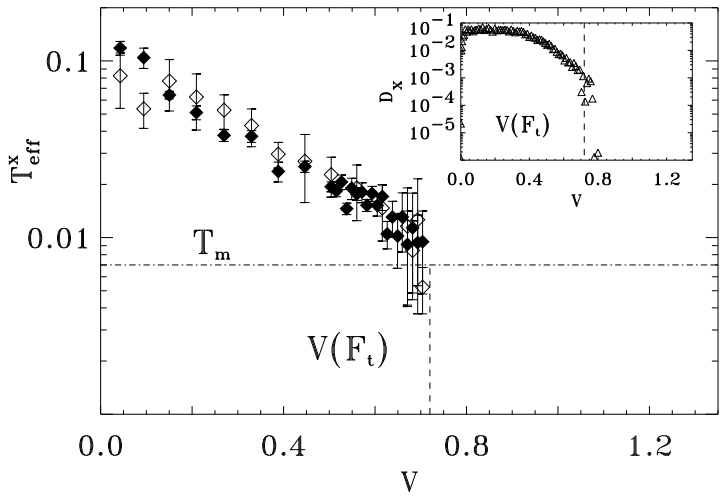


Figure 6.4: Transverse effective temperature T^x_{ef} vs. voltage V for $A_p = 0.35$, $T = 0$ and $n_v = 0.07$, using the diffusion relation (filled diamonds) and the generalized Kubo formula (open diamonds). Inset: transverse diffusion constant D_x vs. V. The dashed line indicates the transverse freezing transition at $F = F_t$ and the dotted line indicates the melting temperature of the unpinned system, $T_m \approx 0.007$.

T_{sh} can then be obtained from (6.6) if we replace $R_x(t)$ with the value corresponding to a single vortex, $R_0 = 1/\eta$, and take the integral of the correlation of $V_x(t)$ over all t [since in the transverse direction $V_x(t) \propto F^x_{pin}(t)$]. In other words, the T_{sh} of [29] corresponds to taking the average slope in a parametric plot of the generalized Kubo formula [or in the parametric plot of the fluctuation–dissipation relation shown in Fig. 6.2(c)], see also [148]. The scheme we carry out here allows us to define an effective temperature that takes into account all the information in its dependence on the time scale and allows a thermodynamic interpretation of T_{ef}. In this way we clearly see that there is a non-trivial value of the transverse effective temperature T^x_{ef} for time scales $t > r_p^2/D_x$. We also observe that in the longitudinal direction $T^y_{ef}(t)$ is very different, since the system is strongly driven out of equilibrium in this direction[1]. We further find that the short-range correlations of the moving fluid are important and give a non-trivial dependence on the disorder strength A_p, $T^x_{ef} = f(A_p^{2-\alpha}/V)$ with $\alpha \neq 0$. Despite this, we have shown that in the moving fluid phase T^x_{ef} satisfies two important results of [29]: (i) additivity of temperatures,

$$T^x_{ef}(T) = T^x_{ef}(0) + T \tag{6.9}$$

and (ii) the dynamical freezing occurs when

$$T^x_{ef}(T) = T_m. \tag{6.10}$$

[1]Also in granular matter under gravity [141] and in sheared fluids [143, 144], T_{ef} has been obtained only in the direction perpendicular to the driving force.

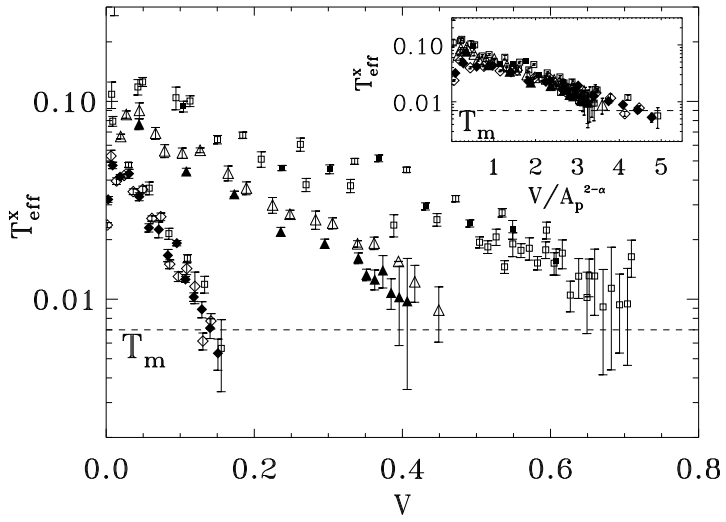


Figure 6.5: Transverse effective temperature T^x_{ef} vs. voltage V, for different values of the pinning strength A_p and the vortex density n_v, at $T = 0$. $A_p = 0.35$, $n_v = 0.05$ (■), $A_p = 0.35$, $n_v = 0.07$ (□), $A_p = 0.2$, $n_v = 0.05$ (▲), $A_p = 0.2$, $n_v = 0.07$ (△), $A_p = 0.1$, $n_v = 0.05$ (◊), $A_p = 0.1$, $n_v = 0.07$ (⧫). The inset shows T^x_{ef} vs. $V/A_p^{2-\alpha}$, with $\alpha = 0.5$.

6.4.2 Effective temperature of non-interacting vortices

By analyzing the dependence on A_p and V we have shown that $T^x_{ef} \neq T_{sh}$ for the incoherent motion of vortices, although both satisfy Eqs. (6.9) and (6.10). We will show here that the value of T_{sh} corresponds to that of the transverse effective temperature T^x_{ef} at long times only in the limit of non-interacting vortices. T_{sh} is thus a single-vortex result [32]. Using the same method based on the generalized fluctuation–dissipation relation of Eq. (6.4), we will first show that in the limit of non-interacting vortices we obtain $T^x_{ef} \approx T_{sh}$. We will then present a very simple model to derive the same result, based on an analysis of the collision process of a vortex with the static pinning centers.

Fluctuation–dissipation analysis

Using Eq. (6.4) for driven non-interacting vortices we find two slopes in the transverse fluctuation–dissipation relation, similarly to the interacting case. The short-time slope corresponds to the temperature T of the thermal bath, and the long-time one allows us to define a transverse effective temperature T^x_{ef}. In this case it was not possible to define a longitudinal effective temperature either. Figure 6.6 shows the transverse effective temperature T^x_{ef} as a function of the average velocity V of the non-interacting vortices, for different values of the pinning strength $A_p = 0.5$, 0.6, 0.7, 0.8, 1.0, 1.2, 1.5 and for different temperatures $T = 0$, 0.005, 0.01, 0.015, 0.02, 0.025, 0.03. As we see in Fig. 6.6, a good collapse of the curves is achieved by plotting $T^x_{ef} - T$ vs. V/A_p^2. This shows that for non-interacting vortices the result $T^x_{ef} - T \approx A_p^{2-\alpha}/V$ with $\alpha = 0$ describes the effective temperature well. This contrasts with what is shown in the inset of Fig. 6.5 when there

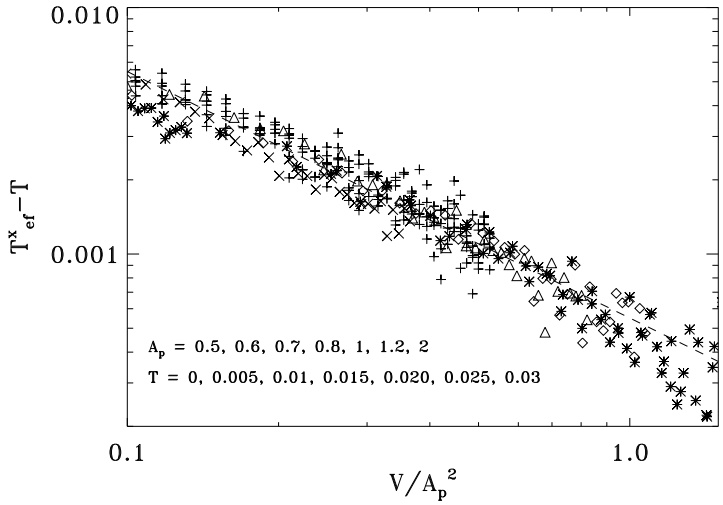


Figure 6.6: Transverse effective temperature T^x_{ef} as a function of the average velocity of a system of non-interacting vortices for different temperatures T and pinning strengths A_p. T^x_{ef} behaves like the shaking temperature T_{sh} proposed by Koshelev and Vinokur to describe the moving vortex fluid.

are interactions, where $T^x_{ef}(0)$ vs. $V/A_p^{2-\alpha}$ is better collapsed with $\alpha \approx 0.5$ than with $\alpha = 0$. This shows that the effective temperature defined from Eq. (6.4) is sensitive to the short-range correlations of the fluid phase.

Collision model

A very simple model, based on an analysis of the average effectiveness of the collisions of a vortex with a pinning center, is able to explain well the origin and the complete dependence of the transverse effective temperature on the driving force and the pinning strength, as well as to describe other effects of pinning on the long-time motion of the vortex. Based on these ideas, we will first give, by way of illustration, a heuristic derivation of the transverse effective temperature for the whole range of forces $F > F_c$. We will then repeat the derivation in more detail and with more justification.

We start with a simple dimensional analysis. Consider a vortex whose equation of motion is $\eta\mathbf{v}(t) = F\mathbf{y}+\mathbf{F}_p(\mathbf{r})$, where F is the driving force and $\mathbf{F}_p(\mathbf{r})$ is the pinning force due to randomly and uniformly distributed pinning centers of strength A_p and range ξ. For high forces the vortices pass very quickly over the pinning centers, and one can make the estimate $\eta\langle v\rangle \approx F$. The time to cross a pinning center is then of the order of $\delta t \sim \xi\eta/F$. During this time a transverse force of the order of $\delta f_x \sim A_p/\xi$ acts on the vortex, producing a transverse square displacement of the order of $\langle\delta^2 x\rangle \sim f_x^2\delta t^2/\eta^2 = (A_p/\xi)^2(\xi\eta/F)^2/\eta^2 = A_p^2/F^2$. In time t, of the order of $N_c \sim n_p\xi F t/\eta$ of these collisions occur, where n_p is the density of pinning centers. The mean transverse displacement in a collision is zero, by symmetry.

The total transverse mean square displacement is then

$$\langle \Delta^2 x \rangle = N_c \langle \delta^2 x \rangle \sim (n_p \xi F t/\eta)(A_p^2/F^2) = \frac{n_p \xi A_p^2}{\eta F} t \tag{6.11}$$

Since the response function of the transverse velocity of a single vortex is simply $1/\eta$, we can define a transverse effective temperature T_{ef}^x using the generalized fluctuation–dissipation relation of Eq. (6.4). In this case it takes the simple form of a generalized Einstein law $D_x = 2T_{ef}^x/\eta$. Therefore we obtain, for $F \gg F_c$:

$$T_{ef}^x \sim \frac{n_p \xi A_p^2}{F} \sim \frac{n_p \xi A_p^2}{\eta \langle v \rangle} \qquad F \gg F_c \tag{6.12}$$

a result that coincides with the shaking temperature T_{sh} of Koshelev and Vinokur [29, 32]. The dependence $T_{ef}^x \propto A_p^2/F$ is thus a result for non-interacting vortices. When the driving force F is close to F_c the argument given above must be modified, since then $\eta\langle v \rangle \ll F$. The time to cross a pinning center is very large, $\delta t \sim \xi/\langle v \rangle \gg 1$. During this long time the transverse force $\delta f_x \sim A_p/\xi$ acts on the vortex, producing a transverse square displacement of the order of $\langle \delta^2 x \rangle \sim \xi^2$, since the trajectory of a vortex within range of the center can be deflected transversally almost completely. Therefore, unlike what happens at high forces, $\langle \delta^2 x \rangle$ does not depend on velocity for $F \gtrsim F_c$. Since in time t now of the order of $N_c \sim n_p \xi \langle v \rangle t$ collisions occur, the total transverse mean square displacement is then, for $F \gtrsim F_c$:

$$\langle \Delta^2 x \rangle = N_c \langle \delta^2 x \rangle \sim (n_p \xi \langle v \rangle t)(\xi^2) = n_p \xi^3 \langle v \rangle t \tag{6.13}$$

Using again the generalized Einstein law $D_x = 2T_{ef}^x/\eta$ we obtain, for $F \gtrsim F_c$:

$$T_{ef}^x \sim n_p \xi^3 \eta \langle v \rangle \qquad F \gtrsim F_c \tag{6.14}$$

Thus at small velocities T_{ef}^x grows linearly with $\langle v \rangle$. Therefore, by equating Eqs. (6.12) and (6.14), we obtain as an estimate a value $\langle v \rangle \sim A_p/\xi$ at which T_{ef}^x has a maximum, separating the low- and high-velocity regimes given by Eqs. (6.14) and (6.12), respectively.

We will now justify in more detail the collision of a vortex with a pinning center, as shown schematically in Fig. 6.7, as a function of the driving force F and the impact parameter s. As usual, we will consider "asymptotic" initial and final states, outside the range of the pinning potential. The equation of motion of the vortex is

$$\eta \mathbf{v}(t) = \mathbf{F} + \mathbf{f}_p(\mathbf{r}(t)) \tag{6.15}$$

where $\mathbf{F} = F\hat{y}$ is the driving force and $\mathbf{f}_p$ is the force exerted by a pinning center located at $\mathbf{r}_p \equiv (x_p, y_p)$ on the vortex at position $\mathbf{r} \equiv (x, y)$. We will assume a Gaussian pinning well,

$$\mathbf{f}_p(\mathbf{r}) = \frac{A_p}{\xi^2}(\mathbf{r}_p - \mathbf{r}) \exp\left(\frac{|\mathbf{r} - \mathbf{r}_p|^2}{2\xi^2}\right) \tag{6.16}$$

where the coherence length ξ is the pinning range and A_p is the pinning strength. When the vortex collides with a center it undergoes a displacement $\delta\mathbf{r} = \mathbf{r}_2 - \mathbf{r}_1$ with respect to the trajectory of the free vortex,

$$\mathbf{r}_1 = \mathbf{r}_0 + \frac{\mathbf{F}}{\eta}\delta t + \delta\mathbf{r} \tag{6.17}$$

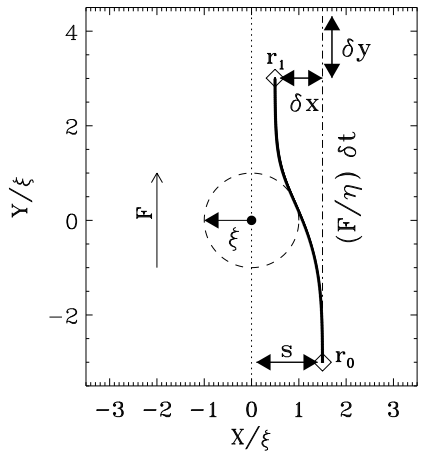


Figure 6.7: Collision of an isolated vortex with a pinning center. The impact parameter is s and F is the driving force in the y direction. The collision produces a transverse displacement δx and a longitudinal one δy with respect to the trajectory of a free, unpinned vortex.

where δt is the time interval involving the complete collision. To compare both trajectories we will take as the initial condition $y_p - y_0 \gg \xi$ and $x_p - x_0 = s$ (see Fig. 6.7). It is clear that $\delta\mathbf{r}$ will be a decreasing function of both the impact parameter s and the driving force F, as can be seen in Fig. 6.8(a) for fixed force F and variable impact parameter s, and in Fig. 6.8(b) for variable force F and fixed impact parameter s. Since the pinning centers are randomly and uniformly distributed over the sample (uncorrelated point disorder), we must consider the impact parameter as a random variable uniformly distributed over the collision range considered, and average the effects of the collision over s. We will then study the resulting probability distribution of $\delta\mathbf{r}$. Note that the nature of the displacement $\delta\mathbf{r}$ will be very different in the transverse direction x than in the longitudinal direction y. While δy is always negative and independent of the sign of s (the well systematically delays the vortex), the sign of δx is always opposite to that of s (see Fig. 6.7(b)). Due to the cylindrical symmetry of the pinning potential, the transverse displacement is positive or negative with equal probability, therefore $\langle \delta x \rangle = 0$ ($\langle \ldots \rangle$ means averaged over s). The complete collision with a defect produces a systematic delay of the vortex with respect to the free trajectory, therefore $\langle \delta y \rangle < 0$. Since the pinning potential is short-ranged we will have $\langle \delta^2 x \rangle < \infty$ and $\langle \delta^2 y \rangle < \infty$, as long as $F > F_c$, where F_c is the critical depinning force of a vortex. In Fig. 6.9 we show the dependence on F of $\langle \delta^2 x \rangle$ (a), of $\langle \delta y \rangle$ (b) and of $\langle \delta^2 y \rangle$ (c). These were obtained by numerical simulations of the equation of motion (6.15), averaging over 1000 different realizations of the impact parameter s of the collision.

As we see in Fig. 6.9, at high forces the correction to the free trajectory clearly decreases as a power law: $\langle \delta^2 x \rangle \propto F^{-2}$ (Fig. 6.9(a)), $\langle \delta y \rangle \propto F^{-2}$ (Fig. 6.9(b)) and $\langle \delta^2 y \rangle \propto F^{-4}$ (Fig. 6.9(c)). For low forces $F \gtrsim F_c \approx 0.6$, however, important deviations are observed. In the longitudinal direction there is a tendency of the moments to diverge when $F \to F_c^+$ (see Fig. 6.9(b)(c)). This is due to the proximity of the bifurcation occurring at F_c, at which the center of the defect becomes a stable fixed point of the dynamics. When $s \ll \xi$ it

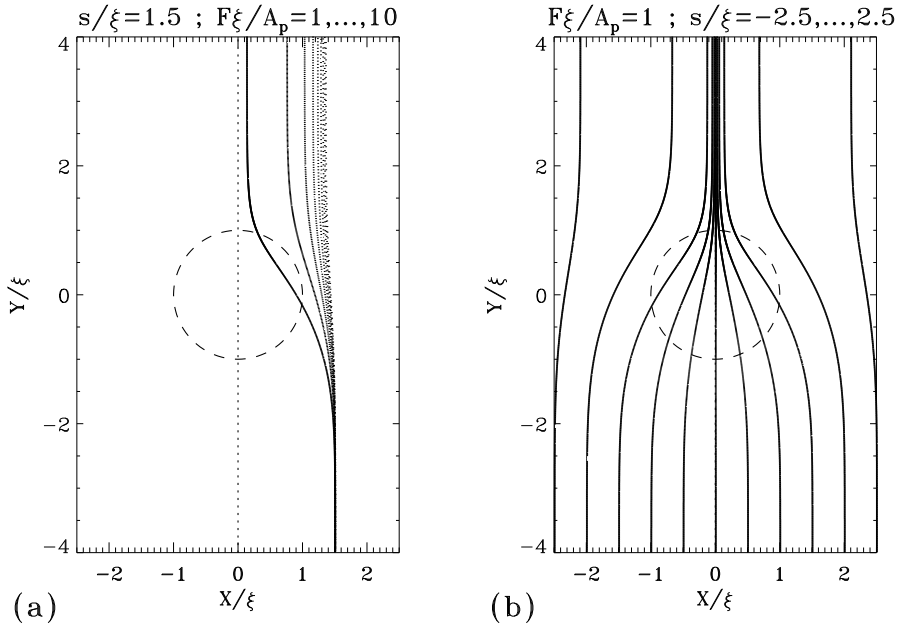


Figure 6.8: Dependence of the collision trajectories on the driving force F and on the impact parameter s. (a) Fixing s and increasing $F > F_c$, the trajectories become straighter and straighter. (b) Fixing $F > F_c$ and increasing $|s|$, the trajectories also become straighter. It is observed that the trajectories tend to "focus" transversally on the transverse coordinate of the pinning center.

takes the vortex a long time to cross the zone of influence of the potential, and $\delta t(F) \to \infty$ when $F \to F_c$. For the same force but with $s \gg \xi$, instead, $\delta t(F) < \infty$ for $F \leq F_c$. This gives rise to a dramatic increase of the moments $\langle \delta y \rangle$ and $\langle \delta^2 y \rangle$ when $F \to F_c^+$. On the other hand, we observe that $\langle \delta^2 x \rangle$ decreases with respect to the power law when $F \to F_c^+$. This is because for $F \gtrsim F_c$, $\delta^2 x \sim 0$ (the vortex passes practically straight) if $s \ll \xi$, while $\delta^2 x \sim s^2$ if $s \sim \xi$. In Fig. 6.9(a) we see that $\langle \delta^2 x \rangle \sim \xi$ when $F \sim F_c$, deviating from the power law $\langle \delta^2 x \rangle \sim F^{-2}$ valid for high forces. Therefore the transverse mean square displacement in a single collision is always finite for $F \geq F_c$.

To represent the motion of a vortex in a disordered sample with many pinning centers we now consider a sequence of many collisions. We will estimate the total displacement $\Delta \mathbf{r} = \hat{x}\Delta x + \hat{y}\Delta y$ accumulated with respect to the trajectory of the free vortex (without disorder). If N_c collisions occur, then $\Delta \mathbf{r} = \sum_{i=0}^{N_c} \delta \mathbf{r}$, for a particular realization of the sequence of impact parameters $\{s_i\}$. We will neglect the possible overlaps of pinning centers within the collision area. With this assumption it is reasonable to consider the s_i as independent, uniformly distributed random variables, since the disorder is uncorrelated. One would expect the details of the potential not to be important for the calculation of $\Delta \mathbf{r}$, and the results obtained with this model to describe general features of the motion of non-interacting vortices in disordered pinning potentials with short-range spatial autocorrelation. Figure 6.10 shows several possible trajectories of a vortex entering a region with many pinning centers and undergoing several collisions. We see that an initially flat

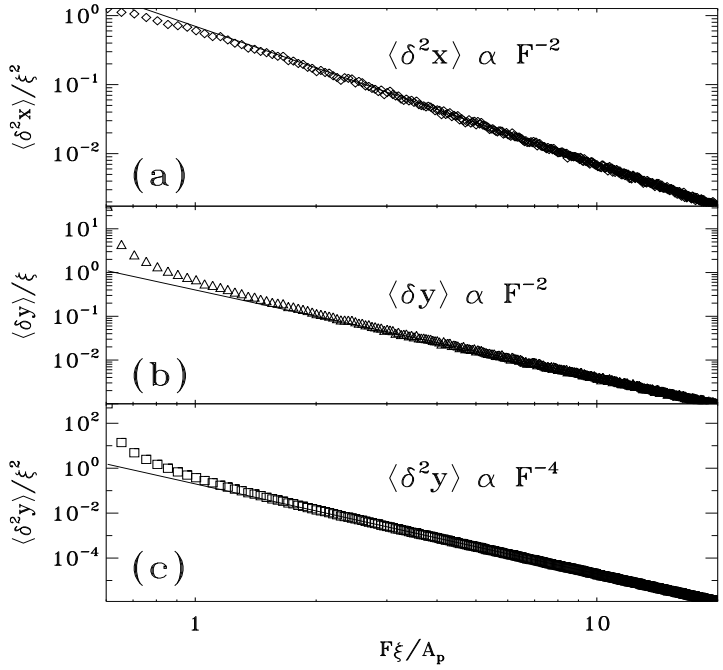


Figure 6.9: Mean transverse and longitudinal displacement in the reference frame of the isolated vortex produced by the collision with a pinning center, as a function of the driving force. The effectiveness of pinning in bending the trajectories decreases as a power law with F, in both directions.

and horizontal front of initial conditions becomes transversally localized in rough channels where a larger flux of trajectories is concentrated.

Taking into account that $\langle\delta x\rangle = 0$ and that $\langle\delta^2 x\rangle < \infty$, we can use the central limit theorem to obtain the dominant contribution to the mean transverse displacement when $N_c \gg 1$,

$$\langle\Delta^2 x\rangle = N_c\langle\delta^2 x\rangle \tag{6.18}$$

while for the longitudinal displacement the dominant contribution is

$$\langle\Delta y\rangle = N_c\langle\delta y\rangle \tag{6.19}$$

The net longitudinal displacement can be interpreted in terms of a correction to the mean longitudinal velocity with respect to the mean velocity of the free vortex,

$$\langle\Delta v\rangle = N_c\langle\delta y\rangle/t \tag{6.20}$$

such that $\langle v\rangle = \frac{F}{\eta} - \langle\Delta v\rangle$. The number of collisions N_c after a long time t is proportional to the density of pinning centers n_p and to the total area explored at long times along the vortex trajectory, $A \approx \langle v\rangle t\xi$ (dominant contribution). Therefore,

$$N_c \approx n_p\xi\langle v\rangle t = n_p\xi t\left(\frac{F}{\eta} - \langle\Delta v\rangle\right) \tag{6.21}$$

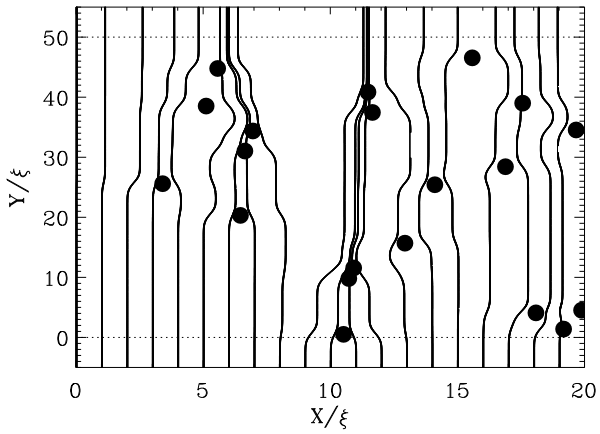


Figure 6.10: Typical trajectories of an isolated vortex in a sample with several pinning centers.

Using Eq. (6.20) we can express N_c in terms of $\langle \delta y \rangle$:

$$N_c \approx \frac{n_p \xi F t}{\eta(1 + n_p \xi \langle \delta y \rangle)} \tag{6.22}$$

Therefore,

$$\langle \Delta^2 x \rangle = \frac{n_p \xi F \langle \delta^2 x \rangle}{\eta(1 + n_p \xi \langle \delta y \rangle)} t = D_x(F) t \tag{6.23}$$

where we have defined the transverse diffusion constant $D_x(F)$. The correction $\langle \Delta v \rangle$ in terms of the mean displacements produced in a single collision is

$$\langle \Delta v \rangle = \frac{n_p \xi F \langle \delta y \rangle}{\eta(1 + n_p \xi \langle \delta y \rangle)} \tag{6.24}$$

We see then that the motion of the pinned vortex with respect to the reference frame attached to the free vortex is diffusive in the transverse direction and ballistic in the longitudinal direction. Since the velocity response function of a single vortex is simply $1/\eta$ in both directions, we can define an effective temperature T_{ef}^x in the transverse direction using the generalized fluctuation–dissipation relation of Eq. (6.4), which in this case takes the simple form of a generalized Einstein law $D_x = 2T_{ef}^x/\eta$. We can then obtain an expression for the transverse effective temperature in terms of the mean displacements undergone by a vortex in a single collision with a pinning center,

$$T_{ef}^x = \frac{n_p \xi F \langle \delta^2 x \rangle}{2(1 + n_p \xi \langle \delta y \rangle)} \tag{6.25}$$

We see then that at long times the pinning potential produces on the driven vortex a transverse diffusion, Eq. (6.23), with an associated transverse effective temperature, Eq. (6.25), and a decrease in the mean velocity with respect to the motion of the free (unpinned) vortex, Eq. (6.24).

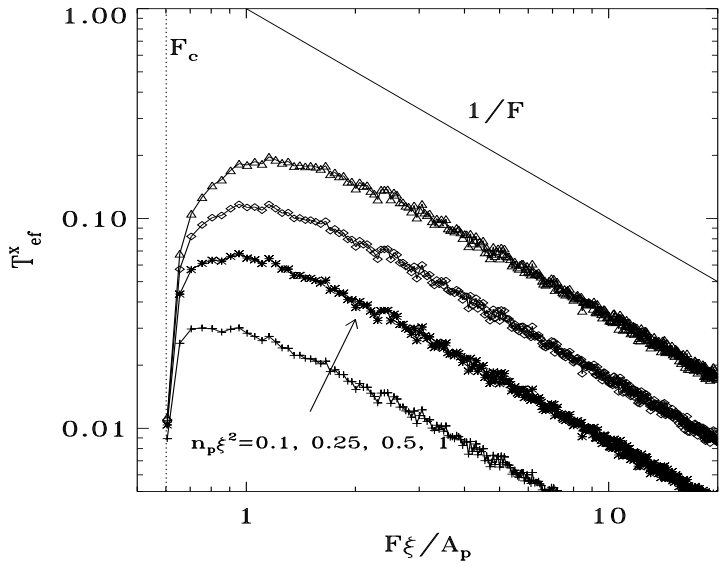


Figure 6.11: Transverse effective temperature for non-interacting vortices as a function of the force F, derived using the collision model.

In Figs. 6.11 and 6.12 we show T^x_{ef} vs. F and vs. $\langle v\rangle$ respectively, obtained using Eq. (6.25) from the computed values of $\langle\delta^2 x\rangle$ and $\langle\delta y\rangle$ (shown in Fig. 6.9(a)). In Fig. 6.13 we show the correction to the mean velocity given by Eq. (6.24). We show the results for several densities of pinning centers.

In Fig. 6.11 we see that T^x_{ef} is zero at F_c ($\langle v\rangle = 0$), and upon increasing F it first has a maximum that depends on the pinning density and then decreases following a clear $1/F$ power law at high forces. That T^x_{ef} is zero at F_c is reasonable since, when motion in the longitudinal direction ceases, so do the collisions per unit time, and therefore transverse diffusion also ends, given that $\langle\delta^2 x\rangle$ saturates to a finite value at F_c. The existence of the maximum had already been anticipated by the dimensional analysis at the beginning of this section, Eqs. (6.12), (6.14). As can be seen in Fig. 6.12, the maximum of T^x_{ef} close to F_c is associated with the condition $\eta\langle v\rangle = A_p/\xi$ (note that when plotting T^x_{ef} vs. $\langle v\rangle$ the maximum appears approximately at the same location, independently of the pinning density). This condition is in turn associated with $\langle\delta y\rangle \approx \sqrt{\langle\delta^2 x\rangle}$, which occurs when the magnitude of the transverse displacement is of the order of the magnitude of the longitudinal displacement in a collision. It is then interesting to note that, since the magnitude of the velocity fluctuations is similar in both directions at this point, it is very plausible that this is also a point of isotropic noise. The decay $T^x_{ef} \sim A_p^2/F \sim A_p^2/\eta\langle v\rangle$ at high forces is a direct consequence of the fact that the efficiency of the collision in the transverse direction is measured by $\langle\delta^2 x\rangle \sim F^{-2}$ per collision, as shown in Fig. 6.9(a). Since the number of collisions grows linearly with F at long times, we obtain the dependence $1/F \sim 1/\langle v\rangle$ for the transverse effective temperature. Using in Eq. (6.25) that at high forces $\langle\delta^2 x\rangle \sim A_p^2 F^{-2}$, and neglecting $\langle\delta y\rangle$ compared with 1 in the denominator, we obtain

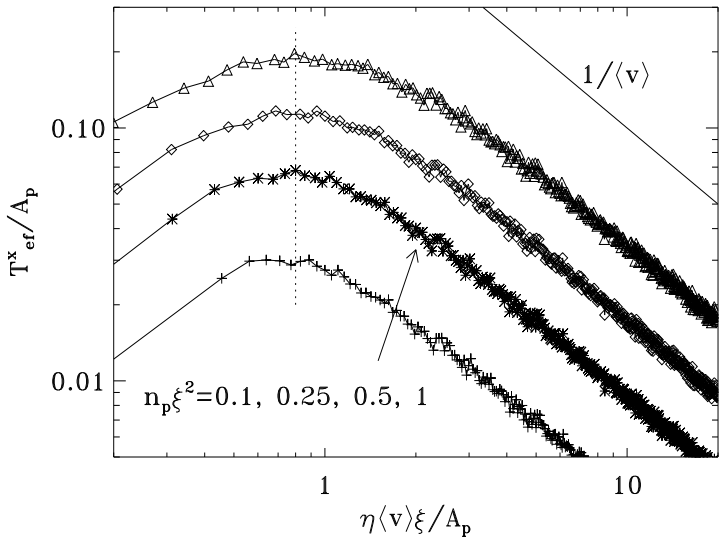


Figure 6.12: Transverse effective temperature for non-interacting vortices as a function of the mean velocity $\langle v\rangle$, derived using the collision model.

the following expression for T^x_{ef}:

$$T^x_{ef} \sim \frac{n_p \xi A_p^2}{F} \sim \frac{n_p \xi A_p^2}{\eta \langle v \rangle} \tag{6.26}$$

This expression coincides with that of Eq. (6.12), obtained by a simple dimensional analysis, and with the expression for the shaking temperature T_{sh} of Koshelev and Vinokur [29]. This better justifies the result that T_{sh} is a single-vortex result [32]. Therefore T_{sh} is not applicable to the case of interacting vortices, even if the motion is incoherent, as we already noted in section 6.3.2 in relation to the result of the inset of Fig. 6.5.

In Fig. 6.13 we show the correction $\langle \Delta v\rangle$ to the mean velocity due to pinning as a function of F for several pinning densities. We see that at $F_c \sim 0.6$ all the curves meet at the point $\eta\langle \Delta v\rangle = F_c$. This is simply because F_c does not depend on the density of pinning centers for non-interacting vortices, and therefore $\eta\langle v\rangle = F_c - \eta\langle \Delta v\rangle = 0$ for all densities. However, it must be noted here that our calculations cease to be valid at very high densities, when the probability of overlap of pinning centers becomes large. Nevertheless, as mentioned earlier, this effect could be included effectively and to a first approximation by treating A_p as a random variable (although in the case of extreme overlap the collision scheme developed here ceases to hold). Within the range of validity of our model we see in Fig. 6.13 that $\langle \Delta v\rangle$ is larger the larger the density of pinning centers, but that the depinning transition is more abrupt the lower the pinning density. At sufficiently high forces all curves show an identical $1/F$ decay, as happens with T^x_{ef}.

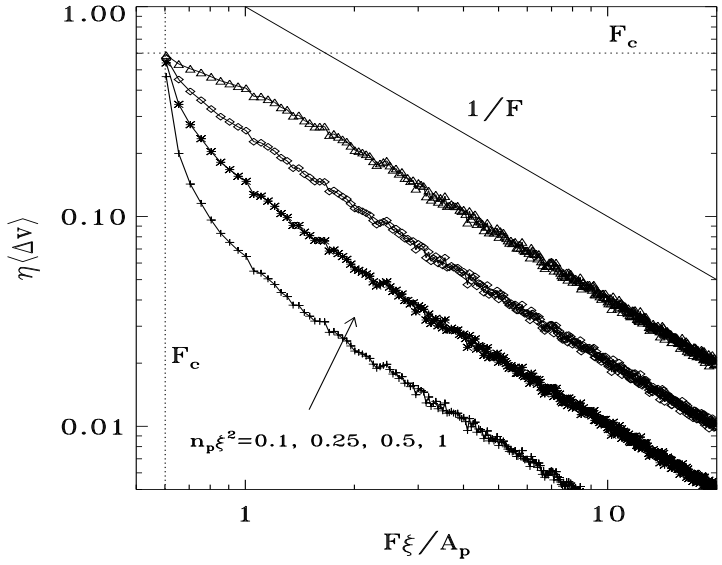


Figure 6.13: Correction $\langle\Delta v\rangle$ to the mean velocity of non-interacting vortices as a function of force for different densities of pinning centers. The mean velocity of the vortex on the pinning potential is $\langle v\rangle = F/\eta - \langle\Delta v\rangle$.

6.4.3 Can T^x_{ef} be defined at high velocities?

The works of references [30–32] agree that in dimensions less than or equal to three the long-range order of the moving vortex lattice is always destroyed, even at high velocities. There is, however, no agreement as to what the nature of the resulting high-velocity phase would be (if no longer a moving crystal). In three dimensions Le Doussal and Giamarchi [30] propose the existence of a topologically ordered moving structure called the "moving Bragg glass". For this proposal Le Doussal and Giamarchi rely on the elastic self-consistency of an effective model for the vortex lattice. Balents, Marchetti and Radzihovsky [31] criticize the effective model of Le Doussal and Giamarchi (which turns out to be elastically self-consistent) and conjecture that the only order that survives is a smectic one, which they then study using another effective model in which the longitudinal elastic coupling between channels is removed from the outset. In two dimensions (or at intermediate currents in $d = 3$), on the other hand, although the instability of the vortex lattice against topological defects is not questioned, no agreement has been reached either on the resulting nature of the high-velocity dynamical phase. Le Doussal and Giamarchi [30] propose the "moving transverse glass": a structure with smectic order that has a transverse critical depinning current at $T = 0$. Balents, Marchetti and Radzihovsky [31], instead, propose the "driven smectic" (in two dimensions with short-range transverse order): a structure with smectic order that does not present a transverse critical depinning current, due to the existence of "permeation modes". These modes imply normal diffusion of vortices in the transverse direction [31] at high longitudinal velocities.

The review made above serves to put into context the important discussion of whether or not it is possible to define a transverse effective temperature at high velocities, in

the moving transverse solid. It is clear that to be able to define a T^x_{ef} associated with a long time scale using Eq. (6.4), we need: (1) that $\Delta_x(t)$ (Eq. 6.5) and $\chi_x(t)$ (Eq. 6.3) are not both bounded at the same time, in order to find a slope in the $\chi_x(t)$ vs. $\Delta_x(t)$ plot; (2) linear response: that is, $\chi_x(t)$ well defined, $\overline{\langle A_x(t)\rangle}_\epsilon - \overline{\langle A_x(t)\rangle}_{\epsilon=0} \sim \epsilon\chi_x(t)$ for $\epsilon \to 0$; (3) $\chi_x(t) \approx a\Delta_x(t) + b$ at long times, with a and b constants, in order to define a time-independent T^x_{ef} according to Eq. (6.4).

At $T = 0$ it is clear that (1) does not hold since, as we showed in chapter 3, all jumps of vortices between channels cease and $\Delta_x(t) \sim$ const at long times. In the simulation at $T = 0$ we have also found that the response $\chi_x(t)$ saturates at long times. Therefore the fluctuation–dissipation relation of the moving transverse solid at $T = 0$ ends at an accumulation point and it is not possible to define T^x_{ef}. We may then ask whether this is a limitation particular to $T = 0$ only. For example, if at $T \neq 0$ the permeation modes predicted in [31] for the "driven smectic" existed, we know that conditions (1) and (2) would be satisfied automatically [31]. In this situation, if condition (3) also holds, it is perfectly possible to define T^x_{ef} based on Eq. (6.4). On the other hand, if at $T \neq 0$ the permeation modes of the "driven smectic" did not exist, and there were instead a transverse critical current, as occurs in the "moving transverse glass" of Le Doussal and Giamarchi, it is not easy to see whether or not conditions (1) and (2) hold. A transverse critical current at $T \neq 0$ implies that the force–velocity curve in the transverse direction is non-linear at small forces, of the type $V_t \sim \epsilon^\delta$ with $\delta > 1$. This apparently violates condition (2) of linear response[2]. If so, we could not define T^x_{ef} in the "moving transverse glass". A simple example serves to show that the situation is not necessarily so. Suppose that condition (2) of linear response holds, with $\chi_x(t)$ well defined, and suppose that it has a dependence of the type $\chi_x(t) \sim t^\gamma$ at long times, with $0 < \gamma < 1$. If the same very small transverse force ϵ acts on all vortices, the instantaneous transverse voltage (or instantaneous mean transverse velocity) $v_t(t)$ in response to it can be obtained from $\chi_x(t)$ as follows: $v_t(t) \approx \epsilon\, d\chi_x(t)/dt \sim \epsilon t^{\gamma-1}$. The instantaneous transverse voltage is then linear in ϵ. However, the mean voltage $V_t = \frac{1}{T}\int_0^T v_t(t)dt \sim \epsilon T^{\gamma-1} \to 0$ for $T \to \infty$. This is consistent with a non-linear velocity–force curve in the transverse direction at small forces, of the form $V_t \sim \epsilon^\delta$ with $\delta > 1$, as predicted for the "moving transverse glass". Therefore, a non-linear transverse force–velocity curve does not necessarily mean that condition (2) of linear response is violated. The confusion comes from not noticing that, although $\chi_x(t)$ is well defined, and therefore there is linear response, it can have vanishing Fourier components. In particular, in our simple example we show that $V_t \propto \chi(\omega = 0) = 0$ to first order in ϵ, and therefore V_t vs. ϵ is non-linear. It is very interesting to note that if we had a dependence of $\chi_x(t)$ like that of the simple example we gave, provided condition (3) holds we could perfectly well define a transverse effective temperature T^x_{ef}, and the transverse diffusion would be anomalous (being proportional to $\chi_x(t)$).

We see then that both in the "driven smectic" of [31] and in the "moving transverse glass" of [30] there are, in principle, no incompatibilities with the definition of a transverse

[2]Note that in the undriven case, if the static phase were for example the Bragg glass or the vortex glass, we would also have a non-linear force–velocity curve at small forces, due to the existence of diverging barriers for vortex creep when the current $J \to 0$.

effective temperature T_{ef}^x from Eq. (6.4). We venture to conjecture that, if it is possible to determine T_{ef}^x, its dependence on the external temperature T should be different from that of the low-velocity fluid phase, where we find $T_{ef}^x(T) = T_{ef}^x(0) + T$. We base this on the fact that at high velocities the only mechanism that can give rise to transverse diffusion is thermal fluctuations, since when $T \to 0$ we fall into the moving transverse solid presented in chapter 3. A "multiplicative" dependence of the type $T_{ef}^x(V,T) = Tf(V)$ could be a simple possibility that takes into account that transverse diffusion at high velocities requires thermal activation. Note in passing that in the hydrodynamic descriptions of the moving vortex lattice of refs. [30–32], the renormalized temperature is multiplicative with the external temperature. We are currently carrying out simulations at $T \neq 0$ to see whether we can determine the transverse effective temperature T_{ef}^x at high velocities. We believe that, if we can do so, we could better pin down the nature of the transverse freezing transition at $T \neq 0$.

6.4.4 Conclusions

We have numerically studied correlation functions and response functions in vortex lattices driven out of equilibrium over random pinning potentials. From a generalized fluctuation–dissipation relation we computed a transverse effective temperature T_{ef}^x in the moving fluid phase. Unlike the shaking temperature T_{sh} of Koshelev and Vinokur [29], the proposed definition of T_{ef}^x takes into account all the information in its dependence on the time scale and allows a thermodynamic interpretation of it. We find, however, that T_{ef}^x satisfies some important properties of T_{sh}, such as being additive with the external temperature, $T_{ef}^x(T) = T_{ef}^x(0) + T$, and the property that dynamical freezing occurs when $T_{ef}^x(T) = T_m$, where T_m is the equilibrium melting temperature of the unpinned system. We find that short-range correlations give a non-trivial dependence on the pinning strength A_p, different from that predicted for T_{sh} in [29]. We further showed that the value of T_{sh} corresponds to T_{ef}^x only in the limit of non-interacting vortices. The generalized Kubo formula suggests that T_{ef}^x could be obtained experimentally from measurements of the voltage noise and of the instantaneous transverse resistivity[3]. It would be interesting to use such experiments to quantitatively test the dynamical freezing transition. Finally, we emphasize that a complete dynamical theory of the moving vortex system should capture the features described in this work.

Very important questions remain open, such as computing an effective temperature for large forces, in the transverse solid, and for very small forces, in the creep regime. The study of the non-equilibrium relaxation in the static limit is another key question that would allow us to enrich the concept of the vortex glass, placing it in the emerging theoretical context of the dynamics of glassy systems in general [86].

Part of the results described in this chapter were published in [127] in collaboration with Raphael Exartier, Leticia Cugliandolo and Niels Grønbech-Jensen. We thank A.

[3]Voltage noise measurements could depend on the contact configuration, see for example [149]. To test the Kubo formula correctly, the same voltage contacts must be used for the measurements of the spontaneous fluctuations of the transverse voltage and of the transverse resistance. Careful alignment of the contacts in the direction perpendicular to the current will be crucial.

Barrat, L. Berthier, J. Kurchan, T. Giamarchi, P. Le Doussal, M. C. Marchetti and V. M. Vinokur for stimulating discussions.

Chapter 7

Out-of-equilibrium relaxation in disordered systems with strongly localized states

We study the slow non-equilibrium relaxation in disordered systems with strongly localized electronic states by means of Monte Carlo simulations of the Efros–Shklovskii Coulomb glass model. Studying two-time autocorrelation functions $C(t, t_w)$ we find that at sufficiently low temperatures this system falls out of equilibrium and displays simple aging, $C(t, t_w) \sim f(t/t_w)$, where t_w is the waiting time or "age" of the system. Upon increasing the temperature the aging effects disappear and stationarity is recovered. The results obtained agree with recent experiments in doped semiconductors and could also describe the relaxation of the vortex Bose glass in superconductors with columnar defects, in the variable-range-hopping regime, for magnetic fields $H_{c1} \ll B < B_\Phi$, where B_Φ is the matching field.

7.1 Introduction

Glasses are characterized by a very slow, non-exponential temporal relaxation to equilibrium, with a characteristic time that can appreciably exceed the observation time. As a consequence, time-translation invariance is lost and aging phenomena become observable, in which static and dynamical properties can depend on the "age" of the system, defined as the waiting time t_w since the system was prepared for the measurement. Although in different materials the mechanism giving rise to this slow non-equilibrium dynamics varies, and is often not evident, important advances have been made by analytically studying the slow dynamics in schematic models (see [86] and references therein).

In recent experiments on doped semiconductors with a very low donor concentration, non-ergodic behavior has been observed, with slow relaxation and memory and aging effects [150–154]. In this chapter we will analyze the non-equilibrium relaxation of this disordered electronic system using the model of Efros and Shklovskii [155]. We will first

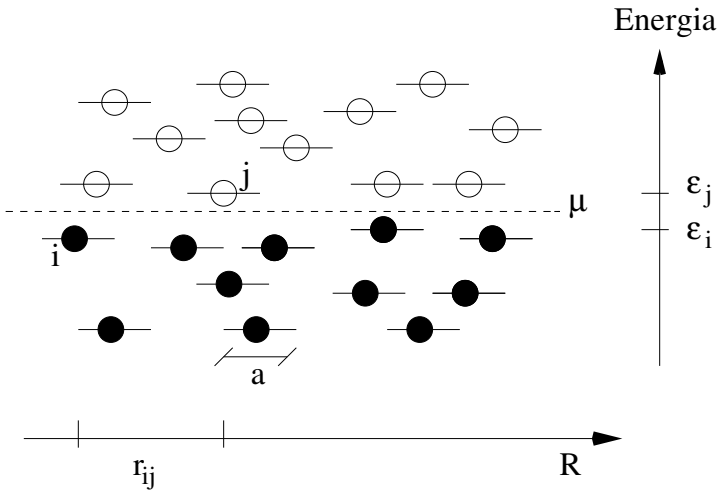


Figure 7.1: Illustrative sketch of the impurity band in an Anderson insulator (label: *Energía* = energy). μ indicates the Fermi level and a the Anderson localization radius of the one-electron wave functions. When the density N_D of sites (donors) is $N_D a^3 \ll 1$ the band can be treated classically. The Coulomb interactions make the (classical) one-particle levels depend on the whole electronic configuration, giving rise to important restrictions on the one-particle density of states near the Fermi level.

briefly describe the basic physics of this system, known as the *Coulomb glass* or electron glass [156]. We will then describe in detail the experimental results and the analogy with the vortex Bose glass [19, 157] in the "*variable-range-hopping*" (VRH) regime.

7.2 Interacting localized electrons

7.2.1 The Coulomb gap

The disordered system in question is, at low temperatures, a good realization of an Anderson insulator, in which the electronic states near the Fermi level are strongly localized, forming the so-called *classical impurity band* [158]. An illustrative sketch of it is shown in Fig. 7.1. The low donor concentration $N_D a^3 \ll 1$, compared with the Anderson localization length a, allows this band to be treated classically (and also allows the spin–spin interaction between electrons localized on neighboring donors to be neglected). Assuming an n-type semiconductor, with acceptor concentration $N_A < N_D$, and ignoring quantum effects, the Hamiltonian governing the system is basically the electrostatic interaction energy,

$$H = \frac{e^2}{\kappa}\left[\sum_{i\neq j}\frac{(1-n_i)(1-n_j)}{r_{ij}} - \sum_{i,\nu}\frac{(1-n_i)}{r_{i\nu}} + \frac{1}{2}\sum_{\nu\neq\gamma} r_{\nu\gamma}^{-1}\right] \tag{7.1}$$

where e is the absolute value of the electron charge, κ is the dielectric constant, $r_{ij} = |\mathbf{r}_i - \mathbf{r}_j|$ with $\mathbf{r}_i$ and $\mathbf{r}_j$ the positions of the donors, and $\mathbf{r}_\nu$ and $\mathbf{r}_\gamma$ are the positions of the acceptors.

The occupation is $n_i = 1$ if donor i is occupied (neutral) and $n_i = 0$ if it is empty (positively ionized). We assume that the temperature is low enough to neglect activated jumps to the conduction band and double occupation of donors. Then a donor site is either occupied and neutral, or empty and positively charged, while the acceptors have all captured an electron, becoming negative. The first term of Eq. (7.1) therefore represents the Coulomb interaction between donors, whose charges can vary. The second term, which represents the interaction of donors with acceptors, can be thought of as the interaction of the donor sites with a static disordered potential created by the negatively charged acceptors. The third term does not involve the dynamical variables n_i and represents the interaction energy between acceptor sites.

At low temperatures the system in equilibrium will be described by a set $\{n_i\}$ that minimizes H (Eq. 7.1), with the condition that the total number of electrons, $\sum_i n_i$, corresponds to a given degree of compensation that guarantees the neutrality of the whole system. It is convenient to pose this problem in terms of the one-particle energies at the donor sites,

$$\epsilon_i = \frac{e^2}{\kappa}\left[\sum_{\nu}\frac{1}{r_{i\nu}} - \sum_{j\neq i}\frac{1-n_j}{r_{ij}}\right] \tag{7.2}$$

where $-\epsilon_i/e$ clearly represents the potential created at donor i by all the other charges of the system. The Hamiltonian of Eq. (7.1) can then be rewritten as

$$H = \frac{e^2}{\kappa}\left[\sum_i \epsilon_i n_i + \frac{1}{2}\sum_{\nu\neq\gamma} r_{\nu\gamma}^{-1}\right] \tag{7.3}$$

Minimizing $\tilde{H} = H - \mu\sum_i n_i$ at a given value of the chemical potential μ (determined by imposing the neutrality condition), one immediately sees that the condition that there be a positive increment of $\tilde{H}$ as a result of changing an occupation number n_i implies $n_i = \Theta(\mu - \epsilon_i)$, where Θ is the Heaviside function. The density of states $g(\epsilon)$ and the Fermi level μ are the main characteristics of the classical impurity band, from which important low-temperature properties of doped semiconductors can be computed, such as the temperature dependence of the conductance, the specific heat, etc. In the case of a random distribution of impurities, the structure of the band is completely determined by the donor concentration N_D and the degree of compensation $K = N_A/N_D$, where N_A is the acceptor concentration. Efros and Shklovskii showed in a very general and simple way that Coulomb interactions impose important additional restrictions on $g(\epsilon)$ [159]. Suppose that in the ground state site i is occupied by an electron while site j is empty. The energy change of moving the electron from i to j is

$$\Omega_i^j = \epsilon_j - \epsilon_i - e^2/\kappa r_{ij} \tag{7.4}$$

This can be understood by dividing the process into two steps. In the first we take the electron from i to infinity. The total energy change is then $-\epsilon_i$. In the second step we bring the electron from infinity to site j. The energy needed for this second step would be ϵ_j if the system were in the ground state with site i occupied. However, since we have

just emptied site i in the first step, there will be an extra attraction of magnitude $e^2/\kappa r_{ij}$ on the electron, coming from the charge of site i, which explains the presence of the last term of (7.4). Since we want the ground state to be stable with respect to any of these one-electron processes, the energy change Ω_i^j must be positive. Therefore the inequality

$$\epsilon_j - \epsilon_i - e^2/\kappa r_{ij} \geq 0 \tag{7.5}$$

must hold for all occupied sites i and all empty sites j of the system. Efros and Shklovskii showed that this condition leads to an essential reduction of $g(\epsilon)$ in the vicinity of the Fermi level, called the *Coulomb gap*. To see this, consider an interval of width ϵ around the Fermi level, that is, consider all the sites satisfying

$$\epsilon_j - \epsilon_i < \epsilon \tag{7.6}$$

From condition (7.5) it follows that the distance between the occupied and the empty site cannot be smaller than $e^2/\kappa\epsilon$. Therefore the concentration $N(\epsilon)$ of sites within the interval ϵ cannot exceed $\epsilon^d\kappa^d/e^{2d}$, with d the space dimension. Then the density of states $g(\epsilon) = dN/d\epsilon$ cannot exceed $\epsilon^{d-1}\kappa^d/e^{2d}$. Since a reduction stronger than ϵ^{d-1} is not self-consistent, we have

$$g(\epsilon) = \alpha_d|\epsilon - \mu|^{d-1}\kappa^d/e^{2d} \tag{7.7}$$

where ϵ is a one-particle energy and α_d is a dimensionless constant. Quantitative estimates of $g(\epsilon)$ using the self-consistent equation method [160] or numerical simulations [161] show that $\alpha_2 = 2/\pi$ and $\alpha_3 = 3/\pi$. It should be noted that the argument used here to obtain evidence of the Coulomb gap is the stability of the state of the system against one-electron hopping processes, and it is therefore a pseudo-ground state. More careful and complicated studies show, however, that the requirement of stability against many-electron transitions, which corresponds to requiring the true ground state, does not qualitatively change the result (7.7) [159].

A very interesting thing about the Coulomb gap in the one-particle density of states is that it is an almost universal property, which depends only on the fact that the interactions are long-ranged but is independent of the details of the model under study. In particular, Täuber *et al.* [157] found a "Coulomb gap" in the one-particle (vortex) density of states in a BSCCO superconducting sample in the Bose glass phase, using the positions of the columnar defects and of the vortex lines obtained simultaneously by magnetic decoration experiments [162, 163]. We will discuss this motivating result in section 7.3.2.

7.2.2 Conductivity

The Coulomb *gap* should manifest itself in dc variable-range-hopping (VRH) conduction. The VRH mechanism was originally proposed by Mott under the assumption that the one-particle density of states is a constant $g(\epsilon) \sim g_0$ near the Fermi level. Mott's derivation [164], which is worth reproducing for its simplicity and great physical content, is basically the following. If we consider an energy band of width Γ near the Fermi level, the mean distance R between electronic states within the band is given by the relation

$$g_0 R^d \Gamma \approx 1 \tag{7.8}$$

where d is the dimension. The phonon-assisted hopping conductance of electrons between sites will then be proportional to

$$\exp(-2R/a - \Gamma/kT) \tag{7.9}$$

where a is the localization radius. The first term in the exponent describes *tunneling* and the second the activation probability. Using relation (7.8), the maximum conduction is obtained for

$$\Gamma_{\frac{1}{d+1}} \approx kT \left(\frac{T_{\frac{1}{d+1}}}{T} \right)^{\frac{1}{d+1}} \tag{7.10}$$

where $kT_{1/d+1} = \beta_0/g_0 a^3$, with β_0 a numerical factor. The optimal hopping length for this band is

$$R_{\frac{1}{d+1}} \approx a \left(\frac{T_{\frac{1}{d+1}}}{T} \right)^{\frac{1}{d+1}} \tag{7.11}$$

and therefore, substituting into Eq. (7.8), we obtain the well-known *Mott law*:

$$\sigma \propto \exp \left[- \left(\frac{T_{\frac{1}{d+1}}}{T} \right)^{\frac{1}{d+1}} \right] \tag{7.12}$$

The correction due to the Coulomb *gap* becomes important at low temperatures, when $\Gamma_{1/d+1}$ becomes smaller than the width Δ of the *gap*. The relation between Γ and R is no longer given by Eq. (7.8). Instead, replacing g_0 in (7.8) by $g(\Gamma)$ from Eq. (7.7), we find that the mean distance is given by

$$R \approx \frac{e^2}{k\Gamma} \tag{7.13}$$

independent of the dimension d and of g_0, determined only by the Coulomb interaction. Repeating Mott's derivation with this relation between Γ and R, we find that the maximum conduction will be given by a band of width

$$\Gamma_{\frac{1}{2}} \approx kT \left(\frac{T_{\frac{1}{2}}}{T} \right)^{\frac{1}{2}} \tag{7.14}$$

where $kT_{1/2} = \beta e^2/\kappa a$, with β a numerical factor. The optimal hopping length for this band turns out to be

$$R_{\frac{1}{2}} \approx a \left(\frac{T_{\frac{1}{2}}}{T} \right)^{\frac{1}{2}} \tag{7.15}$$

and therefore the conductivity obeys the Efros–Shklovskii (ES) law [158],

$$\sigma \propto \exp \left[- \left(\frac{T_{\frac{1}{2}}}{T} \right)^{\frac{1}{2}} \right] \tag{7.16}$$

instead of the Mott law of Eq. (7.12). We see that both laws are identical except for the exponent of the temperature. In Mott's law the exponent is $1/(1+d)$, while in the

Efros–Shklovskii law it is 1/2, independent of the dimension (i.e., a mean-field-like result). To compute β the percolation method is used [159]. Although the result of Eq. (7.7) is well established by different methods, the ES law (Eq. 7.16) for the conductivity remains controversial today, from both the experimental and the theoretical point of view. Although many experiments in two dimensions report agreement with the ES law, the evidence is very often ambiguous, because a large interval of σ is needed to discern between Mott's law (Eq. 7.12) and the ES law (Eq. 7.16). Pollak's group [165] and other authors, on the other hand, question the simple theoretical derivation of Efros and Shklovskii, arguing that other hopping processes, sequential and simultaneous, of several electrons, at a different length scale, are equally important for the calculation of the conductivity. These processes are not contained in the derivation of the ES law.

The observation of a "Coulomb gap" in the density of states of the vortex Bose glass by Täuber *et al.* [157] also opens the interesting question of the sensitivity of vortex transport in the VRH regime to long-range interactions. In section 7.3.2 we will show that an argument similar to that of ES can be used to compute the current–voltage curve of the superconductor. We will see that in the vortex system the interactions can also be relevant for the transport properties in the VRH regime, even when the structure of the vortex lattice is completely disordered.

7.2.3 Electron glass

Davies, Lee and Rice carried out Monte Carlo numerical simulations with a simplified model of a system of interacting localized electrons [156]. They found the Coulomb gap in the one-particle excitation spectrum and showed that the gap fills in as the temperature increases. Drawing an analogy with the Ising spin-glass model with a random local field and $1/r$ interactions, and using a modified Edwards–Anderson parameter, they found evidence of "glassy" order at low temperatures. They called this phase the *electron glass*, nowadays also commonly known as the Coulomb glass. To see the analogy with spin glasses it is convenient here to rewrite the Hamiltonian (7.1) as follows, in units of $e^2/\kappa a$,

$$H = \sum_i n_i \tilde{\phi}_i + \sum_{i>j} \frac{(n_i - K)(n_j - K)}{r_{ij}} \tag{7.17}$$

where K represents the compensating charge that guarantees the neutrality of the whole system and $\tilde{\phi}_i$ is a random site energy originating from the static charge randomly distributed on the acceptor sites. Davies, Lee and Rice considered a simplified version of the Efros–Shklovskii model, in which the sites of Eq. (7.17) are placed on a square or simple cubic lattice instead of being randomly distributed. Disorder is then introduced only through the site energies $\tilde{\phi}_i$, which were assumed to have a uniform and symmetric distribution. The case $K = 1/2$ is interesting because there is electron–hole symmetry. If in that case we replace the variables n_i by the Ising variables $S_i = 2n_i - 1 = \pm 1$, the Hamiltonian becomes, up to terms independent of the S_i,

$$H = \sum_i S_i \phi_i + \frac{1}{4} \sum_{i>j} \frac{S_i S_j}{r_{ij}} \tag{7.18}$$

where $\phi_i = \tilde{\phi}_i/2$. This Hamiltonian, if we consider the sites on a regular lattice, is that of the random-field Ising spin glass with $1/r$ interactions. Davies, Lee and Rice noted that the Edwards–Anderson order parameter $q_{EA} = \langle \langle S_i \rangle_t^2 \rangle_S$, where $\langle \rangle_t$ and $\langle \rangle_S$ are the averages over time and samples respectively, is not useful to characterize a glass transition in this system. This is because the terms ϕ_i make $q_{EA} > 0$ even in the high-temperature phase, since the spins preferentially orient in the direction of the local field ϕ (even in the absence of interactions). They therefore proposed a modification of the order parameter of the form $q = \langle [\langle S_i \rangle_t - f(\phi_i)]^2 \rangle_S$, such that it vanishes in the absence of interactions. A similar proposal had already been made by Morgenstern, Binder and Hornreich [166] for a random-field Ising model with short-range instead of Coulomb interactions. Davies, Lee and Rice interpreted the finite value of q at low temperatures as an indication of "glassy order".

More recently Xue and Lee [167] carried out Monte Carlo simulations of the Hamiltonian (7.18) with $\phi_i = 0$, but distributing the sites randomly and uniformly over the sample. This model is therefore different from that of Davies, Lee and Rice [156] in the way disorder is introduced. The advantage of this model is that q_{EA} can be used as the glass order parameter instead of its modified version. For this model in two dimensions they found that the transition temperature is zero. Computing dynamical autocorrelation functions $\langle q(t)q(0) \rangle$, they found that there is a typical dynamical crossover to a regime of glassy behavior in which the relaxation times diverge at $T = 0$ following an Arrhenius law $\tau \sim \exp(1/T)$ at low temperatures. This behavior is typical of some supercooled liquids that form glasses and in which the static transition temperature is zero, as happens for example with window glasses or strong glasses [86]. On the other hand Grannan and Yu [168], using the same model with $\phi_i = 0$, studied the critical behavior of the Coulomb glass using finite-size scaling, and in three dimensions they did find a thermodynamic glass transition temperature. Vojta and Schreiber [169], however, criticized the conclusion that in three dimensions there is a true glass transition, arguing that $\phi_i = 0$ is not realistic in the ES model, and that the fact that $q_{EA} > 0$ actually indicates precisely that there is no spin-glass-type transition in this system. The existence of a static, thermodynamic transition in the Coulomb glass is therefore a controversial issue. However, all authors agree that at low temperatures the system should display glassy dynamical behavior, with slow relaxation and memory effects. Despite this, there were practically no theoretical works aimed at analyzing this slow non-equilibrium dynamics. This is partly because clear experiments on the subject appeared only very recently. On the other hand, the interest in achieving a good unification of concepts for the general characterization of slow non-equilibrium dynamics in glasses is also recent [86]. Recently Ovadyahu's group in Israel showed, with various techniques, that at low temperatures the electron system clearly displays "glassy" non-equilibrium dynamics on observation scales of many hours, with interesting regularities. If we do not want to miss the physics of this system on such a macroscopically relevant observation scale, we believe we have no choice but to analyze its non-equilibrium physics.

7.3 Motivation

7.3.1 Slow non-equilibrium dynamics... of electrons?

Evidence of non-ergodic behavior in electronic systems was recently observed in field effect experiments in the Anderson localization regime in crystalline and amorphous indium oxide films, and in granular gold and lead films [150–154]. Figure 7.2 schematically shows the typical MOSFET configuration used for the measurements. We will mention here the results of two types of experiment. One is the "two dip experiment" (TDE) and the other the "aging experiment" (AE). The TDE and the AE are motivated by two generic features of charge transport in the hopping regime [170]: (i) Exciting the Anderson insulator from its thermal equilibrium state always increases its conductance with respect to the equilibrium value; (ii) The relaxation of the excited electronic state to the equilibrium state can be a slow and non-ergodic process [171].

In the TDE the sample is cooled to the measurement temperature while keeping $V_g = V_{g0}$ for many hours. Then fast (4 min long) and sporadic sweeps of V_g around V_{g0} are performed, recording the non-equilibrium conductance traces $G(V_g)$. In these sweeps a large number of carriers are rapidly added to or removed from the sample. It is well known that the conductance in the VRH regime is a local minimum in the thermal equilibrium state, and therefore any excitation has the effect of increasing it [170]. This fact is used in the TDE, where the non-equilibrium traces of $G(V_g)$ show a pronounced minimum or cusp at the value $V_g = V_{g0}$ at which the sample was cooled and equilibrated. To study the slow relaxation, the value of V_{g0} is then changed to V_{g1} and fast sweeps are again performed to obtain the $G(V_g)$ traces. It is then that the glassy behavior of the system becomes evident: $G(V_g)$ develops another minimum at V_{g1} that develops very slowly, while the old minimum at V_{g0} also disappears very slowly. This process of destruction of one minimum and construction of another takes more than 20 hours of measurement. This is very interesting, since electron dynamics has traditionally always been considered very fast. For intermediate times two minima are observed: one that "remembers" the old parameters and another that gradually recognizes the new ones. The characteristic time, defined by the instant at which both minima have the same depth, depends on disorder, magnetic field and carrier concentration, which leads one to associate this phenomenon with a complex competition between electron–electron interactions and disorder.

In the AE the system is cooled at a given gate potential V_{g0} and allowed to equilibrate for many hours, until the conductance is stationary at a value taken as a reference. The gate potential is then abruptly changed to the value V_{gn} and kept at this value for a time t_w. Finally the gate potential is returned to its original value V_{g0} and the excess conductance $\Delta G(t)$ is monitored. The relaxation of $\Delta G(t)$ to zero is very slow, almost logarithmic, and depends on the measurement temperature T_m, on the change of gate potential $\Delta V_g = V_{gn} - V_{g0}$, and on the waiting time t_w. The most notable dependence is on t_w: plotting $\Delta G(t, t_w)$ for several t_w as a function of t/t_w, all the curves collapse onto one. This dependence on t_w, $\Delta G(t, t_w) \sim \Delta G(t/t_w)$, is typical of the non-equilibrium relaxation of many glasses, and is known as *simple aging*. On the other hand, the observed dependence on ΔV_g simply changes the scale of ΔG but not the time scale. A very

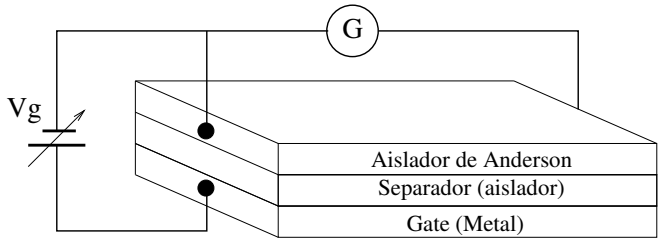


Figure 7.2: Basic sketch of the MOSFET-type experimental configuration used to study the conductance G of the Anderson insulator (labels: *Aislador de Anderson* = Anderson insulator, *Separador (aislador)* = spacer (insulator)). V_g controls the density of charge carriers in the sample studied.

intriguing issue, which we will analyze in relation to our work, is that in these experiments no dependence of aging on temperature was observed over the temperature range analyzed.

From the theoretical point of view there were only two works aimed at explaining the aging and slow relaxation effects mentioned. Both focused on the dynamics of formation of the Coulomb gap, starting from different approximations to the master equation that governs the dynamics of the one-particle density of states [172, 173]. Although with some quantitative differences, both works predict that the formation of the Coulomb gap is logarithmically slow. However, they do not unambiguously explain the slow relaxation or the aging phenomena observed in the conductance. This is because in principle the relation between the conductance and the density of states in a non-equilibrium situation is not known, and even in equilibrium, when the relation is known, it is not only the density of states near the Fermi level that determines the conductance, but also the mobility of the carriers. Until the mobility or diffusivity of electrons out of equilibrium is adequately analyzed, the slow formation of the Coulomb gap is not unambiguous evidence of the slow relaxation of the conductance.

7.3.2 Analogy between the electron glass and the vortex glass

We will briefly describe here the relation between the electron glass and the vortex Bose glass. The use of columnar defects, produced by heavy-ion irradiation of type II superconducting materials [174], has proven very efficient for pinning vortex lines. A theory for the vortex phase in the presence of these correlated defects was developed by Nelson and Vinokur [19], exploiting a formal mapping between the classical statistical mechanics of directed elastic lines in three dimensions at finite temperature and the quantum statistical mechanics of interacting bosons in two dimensions at zero temperature. In this theory the repulsive interaction between vortices, whose range is determined by the London penetration depth λ, was treated approximately, using order-of-magnitude estimates. However, if $\lambda \geq a_0$, where $a_0 = (4/3)^{1/4}(\Phi_0/B)^{1/2}$ is the mean distance between vortices, the interaction becomes strong and can give rise to important correlation effects, even when the structure of the vortex lattice is disordered. A central concept for studying these correlation effects is the distribution of pinning energies $g(\epsilon)$. The analogy between vortex lines pinned on

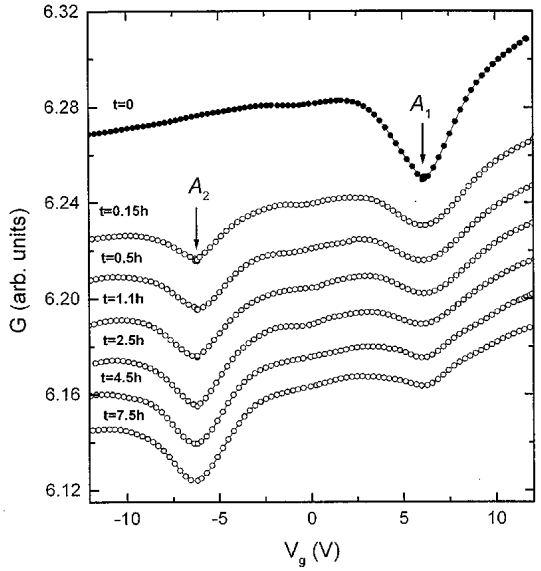


Figure 7.3: Two-dip experiment in an Anderson insulator. The right dip (A_1) occurs at the value of V_g at which the sample was cooled, and decays in time. The left dip (A_2) occurs at the value of V_g to which the gate is switched at $t = 0$, and grows with time.

columnar defects and charge carriers localized in doped semiconductors is then evident. When $\lambda \gg a_0$ the repulsive potential between vortices becomes logarithmic, replacing the $1/r$ Coulomb interaction between electrons or holes in the semiconductor. The analogy then suggests the appearance in $g(\epsilon)$ of a gap similar to the "Coulomb gap" discussed above. Since the existence of such a gap would in principle affect the current–voltage characteristics in the VRH regime of the Bose glass, it is very important to know its size or shape.

Täuber *et al.* [157] investigated the shape of $g(\epsilon)$ by combining experimental results of magnetic decorations, in which the positions of the vortices and of the columnar defects can be determined simultaneously, with Monte Carlo simulations to estimate the distribution of pinning energies compatible with the experimentally observed configuration. The free-energy model F they considered for N flux lines at positions $\mathbf{r}_i(z)$, with the magnetic field $\mathbf{B}$ aligned with the z axis, is

$$F = \int_0^L dz \sum_{i=1}^{N} \left\{ \frac{\tilde{\epsilon}_1}{2} \left(\frac{d\mathbf{r}_i(z)}{dz} \right)^2 + \frac{1}{2} \sum_{j \neq i}^{N} V[r_{ij}(z)] + \sum_{k=1}^{N_D} V_D[\mathbf{r}_i(z) - \mathbf{R}_k] \right\} \tag{7.19}$$

where $r_{ij}(z) = |\mathbf{r}_i(z) - \mathbf{r}_j(z)|$ and $V(r) = 2\epsilon_0 K_0(r/\lambda)$ is the repulsive interaction potential between lines. λ then defines the range of the interaction. The energy scale is $\epsilon_0 = (\phi_0/4\pi\lambda)^2$ and $\tilde{\epsilon}_1$ is the "tilt" modulus. The pinning energy is a sum of N_D z-independent potential wells, with mean separation d, centered at the positions $\{\mathbf{R}_k\}$, and whose diameters are typically $c_0 \approx 100$ Å, with a dispersion $\delta c_k/c_0 \approx 15\%$, caused by the dispersion of the ion beam. This introduces a distribution of pinning energies U_k. In the boson analogy [19] the real temperature T plays the role of $\hbar$ in the quantum problem, and

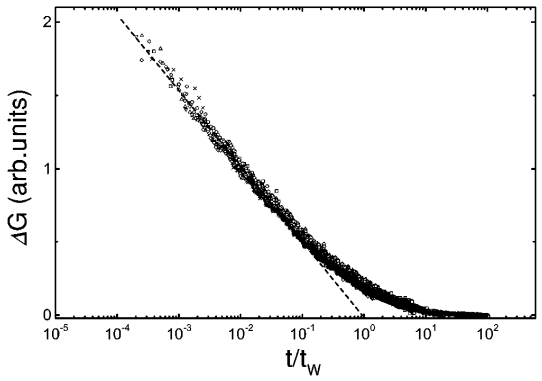


Figure 7.4: $\Delta G(t, t_w)$ vs. t/t_w measured in different samples, during an aging experiment after V_g was returned to its original value V_{g0}. The curves for different t_w in the same sample were averaged. The relaxation of the excess conductance is logarithmic and displays simple aging.

the boson electric field and current density map onto the supercurrent density J and the true electric field E. At very low temperatures and for filling fractions $f = N/N_D = (d/a_0)^2 < 1$, in the Bose glass phase, most vortices are pinned. For $T < T_1$, where T_1 is a characteristic temperature ($T_1 \approx 0.9T_c$ in BSCCO), one reaches the corresponding classical limit of the bosonic problem, $\hbar \to 0$. Since the vortices are well separated, Bose statistics becomes irrelevant. In this limit the vortex lines are essentially straight and the tilt energy $\tilde{\epsilon}_1$ of Eq. (7.19) can be neglected. The ground state is then obtained by minimizing an effective, z-independent, two-dimensional Hamiltonian,

$$H = \frac{1}{2}\sum_{i\neq j}^{N_D} n_i n_j V(r_{ij}) + \sum_{i=1}^{N_D} n_i t_i \tag{7.20}$$

where $i, j = 1, \ldots, N_D$ label the defects randomly distributed in the sample. $n_i = 0, 1$ is the corresponding occupation of site i and t_i are the random site energies originating from the dispersion of pinning diameters. This can be assumed to be uniformly distributed, $P(t_i) = 1/2w$, over a width w ($P(t_i) = 0$ if $|t_i| > w$). The Hamiltonian (7.20) then has the same form as the Hamiltonian (7.23) for electrons localized in a doped semiconductor. From the ground state given by (7.20), the distribution of pinning energies $\epsilon_i = \partial H/\partial n_i = \sum_{j\neq i}^{N_D} n_j V(r_{ij}) + t_i$ can be computed. The distribution function $g(\epsilon)$ is then the equivalent of the one-particle density of states in doped semiconductors. In the work of Täuber *et al.* [157] realistic parameters were used for λ and w was adjusted so that the structure of the ground state of (7.20) corresponds to that observed experimentally in the Bitter magnetic decoration picture. In this way they found a *gap* in $g(\epsilon)$ well described by the formula

$$g(\epsilon) \propto |\epsilon - \mu|^{s_{eff}} \tag{7.21}$$

in the vicinity of μ, with effective gap exponent $s_{eff} \approx 1.2$, see Fig. 7.5. In later work they found that for $\lambda \to \infty$ a value $s_{eff} \approx 3$ can be reached [175].

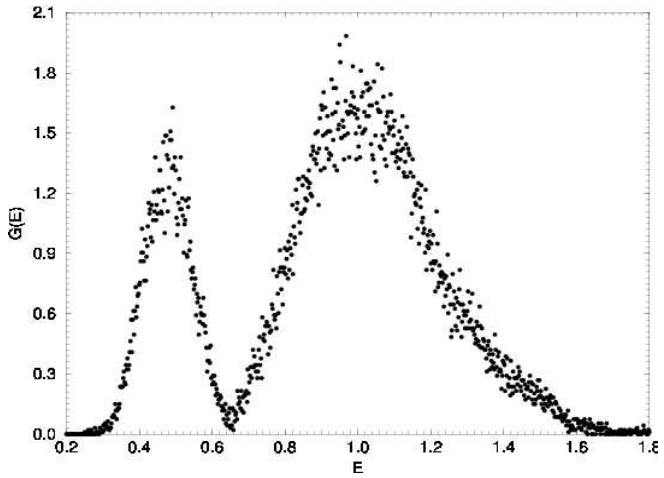


Figure 7.5: Normalized distribution of pinning energies $G(E) = 2\epsilon_0 d^2 g(\epsilon)$ obtained in reference [157] as a function of the site energies $E = \epsilon/2\epsilon_0$. The curve obtained is analogous to the one-particle density of states in the electron glass in an Anderson insulator. The corresponding "Coulomb gap" is observed around the mean chemical potential $\mu/2\epsilon_0 = 0.65$.

To extract the consequences, for vortex transport, of the correlations revealed in $g(\epsilon)$ (if there were no correlations $g(\epsilon)$ would be constant), they analyzed the excitations that contribute to VRH. The most important excitation is that of sending a pair of superkinks, separated by a distance Z, to another columnar defect at a distance R, such that the tunneling probability is optimal, see Fig. 7.6. The energy of the superkink pair is $\delta F_{SK} = 2E_K R/d + Z\Delta(R) - f_L RZ$ [19]. The first term is the elastic energy of the double kink, with $E_K = \sqrt{\tilde{\epsilon}_1 U_0} d$, and the third the work of the Lorentz force $f_L = \Phi_0 J/c$ induced by the current J. The second term comes from the fact that the energies available for a jump at a distance R fall in the interval $[\mu, \mu + \Delta(R)]$, where $\Delta(R)$ is determined from $\int_\mu^{\mu+\Delta} g(\epsilon) d\epsilon = R^{-2}$. Minimizing first δF_{SK} for $J = 0$ gives the double-kink length $Z^* = -2E_K/d(\partial\Delta/\partial R)_{R^*}$. Then, to first order in J, one finds that $J\Phi_0/c = \Delta(R^*)/R^*$, and therefore the optimized energy is $\delta F^* = 2E_K R^*(J)/d$. This is the energy barrier for thermal activation that determines the resistivity, $E = \rho_0 J \exp(-\delta F^*/k_B T)$. In the regime where Eq. (7.21) holds we obtain

$$E \approx \rho_0 J \exp[-(2E_K/k_B T)(J_0/J)^p] \tag{7.22}$$

where p is an exponent that generalizes the Mott exponent $p_0 = 1/3$, valid when there are no interactions. In Fig. 7.7 we can appreciate the difference between the interacting and the non-interacting case by comparing $R^*(J)/d$ vs. J (which is proportional to the energy barrier δF^* in each case). For long-range interactions producing the Coulomb gap (7.21) we have $p = (s+1)/(s+3) = 0.68$, a value corresponding to the limit $\lambda \to \infty$. Since λ/d is finite, p_{eff} is not universal. However, in [157] it was found that the law fits the results obtained well with $p_{eff} \approx 0.5$. There is therefore an increase in the resistivity due to the correlations induced by the repulsion even for $\lambda \sim a_0$. Comparing the derivation given here for the resistivity due to vortices with that of the conductivity due to electrons

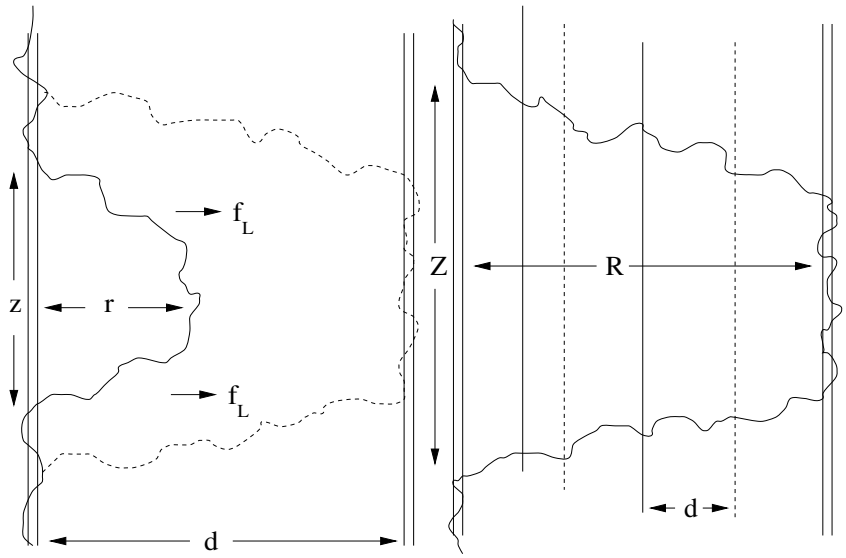


Figure 7.6: Left: two columnar defects at a distance d with a "half-loop" excitation (solid line) and a double-kink excitation (dashed line). The Lorentz force tends to push the vortices to the right. Right: double superkink configuration, required by variable-range hopping. The excitations seek a low-energy columnar defect, not necessarily an adjacent one, at a distance R.

localized in a semiconductor, we see that although both rest on Mott's VRH argument, the hopping processes are very different. In the case of electrons, thermally assisted hopping depends, besides the temperature, on the distance of the jump. This is because the finite localization length penalizes jumps between states localized on sites with little overlap of the respective wave functions (Fermi's golden rule). Taking into account the density of states $g(\epsilon)$ corrected by correlations, the optimization gives rise to a non-trivial temperature dependence of the conductivity, different from Mott's, but in which the current–voltage curve remains linear for small electric fields. This is because dissipation-free tunneling is considered, and therefore the work of the electric field on the electron does not appear in the energy balance. In the Bose glass, instead, the optimization of the hopping process of superkink pairs importantly involves the work of the Lorentz force. This makes VRH give rise, in both the interacting and the non-interacting case, to a non-ohmic current–voltage curve at small currents[1]. The effect of correlations shows up in this case in the change of the current dependence of the non-linear current–voltage curve at small currents.

An important motivation for the work presented in this chapter is to continue exploiting the analogy of the Coulomb glass with the vortex Bose glass as regards the slow non-equilibrium dynamics. Since both systems share a very similar physics in which interactions and disorder compete, and correlation effects are observable, one would expect the vortex system also to display slow relaxation and aging effects like those described in the previous

[1]Strictly speaking this is valid only in the thermodynamic limit, with infinitely wide samples. If the width L is finite there will be a crossover at a current j_L such that for $j < j_L$ the current–voltage curve recovers linearity [14].

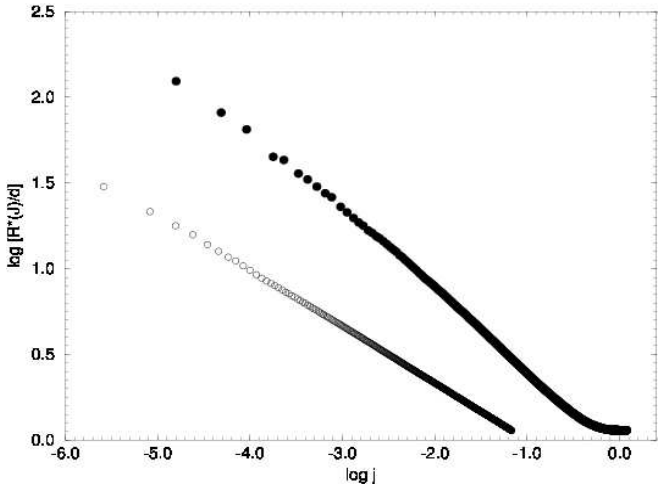


Figure 7.7: Comparison of $R^*(J)/d$ vs. $j = J\phi_0 d/2\epsilon_0 c$ obtained in reference [157] with the density of states $g(\epsilon)$ of Fig. 7.5 (filled circles), with the one corresponding to the non-interacting case (open circles).

section for Anderson insulators.

7.4 Model and method

To study the relaxation dynamics of the Coulomb glass we consider the following dimensionless Hamiltonian,

$$H = \sum_i n_i \tilde{\phi}_i + \sum_{i>j} \frac{(n_i - K)(n_j - K)}{r_{ij}} \tag{7.23}$$

with $K = 1/2$, sites distributed randomly and uniformly, and the ϕ_i uniformly distributed in the interval $[-W_0, W_0]$. We take $e^2/\kappa a$ as the unit of energy and the Anderson localization radius a as the unit of length. We use the kinetic Monte Carlo method for N sites randomly distributed in a sample of size $L \times L$ in two dimensions with periodic boundary conditions, for a fixed number of electrons $N_e = N/2$. The Coulomb interaction due to all periodic images is evaluated exactly using a Lekner sum [176]. An electron on a site i can only jump to an empty site j, $n_j = 0$. If the site is empty, the jump is accepted with probability $\exp(-2r_{ij} - \epsilon_{ij}/T)$, where $r_{ij} = |\mathbf{r}_i - \mathbf{r}_j|$ is the distance between sites, ϵ_{ij} the total energy change of the system due to the jump, and T the temperature. The first term of the exponential comes from using Fermi's golden rule and represents the overlap of the wave functions localized on sites i and j. The second simply represents the Metropolis algorithm. Other, more approximate models have been considered in the literature: (i) with the sites on a regular, square or triangular lattice, and random site energies [156, 161], and (ii) with the sites at random positions but without random site energies [167, 168]. In both cases it is argued that the exact nature of the disorder is not essential for studying the equilibrium states. For the dynamics, instead, we believe that the exact nature of the disorder may be important, since relaxation involves correlated

transitions of many electrons between different configurations, where there is a whole sensitive hierarchy of constraints that can determine its form and speed. We also note that if one wanted to study only the equilibrium states (even though these are difficult to reach, even experimentally), it is pointless to use the transition probability $\exp(-2r_{ij} - \epsilon_{ij}/T)$, since the equilibrium state is independent of the relaxation dynamics. If one is interested only in the equilibrium states and not in the relaxation dynamics, it is convenient to simply take $\exp(-\epsilon_{ij})$ as the transition probability and to propose exchanges of electrons at arbitrarily large distances. However, to study the relaxation dynamics, as with the nature of the disorder, it is important to retain a realistic form for this probability.

The one-particle density of states is computed by building a histogram of the site energies $\epsilon_i = \phi_i + \sum_j (n_j - 1/2)/r_{ij}$ over the whole sample. To study the relaxation, the system is first prepared in an initial condition corresponding to a very high temperature, occupying N_e sites at random. A given temperature T is then set and the system is allowed to evolve during a waiting time t_w, after which the following temporal correlation function starts to be recorded,

$$C(t, t_w) = \left\langle \frac{1}{N_e} \sum_i^N n_i(t_w) n_i(t) \right\rangle \tag{7.24}$$

where t is the time elapsed since the waiting time t_w and $\langle \ldots \rangle$ means averaged over disorder realizations (site positions). The correlation function (7.24) is computed for different temperatures T and different waiting times t_w. When the system reaches the thermal equilibrium state or reaches a steady state, we will have $C(t, t_w) \equiv \tilde{C}(t)$, independent of t_w. This certainly happens when $t_w \to \infty$, since the equilibration time of a finite system is always finite. In particular, the limit $\lim_{t\to\infty} \lim_{t_w\to\infty} C(t, t_w) = q_{EA}$, where q_{EA} is the Edwards–Anderson parameter. If $W_0 = 0$ we will have $q_{EA} = 0$ at high temperatures, and if there were a spin-glass-type transition in the system we would have $q_{EA} > 0$ at sufficiently low temperatures, indicating the "freezing" of the disordered structure. If there are aging or non-stationarity effects, instead, there will be a dependence of the function $C(t, t_w)$ on t_w. Although the detailed form of $C(t, t_w)$ depends on the model in question, in glasses it is usual to find, for sufficiently large t_w, a separation of time scales: (i) a short time scale $t \ll t_w$, where $C(t, t_w) \sim \tilde{C}(t)$, which describes the fast relaxation of the system within a bounded domain of the phase space accessible to the system, and (ii) a long time scale $t \gtrsim t_w$, where $C(t, t_w)$ depends on t_w, describing the slow evolution dynamics of the domain just mentioned. We will later analyze and discuss, in relation to our results, the details of this separation of scales.

7.5 Results

In this chapter we will show only the preliminary results (not yet published) of Monte Carlo simulations obtained for a two-dimensional system of size $16a \times 16a$, $N = 256$ sites, $N_e = 128$ electrons and $W_0 = 0$. The averages were taken over 24 to 120 disorder realizations. Simulations for larger systems, with averages over a larger number of disorder realizations, in two and also in three dimensions, and with $W_0 \neq 0$, are being carried out while I write this thesis. The results will be included in a future publication.

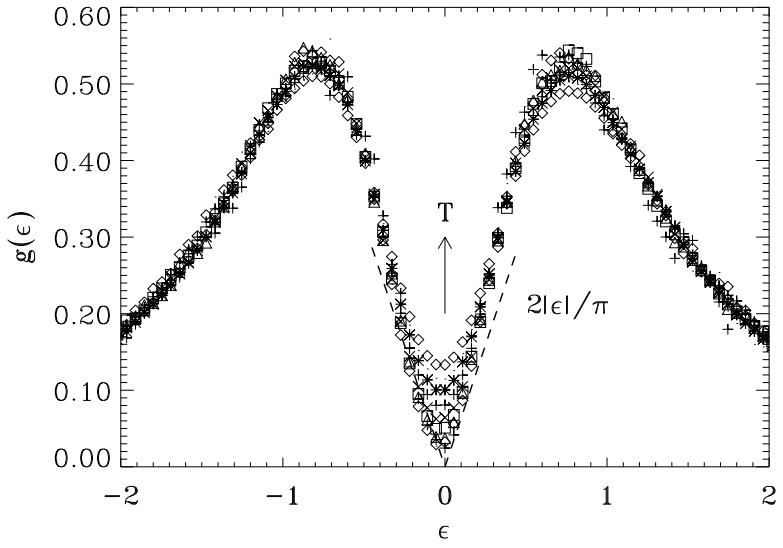


Figure 7.8: One-particle density of states in the Coulomb glass model in two dimensions, for temperatures in the range $0.01 \leq T \leq 0.1$. The dip around $\epsilon = 0$ is the so-called Coulomb gap, a result of the correlations between localized electrons due to their long-range interaction. The dashed line is the theoretical prediction for the density of states of the ground state at $T = 0$ in the vicinity of the Fermi level $\mu = 0$.

7.5.1 One-particle density of states

In Fig. 7.8 we show the one-particle density of states $g(\epsilon)$ for temperatures $T = 0.1$, 0.2, 0.3, 0.4, 0.5, 0.6, 0.7, 0.8, 0.9, 1.0, averaged over 24 disorder realizations. Since we could not appreciate a time dependence of $g(\epsilon, t, T)$ [173], we define $g(\epsilon)$ as the apparently asymptotic and stationary value of $g(\epsilon, t)$. We see that for the temperature range considered the Coulomb gap is well developed and that $g(0) \to 0$ when $T \to 0$. At low temperatures we find $g(\epsilon) \approx 2|\epsilon|/\pi$ for $\epsilon \ll 1$, in agreement with Baranovskii's prediction for $g(\epsilon)$ using the self-consistent equation method for $T = 0$ [177].

7.5.2 Two-time correlation function

To characterize the relaxation and aging effects it is convenient to use the two-time correlation function of Eq. (7.24).

On the left of Fig. 7.9 we show $C(t, t_w)$ vs. t averaged over 120 disorder realizations for three temperatures $T = 0.01$, 0.05, 0.1 and for $t_w = 10^2$, 10^3, 10^4, 10^5 Monte Carlo steps. The curve of Fig. 7.9(a) for $T = 0.01$ has the typical relaxation shape found in many spin glasses at low temperatures. For times $t < t_w$, $C(t, t_w)$ is practically independent of t_w and first relaxes to a more or less well-defined *plateau*. The value of $C(t, t_w)$ on this plateau corresponds approximately to the Edwards–Anderson parameter $q_{EA} \equiv \lim_{t\to\infty} \lim_{t_w\to\infty} C(t, t_w)$ of this system. For $t \sim t_w$, approximately, the correlation function starts to decay logarithmically from its plateau value. The separation of the curves for different t_w at $t > t_w$ indicates that the system displays aging at long times,

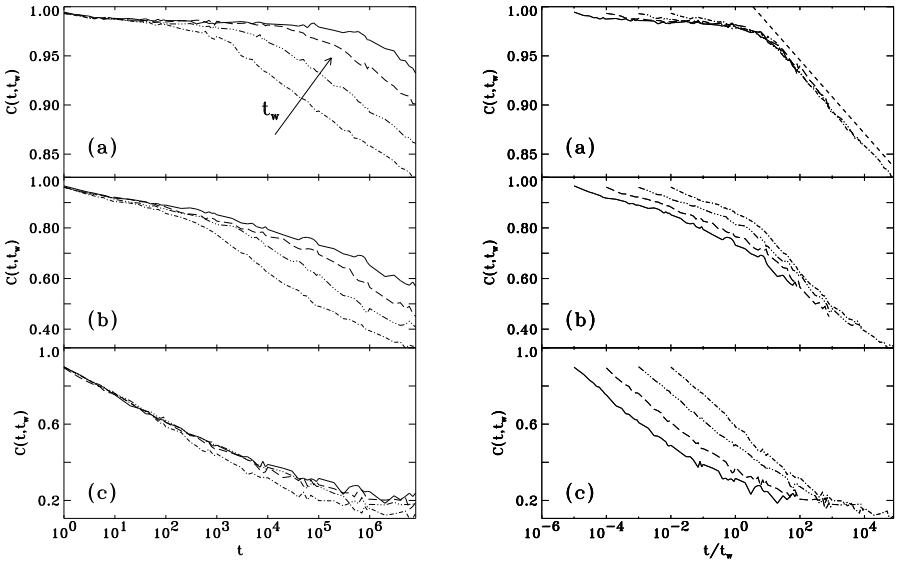


Figure 7.9: Correlation functions $C(t, t_w)$ for $t_w = 10^2$, 10^3, 10^4, 10^5. (a) $T = 0.01$, (b) $T = 0.05$, (c) $T = 0.10$. Left: $C(t, t_w)$ vs. t. Right: $C(t, t_w)$ vs. t/t_w. The dashed line in panel (a) on the right indicates the logarithmic relaxation at long times.

t_w being the only characteristic time of the system. The larger t_w, the longer the system remains on the plateau with $C(t, t_w) \sim q_{EA}$. As we can see in Figs. 7.9(b) for $T = 0.05$ and 7.9(c) for $T = 0.10$, the aging effects decrease with increasing temperature, and already for $T = 0.1$ they have practically disappeared. We also see that the plateau observed at low temperatures becomes blurred. It is interesting to note that in the experiments logarithmic relaxation is also observed in the conductance [154], as we indicate in Fig. 7.9(a) on the right.

On the right of Fig. 7.9 we show the same correlation functions as on the left of Fig. 7.9 but as a function of t/t_w instead of t. In Fig. 7.9(a) on the right we see that at low temperatures the different $C(t, t_w)$ collapse onto a single curve for $t > t_w$. Therefore the system displays the so-called *simple aging*, like that observed experimentally in the conductance [153]. In Fig. 7.9(b) on the right we see that there is no collapse of the correlation functions for different t_w, although the system still displays aging, as we can see in 7.9(b) on the left. This indicates that there is a crossover from simple-aging behavior to behavior without aging upon increasing the temperature. The interesting possibility remains open that, even if there is no static (spin-glass-type) phase transition in this system [167–169, 178], there is a dynamical phase transition in the thermodynamic limit. To settle this question it is necessary to analyze whether the relaxation times diverge at a given temperature. According to the dynamical scaling ansatz, the autocorrelation function near a second-order transition has the form

$$C(t_w = \infty, t) \sim t^{-\lambda} f(t/\tau) \tag{7.25}$$

where τ is the relaxation time at a given temperature and λ a critical exponent. This form represents a crossover around τ from a short-time critical behavior $t^{-\lambda}$ to a long-time

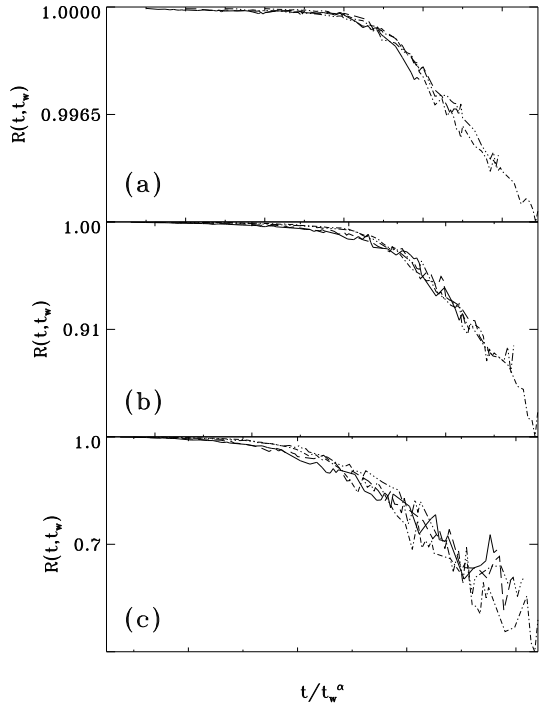


Figure 7.10: Modified correlation functions $R(t, t_w)$ vs. t/t_w^α for $t_w = 10^2$, 10^3, 10^4, 10^5. (a) $T = 0.01$, (b) $T = 0.05$, (c) $T = 0.10$.

relaxation described by $f(t/\tau)$. When the temperature approaches the critical point T_c, the relaxation time diverges as $\tau \sim |T - T_c|^{-z\nu}$. One could therefore try to compute τ near the transition. The problem is that the dynamics is extremely slow and that the relaxation time depends sensitively on the long-time tail of the autocorrelation function. To avoid these and other difficulties, and at the same time study the aging problem, Matsumoto *et al.* [179] extended a method devised by Bhatt and Young [180], proposing to analyze the following dimensionless correlation function

$$R(t_w, t) = \frac{C(t_w, t)}{\sqrt{\left\langle \left(\frac{1}{N_e} \sum_i^N n_i(t_w) n_i(t) \right)^2 \right\rangle}} \tag{7.26}$$

The nice thing about this expression is that the prefactor $t^{-\lambda}$ of Eq. (7.25) is canceled, and therefore we can define the time τ well from $R(t, t_w) \sim \tilde{R}(t/\tau(t, t_w))$. The characteristic equilibrium relaxation time would be $\tau_0(T, L) = \lim_{t_w \to \infty} \tau(t, t_w; T, L)$. We will assume a dependence $\tau(t, t_w)^{-1} \sim \tau_0^{-1} + t_w^{-\alpha}$, where $\alpha \equiv \alpha(T, L)$ is an exponent characterizing aging. This assumption is based on the fact that if the equilibrium relaxation time is too large, $\tau_0 \gg t_w$, the system is always out of equilibrium, t_w being the only characteristic time, while if $t_w \gg \tau_0$, on the other hand, the system falls into the equilibrium state during the wait t_w. Since the latter is stationary, it loses the dependence on t_w.

We tried to extract τ_0 and α from our data using the function $R(t, t_w)$. Unfortunately we could not extract any good estimate of τ_0, but we concluded that $\tau_0 \gg t_w$ for all the t_w

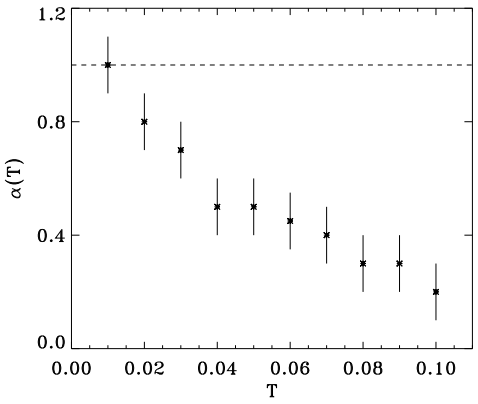


Figure 7.11: Aging exponent α vs. temperature T.

analyzed. For this reason, for practical purposes, we took $\tau_0 = \infty$ and set out to compute $\alpha(T)$ for our sample of size $L = 16$, compatible with our current computational resources and available time. To do this we computed $R(t, t_w)$ for several temperatures and adjusted the value of $\alpha(T)$ so as to optimize the overlap of the different curves $R(t, t_w)$ vs. t/t_w^α. In Fig. 7.10 we show three examples, for $T = 0.01$ (Fig. 7.10(a)), $T = 0.05$ (Fig. 7.10(b)) and $T = 0.10$ (Fig. 7.10(c)). Comparing with $C(t, t_w)$ we see that $R(t, t_w)$ is practically unity for short times $t < t_w$ and then displays a slow logarithmic decay. We see that the curves can be overlapped well for some value of α, which supports our ansatz $\tau \sim t_w^\alpha$. In Fig. 7.11 we show the aging exponent $\alpha(T)$ vs. T. Upon increasing the temperature we see the crossover in α from the simple aging regime $\alpha \sim 1$ at temperatures $T \lesssim 0.01$ to a stationary regime $\alpha \sim 0$ for temperatures $T \gtrsim 0.10$. It would be very interesting to carry out a size analysis of the function $\alpha(T, L)$ in order to analyze, with this same method, whether the observed dynamical crossover represents a possible dynamical transition.

7.6 Discussion and conclusions

We have numerically studied the non-equilibrium relaxation in the Efros–Shklovskii Coulomb glass. Our (preliminary) numerical results show that even for relatively very small systems, at sufficiently low temperatures, the relaxation is extremely slow and non-stationary. Studying two-time autocorrelation functions we found simple aging and logarithmic relaxation of the electronic system. These two features were observed experimentally in the relaxation of the conductance in doped indium oxide semiconductors [150–154]. The Monte Carlo simulations show that, upon increasing the temperature, there is a crossover from the simple aging regime to a stationary one, without aging, in the range $T_0 < T < T_1$, with $T_0 \approx 0.01(e^2/k_B\kappa a)$ and $T_1 \approx 0.1(e^2/k_B\kappa a)$. For semiconductors such as those used in the experiments we have: $a \sim 5$ Å, $\kappa \sim 10$. This gives $(e^2/k_B\kappa a) \sim 10^4$ K as the unit of temperature. The simple aging observed experimentally in the conductance is compatible with our numerical results, since the samples are thermalized at the liquid helium temperature $T = 4.11\,\mathrm{K} \sim 0.001(e^2/k_B\kappa a) < T_0$. The temperature independence

of the simple aging of the conductance, observed experimentally, can be explained by taking into account that the temperature range analyzed corresponds to $T < T_0$, where T_0 is our crossover temperature to the simple aging regime.

Important questions remain open. One is to better understand the mechanisms that make relaxation so slow in this system. In this respect it is necessary to systematically study the dependence of the relaxation on the magnitude and type of disorder, on the type of interaction, on the transition probabilities, on the temperature and on the system size. This would allow us to know which are the minimal ingredients that determine the glassy dynamics. Another very important question, in relation to the interpretation of the experimental results, is to better establish the connection between the observed behavior of the conductance and that of the computed correlation functions, since the relations existing in equilibrium must be revised in non-equilibrium situations. In this respect it becomes necessary to analyze simultaneously autocorrelation functions and response functions during the relaxation. Characterizing the system by its violation of the fluctuation–dissipation theorem opens the interesting possibility of associating an effective temperature with the slowest modes of the relaxation [86].

The analogy between the Efros–Shklovskii model of interacting localized electrons and that of vortices in superconductors with columnar defects in the variable-range-hopping regime ($H_{c1} \ll B < B_\Phi$) makes it plausible that the results of this work are also applicable to superconductors.

We thank Daniel Grempel for the stimulating collaboration during the development of this work.

Chapter 8

General conclusions

We have numerically studied the non-equilibrium steady dynamical regimes of driven vortex lattices in thin superconducting films and in strongly anisotropic layered superconductors. We analyzed the non-equilibrium statistical mechanics and characterized the dynamical phases and transitions through experimentally accessible properties. We also studied the non-equilibrium relaxation dynamics of a system of strongly localized electrons in an Anderson insulator, in relation to the relaxation of the vortex Bose glass in superconductors with columnar defects in the variable-range-hopping regime.

- In thin superconducting films we find that above the critical current F_c there are two dynamical phase transitions at F_p and F_t, which could be observed through simultaneous measurements of the longitudinal voltage and of the transverse or Hall voltage. At F_p there is a transition from a plastic flow regime to a smectic flow regime where the voltage noise is isotropic (Hall noise = longitudinal noise), there is a peak in the differential resistance and the transverse diffusivity is maximal. At F_t there is a sharp transition to a frozen transverse solid where the Hall noise drops abruptly and vortex motion becomes localized in the transverse direction.

- We find mode-locking steps in the current–voltage characteristics when an ac current is applied parallel or perpendicular to the dc current. For low frequencies there is mode-locking above a finite ac amplitude, while for high frequencies there is mode-locking for any small ac force. This is correlated with the nature of the longitudinal and transverse temporal order in the different regimes in the absence of the ac force. The synchronized state is a frozen solid pinned in the center-of-mass reference frame. In the case of longitudinal ac, depinning from the step shows plastic flow and hysteresis. The results obtained show a strong contrast with respect to the case of periodic pinning, due to the very different nature of the temporal order in each case.

- We also studied correlation functions and response functions in vortex lattices driven out of equilibrium over random pinning potentials. From a generalized fluctuation–dissipation relation we computed a transverse effective temperature in the moving fluid phase. We find that the effective temperature decreases with increasing driving force and is approximately equal to the equilibrium melting temperature of the

unpinned system when the dynamical transverse freezing occurs. We also discussed how the effective temperature could be measured experimentally from a generalized Kubo formula.

- We also studied the dynamical regimes in a three-dimensional model of driven vortices in layered superconductors with weakly coupled planes and strong pinning. Above the critical current F_c, we find a plastic flow regime in which pancakes in different planes are decoupled, corresponding to a "pancake gas". At a higher force F, there is a "smectic flow" regime with short-range interlayer order, corresponding to an entangled line liquid. At an even higher force, the transverse displacements freeze and the vortices become correlated along the c axis, resulting in a transverse solid. Finally, at a force F_s the longitudinal displacements freeze and we find a coherent solid of rigid lines.

- We studied the slow non-equilibrium relaxation in disordered systems with strongly localized electronic states by means of Monte Carlo simulations of the Efros–Shklovskii Coulomb glass model. Studying two-time autocorrelation functions $C(t, t_w)$ we find that at sufficiently low temperatures this system falls out of equilibrium and displays simple aging, $C(t, t_w) \sim f(t/t_w)$, where t_w is the waiting time or "age" of the system. Upon increasing the temperature the aging effects disappear and stationarity is recovered. The results obtained agree with recent experiments in doped semiconductors and could also describe the relaxation of the vortex Bose glass in superconductors with columnar defects, in the variable-range-hopping regime, for magnetic fields $H_{c1} \ll B < B_\Phi$, where B_Φ is the matching field.

In conclusion, we have learned several things about disordered systems out of equilibrium. As we have already discussed in the conclusions of each chapter, several questions remain open. And they are of two types. The first type comprises those questions that have to do with supporting the results obtained more strongly: making the same study more extensive, improving the quality of the results, understanding the details, improving the methods. The second type comprises the new questions, those that arose from our results, and those that perhaps generated a new way of thinking about some things. In our view, these new questions are at the same time the most important result of the thesis.

Bibliography

[1] F. London. *Superfluids Vol. 1: Macroscopic Theory of Superconductivity*, Wiley & Sons, New York, 1950.

[2] V. L. Ginzburg and L. D. Landau. Zh. Eksp. Teor. Fiz. **20**, 1064 (1950).

[3] A. A. Abrikosov. Sov. Phys. JETP **5**, 1174 (1957).

[4] Y. Fasano. Licenciatura Thesis in Physics, Instituto Balseiro, 1998.

[5] M. Menghini. PhD Thesis in Physics, Instituto Balseiro, 2003.

[6] V. L. Ginzburg. Sov. Phys. Solid State **2**, 1824 (1961).

[7] P. W. Anderson and Y. B. Kim. Rev. Mod. Phys. **36**, 39 (1964).

[8] A. I. Larkin. Sov. Phys. JETP **31**, 784 (1970).

[9] J. G. Bednorz and K. A. Müller. Z. Phys. B **64**, 189 (1986).

[10] H. Pastoriza *et al.* Phys. Rev. Lett. **72**, 2951 (1994).

[11] E. Zeldov *et al.* Nature (London) **375**, 373 (1995).

[12] A. P. Young. *Spin Glasses and Random Fields*, World Scientific, Singapore, 1998.

[13] D. R. Nelson. Phys. Rev. Lett. **60**, 1973 (1988).

[14] G. Blatter *et al.* Rev. Mod. Phys. **66**, 1125 (1994).

[15] M. P. A. Fisher. Phys. Rev. Lett. **62**, 1415 (1989).

[16] T. Giamarchi and P. Le Doussal. Phys. Rev. Lett. **72**, 1530 (1994).

[17] T. Giamarchi and P. Le Doussal. Phys. Rev. B **52**, 1242 (1995).

[18] D. R. Nelson and V. M. Vinokur. Phys. Rev. Lett. **68**, 2398 (1992).

[19] D. R. Nelson and V. M. Vinokur. Phys. Rev. B **48**, 13060 (1993).

[20] C. J. Gorter. Physica **23**, 45 (1957).

[21] C. J. Gorter. Phys. Lett. **1**, 69 (1962).

[22] P. W. Anderson. Phys. Rev. Lett. **9**, 309 (1962).

[23] Y. B. Kim *et al.* Phys. Rev. Lett. **12**, 145 (1964).

[24] A. Schmid and W. Hauger. J. Low Temp. Phys. **11**, 667 (1973).

[25] A. I. Larkin and Yu. N. Ovchinnikov. Zh. Eksp. Teor. Fiz. **65**, 1704 (1973) [Sov. Phys. JETP **38**, 854 (1974)].

[26] A. T. Fiory. Phys. Rev. Lett. **27**, 501 (1971).

[27] S. Bhattacharya and M. J. Higgins. Phys. Rev. Lett. **70**, 2617 (1993).

[28] R. Thorel *et al.* J. Phys. (Paris) **34**, 447 (1973).

[29] A. E. Koshelev and V. M. Vinokur. Phys. Rev. Lett. **73**, 3580 (1994).

[30] P. Le Doussal and T. Giamarchi. Phys. Rev. B **57**, 11356 (1998).

[31] L. Balents, M. C. Marchetti and L. Radzihovsky. Phys. Rev. B **57**, 7705 (1998).

[32] S. Scheidl and V. M. Vinokur. Phys. Rev. E **57**, 2574 (1998).

[33] M. Tinkham. *Introduction to Superconductivity*, McGraw-Hill, second edition, 1996.

[34] R. P. Huebener. *Magnetic Flux Structures in Superconductors*, Springer, second edition, 2001.

[35] T. Nattermann and S. Scheidl. Adv. Phys. **49**, 607 (2000).

[36] W. E. Lawrence and S. Doniach. In *Proc. 12th Int. Conf. Low Temp. Phys.*, E. Kanda (ed.), Kyoto, 1970, p. 361.

[37] L. Bulaevskii, M. Ledvij and V. G. Kogan. Phys. Rev. B **46**, 11807 (1992).

[38] J. R. Clem. Phys. Rev. B **43**, 7837 (1991).

[39] J. Pearl. Appl. Phys. Lett. **5**, 65 (1964).

[40] P. M. Chaikin and T. C. Lubensky. *Principles of Condensed Matter Physics*, Cambridge University Press, 1995.

[41] M. C. Hellerqvist *et al.* Phys. Rev. Lett. **76**, 4022 (1996).

[42] S. Ryu and D. Stroud. Phys. Rev. B **54**, 1320 (1996).

[43] N. K. Wilkin and H. J. Jensen. Phys. Rev. Lett. **79**, 4254 (1997).

[44] A. van Otterlo, R. T. Scalettar, and G. T. Zimányi. Phys. Rev. Lett. **81**, 1497 (1998).

[45] D. Domínguez, N. Grønbech-Jensen and A. R. Bishop. Phys. Rev. Lett. **78**, 2644 (1997).

[46] A. B. Kolton, D. Domínguez, N. Grønbech-Jensen. Physica C **341–348**, 1007 (2000).

[47] D. Reefman and H. B. Brom. Physica C **213**, 229 (1993).

[48] S. R. A. Salinas and C. Tsallis. Brazilian Journal of Physics **29**, 1 (1999).

[49] T. Giamarchi and S. Bhattacharya. arXiv:cond-mat/0111052 (2001).

[50] P. Chauve, T. Giamarchi, and P. Le Doussal. Phys. Rev. B **62**, 6241 (2000).

[51] N. Grønbech-Jensen, A. R. Bishop and D. Domínguez. Phys. Rev. Lett. **76**, 2985 (1996).

[52] F. Pardo, F. de la Cruz, P. L. Gammel, E. Bucher, and D. J. Bishop. Nature (London) **396**, 348 (1998).

[53] A. M. Troyanovski *et al.* Nature (London) **399**, 665 (1999).

[54] T. Giamarchi and P. Le Doussal. Phys. Rev. Lett. **76**, 3408 (1996).

[55] V. I. Marconi. PhD Thesis in Physics, Instituto Balseiro, 2002.

[56] M. C. Faleski *et al.* Phys. Rev. B **54**, 12427 (1996).

[57] S. Spencer and H. J. Jensen. Phys. Rev. B **55**, 8473 (1997).

[58] I. S. Aranson, S. Scheidl and V. M. Vinokur. Phys. Rev. B **58**, 14541 (1998).

[59] H. J. Jensen, A. Brass, and A. J. Berlinsky. Phys. Rev. Lett. **60**, 1676 (1988).

[60] A.-C. Shi and A. J. Berlinsky. Phys. Rev. Lett. **67**, 1926 (1991).

[61] A. E. Koshelev. Physica C **198**, 371 (1992).

[62] C. Reichhardt *et al.* Phys. Rev. Lett. **78**, 2648 (1997).

[63] C. J. Olson, C. Reichhardt and F. Nori. Phys. Rev. Lett. **80**, 2197 (1998).

[64] T. Giamarchi and P. Le Doussal. Phys. Rev. Lett. **76**, 3408 (1996).

[65] S. Scheidl and V. M. Vinokur. Phys. Rev. B **57**, 13800 (1998).

[66] S. Scheidl and V. M. Vinokur. Phys. Rev. B **56**, R8522 (1997).

[67] S. Bhattacharya and M. J. Higgins. Phys. Rev. B **52**, 64 (1995).

[68] M. J. Higgins and S. Bhattacharya. Physica C (Amsterdam) **257**, 232 (1996).

[69] U. Yaron *et al.* Nature (London) **376**, 743 (1995).

[70] K. Moon, R. T. Scalettar and G. Zimányi. Phys. Rev. Lett. **77**, 2778 (1996).

[71] C. J. Olson, C. Reichhardt and F. Nori. Phys. Rev. Lett. **81**, 3757 (1998).

[72] D. Domínguez. Phys. Rev. Lett. **82**, 181 (1999).

[73] I. Aranson, A. Koshelev and V. Vinokur. Phys. Rev. B **56**, 5136 (1997).

[74] N. Grønbech-Jensen. Int. J. Mod. Phys. C **7**, 873 (1996).

[75] W. J. Yeh and Y. H. Kao. Phys. Rev. B **44**, 360 (1991).

[76] A. C. Marley *et al.* Phys. Rev. Lett. **74**, 3029 (1995).

[77] R. D. Merithew *et al.* Phys. Rev. Lett. **77**, 3197 (1996).

[78] M. W. Rabin *et al.* Phys. Rev. B **57**, R720 (1998).

[79] T. Tsuboi *et al.* Phys. Rev. Lett. **80**, 4550 (1998).

[80] *Tessellated*: from the Latin *tessellatus*, an adjective meaning "made of tesserae". *Tessera*: from the Latin *tessella*, "each of the cubic pieces of marble, stone, baked clay or any other material with which the ancients made mosaic pavements". Source: *Diccionario de la Real Academia Española*, 19th edition.

[81] N. Grønbech-Jensen *et al.* Phys. Rev. B **46**, 11149 (1992).

[82] J.-P. Bouchaud and A. Georges. Physics Reports **195**, 127 (1990).

[83] G. Matheron and G. de Marsily. Water Resour. Res. **16**, 901 (1980).

[84] M. C. Marchetti *et al.* arXiv:cond-mat/0302275v1 (2003).

[85] See http://cabtes55.cnea.gov.ar/miembros/koltona.

[86] L. Cugliandolo. Lecture notes, Les Houches, arXiv:cond-mat/0210312 (2002).

[87] H. Fangohr, S. J. Cox, and P. A. J. de Groot. Phys. Rev. B **64**, 064501 (2001).

[88] K. Saunders and M. C. Marchetti. Phys. Rev. B **66**, 224113 (2002).

[89] L. Cugliandolo, J. Kurchan, and L. Peliti. Phys. Rev. E **55**, 3898 (1997).

[90] A. I. Larkin and Yu. N. Ovchinnikov. J. Low Temp. Phys. **34**, 409 (1979).

[91] Z. L. Xiao *et al.* Phys. Rev. Lett. **85**, 3265 (2000).

[92] A. B. Kolton, D. Domínguez, N. Grønbech-Jensen. Phys. Rev. Lett. **83**, 3061 (1999).

[93] D. López *et al.* Phys. Rev. Lett. **76**, 4034 (1996).

[94] P. Olsson and S. Teitel. Phys. Rev. Lett. **82**, 2183 (1999).

[95] C. J. Olson, R. T. Scalettar, and G. T. Zimányi. Phys. Rev. B **62**, 3612 (2000).

[96] N. Grønbech-Jensen. Comp. Phys. Comm. **119**, 115 (1999).

[97] C. J. Olson, G. T. Zimányi, A. B. Kolton and N. Grønbech-Jensen. Phys. Rev. Lett. **85**, 5416 (2000).

[98] H. Fangohr, A. E. Koshelev, and M. J. W. Dodgson. arXiv:cond-mat/0210580v1 (2002).

[99] O. Tsui *et al.* Phys. Rev. Lett. **73**, 724 (1994).

[100] L. Bulaevskii, M. Maley and M. Tachiki. Phys. Rev. Lett. **74**, 801 (1994).

[101] Private communication with Mariela Menghini.

[102] A. B. Kolton, D. Domínguez, C. J. Olson, N. Grønbech-Jensen. Phys. Rev. B **62**, R14657 (2000).

[103] S. Shapiro. Phys. Rev. Lett. **11**, 80 (1963).

[104] G. Grüner. Rev. Mod. Phys. **60**, 1129 (1988).

[105] S. Bhattacharya, J. P. Stokes, M. J. Higgins, and R. A. Klemm. Phys. Rev. Lett. **59**, 1849 (1987).

[106] M. J. Higgins, A. A. Middleton, and S. Bhattacharya. Phys. Rev. Lett. **70**, 3784 (1993).

[107] L. Sneddon, M. C. Cross, and D. S. Fisher. Phys. Rev. Lett. **49**, 292 (1982).

[108] S. N. Coppersmith and P. B. Littlewood. Phys. Rev. Lett. **57**, 1927 (1986).

[109] A. A. Middleton, O. Biham, P. B. Littlewood, and P. Sibani. Phys. Rev. Lett. **68**, 1586 (1992).

[110] E. Barthel *et al.* Phys. Rev. Lett. **71**, 2825 (1993).

[111] S. Benz, M. S. Rzchowski, M. Tinkham, and C. J. Lobb. Phys. Rev. Lett. **64**, 693 (1990).

[112] P. Martinoli, O. Daldini, C. Leemann, and E. Stocker. Solid State Commun. **17**, 207 (1975).

[113] L. Van Look, E. Rosseel, M. J. Van Bael, K. Temst, V. V. Moshchalkov. Phys. Rev. B **60**, R6998 (1999).

[114] C. Reichhardt, R. T. Scalettar, G. T. Zimányi, and N. Grønbech-Jensen. Phys. Rev. B **61**, R11914 (2000).

[115] J. M. Harris, N. P. Ong, R. Gagnon, and L. Taillefer. Phys. Rev. Lett. **74**, 3684 (1995).

[116] Y. Togawa, R. Abiru, K. Iwaya, H. Kitano, and A. Maeda. Phys. Rev. Lett. **85**, 3716 (2000).

[117] L. Balents and M. P. A. Fisher. Phys. Rev. Lett. **75**, 4270 (1995).

[118] K. E. Bassler, M. Paczuski, and E. Altshuler. Phys. Rev. B **64**, 224517 (2001).

[119] C. Reichhardt, A. B. Kolton, D. Domínguez, and N. Grønbech-Jensen. Phys. Rev. B **64**, 134508 (2001).

[120] D. Domínguez, V. I. Marconi, A. B. Kolton and N. Grønbech-Jensen. arXiv:cond-mat/0304402 (2003).

[121] A. B. Kolton, D. Domínguez, N. Grønbech-Jensen. Phys. Rev. Lett. **86**, 4112 (2001); **88**, 079902(E) (2002).

[122] S. O. Valenzuela and V. Bekeris. Phys. Rev. Lett. **86**, 504 (2001).

[123] S. O. Valenzuela and V. Bekeris. Phys. Rev. Lett. **88**, 247003 (2002).

[124] R. Besseling *et al.* arXiv:cond-mat/0304046 (2003).

[125] R. Besseling *et al.* arXiv:cond-mat/0302187 (2003).

[126] N. Kokubo *et al.* Phys. Rev. Lett. **88**, 247004 (2002).

[127] A. B. Kolton, D. Domínguez, N. Grønbech-Jensen. Phys. Rev. B **65**, 184508 (2002).

[128] L. Cugliandolo and J. Kurchan. J. Phys. Soc. Jpn. **69**, 247 (2000).

[129] L. Cugliandolo and J. Kurchan. Phys. Rev. Lett. **71**, 173 (1993).

[130] L. Cugliandolo and J. Kurchan. J. Phys. A **27**, 5749 (1994).

[131] Th. M. Nieuwenhuizen. J. Phys. A **31**, L201 (1998).

[132] S. Franz and H. Rieger. J. Stat. Phys. **79**, 749 (1995).

[133] G. Parisi. Phys. Rev. Lett. **79**, 3660 (1997).

[134] J.-L. Barrat and W. Kob. Europhys. Lett. **46**, 637 (1999).

[135] R. Di Leonardo *et al.* Phys. Rev. Lett. **84**, 6054 (2000).

[136] T. S. Grigera and N. Israeloff. Phys. Rev. Lett. **83**, 5038 (2000).

[137] L. Bellon *et al.* Europhys. Lett. **53**, 511 (2000).

[138] D. Herisson and M. Ocio. Phys. Rev. Lett. **88**, 257202 (2002).

[139] A. Barrat *et al.* Phys. Rev. Lett. **85**, 5034 (2000).

[140] H. Makse and J. Kurchan. Nature (London) **415**, 614 (2002).

[141] A. Barrat *et al.*

[142] L. Berthier *et al.* Phys. Rev. E **61**, 5464 (2000).

[143] J.-L. Barrat and L. Berthier. Phys. Rev. E **63**, 012503 (2001).

[144] L. Berthier and J.-L. Barrat. J. Chem. Phys. **116**, 6228 (2002).

[145] L. Cugliandolo *et al.* Phys. Rev. Lett. **78**, 350 (1997).

[146] J. M. Caillol *et al.* J. Stat. Phys. **28**, 325 (1982).

[147] H. Yoshino. Phys. Rev. Lett. **81**, 1493 (1998).

[148] I. K. Ono *et al.* Phys. Rev. Lett. **89**, 095703 (2002).

[149] J. R. Clem. Phys. Rep. **75**, 1 (1981).

[150] Z. Ovadyahu and M. Pollak. Phys. Rev. Lett. **79**, 459 (1997).

[151] A. Vaknin, Z. Ovadyahu, and M. Pollak. Phys. Rev. Lett. **81**, 669 (1998).

[152] A. Vaknin, Z. Ovadyahu, and M. Pollak. Phys. Rev. B **61**, 6692 (2000).

[153] A. Vaknin, Z. Ovadyahu, and M. Pollak. Phys. Rev. Lett. **84**, 3402 (2000).

[154] A. Vaknin, Z. Ovadyahu, and M. Pollak. Phys. Rev. B **65**, 134208 (2002).

[155] A. L. Efros and B. I. Shklovskii. J. Phys. C **8**, L49 (1975).

[156] J. H. Davies, P. A. Lee, and T. M. Rice. Phys. Rev. Lett. **49**, 758 (1982).

[157] U. C. Täuber, H. Dai, D. R. Nelson, and C. M. Lieber. Phys. Rev. Lett. **74**, 5132 (1995).

[158] B. I. Shklovskii and A. L. Efros. *Electronic Properties of Doped Semiconductors*, Springer-Verlag, Berlin, 1984.

[159] A. L. Efros and B. I. Shklovskii. In *Electron-Electron Interactions in Disordered Systems*, edited by A. L. Efros and M. Pollak, Elsevier Science Publishers B.V., 1985, p. 409.

[160] S. D. Baranovskii, B. I. Shklovskii, and A. L. Efros. Zh. Eksp. Teor. Fiz. **78**, 395 (1980).

[161] S. D. Baranovskii *et al.* J. Phys. C **12**, 1023 (1979).

[162] H. Dai *et al.* Science **265**, 1552 (1994).

[163] S. Behler *et al.* Phys. Rev. Lett. **72**, 1750 (1994).

[164] N. F. Mott. J. Non-Cryst. Solids **1**, 1 (1968).

[165] M. Pollak and M. Ortuño. In *Electron-Electron Interactions in Disordered Systems*, edited by A. L. Efros and M. Pollak, Elsevier Science Publishers B.V., 1985, p. 287.

[166] I. Morgenstern, K. Binder, R. M. Hornreich. Phys. Rev. B **23**, 287 (1981).

[167] W. Xue and P. A. Lee. Phys. Rev. B **38**, 9093 (1988).

[168] E. R. Grannan and C. Yu. Phys. Rev. Lett. **71**, 3335 (1993).

[169] T. Vojta and M. Schreiber. Phys. Rev. Lett. **73**, 2933 (1994).

[170] M. Ben-Chorin, Z. Ovadyahu, and M. Pollak. Phys. Rev. B **48**, 15025 (1993).

[171] M. Pollak. Philos. Mag. B **50**, 265 (1984).

[172] A. A. Mogilyanskii and M. E. Raikh. Sov. Phys. JETP **68**, 1081 (1989).

[173] C. Yu. Phys. Rev. Lett. **82**, 4074 (1999).

[174] L. Civale *et al.* Phys. Rev. Lett. **67**, 648 (1991).

[175] U. C. Täuber and D. R. Nelson. Phys. Rev. B **52**, 10106 (1995).

[176] J. Lekner. Physica A **176**, 485 (1991).

[177] S. D. Baranovskii and A. A. Uzakov. Solid State Commun. **36**, 829 (1980).

[178] E. R. Grannan and C. Yu. Phys. Rev. Lett. **73**, 2934 (1994).

[179] M. Matsumoto, K. Hukushima, and H. Takayama. arXiv:cond-mat/0204225 (2002).

[180] R. N. Bhatt and A. P. Young. Europhys. Lett. **20**, 59 (1992).